SYNTHESIS AND CHARACTERISATION OF COMPLEX OXYCHALCOGENIDES

by

Reeya Krishvi Oogarah

A thesis submitted in partial fulfilment of the requirements
for the degree of Doctor of Philosophy at the University of
Kent

School of Physical Sciences

September 2017

Abstract

Mixed-anion compounds like oxychalcogenides, where there are both oxide anions and chalcogen anions (S-Te) create quite a rare class of materials which is gaining increasing attention. The anions have different sizes and chemical requirements which promise ordering of the oxide crystallographically, whereby their structures can be described as a mixture of 2-D structural building blocks (e.g. perovskite, fluorite, or rock-salt) stacked on top of each other along a given direction, thus giving a layered structure. These results in interesting electrical, optical and physical properties. This thesis reports a study of oxychalcogenide compounds with general formula $Ln_2O_2Fe_2OQ_2$ (Ln = lanthanide, Q = chalcogenides) and $LnMOCh_2$ (Ln = Lanthanides, M = cation and Ch = chalcogenides). These compounds offer big opportunities for chemical substitution and doping within and between the layers, hence it is possible to tune the layer distances and in turn, tune the properties of these solids. The crystal structures and properties of all materials were investigated using several in-house techniques and those at central facilities. Electron doping $La_2O_2Fe_2OSe_2$ with Co and Ni ions onto the Fe^{2+} site gave limited solid solutions and semiconductor materials. Co-doping increased the transition temperature of $La_2O_2Fe_2OSe_2$ indicating that the distance between the Fe_2O layers is reduced. Variable temperature neutron powder diffraction data of $La_2O_2Fe_2OS_2$ showed 2-D short range order while neutron powder diffraction data in applied magnetic field of $Pr_2O_2Fe_2OSe_2$ showed a subtle orthorhombic distortion around 23 K. Additional magnetic Bragg reflections, seen in both compounds, are consistent with a 2-k magnetic structure with a 2a x 2a x 2c unit cell. Moreover, both compounds showed stacking faults in the magnetic ordering on the Fe^{2+} sublattice which are absent in Mn_2O or Co_2O systems, implying that they are exclusively to the Fe_2O layers and could be sensitive to the distance between Fe_2O layers. Isovalent doping $LaGaOS_2$ with Nd and Ce ions onto the La site gave limited solid solutions. From the diffuse reflectance spectroscopy data, Nd-doping and Ce-doping the parent compound gave no significant change in optical band gaps and the colour change observed in colour in Nd-doped samples are presumably due to f-f transitions. This work suggests that $LaGaOS_2$ has a quite limited compositional flexibility in its structure and that it is not easy to modify its electronic structure using chemical pressure. Electron doping BiCuOSe with Ce (onto the Bi^{3+} site) and F ions (onto the O^{2-} site) gave limited solid solutions. BiCuOSe had some Cu vacancies. The Ce-doped samples contained Ce^{4+} ions. Electron doping BiCuOSe with F gave metallic compounds, while doping BiCuOSe with Ce gave compounds with both semiconducting and metallic behaviour. The semiconducting behaviour may be due to impurities.

Abbreviations

AFM	Antiferromagnetic
χ^2	Chi squared
CIF	Crystallographic Information file
DFT	Density Functional theory
DRS	Diffuse Reflectance Spectroscopy
E_a	Activation energy
ξ_c	Correlation length
EXAFS	Extended X-ray Absorption Fine Structure
FC	Field cooled
FM	Ferromagnetic
ICSD	Inorganic crystal structure database
MPMS	Magnetic properties measurement system
NPD	Neutron powder diffraction
Oe	Oersted
PPMS	Physical Property Measurement System
ρ	Electrical resistivity
R_p	Profile R-factor
R_{wp}	Weighted R-factor
SEM-EDX	Scanning Electron Microscopy-Energy Dispersive X-ray
SQUID	Superconducting quantum interference device
t.o.f	Time of flight
VT	Variable temperature
XANES	X-ray absorption near-edge structure
XAS	X-ray absorption Spectroscopy
XRPD	X-ray powder diffraction
XPS	X-ray Photoelectron Spectroscopy
Z	Atomic number
ZFC	Zero-field cooled
ZT	Thermoelectric figure of merit
2D-VRH	Two-dimensional variable range hopping

Declaration and Copyright

I hereby declare that the work presented in this thesis is entirely that of the author, apart from where due acknowledgment has been made. This work has not been previously submitted, in whole or in part, for any other academic degree.

Acknowledgements

First of all, I would like to thank my supervisor Dr Emma E. McCabe for giving me the opportunity to do this PhD and for all her guidance, help and support. I would also like to thank my second supervisor Dr Donna Arnold for reading my first year report, doing my first year Mock Viva and for driving us to conferences. I would also like to thank my collaborators: Dr Mike Reece for SPS measurements, Dr Robert Palgrave for XPS and photocatalytic measurements, Dr Alan Chadwick and Dr Dave Pickup for XANES measurements and helpful discussions and Dr Paz Vaqueiro for thermoelectric measurements.

I have numerous people to thank to make this PhD and thesis possible:

- Dr Maria Alfredsson for all her support and guidance throughout all my years at the University of Kent and for making me feel welcome when I moved to Ashford (dinners, quiz nights, useful discussions).
- Technicians: Ian Ross and Dave pickup for advising me when devising equipment set-ups. Ian Ross for connecting gas lines and for all the good banters.
- Marcus and Francesco for their help with Athena (especially at 1am and 3am respectively that one particular day). Marcus for his help with Absorbix and Francesco for his help with TGA.
- Dr Paul Saines for driving us to conferences.
- The Solid State Chemistry group (Laura, Dan, Lindsay, Chris and Ben) for helping me with everything really and for always tagging along to conferences and workshops. We always did everything together. You were my family!
- All the people from room 104 (2013-2016) for all their help with my work, throwing stress balls at each other, Justin for attacking me with his rocket launcher and for his various games nights (especially the famous Resistance game night). Also, thanks for the regular Friday evenings at the Unicorn pub which led to awesome nights and helpful discussions.
- My brother Ronish and Helen for proofreading my thesis, my parents for making my academic career possible and for their continued support, and the rest of my family.

And, finally, Rachael for, well, everything.

List of publications from this work

R. K. Oogarah, C. P. J. Stockdale, C. Stock, J. S. O. Evans, A. S. Wills, J. W. Taylor, and E. E. McCabe, "*Crystal field excitations and magnons: Their roles in oxyselenides $Pr_2O_2M_2OSe_2$ (M=Mn, Fe)*", Phys. Rev. B, 2017, 95, 174441

R. K. Oogarah, E. Suard, and E. E. McCabe, "*Magnetic order and phase transition in the iron oxysulfide $La_2O_2Fe_2OS_2$*", Journal of Magnetism and Magnetic Materials, **2017**.

R. K. Oogarah, G. Stenning, J. S. O. Evans, and E. E. McCabe, "*Electron-doping studies of Mott-insulating $La_2O_2Fe_2OSe_2$*" (In preparation)

Table of contents

List of Figures

12

List of Tables

List of Appendices

Chapter 1: Introduction

<u>1.0 Layered oxychalcogenides</u>

Oxychalcogenides are materials which contain an oxide (O^{2-}) ion and a chalcogenide (S^{2-}, Se^{2-}, Te^{2-}) anion in contrast to common species such as sulfates where the chalcogen has a more positive formal charge. The presence of more than one anion (with different sizes and bonding characters) can lead to anion-ordering and unusual crystal structures. These anions are coordinated to one or more cations in the crystal structure creating alternating layers of oxides and chalcogenides. The structures of layered oxychalcogenides can be described as a mixture of structural building blocks (e.g. perovskite, fluorite, or rock-salt which are two-dimensional building blocks) which are stacked on top of each other along a given direction, thus generating the layered structure.[1] These mixed anion systems are thought-provoking because they usually contain transition metals in unconventional chemical or electronic environments. The "hard" cations (group 1 and 2 metals, early transition metals and lanthanides), which are less polarisable, are usually coordinated to smaller, more electronegative O^{2-} anions while the "soft" cations (with low energy d orbitals), which are more polarisable, are coordinated to bigger chalcogenide anions. This usually gives rise to distinct oxide like portions and chalcogenide-like portions along with exciting electronic properties. Moreover, the chalcogenide layers have covalent character which encourages semiconductivity, while the oxide layers have ionic character which encourages low thermal conductivity. Having the alternate layers in oxychalcogenides makes it interesting to manipulate them by tuning their properties by chemical substitution in both layers. This suggests possible uses as thermoelectric materials, photocatalysts for water splitting, and p-type transparent semiconductors for optoelectronic applications, superconductivity amongst others.[2–5]

Oxychalcogenides are an underexplored class of compounds when compared with pure oxides and chalcogenides. Ternary oxysulfides (having the cation of one electropositive element, oxide and sulfide) are acknowledged for the group 3 elements, and the lanthanides and Ln_2O_2S ($Ln=$ lanthanides) are of much importance as they can be used as inorganic phosphor materials.[6] Besides these materials, the only other ternaries' crystal structure having been characterised are ZrOS, HfOS, Bi_2O_2S and Sb_2OS_2.[7–11]

In quaternary and higher oxychalcogenides (one or more cations of electropositive elements are coordinated by both oxide and chalcogenide anions), the oxide ions are usually coordinated by "hard" cations, while the chalcogenide ions (which are more polarisable), are coordinated by "softer" cations, which are more polarising. As a result, both the *Ln*CuOS (*Ln* = Lanthanides) series where the fluorite-type *Ln*O layers and the antifluorite-type CuS layers alternate, and the quinary compounds $A_2MO_2Cu_2S_2$ (*A* = electropositive metal, *M* = transition metal), where there are alternate CuS layers and A_2MO_2 layers, have shown to be *p*-type transparent semiconductors.[12–16] This is due to the Cu 3*d* and S 3*p* antibonding states in the top of the valence.[17]

1.1 ZrCuSiAs-type structures

The first 1111 oxychalcogenide which was synthesised was LaOAgS, which is an ionic conductor.[18] This material crystallises in a ZrCuSiAs type-structure with conductive AgS layers separated by charge reservoir LaO layers, similar to the cuprates.[19] The ZrSiCuAs structure is very common for quaternary mixed-anion systems, and shows a great amount of compositional flexibility.[20] The structure consists of alternating layers of PbO-type lanthanide-oxide and anti-PbO type metal-chalcogenide (Figure 1.01). Materials with the general formula [*AO*][*BCh*] (where *A* = Bi, Y, La-Yb, *B* =Cu, Ag and *Ch* = chalcogenide anion) crystallise in the tetragonal ZrCuSiAs structure.[18,21–25] Previously, the A^{3+} ions were primarily the lanthanides and Y^{3+} until Kholodkovskaya *et al* presented the world with the substitution of Bi^{3+} onto the *A* site. The [*AO*][*BCh*] crystal structure consists of PbO-type $[A_2O_2]^{2+}$ layers and anti-PbO type $[B_2Ch_2]^2$ layers alternatively stacked along the c-axis (Figure 1.02).[24] This type of structure has been reported for numerous compounds consisting of O^{2-}, F^-, chalcogenides, pnictides, hydrides, silicide and germanide.[20] These rare-earth-oxychalcogenides have been mainly investigated for their optoelectronic properties, since several are transparent p-type semiconductors.[26]

LaCuOS is a layered mixed-anion oxysulfide with PbO-type $(LaO)^+$ layers and anti-PbO type $(CuS)^-$ layers which alternate along the c-axis (Figure 1.02).[27] The Cu ion is only coordinated to sulfide while the oxide anion is coordinated to the lanthanide, both in a tetrahedral arrangement. It has a wide band gap (3.1 eV) and shows *p*-type electrical conductivity due to allowed direct transition between the valence band maximum and the conduction band minimum.[4,28,29] Doping Se on the S site, showed improved properties in their electrical and optical properties.[30]
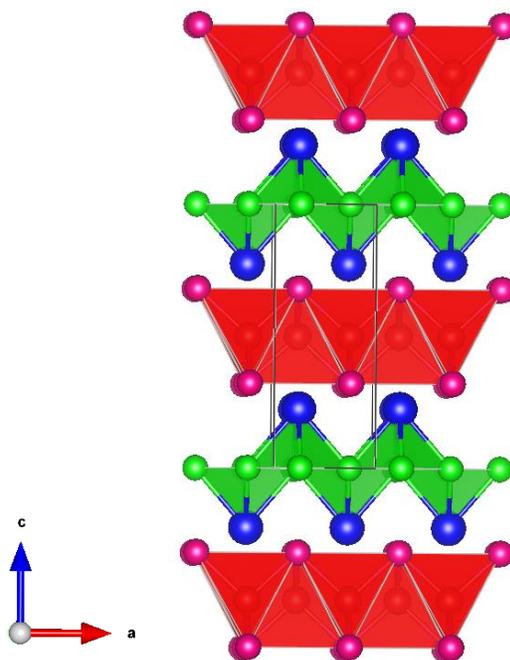
Figure 1.01. ZrCuSiAs structure. Zr cations are in blue, Cu^+ cations in red, Si anions in green and As anions in pink.

Several lanthanide ions can replace La^{3+} ions in LaCuOS and they show similar crystal structures to LaCuOS, although CeCuOS behaves slightly anomalously.[22,31,32] Chan et al investigated non-stoichiometric $CeCu_{0.8}OS$ and through refined crystal structure and chemical analyses, they showed that the reason why CeCuOS has a smaller unit cell was because of the formation of the Cu vacancies and the associated oxidation of some Ce^{3+} ions to Ce^{4+}.[21] Due to their similar crystal structures, it is expected that *Ln*CuOS analogous (*Ln* = Ce, Pr and Nd) will have similar electrical and optical properties, although the 4*f* electrons found in the lanthanide ions can have an effect on their electronic structure and hence, give different properties. Ueda *et al* investigated this and showed that they exhibit wide band gap p-type semi-conductivity and the *f-f* transitions absorption showed that the 4*f* electrons are localised and hence, have no effect on the optical properties.[29] Because of lanthanide contraction, ionic size decreases across the lanthanides and this decreases the *a*-axis and *c*-axis. This, in turn, maximises the Cu ions interactions inside the $(Cu_2S_2)^{2-}$ layers, while causing a greater interaction between the $(Cu_2S_2)^{2-}$ layers. This results in the energy gap decreasing in LnCuOS (Ln = La-Nd). CeCuOS has a high electrical conductivity and is a degenerate semiconductor in a semi-metallic state with an empty band near the Fermi level which might contribute to CeCuOS's unique electrical and optical properties. It was suggested that this might be because the concentration of the carriers was not as much as for the other metals.
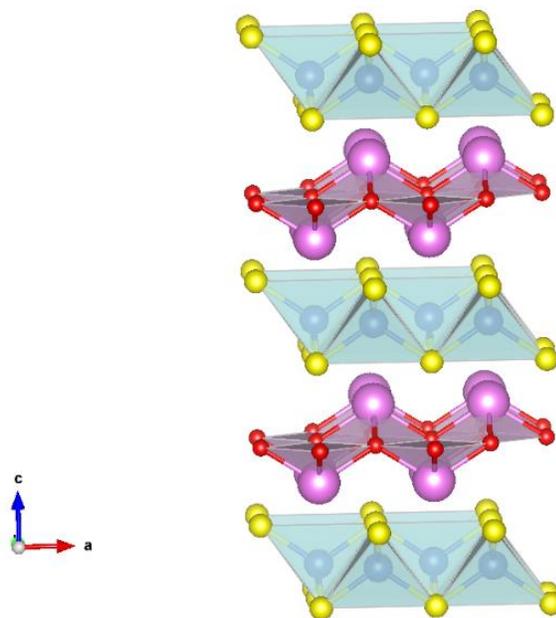
Figure 1.02 Crystal structure of LaCuOS. Lanthanum ions are in pink, oxygen ions are in red, copper ions are in blue and sulfur ions are in yellow.

1.2 *LnMOCh₂*-type structures

Relatively few *LnMOCh₂* (*Ln* = Lanthanides, *M* = cation and *Ch* = chalcogenides) type structures are known. They consist of rigid $(Ln_2O_2)^{2+}$ and $(M_xCh_z)^{2-}$ (x and z are integers) layers. The $(Ln_2O_2)^{2+}$ layers contain edge sharing LnO_4 tetrahedral while the *M* (cation) can be in tetrahedral or octahedra of chalcogenide atoms.

$La_4O_4Ga_{1.72}S_{4.58}$ adopts a tetragonal, layered structure, consisting of fluorite-like $[La_2O_2]^{2+}$ layers (similar to those of the ZrSiCuAs structure, Figure 1.01) separated by Ga-S layers in which Ga^{3+} cations partially occupy octahedral sites (Figure 1.03).[33] The crystal structure of $La_4O_4Ga_{1.72}S_{4.58}$ resemble those of $Ce_4O_4Ga_2S_5$, except that in the latter more metal atoms of smaller charges can be introduced and they differ in their lattice structure where $La_4O_4Ga_{1.72}S_{4.58}$ has a primitive lattice while $Ce_4O_4Ga_2S_5$ has a face-centred lattice.[34]This paper allowed Benazeth et al to synthesise and study the structure of $La_4O_4Ga_{1.88}S_{4.82}$ which means that other non-stoichiometric versions of $La_4O_4Ga_{1.72}S_{4.58}$ are feasible. $La_4O_4Ga_{1.72}S_{4.58}$ is observed as an impurity in Chapter 5 when dealing with *Ln*-doped $LaGaOS_2$ (*Ln* = Lanthanides).[35]
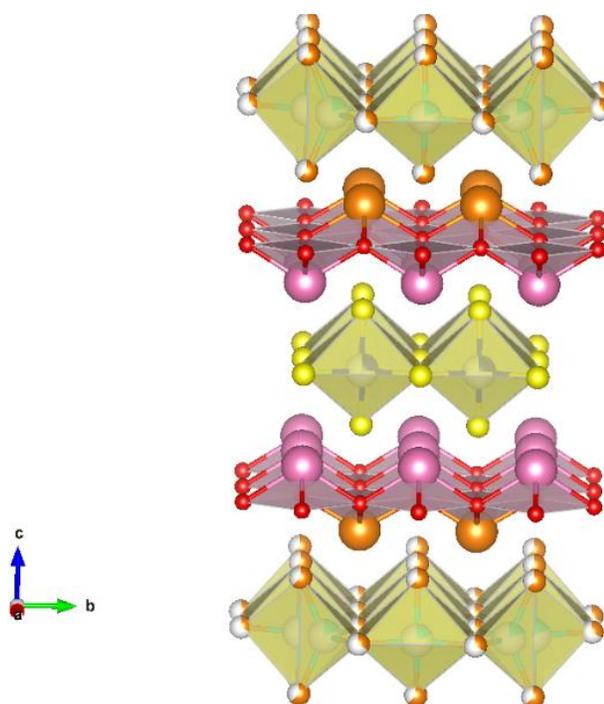
Figure 1.03. Crystal structure of $La_4O_4Ga_{1.72}S_{4.58}$. Lanthanum (1) ions are in dark orange, Lanthanum (2) ions are in pink, oxygen ions are in red, gallium (1) ions are in blue, gallium (2) ions are in aqua, sulfur (1) and sulfur (2) ions are in yellow and sulfur (3) and sulfur (4) ions are in pale-orange.

In contrast, $Nd_4O_4Ga_2S_5$ adopts an orthorhombic structure, space group *Pbca* (Figure 1.04). The layers are composed of fluorite-like $(Ln_2O_2)^{2+}$ layers and Ga-S layers similar to those in $La_4O_4Ga_{1.72}S_{4.58}$ and $Ce_4O_4Ga_2S_5$ but rather than being octahedrally coordinated for Ga^{3+} ions in the larger La^{3+} and Ce^{3+} analogues, the Ga^{3+} cations fully occupy tetrahedral sites and the layers are buckled (Figure 1.04). No properties have yet been reported for this compound.
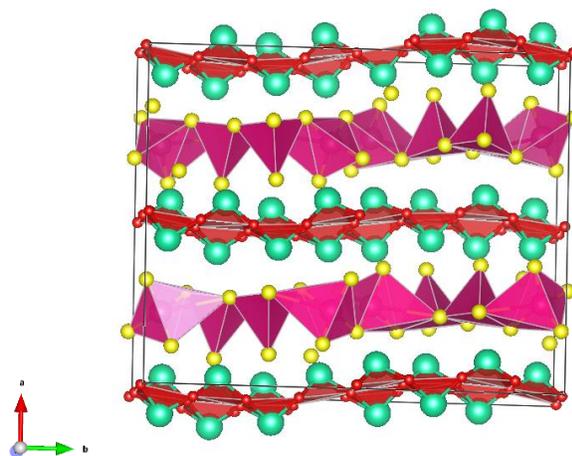
Figure 1.04. Crystal structure of $Nd_4O_4Ga_2S_5$. Nd ions are in aqua, oxygen ions are in red, gallium ions are in pink, sulfur ions are in yellow.

LaGaOS$_2$ was first reported in 1978 by Jaulmes from studying the phase diagram of La$_2$O$_2$S-Ga$_2$S$_3$.[36] The paper investigated the structure of LaGaOS$_2$ but no properties were reported. LaGaOS$_2$ has a KVO$_3$-type structure with an orthorhombic unit cell and a *Pmca* space group. In this structure, double chains of corner linked tetrahedra (GaO$_2$S$_2$) extend along the *a*-axis with La^{3+} cations separating these chains along the *c*-axis (Figure 1.05). These Ga-containing phases have shown to exhibit good photocatalytic activity.[37,38] Hence, the investigation of isovalent doping of LaGaOS$_2$ will be carried out and the effect it has on its corresponding changes in properties as well as investigate the flexibility of the compound which might suggest why this class of materials is not abundant.
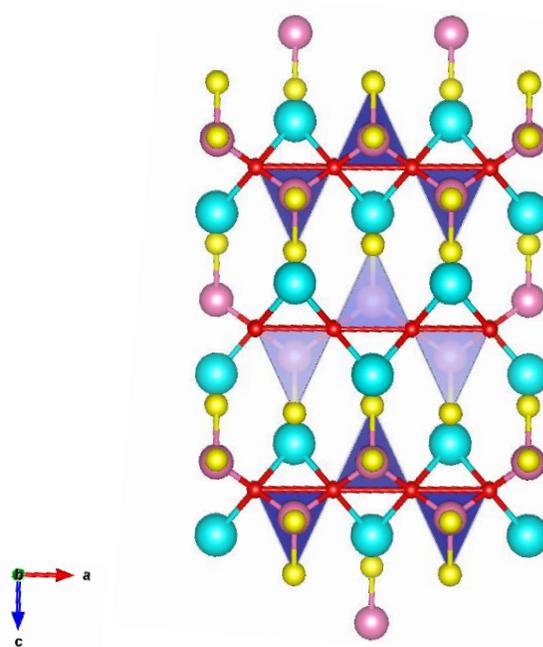
Figure 1.05. KVO$_3$-type structure of LaGaOS2 with lanthanum ions in aqua, gallium ions in pink, oxygen ions in red and sulfur ions in yellow.

1.3 *M$_2$*O-type layered-materials

These materials adopt a layered structure, with [*Ln*$_2$O$_2$]$^{2+}$ layers and anti-CuO$_2$-type [*M*$_2$O]$^{2+}$ (*M* = transition metal) layers, separated by Se^{2-} ions (Figure 1.06). This crystal structure is not common as the transition metal is in a face-sharing octahedron, where the *M*$^{2+}$ ion is linked with two axial O^{2-} ions and four equatorial *Ch*$^{2-}$ ions. The lanthanide ions are linked to four O^{2-} ions and four *Ch*$^{2-}$ ions creating a square anti-prismatic arrangement. This structure arrangement is very unusual and hence, prompted research into those compounds. The La$_2$O$_2$Fe$_2$OSe$_2$ structure and La$_2$O$_2$Fe$_2$OS$_2$ were first reported by Mayer *et al* and since then, other compounds have been synthesised and

investigated such as $Ln_2O_2M_2OSe_2$ (Ln = La-Pr and M = Mn, Fe, Co) systems. [39–41] Resistivity measurements for $La_2O_2M_2OCh_2$ (M = Mn, Co and Fe, Ch = chalcogenide) systems showed that they are semiconducting at room temperature.[39,42] Theoretical studies for $La_2O_2Fe_2OCh_2$ (Ch = chalcogenides) indicated that that mainly the Fe 3d electrons contribute to the density of states near the Fermi level and that the 3d bandwidths which are seen are more narrow than in the LaOFeAs structure, thus, these materials are Mott insulators.[43] Therefore, electron doping $La_2O_2Fe_2OSe_2$ on the Fe site will be carried out and the properties will be tuned.
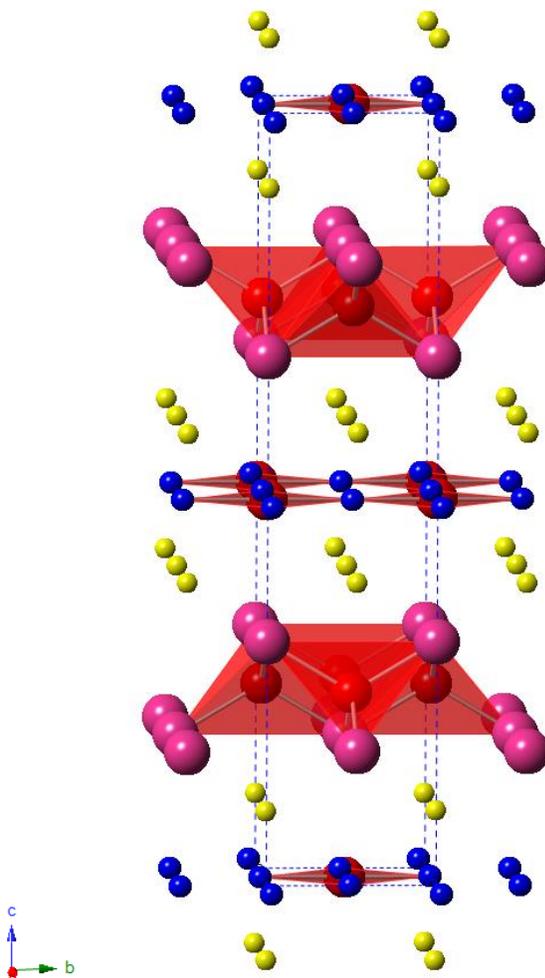
Figure 1.06 Crystal structure of $La_2O_2Fe_2OSe_2$. La atoms are in pink, Fe atoms are in blue, O atoms are in red and Se atoms are in yellow.

1.4 Electrical properties

The electrical conductivity of a material is defined in terms of how easily charge flows through it. Ohm's law relates the current and applied voltage as follows:

$$V = IR$$ Equation 1.01

Where, V = Applied voltage (V)

I = Current (A)

R = Resistance (Ω)

The material's electrical resistance depends on the object's geometry and is not an intrinsic property:[124]

$$\rho = RA/l$$ Equation 1.02

Where, R = Electrical resistance of a uniform specimen of the material

A = Cross-sectional area

l = Length of object

ρ = Resistivity

Electrical resistivity is an intrinsic property that quantifies how much a material opposes the electric current flow where a low resistivity means that the current can easily flow. Resistance is dependent on the sample's length and cross-sectional area and each material has its own distinguishing resistivity. In quantum mechanics, electrons in atoms occupy discrete energy levels and energies between these levels are impossible. When a sufficiently large number of these allowed energy levels are close together, they can be seen as an energy band. This depends on the atomic number and their distribution. The electrons try to decrease the total energy in the material by inhabiting low energy states, however, due to the Pauli exclusion principle, the electrons instead fill up the band structure by starting from the bottom lowest energy states.[125]The Fermi level is the energy level up to which the electrons have filled up and its position in the band structure is crucial for electrical conduction. Above absolute zero temperatures, the electrons located in the energy levels which are near the Fermi level have enough thermal energy to get promoted to the empty levels above the Fermi level. This drift in electrons cause electrical conductivity. The electrons which are not involved in bonding will stay in the core band whereas the valence electrons which form the

electron gas go into the valence band. The leftover unfilled orbitals form higher energy bands (conduction bands) which allow electron conduction int eh material. The locations of the bands and the band gaps are dependent on the type of atom, how far apart the atoms are in the solid, and the atomic arrangement. Electrical conductivity of a material can be controlled by regulating either the number or the mobility of the charge carriers. Electrons and holes are prime charge carriers.[126–128]

In metals, the Fermi level is located in the conduction band and the electrons can move around, hence the high electronic conductivity in metals. The electrical resistivity increases with temperature due to electron-phonon interactions and at high temperatures, there is a linearity between the resistance and the temperature. This is given by the Bloch-Gruneisen formula:[129]

$$\rho(T) = \rho(0) + A\left(\frac{T}{\Theta_R}\right)^n \int_0^{\Theta_R/T} \frac{x^n}{(e^x-1)(1-e^{-x})}dx \qquad \text{Equation 1.03}$$

Where, $\rho(0)$ = Residual resistivity because of defect scattering (when resistivity has a constant value as all the phonons are frozen)

      A = Constant depending on velocity of electrons at Fermi surface, the Debye radius and number of electrons density in the metal

      Θ_R = Debye temperature[130] obtained from resistivity measurements

      n = Integer depending on nature of interaction.

Band theory suggests there may be forbidden bands in energy, that is, energy intervals that have no energy levels. In semiconductors and insulators, the number of electrons is in exact amount to fill a specific number of low energy bands and the Fermi level is located within a band gap, with the latter being very large compared to the undoped semiconductor. Since the states near the Fermi level are not free, the electrons cannot move, and the electronic conductivity is very low. In semiconductors, the Fermi level is located in between the conduction band minimum and the valence band maximum for undoped semiconductors which means that at 0 K, the resistance is infinite as the electrons cannot move. However, as the charge carrier density in the conduction band is enhanced, the resistance diminishes. Moreover, the resistivity decreases when temperature increases, and the electrons move to the conduction band while creating vacancies in the valence band. In doped semiconductors, the dopants augment most charge carrier concentration by giving electrons to the conduction band or producing vacancies in the valence band. In both cases, increasing dopant decreases resistance. Hence, semiconductors which are highly doped have a metallic behaviour and at very high temperatures, the resistance decreases exponentially with

temperature.[131] Based on the conductivity values, materials can be classified into metals (>10^7 Ωm^{-1}), semiconductors (10^{-6}-10^{-4} Ωm^{-1}) and insulators (<10^{-10} Ωm^{-1}).[126–128]

1.4.1 Metals

In metals, the highest occupied band is partially filled. The electrons occupy states up to the Fermi energy level and there are empty states just above the Fermi level. Conduction happens by promoting electrons into the conduction band, that starts right above the Fermi level (Figure 1.07). The energy needed to promote electrons is tiny such that at any temperature electrons can be found in the conduction band. The number of electrons involved in electrical conduction is very small. Metals have high conductivities as there are several energy levels near the Fermi level. Resistance increases with increasing temperature.[126,127]
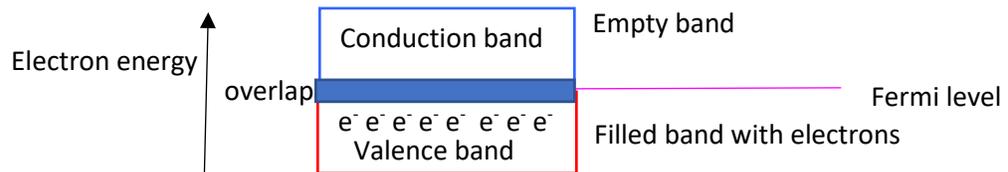
Figure 1.07 Electrical conductivity in metals.

1.4.2 Semiconductors

In semiconductors, the valence band and conduction bands do not overlap like in metals and are separated by an energy band gap (< 2 eV). The valence band is full, and no more electrons can be added as per Pauli's principle. At low temperature, electrons do not have enough energy to occupy the conduction band but at higher temperature some electrons have enough energy to make the transition to the conduction band. The density of electrons in the conduction band at room temperature is not as high as in metals, hence, they cannot conduct current as well as a metal. In semiconductors, resistance decreases with increasing temperature. Most common semiconductors are crystalline solids, but they can also be amorphous and liquid. There are 2 types of semiconductors: intrinsic and extrinsic. In intrinsic semiconductors, the electrical behaviour depends on the inherent electronic structure of the pure material, while in extrinsic semiconductors, the electrical behaviour is governed by dopant concentration.[126–128,132–134]

1.4.2.1 Intrinsic Semiconductors

Intrinsic semiconductors are pure semiconductors with no impurities in them. Consequently, they are characterised by an equal chance of finding a hole in the valence band as that of an electron in the conduction band. This means that the Fermi-level is exactly in between the conduction band minimum and the valence band maximum (Figure 1.08). When electrons are promoted, conduction occurs and charged holes are left behind. This results in a greater number of free electrons and at these temperatures, the concentration of thermally excited electrons located in the conduction band gets so high that the semiconductor behaves similar to a metal. In term of application in devices, semiconductors are rarely used in their intrinsic composition.[115,134]

1.4.2.2 Extrinsic Semiconductors

An extrinsic semiconductor is one into which a dopant has been introduced, which results in different electrical properties compared to the intrinsic semiconductor. They exhibit higher conductivities than intrinsic semiconductors at normal temperatures. By adding dopant atoms to an intrinsic semiconductor, the electron and hole carrier concentrations are altered at thermal equilibrium. Impurity atoms can be either donors or acceptors based on the effect they have on the semiconductor. Donors have more valence electrons than the atoms they replace in the intrinsic semiconductor lattice and these extra electrons occupy a discrete donor level. The band gap between the donor Fermi level and the bottom of the conduction band is tiny. Although there are not enough extra electrons to form a continuous band, they can possess enough thermal energy to be promoted in the conduction band where they increase the electron carrier concentration of the semiconductor, making it *n*-type. Acceptors, on the other hand, have fewer valence electrons than the atoms they replace. The band gap between the acceptor Fermi level and the top of the valence band is tiny. Hence, electrons from the valence band of the semiconductor can possess enough thermal energy and get promoted into the acceptor level. This in turn leave excess positive holes behind which can move and increase the hole carrier concentration of the semiconductor, making it *p*-type. Moreover, doping causes the Fermi energy level to change and its position is determined by the temperature and the concentration of the donor.[115,134]

In *n*-type semiconductors, electrons are the majority carriers and holes are the minority carriers (Figure 1.08). Pentavalent substitutional atoms, such as P, As and Sb, can be used as donors for Si-based semiconductors.[126–128]

Electron energy

Conduction band
e⁻ e⁻ e⁻ e⁻ e⁻   electrons
Donor Fermi level ---------------◆ New band gap
─────── Fermi level of intrinsic semiconductor

Valence band   holes
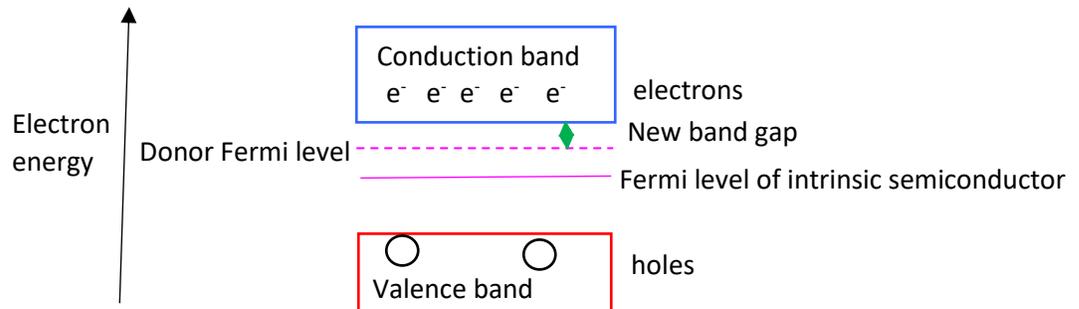
Figure 1.08 *n*-type semiconductor

In *p*-type semiconductors, holes are the majority carriers and electrons are the minority carriers (Figure 1.09). Trivalent substitutional atoms, such as B, Al, Si and Ga, can be used as donors for Si-based semiconductors.[126–128]

Electron energy

Conduction band
e⁻   e⁻   electrons

─────── Fermi level of intrinsic semiconductor
Acceptor Fermi level ------------◆ Band gap
Valence band   holes
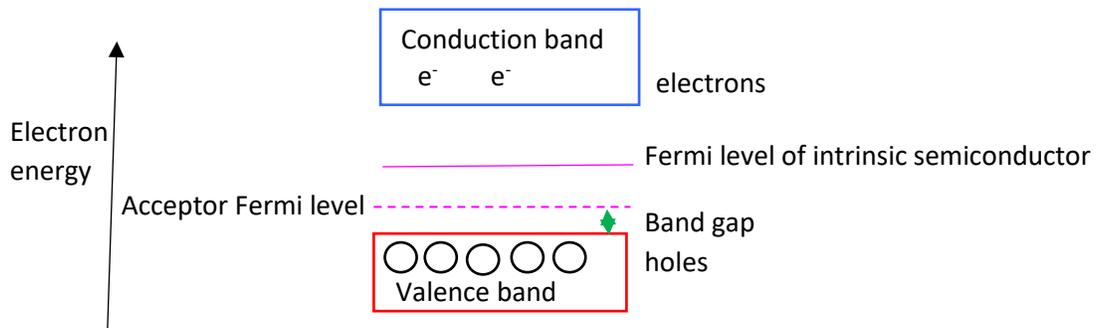
Figure 1.09 *p*-type semiconductor

1.4.3 Insulators

In insulators, the valence band is full, and energy is required to promote an electron from the valence band to the empty conduction band. Electrical conduction requires that electrons be able to gain energy in an electric field. To be free, electrons must be excited, by means of heat or light, across the band gap. However, the forbidden band gap is very large (> 4 eV) (larger than in

semiconductors) and hence, the energy required by the electron to be promoted to the conduction band is too large (Figure 1.10).[126–128]
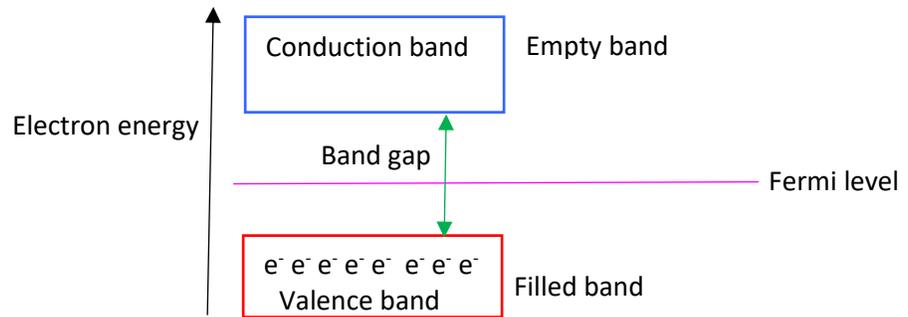
Figure 1.10 Insulator

A Mott insulator has an energy band gap (due to non-metallic character), unpaired electrons (which causes magnetic properties) and displays crystal field transitions which are typical of open-shell ions.[135,136] This is due to electron–electron interactions, which are neglected in conventional band theory and which causes the breakdown of normal band properties for the d electrons.[137] In insulators, the orbitals interaction which creates the band width is as follows: $4f < 5f < 3d < 4d \sim 5d$. The late first row transition metals are Mott insulators and hence, the local effects of electron-electron interactions are quite significant, for example, MnO_2, where the overlap of the two adjacent d orbitals is small and hence give narrow bands. The degeneracy of the formed bands is removed under the strong influence of an anisotropic crystal field. The ligand p orbitals which is close to the Fermi level are strongly hybridized with the corresponding d orbitals or are far from the Fermi level. Hence, a narrow single electronic band remains close to the Fermi level The exact value of the band gap is hard to measure d^n due to compounds having d-d transitions at lower energy, presence of defects and non-stoichiometry.[135] In Mott insulators, the small energy interactions between magnetic ions causes cooperative magnetic ordering below a critical temperature (Curie temperature), while above it, the paramagnetic susceptibility follows a Curie-Weiss behaviour.[115] These effects are however weak in terms of the overall electronic structure.[135] Mott insulators can be used in memristors and actuators.[138,139]

1.5 Thermoelectric materials

Thermoelectric materials can convert a temperature gradient into electrical power and vice versa. They are in high demand in electric power generation as waste heat recovery and in the cooling of

electronic devices. However, they have poor energy conversion efficiency and their use could be expanded. The efficiency for a thermoelectric material is given by the dimensionless figure of merit ZT:

$$ZT = \frac{S^2 \sigma T}{\lambda}$$

Equation 1.04

Where, S = Seebeck coefficient or thermopower

σ = Electrical conductivity

λ = Thermal conductivity

T = Absolute temperature

A ZT = 1 is usually needed for efficient thermoelectric energy conversion. However, the three parameters (λ, S and σ) cannot be tuned independently. λ is directly linked to σ and S decreases with charge carriers concentration while σ increases with charge carriers concentration. The ideal thermoelectric material should have the electrical conductivity of a metal, the thermal conductivity of a glass and the charge carriers concentration of a degenerate semiconductor.

Recently, oxides have been of great interest as thermoelectric materials performing at high-temperature for power generation because they are very thermally stable, resistant to oxidation, and are less harmful. Oxide systems [$(ZnO)_2In_2O_3$, $NaCo_2O_4$, $Ca_3Co_4O_9$, $(Zn_{1-x}Al_x)O$,$(Ba, Sr)PbO_3$, $CaMMnO_3$ (M = Bi, In), (La, Sr)CrO$_3$, Li-doped NiO, $Pr_{0.9}Ca_{0.1}CoO_3$ and $Ho_{0.9}Ca_{0.1}CoO_3$] have shown great performance as thermoelectric materials. [44–60] However, the thermoelectric properties need to be enhanced before these materials can be used more widely. Theoretical studies suggest that artificial superlattice quantum-well materials, which are made up of alternating insulating and conducting layers, should give higher thermoelectric performance.[61] Crystals having a layered structure can be considered as natural superlattices whereby they have thermodynamically stable phases [for e.g. $(ZnO)_5In_2O_3$, $NaCo_2O_4$, $Ca_3Co_4O_9$] and high thermoelectric properties, which were probably due to the link between the crystal structure's low dimensionality and the electrons' and phonons' behaviours in an anisotropic structural environment.[44,45,53–59]

Despite the enormous amount of oxychalcogenides families that have been discovered, many of the literature investigated their optical and magnetic properties and very few have investigated their thermoelectric properties.[1,62] The first report about oxychalcogenides thermoelectric performance was on $La_{1-x}Sr_xOCuSe$[63], but interest in these materials shifted to $Bi_{1-x}Sr_xOCuSe$ as it had a ZT = 0.76 at 873 K.[64] Since then, people started investigating this oxychalcogenide family.

41

Oxychalcogenides having smaller band gaps usually display higher ZT values. The [BiO][BCh] phases have lower band gaps than the [LaO][BCh] phases because Bi 6p states can contribute to the bottom of the conduction band.[65] The oxytellurides actually have the smallest band gap (ZT = 0.66 at 673 K), however, not much work has been done on those materials.[66,67] BiCuOSe has been investigated as a promising thermoelectric material since 2010[68] and most research has focused on p-type semiconducting BiCuOSe-derived systems but in Chapter 6, it will be investigated whether n-type BiCuOSe materials can be synthesised.

1.6 Photocatalysts

Photocatalysis is a reaction where irradiated light is used to activate a substance which then changes the rate of a chemical reaction without participating. The photocatalytic activity of a compound depends on its ability to create electron-hole pairs which give free radicals which in turn can undergo secondary reactions. The important characteristics of a compound exhibiting photocatalysis are having a desired band gap, appropriate morphologies, stability, high surface area and can be used again. There are different types of photocatalysts: Homogeneous (where the reactants and the photocatalysts are in the same phase) and heterogeneous (where the reactants and the photocatalysts are in different phases). The most common homogeneous photocatalysts are the ozone and photo-Fenton systems (Fe$^+$ and Fe$^+$/H$_2$O$_2$).[69] The most common heterogeneous photocatalysts are transition metal oxides and semiconductors. Photocatalysts were discovered after TiO$_2$ was used in water electrolysis. Research is being done on modifying TiO$_2$ for making it suitable as a photocatalyst under indoor lighting conditions by using dopants (nitrogen, sulfur, and different metals).[70–75]Other oxides have been discovered as photocatalysts such as Bi$_2$WO$_6$, BiVO$_4$, Bi$_2$MoO$_6$, ZnO, SnO$_2$, CeO$_2$ as well as layered tantalates and niobates which are suitable for contaminant degradation and H$_2$ generation.[76–92] Photocatalysts have several applications such as conversion of H$_2$O to H$_2$ by photocatalytic water splitting, in self-cleaning glass, oxidation of organic contaminants and in the disinfection of water.[93–98]

Unlike metals which have a continuum of electronic states, semiconductors have an empty energy region where none of the energy levels are accessible to encourage the recombination of an electron and a hole which are produced by photo-activation in the solid. The empty region, which ranges from the top of the filled valence band to the bottom of the empty conduction band, is called the band gap. When a photon of light with energy equal to or greater than the band gap of the materials is absorbed in the semiconductor, an electron is excited from the valence band to the

conduction band and in the process, creates a positive hole in the valence band. Such a photo-generated electron-hole pair is termed an exciton. The excited electron and hole can combine with each other and emit the energy which was obtained from during the excitation in the form of heat. The recombination of photo-generated electron-hole pair (exciton) is undesired and higher levels lead to an inefficient photocatalyst. Hence, it is important to develop functional photocatalysts with extended exciton lifetimes and improved electron-hole separation. Because of the positive holes and electron generation, oxidation-reduction reactions occur at the surface of semiconductors.

Compounds having electronic configuration of d^0 or d^{10} such as In^{3+} can undergo photocatalytic activity under visible light. $La_5In_3S_9O_3$ has shown that it can reduce H^+ to H_2, although the results are not very promising due to perhaps the lack of potential of the minimum conduction band since it consists of In5s-5p orbitals, and that it can oxidise water to form O_2 under visible light in the presence of a sacrificial electron donor, (methanol, Na_2S-Na_2SO_3) and acceptor (Ag^+).[99,100] Sulfides can also reduce H^+ to form H_2 in the presence of a sacrificial electron donor but cannot oxidise water to form O_2 because the oxidation of S^{2-} is more favourable.[101–103] A reason why this might be so is because the valence band of the oxysulfides comprises of O $2p$ and S $3p$ orbitals in a hybridised state.[3,100]

1.7 Magnetic properties

Anything that is magnetic has a magnetic dipole moment which measures the strength and direction of its magnetism. Magnetism in a material occurs due to alignment of magnetic moments. In an applied magnetic field, magnetic moments in a material tend to align and increase the field strength magnitude. This increase is called magnetisation and is given by:

$$B = \mu_0 H + \mu_0 M \qquad\qquad \text{Equation 1.05}$$

$$M = \chi_m H$$

Where, B= Magnetic flux density (magnitude of the field strength within a substance to a field)

   H= Magnetic field

   μ_0 = Permeability (degree to which a material can be magnetised)

   χ_m= Magnetic susceptibility

Magnetism in solids originates in the magnetic properties of an electron. Magnetic properties in systems come from both the orbital angular momentum and the spin angular momentum. This resulting spin moment for a single electron can be determined from the following equation:[126–128]

$$\mu_s = g\sqrt{s(s+1)} \qquad\qquad \text{Equation 1.06}$$

Where, s = Spin quantum number ($\pm 1/2$)

      g = Gyromagnetic ratio (~2.00)

For systems with more than one unpaired electron, s is taken to be the summation of the spin quantum numbers of each single unpaired electron. Since the orbital moment also contributes to the overall magnetic moment, the above equation can be extended to include it: [126–128]

$$\mu_{s+L} = \sqrt{4s(s+1) + L(L+1)} \qquad\qquad \text{Equation 1.07}$$

Where, L = Orbital angular momentum quantum number for the ion (can vary from 0 to n-L)

When the shell is less than half full, $J = L$-S and when the shell is more than half full, $J = L$+S. When J = 0, the atom is non-magnetic. Due to the influence of the crystal field, the orbital contribution, L, is often quenched for the 3d transition metals and hence, act as if $J = S$ instead of $J = L$+S. These compounds and elements have 3d electrons (responsible for paramagnetism) which have orbitals deep inside the ions or in the outermost shell and can interact with nearby atoms. As a result, the electrons are subjected to an electrostatic crystal field which is greater than the electrostatic L-S coupling. The latter is broken up. Moreover, the 2L+1 sublevels are split by the crystal field. Hence, their orbital moments are quenched, and the spin dominates. Exceptions include Fe^{2+} and Co^{2+} in octahedral environments. When all the shells are filled (spins are paired and s = 0), diamagnetism is observed. When there are unfilled shells (unpaired spins), Curie paramagnetism is observed.[126–128]

The lanthanides are strongly coupled. The Russell-Saunders is based upon the conception of the angular momentum possessed by each state and the sources of such angular momenta in the atom. It assumes that spin-spin coupling > orbit-orbit coupling > spin-orbit coupling. The spin-spin coupling (S) is the resultant spin quantum number for a system of electrons from adding the individual m_s

together. The orbit-orbit coupling (*L*) is the total orbital angular momentum quantum number and defines the energy state for a system of electrons. The spin-orbit coupling occurs between the resultant spin and orbital momenta of an electron which in turn *J* (total angular momentum quantum number). Multiplicity occurs when several levels are close together and this is given by (2*S*+1) or (2*S*+1) *L*. Crystal fields will split different orbitals into subsets of different energies, depending on whether they are in an octahedral or tetrahedral environment. *d* orbitals will split to give t_{2g} and e_g subsets and *f* orbitals will split to give t_{1g}, t_{2g} and a_{2g}.

The Curie law relates the magnetisation of a Curie paramagnet and the effective magnetic moment on the ion. Curie paramagnetism is temperature dependent and arises due to thermal energy, k_BT, of the system causing the spins to be randomised away from their alignment to the magnetic field. [126–128] The Curie law is as follows:

$$\chi = \frac{c}{T}$$
Equation 1.08

Where, χ = Magnetic susceptibility

C = Curie constant

T = Temperature

The Curie constant is defined as:

$$C = \frac{N_A \mu_{eff}^2 \mu_B^2}{3k_B}$$
Equation 1.09

Where, N_A = Avogadro's constant

μ_{eff} = Effective magnetic moment

μ_B = Bohr magneton

K_B = Boltzmann constant

When the Curie law is obeyed, the Curie constant can be determined and from it, the effective magnetic moment of the magnetic species. The magnetic moment relates to the number of unpaired electrons present in the material. Different materials have different susceptibilities and many paramagnetic materials follow the Curie Law. Rather than the spins being completely

independent in an ideal paramagnet, there are often some underlying local ferromagnetic (FM) or antiferromagnetic (AFM) interactions which do not lead to long-range magnetic order but are evident from magnetic susceptibility measurements. Hence, the magnetic susceptibility deviates from the Curie law and a Weiss constant needs to be added to correct for interactions between spins when they are significant and for some FM/AFM in the system. This is described as the Curie-Weiss law: [126–128]

$$\chi = \frac{c}{T-\theta}$$ Equation 1.10

Where, θ = Weiss constant

The sign of the Weiss constant is a representation of the type of interaction, whereby a positive sign indicates FM interaction, a negative sign indicates AFM interaction and a zero value indicates that the system is paramagnetic (Figure 1.11). The magnitude of the Weiss constant shows the strength of the interaction between localised spins and is usually found close to the critical temperature (T_c for a ferromagnet and T_N for an antiferromagnet). [126–128]
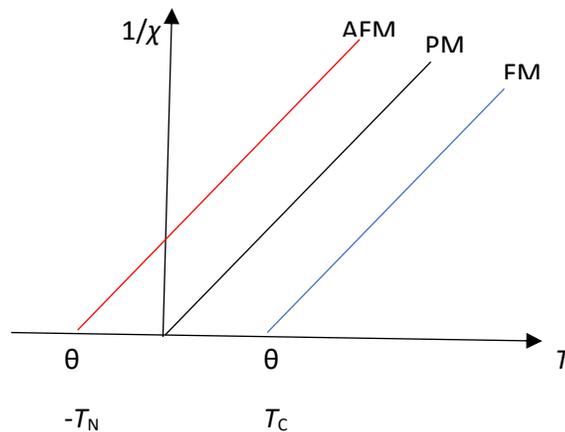
Figure 1.11 Curie-Weiss plot of $1/\chi$ as a function of temperature for antiferromagnetic (red), paramagnetic (black) and ferromagnetic (blue) systems.

There are many different magnetic behaviours depending on the existence and alignment of magnetic moments in the presence or absence of an applied magnetic field: diamagnetism, paramagnetism, ferromagnetism, and antiferromagnetism.

1.7.1 Diamagnetism

Diamagnetism occurs in substances that have no unpaired electrons, that is, all the electrons are paired up. This causes the magnetic field of the electrons to cancel out giving no net magnetic moment. Diamagnetic substances are weakly repelled by an applied magnetic field.[104,105] All materials with paired electrons have a diamagnetic component. Nevertheless, if the atoms have some net magnetic moment such as in paramagnetic materials or as in ferromagnetic materials where the atomic magnetic moments have long-range ordering, these stronger effects are always dominant.[106] The magnetic susceptibility of a diamagnet is negative. Molecular nitrogen, N_2, has no unpaired electrons and is diamagnetic.[104,105]

1.7.2 Paramagnetism

Paramagnetism denotes the magnetic state of an atom containing one or more unpaired electrons. These unpaired electrons have electron magnetic dipole moments which are attracted by a magnetic field. The spins are isolated and independent in an ideal paramagnet. In the absence of an applied field, the magnetic moments do not interact with each other and are randomly aligned due to thermal motion, hence, there is no net magnetization. When a magnetic field is applied, all the dipole moments tend to align in the direction of the field, thus reinforcing it. The magnetic susceptibility is small but positive.[104,105] Paramagnetism is stronger than diamagnetism and causes magnetization in the direction of the applied magnetic field. Relatively few pure elements in their stable forms are paramagnetic, O_2 being a notable paramagnet. In contrast to ferromagnets, paramagnets do not retain any magnetisation when an externally applied magnetic field is removed because the spin orientations are random due to thermal motion randomizes.

1.7.3 Ferromagnetism

Ferromagnetism is exhibited when spins in neighbouring atoms are coupled ferromagnetically such that on cooling below the ordering temperature (Curie temperature, T_c), the neighbouring spins are parallel (Figure 1.12a). This results in an overall magnetisation, the direction of which can be reversed by an applied magnetic field (Figure 1.12b). Unlike in paramagnetism, the spins align even when no magnetic field is applied, due to a strong spin coupling interaction.[104,105,112] Every ferromagnetic material has its own Curie temperature above which there is a second-order phase

transition and it loses all its ferromagnetism as the thermal tendency to disorder is greater than the energy lowering due to ferromagnetic order. Below that temperature, there is a spontaneous symmetry breaking and the magnetic moments become aligned with the neighbouring ones.[112] Ferromagnetic effects are huge, causing magnetisations occasionally orders of magnitude bigger than the applied magnetic field and it is stronger than paramagnetism and diamagnetism.[113,114] Hence, trace amount of ferromagnetic impurities will completely dominate the magnetic susceptibility measurements. Ferromagnetism occurs in a few substances such as nickel, cobalt and some alloys of rare-earth metals whereby the lanthanide elements can carry large magnetic moments in well-localised f-orbitals.[115]
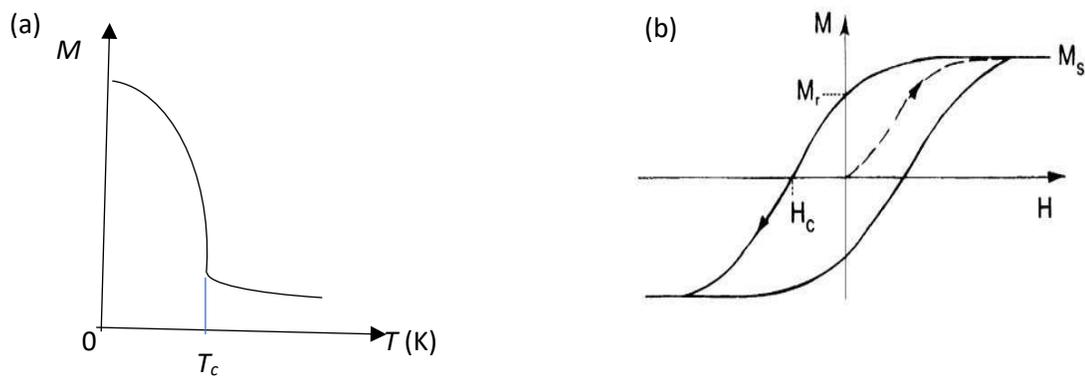
Figure 1.12 (a) Typical magnetisation for a ferromagnet as a function of temperature. (b) Hysteresis loop for a ferromagnet. M = magnetisation of material, H = applied magnetic field intensity, M_s = saturation magnetisation (when the magnetisation reaches a constant value. If the field is removed, the material will retain most of the magnetisation), M_r = remanence (when magnetisation has a positiive value) and H_c = coercive field. The material will follow a non-linear magnetisation plot if it is magnetised starting from origin (as shown by the dashed line).

1.7.4 Antiferromagnetism

Antiferromagnetism is exhibited when the coupling of neighbouring spins is anti-parallel such that on cooling below the Néel temperature (T_N), the spins cancel each other out and no net magnetic moment occurs. It shows ordered magnetism similar to ferromagnetism. In the absence of an external applied magnetic field, there is no net magnetisation. This method of coupling is more often observed than ferromagnetic coupling. At T_N, the AFM coupling is broken. Above T_N, the material is usually paramagnetic.[116] Below T_N, as the temperature decreases, the magnetisation of the sample

decreases towards zero. The magnetic susceptibility of an antiferromagnetic material characteristically shows a maximum at T_N (Figure 1.13).
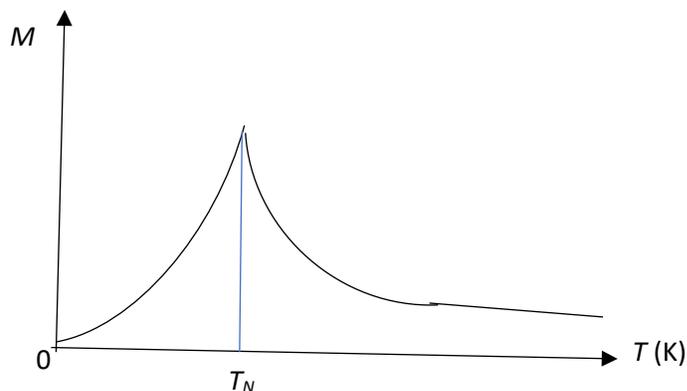
Figure 1.13 (a) Typical magnetisation for an antiferromagnet as a function of temperature.

1.7.5 Magnetic Superexchange

In insulating materials, even if magnetic species are too far apart to couple directly, they may be coupled indirectly via an intervening anion. This is known as superexchange. The coupling can be either ferromagnetic or antiferromagnetic and this is determined by the Anderson-Goodenough-Kanamori rules. Superexchange differs from direct exchange in which the coupling occurs between nearest neighbour cations without an intermediary anion. The superexchange interaction was developed by Kramers, Anderson, Goodenough and Kanamori.[107–110] Kramers, in 1934, noticed that in crystals like MnO there was a magnetic interaction between two magnetic Mn ions even though they were separated by a non-magnetic O ion, where the $3d$ wave functions of Mn^{2+} were hybridising with the $2p$ wave function of O^{2-}.[107] In 1950, Anderson further developed this model.[111] In that same year, Goodenough and Kanamori proposed a set of semi-empirical rules to give the sign of the exchange interaction between these ions based on the bond angle and the type of overlap. These Goodenough-Kanamori rules are based on the symmetry relations and electron occupancy of the overlapping atomic orbitals. The sign depends on *M-O-M* (*M* = cation, O = oxygen anion) angle and the strength depends on the degree of overlap. The rules predict a strong antiferromagnetic structure when the magnetic ion-ligand-magnetic ion angle (d_{xy} orbitals) is 180° with partially filled d shells, since they can interact via $p\pi$ orbitals on the ligand (Figure 1.14a). If the two next-nearest neighbour cations are at 90° to the bridging non-magnetic anion, then the

interaction is ferromagnetic (Figure 1.14b). Superexchange is very common in oxides or sulfides.[109,110]
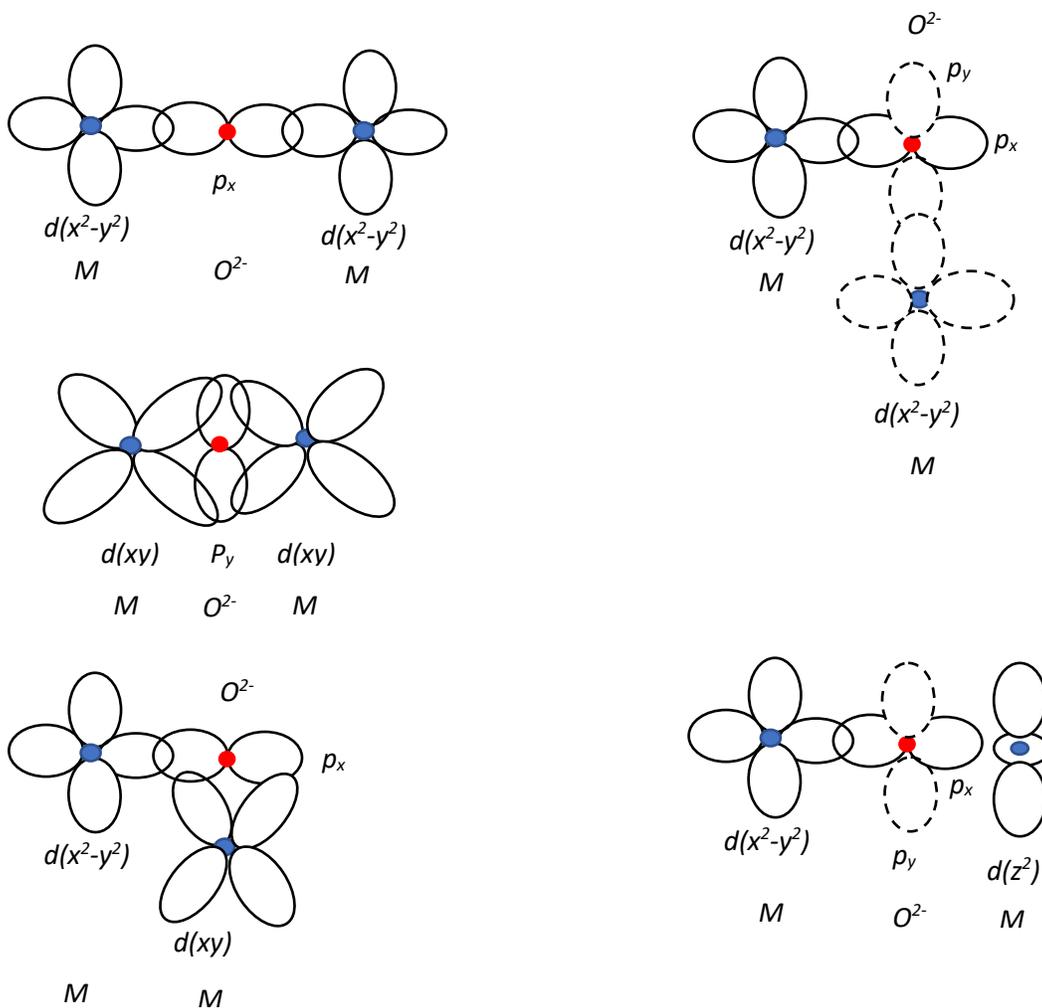
Figure 1.14 (a) AFM and (b) FM superexchange paths showing overlap of orbitals. M (cation) is shown in blue and O^{2-} anion is shown in red.

Magnetic measurements suggested that the transition metal layers in M_2O-type materials order antiferromagnetically (AFM) on cooling. This antiferromagnetic ordering, in which magnetic moments on neighbouring sites are oriented in an antiparallel fashion, arises from magnetic coupling between magnetic transition metals via intervening anions. This magnetic coupling might occur by super-exchange.[107,108,111]

1.7.6 Ising v/s Heisenberg models

The Ising and Heisenberg models are both simplified spin models of magnetic phase transitions but vary in symmetry properties which are vital for finding phase transitions features.[117] The Heisenberg model is beneficial for studying phase transitions in systems that show continuous symmetry under global rotations of the spins.[118] In the nearest neighbour Heisenberg model, the spins are 3-D unit vectors that can point in any direction on the unit sphere in 3-D space as per the Hamiltonian model:[119]

$$\hat{H} = -\sum_{(ij)} JS_i.S_j$$
   Equation 1.11

Where, J = Exchange integral

$\sum_{(ij)}$ = Sum over nearest neighbours

S = Spins

In this model, the dimensionality of the order parameter, D, is 3 since the spins are 3-D unit vectors.[119,120]

The Ising model is valuable when studying magnetic phase transitions in systems which have specific type of discrete symmetry under global reflections of the spins.[121] Different dimensionality corresponds to different universality class.[120] In the Ising model, the spins on each site of a lattice are allowed to point either up or down as per the Hamiltonian model:[119]

$$\hat{H} = -\sum_{(ij)} JS_i^z S_j^z$$
   Equation 1.12

Where, J = Exchange integral

$\sum_{(ij)}$ = Sum over nearest neighbours

S = Spins (allowed to point along ± z component)

In this model, the dimensionality of the order parameter, D, is 1 since the spins are allowed to point along ± z component. In a 1-D Ising model, if a defect is introduced, this costs extra energy which

remains unchanged with the size of the defect while the entropy gain in the system gets infinite. Hence, a $T > 0$, there is no long-range order (no phase transition).[119,122] In the 2-D Ising model, when a defect is introduced, both the energy cost associated with it and the entropy it causes in the system increase with the size of the defect.[119] Hence, there is a continuous phase transition between a low-temperature ordered ferromagnetic phase and a high-temperature disordered paramagnetic phase with zero average magnetisation.[123]

1.8 Aims

The oxychalcogenide compounds, containing at least two types of anions, give rise to interesting properties and it has been seen that most quaternary oxychalcogenides adopt the layered crystal structure. The layers in these structures can be manipulated to change the compounds' properties as seen for BiCuOSe, where doping the layers increased the ZT value and not much work has been done on n-type doping. Hence, the investigation of electron-doping in BiCuOSe was decided. Moreover, the $LnMOCh_2$ (Ln = Lanthanides, M = cation and Ch = chalcogenides) type structures have barely been investigated. Most of the reports available on these compounds are from a good number of years ago and a recent work has shown that they are potential photocatalysts. Therefore, the investigation of the feasibility of those compounds and well as their property-tuning by isovalent doping will be carried out. The $La_2O_2Fe_2OSe_2$ structure has been shown to be a Mott insulator which is caused by the Fe 3d electrons near the Fermi level while their resistivity measurements showed that they are semiconductors. Thus, the investigation of whether their band gaps can be tuned through electron-doping will be carried out. Following on from the $Ln_2O_2Fe_2OSe_2$ (Ln = Lanthanides) family, the magnetic structure of $Pr_2O_2Fe_2OSe_2$ and $La_2O_2Fe_2OS_2$ have not been completely investigated, thus, the need for further studies.

1.9 References

1   S. J. Clarke, P. Adamson, S. J. C. Herkelrath, O. J. Rutt, D. R. Parker, M. J. Pitcher and C. F. Smura, *Inorg. Chem.*, 2008, **47**, 8473–8486.

2   A. M. Kusainova, P. S. Berdonosov, L. G. Akselrud, L. N. Kholodkosvkaya, V. A. Dolgikh and B. A. Popovkin, *J. Solid State Chem.*, 1994, **112**, 189–191.

3   A. Ishikawa, T. Takata, J. N. Kondo, M. Hara, H. Kobayashi and K. Domen, *J. Am. Chem. Soc.*, 2002, **124**, 13547–13553.

4   K. Ueda, S. Inoue, S. Hirose, H. Kawazoe and H. Hosono, *Appl. Phys. Lett.*, 2000, **77**, 2701–

2703.

5   A. S. Sefat, A. Huq, M. A. McGuire, R. Jin, B. C. Sales, D. Mandrus, L. M. D. Cranswick, P. W. Stephens and K. H. Stone, *Phys. Rev. B*, 2008, **78**, 104505.

6   C. Greskovich and S. Duclos, *Annu. Rev. Mater. Sci.*, 1997, **27**, 69–88.

7   P. Bonazzi, S. Menchetti and C. Sabelli, *Neues Jahrb. Fur Mineral.*, 1987, **12**, 557–567.

8   F. Jellinek, *Acta Chem. Scand*, 1962, **16**, 791.

9   A. Gleizes, Y. P. Jeannin and N. Maire, *Bull. Soc. Chim. Fr*, 1974, 1317.

10   K. Stocks, G. Eulenberger and H. Hahn, *Zeitschrift fuer Anorg. und Allg. Chemie*, 1950, **463**, 105–109.

11   E. Koyama, I. Nakai and K. Nagashima, *Acta Crystallogr. Sect. B*, 1984, **40**, 105–109.

12   W. J. Zhu and P. H. Hor, *J. Solid State Chem.*, 1997, **130**, 319–321.

13   H. Hirose, K. Ueda, H. Kawazoe and H. Hosono, *Chem. Mater.*, 2002, **14**, 1037–1041.

14   S. Broadley, Z. A. Gál, F. Corà, C. F. Smura and S. J. Clarke, *Inorg. Chem.*, 2005, **44**, 9092–9096.

15   A. Ishikawa, T. Takata, J. N. Kondo, M. Hara, H. Kobayashi and K. Domen, *J. Am. Chem. Soc.*, 2002, **124**, 13547–13553.

16   H. Hiramatsu, H. Kamioka, K. Ueda, M. Hirano and J. Hosono, *J. Ceram. Soc. Jpn.*, 2005, **113**, 10–16.

17   G. V Vajenine and R. Hoffmann, *Inorg. Chem.*, 1996, **35**, 451–457.

18   M. Palazzi, C. Carcaly and J. Flahaut, *J. Solid State Chem.*, 1980, **35**, 150–155.

19   M. Palazzi and S. Jaulmes, *Acta Crystallogr. Sect. B*, 1981, **37**, 1337–1339.

20   R. Pöttgen and D. Johrendt, *Zeitschrift für Naturforsch. B*, 2008, **63**, 1135–1148.

21   G. H. Chan, B. Deng, M. Bertoni, J. R. Ireland, M. C. Hersam, T. O. Mason, R. P. Van Duyne and J. A. Ibers, *Inorg. Chem.*, 2006, **45**, 8264–8272.

22   B. A. Popovkin, A. M. Kusainova, V. A. Dolgikh and L. G. Aksel'rud, *Russ. J. Inorg. Chem*, 1998, **43**, 1471.

23   H. Hiramatsu, H. Yanagi, T. Kamiya and K. Ueda, *Chem. Mater.*, 2008, **20**, 326–334.

24   L. N. Kholodkovskaya, L. G. Akselrud, A. M. Kusainova, V. A. Dolgikh and B. A. Popovkin, *Mater. Sci. Forum*, 1993, **133**, 693–696.

25   V. Johnson and W. Jeitschko, *J. Solid State Chem.*, 1974, **11**, 161–166.

26   K. Ueda, H. Hiramatsu, M. Hirano, T. Kamiya and H. Hosono, *Thin Solid Films*, 2006, **496**, 8–15.

27   M. Palazzi, *C. R. Acad. Sci*, 1981, **292**, 789.

28   S. ichiro Inoue, K. Ueda, H. Hosono and N. Hamada, *Phys. Rev. B*, 2001, **64**, 245211.

29   K. Ueda, K. Takafuji, H. Hiramatsu, H. Ohta, T. Kamiya, M. Hirano and H. Hosono, *Chem. Mater.*, 2003, **15**, 3692–3695.

30   K. Ueda and H. Hosono, *J. Appl. Phys.*, 2002, **91**, 4768–4770.

31   K. Ueda, K. Takafuji and H. Hosono, *J. Solid State Chem.*, 2003, **170**, 182–187.

32   D. O. Charkin, A. V Akopyan and V. A. Dolgikh, *Russ. J. Inorg. Chem.*, 1999, **44**, 833–837.

33   S. Jaulmes, D. Carré, M. Palazzi and M. Guittard, *C. R. Acad. Sci*, 1985, **II**, 259–262.

34   S. Jaulmes, E. Godlewski, M. Palazzi and J. Etienne, *Acta Crystallogr. Sect. B Struct. Sci.*, 1982, **38**, 1707–1710.

35   S. Benazeth, *J. Solid State Chem.*, 1989, **78**, 147–153.

36   S. Jaulmes, *Sect. B Struct. Crystallogr. Cryst.*, 1978, **5419**, 2610–2612.

37   K. Ikarashi, J. Sato, H. Kobayashi, N. Saito, H. Nishiyama and Y. Inoue, *J. Phys. Chem. B*, 2002, **106**, 9048–9053.

38   K. Maeda, K. Teramura, D. Lu, T. Takata, N. Saito, Y. Inoue and K. Domen, *Nature*, 2006, **440**, 295–295.

39   J. M. Mayer, L. F. Schneemeyer, T. Siegrist, J. V Waszczak and B. Van Dover, *Angew. Chemie Int. Ed.*, 1992, **31**, 1645–1647.

40   E. E. McCabe, A. S. Wills, L. Chapon, P. Manuel and J. S. O. Evans, *Phys. Rev. B*, 2014, **90**, 165111.

41   D. G. Free, N. D. Withers, P. J. Hickey and J. S. O. Evans, *Chem. Mater.*, 2011, **23**, 1625–1635.

42   C. Wang, M. Q. Tan, C. M. Feng, Z. F. Ma, S. Jiang, Z. A. Xu, G. H. Cao, K. Matsubayashi and Y. Uwatoko, *J. Am. Chem. Soc.*, 2010, **132**, 7069–7073.

43   J. X. Zhu, R. Yu, H. Wang, L. L. Zhao, M. D. Jones, J. Dai, E. Abrahams, E. Morosan, M. Fang and Q. Si, *Phys. Rev. Lett.*, 2010, **104**, 216405.

44   H. Ohta, W. S. Seo and K. Koumoto, *J. Am. Ceram. Soc.*, 1996, **79**, 2193–2196.

45   M. Kazeoka, H. Hiramatsu, W. S. Seo and K. Koumoto, *J. Mater. Res.*, 1998, **13**, 523–526.

46   Y. Masahiro and M. Norimitsu, *J. Mater. Sci. Lett.*, 1997, **16**, 1731–1734.

47   M. Ohtaki, Hi. Koga, T. Tokunaga, K. Eguchi and H. Arai, *J. Solid State Chem.*, 1995, **120**, 105–111.

48   W. J. Weber, C. W. Griffin and L. J. Bates, *J. Am. Ceram. Soc.*, 1987, **70**, 265–270.

49   W. Shin and N. Murayama, *Jpn. J. Appl. Phys*, 1999, **38**, 1336–1338.

50   J. W. Moon, Y. Masuda, W. S. Seo and K. Koumoto, *Mater. Sci. Eng. B*, 2001, **85**, 70–75.

51   J. W. Moon, W. S. Seo, H. Okabe, T. Okawa and K. Koumoto, *J. Mater. Chem.*, 2000, **10**, 2007–2009.

52   J. W. Moon, Y. Masuda, W. S. Seo and K. Koumoto, *Mater. Lett.*, 2001, **48**, 225–229.

53   T. Tani, S. Isobe, W. S. Seo and K. Koumoto, *J. Mater. Chem.*, 2001, **11**, 2324–2328.

54   Y. Masudaa, M. Ohta, W. S. Seo, W. Pitschke, Koumoto and Kunihito, *J. Solid State Chem.*, 2000, **150**, 221–227.

55   S. Isobe, T. Tani, Y. Masuda, W. S. Seo and K. Koumoto, *Jpn. J. Appl. Phys.*, 2002, **41**, 731–732.

56   I. Terasaki, Y. Ishii, D. Tanaka, K. Takahata and Y. Iguchi, *Jpn. J. Appl. Phys.*, 2001, **40**, L65-67.

57   I. Terasaki, Y. Sasago and K. Uchinokura, *Phys. Rev. B*, 1997, **56**, R12685–R12687.

58   S. Li, R. Funahashi, I. Matsubara, K. Ueno and H. Yamada, *J. Mater. Chem.*, 1999, **9**, 1659–1660.

59   S. Li, R. Funahashi, I. Matsubara, K. Ueno, S. Sodeoka and H. Yamada, *Chem. Mater.*, 2000, **12**, 2424–2427.

60   T. Tsubota, M. Ohtaki, K. Eguchi and H. Arai, *J. Mater. Chem.*, 1997, **7**, 85–90.

61   L. D. Hicks and M. S. Dresselhaus, *Phys. Rev. B*, 1993, **47**, 12727–12731.

62   M. J. Pitcher, C. F. Smura and S. J. Clarke, *Inorg. Chem.*, 2009, **48**, 9054–9056.

63   M. Yasukawa, K. Ueda and H. Hosono, *J. Appl. Phys.*, 2004, **95**, 3594–3597.

64   L. D. Zhao, D. Berardan, Y. L. Pei, C. Byl and L. Pinsard-Gaudart, *Appl. Phys. Lett.*, 2010, **97**, 092118.

65   S. Sallis, L. F. J. Piper, J. Francis, J. Tate, H. Hiramatsu, T. Kamiya and H. Hosono, *Phys. Rev. B*, 2012, **85**, 85207.

66   P. Vaqueiro, G. Guélou, M. Stec, E. Guilmeau and A. V Powell, *J. Mater. Chem. A*, 2013, **1**, 520–523.

67   T. H. An, Y. S. Lim, H. S. Choi, W. S. Seo, C. H. Park, G. R. Kim, C. Park, C. H. Lee and J. H. Shim, *J. Mater. Chem. A*, 2014, **2**, 19759–19764.

68   L. D. Zhao, J. He, D. Berardan, Y. Lin, J. F. Li, C. W. Nan and N. Dragoe, *Energy Environ. Sci.*, 2014, **7**, 2900–2924.

69   C. H. Wu and C. L. Chang, *J. Hazard. Mater.*, 2006, **128**, 265–272.

70   S. Jung and N. Imaishi, *Korean J. Chem. Eng.*, 2001, **18**, 867–872.

71   C. W. Dunnill and I. P. Parkin, in *Sterilisation of Biomaterials and Medical Devices*, eds. S. Lerouge and A. Simmons, Woodhead Publishing, Cambridge, 2012, pp. 240–260.

72   C. W. Dunnill, Z. Aikin, J. Pratten, M. Wilson and I. Parkin, *Electrochem. Soc.*, 2009, **25**, 65–72.

73   C. W. Dunnill, Z. Aiken, J. Pratten, M. Wilson and I. Parkin, *Chem. Vap. Depos.*, 2010, **16**, 50–54.

74   C. W. Dunnill, Z. A. Aiken, A. Kafizas, J. Pratten, M. Wilson, D. J. Morgan and I. P. Parkin, *J. Mater. Chem.*, 2009, **19**, 8747–8754.

75   C. W. Dunnill, Z. Ansari, A. Kafizas, S. Perni, D. J. Morgan, M. Wilson and I. P. Parkin, *J. Mater. Chem.*, 2011, **21**, 11854–11861.

76   L. Wang, W. Wang, M. Shang, S. Sun, W. Yin, J. Ren and J. Zhou, *J. Mater. Chem.*, 2010, **20**, 8405.

77   L. S. Zhang, W. Z. Wang and L. Zhou, *Small*, 2007, **3**, 1618.

78   I. Iwase, K. Saito and A. Kudo, *Bull. Chem. Soc. Jpn.*, 2009, **82**, 514–518.

79   L. Ni, M. Tanabe and H. Irie, *Chem. Commun*, 2013, **49**, 10094–10096.

80   J. F. Luan, S. R. Zheng and Z. G. Zou, *J. Braz. Chem. Soc.*, 2006, **17**, 1368.

81   Z. G. Zou, J. H. Ye and H. Arakawa, *Chem. Mater.*, 2001, **13**, 1765–1769.

82   Z. G. Zou and H. Arakawa, *J. Photochem. Photobiol. A*, 2003, **158**, 145–162.

83   B. Muktha and J. Darriet, *J. Solid State Chem.*, 2006, **179**, 3919–3925.

84   S. S. Dunkle and K. S. Suslick, *J. Phys. Chem. C*, 2009, **113**, 10341–10345.

85   L. Zhou, W. Z. Wang and S. W. Liu, *J. Mol. Catal. A Chem*, 2006, **252**, 120.

86   Y. Shimodaira, H. Kato and A. Kudo, *J. Phys. Chem.*, 2006, **110**, 17790–17797.

87   M. R. Hoffmann, S. T. Martin, W. Choi and D. W. Bahnemann, *Chem. Rev.*, 1995, **95**, 69–96.

88   A. Fujishima and K. Honda, *Nature*, 1972, **238**, 37–38.

89   A. Hernández-Ramírez and I. Medina-Ramírez, *Photocatalytic Semiconductors*, Springer, 2015.

90   Y. Hosogi, H. Kato and A. Kudo, *J. Phys. Chem. C*, 2008, **112**, 17678–17682.

91   P. D. Kanhere, J. Zheng and Z. Chen, *J. Phys. Chem. C*, 2011, **115**, 11846–11853.

92   P. D. Kanhere, J. Zheng and Z. Chen, *Int. J. Hydrog. Energy*, 2012, **37**, 4889–4896.

93   C. McCullagh, J. M. C. Robertson, D. W. Bahnemann and P. K. J. Robertson, *Res. Chem. Intermed.*, 2007, **33**, 359–375.

94   D. A. H. Hanaor and C. C. Sorrell, *Adv. Eng. Mater.*, 2014, **16**, 248–254.

95   A. Kudo, H. Kato and I. Tsuji, *Chem. Lett.*, 2004, **33**, 1534–1539.

96   A. O. Kondrakov, A. N. Ignatev, V. V Lunin, F. H. Frimmel, S. Bräse and H. Horn, *Appl. Catal. B Environ.*, 2016, **182**, 424–430.

97   A. O. Kondrakov, A. N. Ignatev, V. V Lunin, F. H. Frimmel, S. Bräse and H. Horn, *Appl. Catal.*

B Environ., 2014, **160**, 106–114.

98   W. L. Kostedt, J. Drwiega, D. W. Mazyck, S. W. Lee, W. Sigmund, C. Y. Wu and P. Chadik, *Environ. Sci. Technol.*, 2005, **39**, 8052–8056.

99   K. Ogisu, A. Ishikawa, K. Teramura, K. Toda, M. Hara and K. Domen, *Chem. Lett.*, 2007, **36**, 854–855.

100   A. Ishikawa, T. Takata, T. Matsumura, J. N. Kondo, M. Hara, H. Kobayashi and K. Domen, *J. Phys. Chem. B*, 2004, **108**, 2637–2642.

101   J. F. Reber and K. Meier, *J. Phys. Chem.*, 1984, **88**, 5903–5913.

102   I. Tsuji, H. Kato, H. Kobayashi and A. Kudo, *J. Am. Chem. Soc.*, 2004, **126**, 13406–13413.

103   N. Buehler, K. Meier and J. f Reber, *J. Phys. Chem.*, 1984, **88**, 3261–3268.

104   A. Sherman, S. J. Sherman and L. Russikoff, *Basic Concepts of Chemistry*, Houghton Mifflin Company, Boston, 5th edn., 1992.

105   R. H. Pettrucci, *General Chemistry: Principles and Modern Applications*, Pearson Prentice Hall, New Jersey, 9th edn., 2007.

106   C. Westbrook and C. Kaut, *MRI in practice*, Wiley-Blackwell, New Jersey, 2nd edn., 1998.

107   H. A. Kramers, *Physica*, 1934, **1**, 182–192.

108   P. W. Anderson, *Phys. Rev*, 1950, **79**, 705–710.

109   J. Goodenough, *Magnetism and the Chemical Bond*, John Wiley and Sons Inc., New York, 1963.

110   J. Kanamori, *J. Phys. Chem. Solids*, 1959, **10**, 87–98.

111   P. W. Anderson, *Phys. Rev*, 1950, **79**, 350–356.

112   A. Aharoni, *Introduction to the theory of ferromagnetism*, Oxford University Press, Oxford, 2nd edn., 2000.

113   R. M. Bozorth, *Ferromagnetism*, IEEE Press, New York, 1993.

114   S. Chikazumi, *Physics of ferromagnetism*, Oxford University Press, Oxford, 2nd edn., 2009.

115   C. Kittel, *Introduction to Solid State Physics*, Wiley & sons, New York, 6th edn., 1986.

116   L. Néel, *Ann. Phys. (Paris).*, 1948, **3**, 137–198.

117   G. Gallavotti, *Statistical mechanics*, Springer-Verlag, Berlin, 1999.

118   A. Wietek, M. Schuler and A. M. Lauchli, *Autumn Sch. Correl. Electrons 2016*, 2016, 1–28.

119   S. Blundell, in *Magnetism in Condensed Matter*, Oxford University Press, New York, 2001.

120   H. E. Stanley, *Rev. Mod. Phys.*, 1999, **71**, 358–366.

121   C. K. Majumdar and D. K. Ghosh, *J. Math. Phys*, 1969, **10**, 1388–1399.

122   F. J. Dyson, *Comm. Math. Phys.*, 1969, **12**, 212–215.

123   M. J. G. Rocha-Neto, G. Camelo-Neto, E. Nogueira and S. Coutinho, *Phys. A Stat. Mech. its Appl.*, 2018, **494**, 559–573.

124   G. Rowell and S. Herbert, in *Physics*, Cambridge University Press, Cambridge, 1st edn., 1987.

125   W. Pauli, *Zeitschrift für Phys.*, 1925, **31**, 765–783.

126   A. R. West, *Solid State Chemistry and its applications*, John Wiley and sons, New Jersey, 1987.

127   A. R. West, *Basic solid state chemistry*, Wiley & sons, New Jersey, 2nd edn., 1999.

128   L. Smart and E. Moore, *Solid State Chemistry*, Springer, New York, 1st edn., 1992.

129   M. Fuhrer, *Physics (College. Park. Md).*, 2010, **3**, 106.

130   P. Debye, *Ann. Phys.*, 1912, **344**, 789–839.

131   J. Seymour, in *Physical Electronics*, Wiley, New York, 1st edn., 1972.

132   B. G. Yacobi, *Semiconductor Materials: An Introduction to Basic Principles*, Springer US, New York, 1st edn., 2003.

133   P. Yu and M. Cardona, *Fundamentals of Semiconductors.*, Springer-Verlag, Berlin, 4th edn., 2010.

134   W. Shockley, *Electrons and Holes in Semiconductors with Applications to Transistor Electronics*, D. Van Nostrand, New York, 1st edn., 1950.

135   P. A. Cox, in *Transition Metal Oxides*, Oxford University Press, New York, 1992.

136   B. I. Shklovskii, *Sov. Phys. Semicond*, 1973, **6**, 1053.

137   N. F. Mott and R. Peierls, *Proc. Phys. Soc.*, 1937, **49**, 72–73.

138   L. Kai, C. Cheng, Z. Cheng, K. Wang, R. Ramamoorthy and J. Wu, *Nano Lett.*, 2012, **12**, 6302–6308.

139   T. Driscoll, H. T. Kim, B. G. Chae, M. Di Ventra and D. N. Baso, *Appl. Phys. Lett.*, 2009, **95**, 043503.

Chapter 2: Experimental Techniques

This chapter focuses on the synthesis technique used to synthesise the samples investigated in this thesis along with all the experimental techniques and analysis used to do the measurements in house, at central facilities or with collaborators. The theory and application of these techniques are discussed along with the sample preparation details and the methods used for data analysis.

2.1 Synthesis Techniques (Solid-state reaction)

Solid state materials can be classified into several forms. They can be single crystals. These can be pure and have the least number of defects possible and can be useful for structural characterisation and for property measurements. They can also be polycrystalline powders which are very crystalline. These can be useful for characterisation in the absence of single crystals and are usually used in industrial processes. The polycrystalline powders can have large surface areas, and these are used in some applications such as electrode materials and catalysis and for further reactions. Solid state materials can also be amorphous, and these have no long range translational order such as in glass or they can be thin films. These are used mainly in optics, coatings and microelectronics.[1]

The term solid-state synthesis is usually used to outline interactions where neither a solvent medium nor controlled vapour-phase interactions are used. These reactions generally require high temperature and/or high pressure. For solid-state reactions to be successful, we need to use reagents with a large surface area or make the mixture into a pellet so as to maximise the area of contact between the reactants. We need a high rate of diffusion and the latter can be increased by increasing the temperature or by introducing defects by using reagents that decompose before or during the reaction such as carbonates or nitrates.

The easiest way to synthesise a lot of solid state materials is the standard ceramic route. Appropriate starting reagents (fine grain powders to increase surface area of well-defined compositions) are weighed, ground together using an agate mortar and pestle (or a ball mill if we have a large quantity of material), pressed into pellets to increase contact between reactants while decreasing contact with the crucible and placed inside appropriate crucibles (usually alumina).[1] The reaction mixture is

then reacted in the furnace for a long time and usually taken out of the furnace and reground to bring fresh surfaces into contact which increases the speed of the reaction. A complete reaction can take hours, days or weeks.

The problem with this method is that high temperatures are needed for diffusion to occur since it requires a large amount of energy for a cation or anion to diffuse into another site. This can be expensive, give incomplete reaction, decompose the desired product, give undesired microstructures and lead to the loss of some of the reactants. Moreover, oxygen stoichiometry can change greatly depending on the cooling conditions. The mixture can be cooled slowly in the furnace under controlled conditions or be cooled quickly in air or quenched into water or liquid nitrogen.

Some reagents or products involved in the processes can be air-sensitive. Hence, it is crucial that inert atmosphere conditions are used during the different synthesis stages where required. The handling of the air-sensitive materials can be done inside a glovebox. The latter is filled with argon which is recirculated through a molecular sieve bed and copper catalyst to remove any contaminating water or oxygen respectively that could leak inside the glovebox through gloves or ports. The water and oxygen concentrations are monitored by integrated sensors and are kept below 0.5 ppm. Pellets can be pressed inside the glovebox or outside, depending of the facilities available and the stability and harmfulness of the samples.

In this thesis, a standard ceramic route was used. Some of the reagents (La_2O_3, CeO_2, Nd_2O_3) were dried in a furnace at appropriate temperatures prior to usage to remove any absorbed moisture and stored in the glovebox until required while copper was reduced by heating to 600 °C in 5% H_2 and stored in the glovebox before using. All the other reagents used were stored in the glovebox. For Chapter 5, the reagents were mixed with acetone to minimise the formation of dust particles, (since some of the reagents are harmful), and to get a homogenous mixture in a fume cupboard. For the Chapters 3, 4 and 6, the reagents to synthesise the oxychalcogenide samples were weighed and mixed in the glovebox. The reagents were then pressed into pellets, except for Chapter 5, outside the glovebox making sure to minimise the time to air exposure as much as possible. The pellets were then placed in quartz tubes and sealed under vacuum (Figure 2.01) since we want to control the oxygen stoichiometry in the product to prevent oxidation of our chalcogenide. To prepare the $LaGaOS_2$-related phases in Chapter 5, the powders were placed in alumina crucibles at the bottom of the quartz tubes while the oxygen getter (10 % molar excess Ti powder) was placed in an alumina crucible on top of the sample (Figure 2.02). Oxygen getters are used to remove excess oxygen.

Quartz tubes are quite inert and can be sealed with a flame easily under a dynamic vacuum of < 7.8 x 10^{-2} mbar after having been evacuated for at least 10 minutes to make sure that the maximum amount of air/moisture has been eliminated. The sealed tubes were then heated in a furnace to the appropriate temperature in order to complete the reaction. A slow heating rate is needed because sulfur and selenium are volatile; S sublimes at about 440°C and Se at 600°C and to avoid a high pressure of chalcogen vapour building up. The cooling method sometimes influences the product formed and for some samples quenching the products in iced water produced greater crystallinity as seen in Chapter 5. The sealed tubes were broken with a hammer inside a fume hood and the products were removed with tweezers. The products were ground in an agate mortar and pestle, remixed in a fume hood for Chapter 5 and glovebox for Chapters 3, 4 and 6, re-pelletised where appropriate, re-sealed under vacuum and reheated to increase crystallinity. The amount of time that the reagents/products were exposed to air was kept to a minimum.
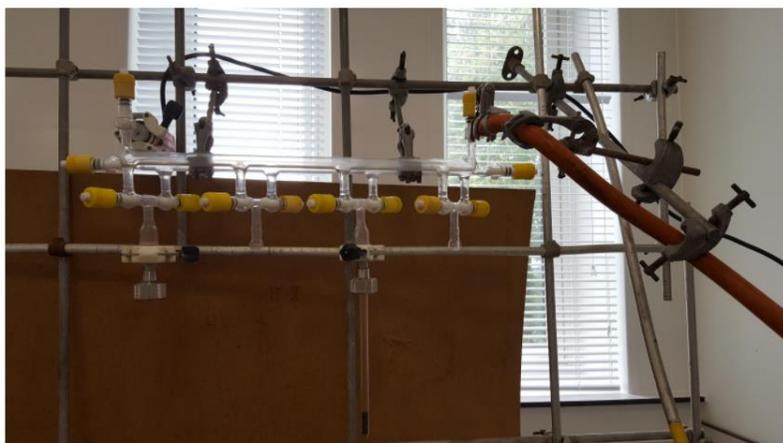
Figure 2.01 Sealing line with a sealed quartz tube containing sample pellets being evacuated under vacuum
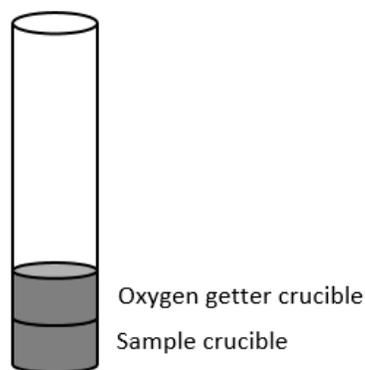
Figure 2.02 Quartz tube showing the arrangement of crucibles with the sample at the bottom and the oxygen getter on top.

2.2 Characterisation techniques

2.2.1.0 X-Ray Powder Diffraction

X-ray powder diffraction (XRPD) is a non-destructive technique. X-rays can be scattered by a crystalline material to give a diffraction pattern. This pattern can be used as a 'fingerprint' of the sample. XRPD is therefore good for characterising and identifying polycrystalline phases.

Initial characterisation of reaction products is done by powder diffraction since a lot of solid state reactions produce polycrystalline powders. Powder diffraction makes it easy to identify known phases found in the mixture by comparing the observed diffraction pattern against a database of known patterns and structures such as ICSD. The pattern can also be indexed, that is, the symmetry and the unit cell size can be identified. The samples ready to be characterised must be powdered. Small particle sized materials (0.1 μm or less) will produce a diffraction pattern with broader peaks. Samples in bulk should be polished so as to have a smooth surface and later annealed in order to take away any surface deformations which have arisen from the polishing.[2]

2.2.1.1 Intensities of diffracted X-rays

Crystalline materials are made up of regularly repeating units known as unit cells. A unit cell is the smallest volume which contains the full symmetry of the crystal structure and its dimensions are shown by three axes: a, b and c and angles α, β and γ as shown in Figure 2.03.[3] Unit cells can be categorized into seven crystal systems and one of fourteen Bravais lattices. XRPD can resolve the lattice parameters for seven crystal systems.[2]
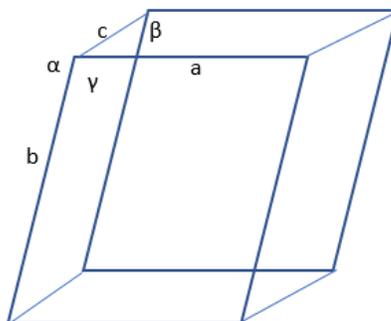
Figure 2.03. Unit cell with axes a, b and c and angles α, β and γ. α is the angle between b and c, β is the angle between a and c and γ is the angle between a and b.

When a crystalline material is bombarded by X-rays, the latter are scattered by the electron clouds of the atoms in the material. A crystal can be thought of as planes of atoms, each acting as a semi-transparent mirror, separated from one another by distance, d, commonly known as d-spacing. These planes can be represented by Miller indices (*h, k* and *l*). This separation is the perpendicular distance from the origin to the closest plane and can be written as d_{hkl}. Destructive interference happens in almost all directions, where the scattered X-rays cancel. However, constructive interference will happen in a few directions where well defined beams of X-rays will leave the solid sample in certain directions, consistent with Bragg's law:[1]

$$n\lambda = 2d_{hkl} \sin \Theta \qquad \text{Equation 2.01}$$

These planes of atoms scatter the X-rays in a way similar to reflection as in Figure 2.04. The difference in path length for X-rays scattered from successive planes must be an integer number of wavelengths for constructive interference, and hence, Bragg diffraction.[1]
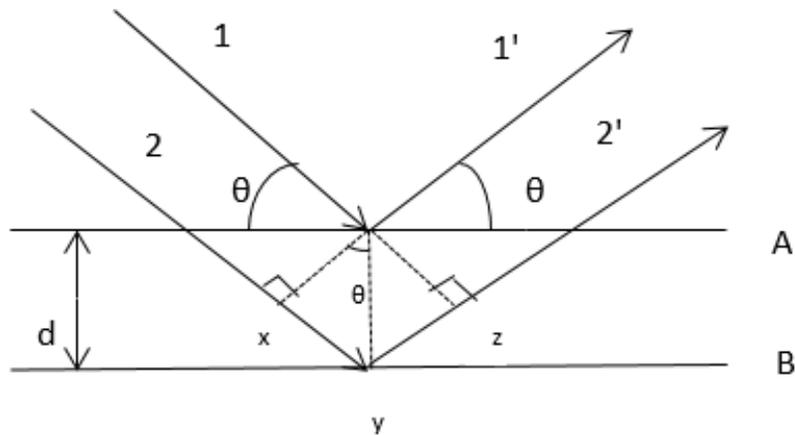
Figure 2.04. This shows a beam of X-ray being incident on two parallel planes 1 and 2, located at a distance, d, from each other. The two parallel incident rays, labelled 1 and 2, make an angle θ with the planes. These rays are then reflected at the same angle θ. The reflected rays are labelled 1' and 2'.

Usually, *n*= 1 is used for all the reflections when using Bragg's law. The resulting diffraction pattern is a graph of intensities against the angle, 2θ. The 2θ values for the peak depend on the wavelength of the anode material in the X-ray tube. The d-spacing value depends on the crystal structure.

The intensity of the (*h, k, l*) reflections is proportional to the square modulus of the structure factor F_{hkl} as follows:

$$F_{hkl} = \sum_{j=1}^{N} f_i \, exp\big[2\pi_i\big(hx_j + ky_j + lz_j\big)\big] \qquad\qquad \text{Equation 2.02}$$

where, (x_j, y_j, z_j) = Position of jth atom in the unit cell coordinates

f = Scattering amplitude

h, k, l = Miller Indices which define reflecting plane

Alongside the fraction of each phase in a sample, the area of diffraction peaks depends on the multiplicity of the reflections as well as the arrangement of atoms (and their associated densities) within the unit cell and any thermal motion (modelled by the thermal parameters).

X-rays scatter by interacting with the electron density of a material. The scattering from an atom is the sum of the scattering from each electron within the atom. The X-ray scattered from an atom is the resultant wave from all its electrons and there is zero phase difference for the forward/backward scattering. As a result, the scattering factor is proportional to the number of electrons and there is a regular increase in the scattering amplitude with atomic weight. Hence, light atoms scatter weakly and are difficult to locate. Moreover, there is increasing destructive interference with larger scattering angle and as a result, there is a decrease of scattering amplitude with increasing 2θ. Hence, powder patterns show weak lines at large 2θ.[4]

Peak positions depend on size and shape of the unit cell as well as systematic absences and macrostrain. Preferred orientation can limit the peaks seen and produce large variations in the intensity of peaks, hence, changing the appearance of the powder pattern. Preferred orientation occurs when crystallites in a powder sample tend to orient themselves in specific directions as per a preferred crystallographic plane. If the crystallites have plate or needle-like shapes as they are placed and pressed into a specimen holder, then it can be hard for them to have random orientations as they tend to lie flat on the surface. In sample like wires or metal sheets, preferred orientation usually occurs due to the manufacturing process.

Several factors can affect the peak intensities in an X-ray powder diffraction pattern. Peak intensities are determined by the atomic number and positions of the atoms within the unit cell as well as their scattering power and the multiplicity of reflections observed. Moreover, the form of the sample and the geometry of the instrument influence how the sample absorbs X-rays and hence, can affect the intensities. The decrease in the intensities of X-ay diffraction peaks at high 2θ is due to the

Lorentz and polarisation factors. The polarisation factor depends on the angle of the intensity which electrons scatter and occurs because incident wave (beam) is unpolarised. It is dependent solely on reciprocal lattice coordinate and does not depend on how it is measured. The Lorentz factor is a geometric correction factor that accounts for how long a moving crystal stays in the diffracting position for any specific beam which is scattered. The various reciprocal lattice points correspond to different sets of diffracting planes in a crystal which in turn, have different geometries relative to the instrument. Hence, the Lorentz factor is dependent on the type of instrument used and it changes with the Bragg angle. It is normally combined with the polarisation factor to give Lorentz-Polarisation factor. Furthermore, the temperature factor affects the intensities, whereby the thermal vibrations of atoms reduce the diffracted beam intensities while increasing background scatter. Additionally, specimen thickness affects the accuracy of peak positions and intensities while particle inhomogeneity and the polarization factor can change the diffraction intensities.[5]

2.2.1.2 Generation of X-rays

The X-ray tube generates X-rays where a beam of electrons is produced in a vacuum tube by thermionic emission from a tungsten filament. These electrons are then accelerated towards a target, usually copper, via a high voltage (20-60 kV) between the filament and the target. When the beam of electrons hits the target, X-rays are generated by two processes: A continuous band of white radiation (Bremsstrahlung) is emitted as the electrons decelerate in the electron cloud of the target metal. In addition, X-rays of specific wavelengths characteristic of the target metal are also produced. The white radiation spectrum has a maximum energy which is related to the incident radiation beam kinetic energy and carries on to lower energies.[6,7]

When the electron beam energy is higher than a specific threshold value (the excitation potential) dependent on the metal anode, an extra set of discrete X-ray peaks is seen. This characteristic radiation contains discrete peaks with energies which are characteristic of the type of target material and are generated by a two-stage process: an electron coming from the filament hits an atom of the target and ejects a core electron. An electron found in a higher energy state falls to fill the lower energy vacant hole and emits an X-ray photon with energy equal to the difference between the upper and lower energy levels. Thus, the excitation potential for a material is the minimum energy required to eject the core electron. The characteristic lines in an atom's emission spectra are called K, L, M, ... and correspond respectively to transitions to orbitals with principle quantum numbers n = 1, 2, 3, ... When the two atomic energy levels have a difference of only one

quantum level, the transitions are α lines, for e.g., n = 2 to n = 1. When the two orbitals are separated by another shell, the transitions are β lines, for e.g., n = 3 to n = 1 (Figure 2.05).[6,7]
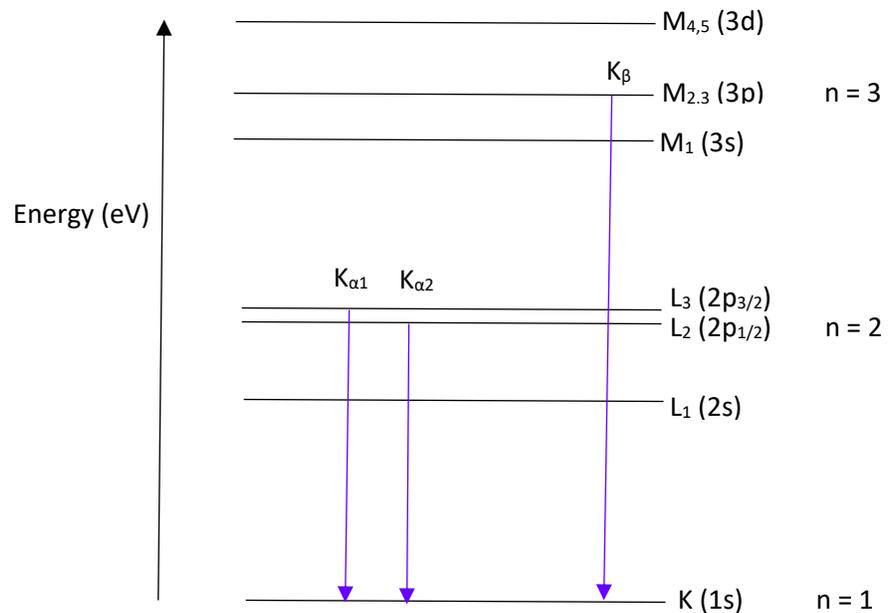
Figure 2.05. Electronic energy levels for a Cu atom

All K lines (n = 1) occur due to loss of electrons in the n = 1 state. The n = 2 and higher energy levels (L, M, N, O) are split into multiple energy levels resulting in splitting of the α and β transitions. Thus, the observed Cu K_α line can be resolved into separate wavelengths of $K_{\alpha1}$ and $K_{\alpha2}$, with the $K_{\alpha1}$ line being twice as intense as the $K_{\alpha2}$ line. At low-energy resolution (lower scattering angle), the K_α wavelength is considered as a weighted average of the $K_{\alpha1}$ and $K_{\alpha2}$ lines. The Cu 2p orbitals energy levels splitting (L_2 and L_3) is very small (0.020 keV) and the two wavelengths $K_{\alpha1}$ (1.5406 Å) and $K_{\alpha2}$ (1.5443 Å) are very similar.[6] In diffraction experiments, a monochromator (normally a germanium crystal) can be used to select the $K_{\alpha1}$ radiation while a Ni filter can be employed to remove the K_β radiation. A high-resolution analysis of Cu K_α spectral lines shows that both the α_1 and α_2 peaks are distinctly asymmetric. The de-excitation process where an outer 2p electron falls from its shell to fill the inner 1s electron shell is rapid but not enough to prevent double ionisation events, especially, the ejection of the initial 1s electron which can be accompanied by the loss of one of the 2s or 2p electrons originating from the energy levels L_1, L_2, or L_3. This increased ionisation on the atom slightly changes the energy gap between the K and L levels, which then results in somewhat different wavelengths for the emitted X-ray photon (Figure 2.06).[8]
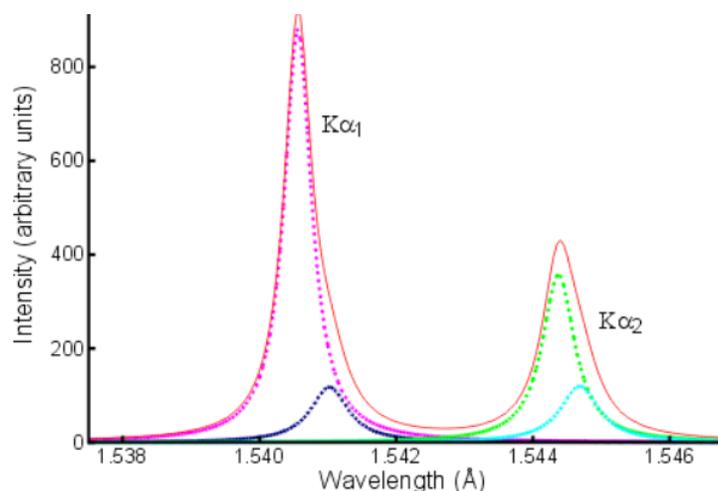
Figure 2.06. The peak asymmetry in the spectral distribution of the Cu K$_\alpha$ lines (red) and the dotted lines (coloured) representing individual spectral contributions to the total.[8]
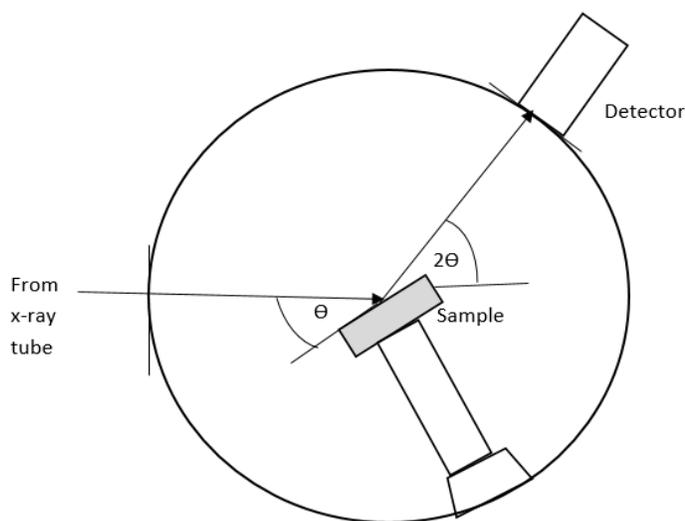
Figure 2.07. Schematic drawing of a powder X-ray diffractometer.[9]

2.2.1.3 XRPD Instrumentation

Samples were mounted on sample holders and rotated during data collection at a constant angular velocity and with a position sensitive detector which moves at double angular velocity around the sample so as to detect the diffracted X-rays (Figure 2.07).

In this thesis, three types of X-ray diffractometers were used. The Bruker AXS D8 X-ray diffractometer was used for phase identification, sample checks of 52 mins each and for high quality scans for full characterisation for Chapter 5 (12 hour) and Chapter 6 (1.5 hours) on bulk sample

holders. When the Rigaku Miniflex was installed, it was used for 1-hour sample checks and for high quality scans for full characterisation for Chapter 3 (1.5 hours) and Chapter 5 and 6 (1.5-2 hours) on zero background sample holders. The Panalytical Empyrean diffractometer was used for high quality scans for full characterisation for Chapter 4 (12 hours) on a zero-background sample holder. Variable temperature (VT)-XRPD data were also collected on the Panalytical Empyrean diffractometer which was connected to an Oxford Cryosystems PheniX closed circuit refrigerator (CCR) cryostat.[10] These instruments are discussed below along with the sample preparation.

2.2.1.3.1 Bruker AXS D8

The Bruker AXS D8 X-ray diffractometer was used for both sample checks and to obtain high quality sample data. It has an X-ray source of a mixture of $CuK\alpha_1/K\alpha_2$ radiation with wavelength of 1.54187 Å. The X-ray generator usually operates at 40 kV and 40 mA. The monochromatic X-rays go through a slit with a 6 mm aperture and through an anti-scatter tube which is attached to a fixed Soller slit and at last through a v6 variable divergence slit. The Soller slits (2.5°) minimise axial divergence, asymmetric broadening and peak shifts. The detector is a Våntec. The data collected was usually between 5-70 ° 2Θ with a step size of 0.0147 ° 2Θ over a period of usually 52 mins for sample checks and 12 hours for high quality data, on a normal sample holder. 'Bruker AXS: XRD Commander' software was used to manipulate the diffractometer and the EVA software was used to analyse the data for impurities by comparing with other powder diffraction patterns on file (ICDD PDF2).[11,12]

2.2.1.3.2 Rigaku Miniflex

The Rigaku Miniflex diffractometer was used for both sample checks and to obtain high quality sample data. It has an X-ray source of a mixture of $CuK\alpha_1/K\alpha_2$ radiation with wavelength of 1.54187 Å. The X-ray generator usually operates at 600 W, 40 kV and 15 mA. The monochromatic X-rays go through a 1.25° divergence slit, fixed 13 mm scattering slit, fixed 13 mm receiving slit, a Ni K_β filter and a 5.0° Soller slit. The detector is a D/teX Ultra which is a high-speed silicon strip detector which creates fast high resolution diffraction pattern and has an NaI scintillator. It has a sample changer stage which allows samples to change after the measurement is finished to the next programmed one. The data collected was usually between 5-90 ° 2Θ with a step size of 0.0147 ° 2Θ over a period of usually 1 hour for sample checks and 1.5-2.0 hours for high quality sample data on a zero background Si sample holder with Vaseline to help hold the sample.

2.2.1.3.3 Panalytical Empyrean

The Panalytical Empyrean diffractometer was used for high quality data. It has an X-ray source of CuKα$_1$ radiation with wavelength of 1.54060 Å. The X-ray generator usually operates at 40 kV and 40 mA. The monochromatic X-rays go through a 0.5° divergence slit, monochromator, fixed scattering slit, a Ni foil K$_β$ filter and a 2.5° Soller slit. The detector is a X'Celerator 1D Si strip detector which produces very high resolution diffraction patterns. The data collected was usually between 5-80° 2Θ with a step size of 0.0167° 2Θ over a period of usually 12 hours. This instrument was mostly used for VT-XRPD data measurements. The diffractometer was connected to an Oxford Cryosystem PheniX closed circuit refrigerator cryostat.[10] This modification allowed diffraction patterns to be measured from 12-300 K. The samples were sprinkled onto a Vaseline coated zero background Si sample holder which screws into the base of the PheniX. A liquid helium compressor cools the sample from the bottom of the sample holder which in turn is surrounded by an inner heat shield assembly. The data collected was usually between 5-90 ° 2Θ with a step size of 0.0167° 2Θ at a time per step of 179.705 and at a temperature range of 12-300 K.

2.2.1.4 Sample preparation

Zero background Si sample holders were used for most measurements. These are cut along the (*1, 1, 1*) Si plane which is systematically absent in a diffraction pattern to minimise the background scattering in the pattern. A small amount of Vaseline is applied to the surface of the zero background Si sample holder. The sample is then poured on a 100-mesh sieve and sifted through onto the sample holder. Once the desired region is covered, the sample holder is tapped gently on its side to remove any loose powder from the surface. For VT-XRPD measurements, in addition of the Vaseline, heat conductive grease was used to hold the slide onto the sample holder.

2.2.2.0 Neutron Powder Diffraction

Neutron diffraction is a powerful analysis technique which uses the interference of a neutron flux encountering nuclei in atoms. The electron density of the atoms is not a limiting factor, meaning that elements with similar *Z* (and therefore distinguishable by X-ray scattering) can give good contrast in neutron scattering experiments. Neutrons have similar wavelengths to atomic spacings; this allows diffraction measurements to be made. When a neutron interacts with an atom, this interaction is weak meaning that, unlike other techniques (XRPD and electron microscopy), the

entire sample is penetrated and not only the surface layers. Neutrons are spin ½ particles, thus have a magnetic dipole moment which can interact with unpaired electrons and nuclei and they get scattered. Since magnetic properties rely on unpaired electrons, this phenomenon makes neutrons useful for investigating magnetic ordering in materials. If there is long range magnetic order in a sample, Bragg peaks will appear in the same way as for long range order of atomic nuclei. If the magnetic unit cell is the same as the atomic unit cell, these peaks will be found at the same d-spacings, otherwise, the magnetic unit cell will be a supercell of the atomic cell.

Neutrons have no charge and their electric dipole moments are either zero or are too small. They can penetrate matter better than charged particles and they interact with atoms though nuclear forces which are short ranged. Hence, neutrons see matter as not dense due to the size of the nucleus and as a result, they can travel long distances through most materials and not get scattered. Hence, there is an irregular variation of neutron scattering amplitude with atomic weight and the scattering length is mostly positive but can have negative values. Neutrons are scattered by nuclei and by any magnetic moments in a sample. The scattering is isotropic since the range of the nuclear interaction between the neutron and the nucleus is very small when compared with the neutron's wavelength, hence, the nucleus looks like a point scatterer. Neutron scattering amplitude shows no angular dependence with 2θ as nuclei are point scattering centres.[13,14]

Since the neutron scattering lengths differ randomly across the periodic table, it is feasible to differentiate between ions with similar numbers of electrons whereas in X-ray scattering, the beam which is incident is scattered by the electrons, causing the scattering power to be proportional to the atomic number. The information obtained from neutron diffraction measurements can hence, differentiate better between atoms which are close in atomic number and study lighter atoms among heavier ones. Moreover, it can easily identify ions with low electron counts which is invisible to X-rays, or O^{2-} in the presence of high atomic number ions which is beneficial for studying oxychalcogenides. Since the cross-section of magnetic scattering and nuclear scattering have the same magnitude, they can be measured at the same time.

2.2.2.1 NPD instrumentation

2.2.2.1.1 Spallation sources

Particle accelerators eject high energy protons which hit a heavy metal target and make pulsed neutron sources. In this spallation process, each proton creates around 30 neutrons giving high neutron flux for diffraction experiments. In time of flight (t.o.f) neutron diffraction experiments, rather than selecting only neutrons of specific wavelength, a range of neutron energies (wavelengths) are used and detected at their different arrival times. The wavelength is dependent on the neutrons' speeds as shown in the de Broglie relationship:

$$\lambda = \frac{h}{mv}$$
<div align="right">Equation 2.04</div>

Where, h = Planck's constant

m = Mass of neutron

Therefore, neutrons having different speeds and different de Broglie wavelengths will arrive at the sample or detector at different times. The diffracted radiation which comes to the detector is separated according to the time taken for the neutron to travel from the source to the detector and hence, wavelength. Θ is fixed and λ and d are varied while in XRPD, λ is fixed and Θ and d are varied. Spallation sources give high neutron flux which allows data to be recorded quickly.

At ISIS, when a high intensity beam of 800 MeV protons is fired at a tungsten target, neutrons are produced. These neutrons are then moderated and carried down beamlines to different sample positions. There are two target stations at ISIS: TS1, which has 25 instruments and TS2, which has 11 instruments including WISH. The neutron beam is carried from the target to WISH via a ballistic supermirror guide, which is elliptical in both the horizontal and vertical planes.[15] The low repetition rate of TS2 makes the "natural" bandwidth (9.4 Å) of WISH higher than any other diffractometer at pulsed sources.[16] Data collected for powder diffraction experiments in an extensive angular range can be focused in either a single histogram or in a few histograms and the data reduction is done using the Mantid software.[16]

NPD data of $Pr_2O_2Fe_2OSe_2$ were collected at ISIS using the WISH (Wide angle In a Single Histogram) instrument with support from instrument scientists Dr Pascal Manuel and Dr Laurent Chapon. WISH is a long-wavelength diffractometer, built mainly for time of flight (t.o.f) powder diffraction at long d-spacing in large and magnetic unit cells.[15] It comprises of a dedicated solid-methane moderator with an optimal frequency of 10Hz.[16] It has an arrangement of 10 detector panels, with 1520 position

sensitive detector tubes, which covers an angular range of 320°. These are orientated in two semi-cylindrical annuli around the position of a central sample at 2.2 m. The high resolution data covers a d-spacing range of 0.7–17 Å with a single frame bandwidth of 8 Å.[15] WISH has a tunable resolution, due to five sets of piezoelectric slits which permit control of the incident beam divergence independently in the vertical and horizontal directions, to allow the deliverance of high-quality data in a broad Q range. Moreover, WISH has choppers, including double-discs and single-disc, which are used to choose bandwidths and avoid the overlapping of frames. Any standard sample environment kits, such as cryostats, furnaces, sub-Kelvin inserts, and pressure cells can be used on WISH.[16]

2.2.2.1.2 Reactor sources

Each atom of Uranium-235 (U-235) contains 92 protons and 143 neutrons in the nucleus. This arrangement of particles is rather unstable and if the nucleus is excited by an external source, it can disintegrate. When a U-235 nucleus absorbs an extra neutron, it swiftly breaks into two parts by fission. When the nuclear reactor starts, uranium nuclei split and give out two or three neutrons and heat. The neutrons will then hit other uranium atoms triggering them to split and give out more neutrons and heat. This creates the likelihood for a chain reaction to occur. Nuclear reactors are designed to endure an ongoing fission chain reaction, producing a stable flow of neutrons which are generated by the heavy nuclei fission. They are comprised of specially designed solid uranium fuel, coolant to transfer the heat from the core, control elements to control the rate of fissions in the uranium nuclei, structural materials and the moderator. Since U-235 nuclei do not easily absorb high energy neutrons emitted during fission, the moderator, usually water, decelerates the neutrons through elastic scattering until a thermal equilibrium between the water and the neutrons is reached.[17]

For this thesis, NPD data of $La_2O_2Fe_2OS_2$ were collected at Institut Laue-Langevin, Grenoble using the D20 instrument with support from instrument scientist Dr Emma Suard. D20 is a very high intensity diffractometer with a 2-axis and has a large microstrip detector. This detector gives a very regular response and extremely stable and high counting rates. This instrument offers the possibility of real-time experiments on tiny samples because of its very high neutron flux. The D20 is very compatible with the Rietveld refinement method. The high resolution over a wide range of positions (1536 positions) covers a scattering range of 153.6° which can be recorded in seconds and can be obtained as a function of temperature. The beam of neutrons used came from the reactor hall H11 and went through a highly oriented pyrolyptic graphite (002) monochromator. The wavelength of

the beam used was 2.41 Å and the data were collected over a period of >12 h, over a 2θ range of 5-130°. The variable monochromator has a take-off angle of up to 120° and augments the instrument's flexibility.[18]

The temperature was controlled using an Orange cryostat.[18] The sample was put in an 8 mm diameter cylindrical vanadium can sample holder to a height of 4 cm (Figure 2.08). Vanadium has a large incoherent cross section and a small coherent scattering length, hence, the vanadium can has a constant input to the background only. Consequently, no sample holder Bragg reflections were seen and all reflections seen came from the sample. Firstly, a 30 minute scan was done at 168 K. 5 mins scans were then performed on cooling at 2 K intervals, followed by a 40 mins scan at 1.8 K. Rietveld refinements of the data were performed using TopasAcademic software.[19] The diffractometer zero point and neutron wavelength were kept fixed to known values from previous work. For each refinement, a background, lattice cell parameters, atomic positions and a pseudo-Voight peak shape were refined. TopasAcademic allows the user to input refinements of both the nuclear-only and magnetic-only phases and the unit cell parameters of the magnetic-only phase were forced to be integer multiples of those of the nuclear-only phase.

Figure 2.08 Sample in vanadium can ready for neutron diffraction measurements

2.2.3 Rietveld refinement

Conventional crystal structure determination is usually done by single crystal experiment, measuring Bragg reflection intensities and solving the structure by Patterson function amongst others. Sometimes, making single crystals may not be feasible. If powder diffraction experiments are performed on the material and integrated intensities are extracted, the peaks will overlap and information will be lost. Rietveld refinement quantitatively find out the amount of phases in the sample and the size of crystallites in the samples. The Rietveld method is not a structure solution method but a structure refinement one. We need to have enough information about the crystal structure of our target material so that we can obtain a partial diffraction pattern. Rietveld refinement methods fit a model to experimental data, hence, we can expect several false minima and diverging solutions. Therefore, initially, we must refine the most important variables and then refine the others little by little until we get a correct solution.[20]

To perform the refinement, we need high quality data from the diffraction pattern, a structural model which is feasible physically and chemically, and appropriate peak and background functions. To get high quality data we need to consider calibrating the instrument, small specimen error, good counting statistics, required step size, sample transparency, how rough the surface is, any preferred orientation and the size of the particles.[20] Information about crystal structures can be found on websites, databases and papers. If nothing is found, similar structural materials should be looked for or the cell could be indexed, and direct methods or ab-initio calculations could be attempted.

The Rietveld method was introduced by H.M. Rietveld in 1967, where each step scanned intensity in a powder diffraction pattern was used as data point.[21] The method was originally made for constant wavelength neutron diffraction but was later used for X-ray diffraction and time-of-flight neutron diffraction. The Rietveld method compares observed and calculated diffraction patterns, provided that the peak intensities were collected at equal angular step sizes. The calculated peak positions and peak sizes are dependent on a theoretical model which contains numerous structural/positional and instrumental parameters such as height error, unit cell parameters, space group, atomic positions, temperature factors and peak shape function. Once the calculated pattern is obtained, least-squares refinements of the model are then performed until a 'best fit' with the observed pattern is attained over the entire 2Θ range. In this thesis, TopasAcademic was used for this least squares refinement or Rietveld.[19]

Rietveld said that for any given refinement, a best-fit is needed which is the best least-squares fit that fits all the observed intensities at the same time.[21] The calculated summation of all the data points, S_y, is given by:

$$s_y = \sum_i w_i \left(y_i - y_{c_i}\right)^2$$

Equation 2.05

Where, $w_i = 1 / y_i$,

y_i = Observed intensity at the ith step

y_{ci} = Calculated intensity at the ith step.

In Rietveld refinement, the intensity at individual point in the diffraction pattern is calculated by the following expression:

$$y_{ic} = y_{ib} + \sum_p \sum_k G_{ik}^p I_k$$

Equation 2.06

where, Y_{ic} = Intensity calculated at point i in the powder diffraction pattern

Y_{ib} = Intensity for the background at point i

G_{ik} = Value of the normalised peak profile function, G, at point I for reflection k.

i_k = Bragg intensity for k^{th} reflection

Σ_P = Summation happens over all phases, p, contributing to the respective point

Σ_k = Summation happens over all reflections, k, contributing to the respective point.

We can also refine parameters about a single sample to find a preferred orientation or about a mixed phase sample to find each phase's proportion. We can know whether the fit is good or not by looking at the difference in the pattern, R_{wp}, which is decreased during least-squares or other fitting process.[20] The calculated value, y_{ci}, is given by:

$$y_{ci} = s \sum_k L_k |F_k|^2 \phi(2\theta_i - 2\theta_k) P_k A + y_{bi}$$
<div align="right">Equation 2.07</div>

Where, s = scale factor

k = Miller indices, h, k, l for a Bragg reflection

L_k = Lorentz polarization and multiplicity factors

ϕ = Reflection profile function

F_k = Structure factor for k^{th} Bragg reflection

P_k = Preferred orientation function

A = Absorption function

Y_{bi} = Background intensity at the ith step

Several measured points in the pattern will show intensity contributions from overlapping reflections. The structure factor, F_{hkl}, quantifies the amount of light being scattered by a crystal; the arrangement of atoms in the unit cell scatters light weakly in some directions and strongly in other directions due to the type of interference produced by the waves. Hence, F_{hkl} is the summation of the scattering which happens over all the atoms in the cell.[22] The intensity of the (h, k, l) reflections is proportional to the square modulus of the structure factor F_{hkl} as follows:

$$F_{hkl} = \sum_{j=1}^{N} f_i \, exp\left[2\pi_i\left(hx_j + ky_j + lz_j\right)\right]$$
<div align="right">Equation 2.08</div>

where, (x_j, y_j, z_j) = Position of jth atom in the unit cell coordinates

f = Scattering amplitude

h, k, l = Miller Indices which define reflecting plane

In real crystals, the scattering intensity is changed by defects in the lattice structure. These cause local structural irregularities, especially in non-stoichiometric samples. Moreover, the thermal motion decreases the scattering intensity because of atomic vibrations moving the atoms away from their ideal in-plane positions, hence causing a disruption in the in-plane behaviour of their collective scattering. The structure factor correction reflected by a plane, hkl, is:

$$T_{hkl} = exp\left[-B_{hkl} \frac{sin^2 \theta}{\lambda^2}\right]$$
<div align="right">Equation 2.09</div>

Hence, for a unit cell, the structure factor is:

$$F_{hkl} = \sum_{j=1}^{N} b_j\, n_j\, exp\left[-B_j \frac{sin^2\theta}{\lambda^2}\right] exp\left[2\pi_i\left(hx_j + ky_j + lz_j\right)\right]$$

<div align="right">Equation 2.10</div>

Where, n_j = Occupation factor of jth atom which is 1 in a structure with no defects

The scattered beam intensity at a specific point also depends on the multiplicity of the precise (*h, k, l*) reflection. Thus, for a particular (*h, k, l*) reflection in a given crystal symmetry class, there exists numerous equivalent planes diffracting at the same angle to give an enhanced intensity.

The scale factor and the background are first refined. Then the zero-point correction and lattice parameters are refined. The peak profile coefficients refinements can also be refined. These permit exact Bragg reflections positions to be pin-pointed. The parameters are non-linear and therefore numerous refinement cycles are needed to get accurate data. The atomic positions are then refined to find the nicest positioned atoms and the temperature factors are refined to define their thermal motion. Lastly, the peak shape functions are refined to refine any symmetry, anisotropic temperature factors and sample broadening effects.[23]

The preferred orientation function is due to the propensity of certain types of crystallites to order in one specific way and is defined as:

$$P_k = \left[G_2 + (1 - G_2)\, exp\left(-G_1\alpha_k^2\right)\right]$$

<div align="right">Equation 2.11</div>

Where, G_1 and G_2 = Refinable parameters

α_k = Angle between assumed cylindrical symmetry and preferred orientation axis direction

Since the intensities are compared at every point, it is important that the calculated profile accurately describes the shape of the Bragg reflections. The diffraction peak shape has both sample and instrument contributions. Gaussian and Lorentzian contribute to the peak shape and the full width at half maximum (FWHM), H_k, varies with scattering angle as follows:

$$H_k^2 = U\, tan^2\theta + V\, tan\,\theta + W$$

<div align="right">Equation 2.12</div>

Where, *U, V* and *W* = Refinable parameters which can account for peak broadening because of particle sizes, strain, amongst others (for constant wavelength data).

The least squares method is used to compare the calculated and observed patterns. The refinable parameters for any least squares refinement can be classified into two groups. The first group describes the structural parameters that define the unit cell contents and include all the overlapping temperature factors, occupancies and coordinates of individual atom. The second group consists of the profile parameters which describes the shape, position and FWHM of each single peak and contains the zero-point, profile scale factor, asymmetry, unit cell parameters, U, V, W, and preferred orientation correction. The 'fit' between the calculated and observed profiles must be assessed and this is done quantitatively using several reliability factors, $R_{profile}$ or R_p, $R_{expected}$ or R_{exp} and $R_{weighted\ profile}$ or R_{wp}. The R-factors formulae are given by:

$$R_\rho = 100 \left[\frac{\sum_i |y_i^{obs} - y_i^{calc}|}{\sum_i y_i^{obs}} \right]$$

Equation 2.13

$$R_{exp} = 100 \left[\frac{(N-P+C)}{\sum_i \omega_i (y_i^{obs})^2} \right]^{1/2}$$

Equation 2.14

$$R_{wp} = 100 \left[\frac{\sum_i \omega_i |y_i^{obs} - y_i^{calc}|^2}{\sum_i \omega_i (y_i^{obs})^2} \right]^{1/2}$$

Equation 2.15

Where, R_{exp} = Obtained from statistics of refinement

N = Number of observations

P = Number of refinable parameters

C = Number of constraints

Mathematically, R_{wp} is most useful as the numerator is the remainder being kept at a minimum and hence, shows the progress of the refinements and is usually mentioned when showing a specific refinement fit. The chi-squared parameter, χ^2, is a measure of the complete fit and is also kept at a minimum during the refinement.

$$\chi^2 = \left[\frac{R_{weighted\ profile}}{R_{expected}} \right]^2$$

Equation 2.16

For a fit to be successful, the R_{wp} should be close to R_{exp} statistically. However, χ^2 can be deceptive as it hinges on the data quality. A long scan will decrease R_{exp} by a lot making χ^2 exaggeratedly big and a shorter scan will increase R_{exp} and make χ^2 very small. We also need to have a good starting approximation to refine in an iterative process. In Rietveld refinement, we decrease the square of the difference between the diffraction pattern that we measure and the profile that we calculate based on the position of the reflections, their intensities and their shapes. Hence, we can obtain information about the unit cell parameters, whether our sample is single phase or mixed phase, size and shape of particles, atomic coordinates, bond lengths and vacancies. The peak intensities are affected by structure factors, absorption, temperature factor, multiplicity, Lorentz factor, Polarization factor, preferred orientation and Extinction coefficients.

In all the samples discussed in this thesis, the following parameters were refined: background, zero error, a scale factor, unit cell parameters, volume, atomic positions, axial, a term to describe peak symmetry and 4 terms of Thompson-Cox Hastings pseudo-Voigt peak shape function (Appendix 2.01). Since the VT-XRPD and neutron data gave lots of scans for each sample, the refinement of all these samples were done using multitopas, a FORTRAN routine for generating a DOS based batch program, in TopasAcademic.[19] This process begins with a seed refinement (Appendix 2.02) which is written manually by running a usual refinement in TopasAcademic and copies the output to a new file which in turn is refined against the next set of data.[24] This process carries on until the last data file has been refined. The multitopas batch file contains all the data filenames, list of files (Appendix 2.03) and associated temperatures, fields and other parameters needed (Appendix 2.04). This process permits the refinements to be done sequentially. The refined parameters that we are interested in are automatically written to a .res file (Appendix 2.05) after each refinement is done and these can be easily plotted in Microsoft Excel to be studied. Since this process uses a structural model which comes from a refinement at a temperature that differs very slightly, the convergence time is decreased, and the occurrence of a false minimum is avoided. Pawley refinements were also used where the data on the cell contents was replaced by a list of reflections which are allowed for the space group looked at in question.[25] These refinements also consisted of unit cell parameters and peak shape terms.

2.2.4 X-ray Absorption Near Edge Structure

X-ray absorption spectroscopy is an electronic spectroscopy technique and is used to find local structure in atoms. It can give information about atomic number, thermal motions of atoms surrounding the element being looked at, structure and structural disorder. It can be used in materials which do not have any long range order. It has 2 parts: X-ray Absorption Near Edge Structure (XANES) and Extended X-ray Absorption Fine Structure (EXAFS).

XANES is an element-specific analysis technique and is sensitive to local bonding. It shows the partial density of the empty states present in a molecule and is very good for measuring oxidation state as many edges of many elements show significant edge shifts with oxidation state. XANES directly probes the angular momentum of the unoccupied electronic states which may be bound, unbound, discrete, broad, atomic or molecular. Higher oxidation states mean the electron states are more tightly bound and they produce higher energy in XANES. In principle, oxidation states results should not vary for XPS and XAS. However, transition metal oxides with narrow levels in the valence band, can have different core-level energies for XPS and XAS because of differences in multiplet effects or selection rules.[26] EXAFS gives information about interatomic distances, lattice dynamics and near neighbour coordination numbers. It is best for looking at details of the local structure around the absorbing cation. XAS corresponds to a core level-unoccupied orbital transition and it primarily reflects the electronic unoccupied states. EXAFS provides information on the local structure based on the results gathered from the interference in the single scattering process of the photoelectron which are scattered by surrounding atoms.

When a core electron absorbs an X-ray photon, absorption occurs when the energy of the radiation is the same as the ionisation energy of that electron. The latter is kicked out of its core shell to an empty spot which is lower than the ionisation threshold (excitonic state or bound state) or to the continuum (unbound state) found above that threshold. This creates a hole which is filled with an electron coming from a higher energy state, thereby giving out energy. This energy can relax via exciting and emitting an electron from a higher energy state (Auger electron) or via X-ray fluorescence to give out a photon. For higher-energy excitation (e.g., for the *K* edges of elements with *Z* > 40), the hole relaxes via X-ray fluorescence. The X-ray fluorescence intensity is directly proportional to the X-ray absorption cross-section of the sample. However, in reality, when an X-ray beam is shone onto a material, various X-rays are produced (fluorescent X-ray from sample,

background X-ray from sample scattering). Hence, detectors which selectively differentiate the background radiation from the data information are used.[26]

When an X-ray beam is transmitted through a sample of thickness x, attenuation occurs, and the absorption cross-section is:

$$ln \frac{I_0}{I} = \mu(E)x \qquad\qquad \text{Equation 2.17}$$

Where, I_0 = Incident beam intensity

I = Transmitted beam intensity

x = Thickness

$\mu(E)x$ = Absorption cross-section

The spectrum obtained shows that when the beam of scanning X-ray hits the absorption edge, transmittance diminishes. Transmission mode is the most common method used as long as the samples are as single crystal or homogenous powders. The sample thickness is usually adjusted to 1-2 absorption length but for samples that have several components, the weighted average cross-section can be used:

$$\mu(E) = \sum_{i=1}^{n} \mu_i wt\% i \qquad\qquad \text{Equation 2.18}$$

XAS spectrum has 4 main parts: the pre-edge, the absorption edge (big jump at 0 eV), the near-edge (XANES) (0-50 eV) and the post edge (EXAFS) (Figure 2.09). The pre-edge can give information about the ligand-field, centrosymmetry and spin-state. The pre-edge is usually used to normalise the data although it contains weak transitions originating from bound states. This metal K-pre-edge comes from the $1s$ to $3d$ transitions, provided the $3d$ orbital is not full, even though the dipole selection rules forbids it. This transition is seen because of the mixing of $3d$ to $4p$ orbitals and direct quadrupolar coupling. The greater the $3d$ to $4f$ mixing, the bigger the $1s$ to $3d$ transition. Hence, the molecular geometric properties of the absorption sites can be analysed. Different core electrons have specific binding energies. An edge occurs when a core electron absorbs energy which is the same or greater than its binding energy and the edges are labelled according to the principle quantum number from which the core electron comes (for e.g., n = 1 is K-edge, n = 2 is L-edge).

An element can exhibit numerous absorption edges. The absorption edge sometimes gives a sharp intense peak called a white line. The absorption edge can give information about the geometric structure, ligand arrangement, charge on the metal centre and metal-ligand overlap. XANES is sensitive to oxidation states. Atoms with big oxidation states need more X-rays to excite its core electron as the nucleus is not much shielded and the effective charge is greater. Hence, as the oxidation-state of an atom increases, so does the energy of the absorption edge. Moreover, the edge can be seen as a continuum resonance, which is a short-lived excitation process where a core electron is excited into a higher energy state, usually higher than the continuum. The bigger the oxidation state, the shorter the bond length is and the bigger the edge energies are. Therefore, the absorption edge is affected by oxidation state, coordination number, geometry, covalency, pre-edge shape and energy. The XANES region is very sensitive to small variations in the structure.[26]

XAS can be used to find the structure of a molecule depending on the way the photoelectrons influence the radiation intensity when they scatter. In the XANES region (low energy), neighbouring atoms are close to the centre atom as well as to each other. Hence, the electrons that get excited can bounce between the neighbouring atoms before they strike the absorbed atom. This is multiple scattering in XANES and it is very sensitive. It gives information about spatial arrangement, bond angles and orientations relative to one another. The difference in energy range between XANES (5-150 eV) and EXAFS (150-2000 eV) can be explained by comparing the photoelectron wavelength and the interatomic distance of photoabsorber-backscatterer pair:

$$E_{kinetic} = hv - E_{binding} = \frac{h^2 k^2}{2m} = \frac{4\pi^2 h^2}{2m\lambda^2} \qquad \text{Equation 2.19}$$

Hence, at high energy, wavelength is smaller than interatomic distances and the EXAFS region is associated with single scattering, while al low energy, wavelength is bigger than the interatomic distances and the XANES region is linked to multiple scattering.
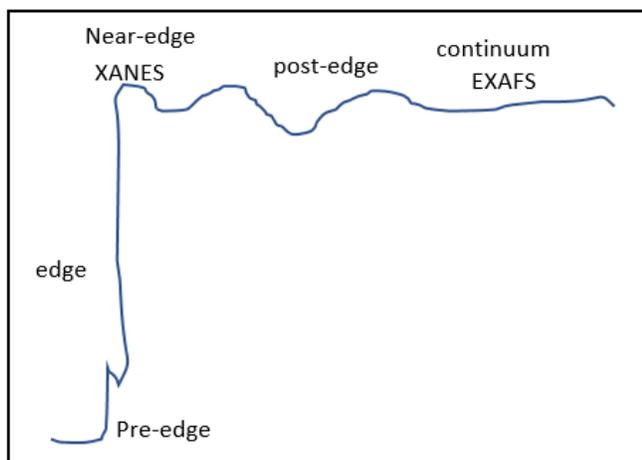
Figure 2.09 Schematic diagram of X-ray absorption edge

In this thesis, the samples were mixed thoroughly with PVP according to Absorbix[27] and pressed into pellets to get a uniform surface. The pellets were then measured on B18 at Diamond Light Source with the help of Prof Alan Chadwick and Dr Silvia Ramos through the BAG. B18 is a general purpose XAS instrument and consists of I18 and I20 which provide a range of energy (2-35 keV). The beamline has 3 main optical components: The focusing mirror, a double crystal monochromator which is cooled by water and a collimating mirror. The collimating mirror is made up of Si and is water-cooled. The vertical mirror has Cr and Pt stripes coatings which measure from 2-35 keV. Similarly, the double toroidal focusing mirror is coated with Cr and Pt and is kept fixed at all times. The monochromator is kept fixed and is able to do rapid scans. It consists of Si (*1, 1, 1*) and Si (*3, 1, 1*) which can permit lower and higher energy ranges to be used. Lastly, two smaller plane mirrors are put in the beam path when low energies are used (< 11 keV). The measurements can be done in either transmission or fluorescence. In the fluorescence mode, the Ge solid-state detector is put perpendicular to the X-ray beam at the sample while in transmission mode, there are three ion chambers which are located along the path of the X-ray beam so as to have information about the beam intensity before and after the sample and after the reference.

The XANES analysis was performed in Athena which is part of the Demeter software suite.[28] The data was normalised by modelling the pre-edge line and post-edge line. The pre-edge line was then subtracted from the data and multiplied by the difference between the pre-edge and post-edge line at the absorption edge step. A *k*-weighting was applied to the data by multiplying the signal with the wavenumber as a power of the weighting, for e.g., a *k*-weight of 2 means that the signal is

multiplied by 16 at a wavenumber of 4 Å. The R-space was also plotted to fit specific coordination shells.

2.2.5 X-ray Photoelectron Spectroscopy

X-ray photoelectron spectroscopy (XPS) is a non-destructive technique which can be used to tell what elements are present on the surface of the samples and how much, information about local bonding of atoms and the density of electronic states. It is sensitive to materials' surfaces and is used to find the constituent components in a sample. During the process, the sample is irradiated with monoenergetic Al K_α X-rays and the electrons get excited to several energy levels of the atom. These electrons get ejected with a specific kinetic energy. Because the electronic energy levels are quantised, the binding energy for each energy level is exclusive, hence, giving off characteristic peaks for specific atoms. These spectral peaks can be matched to the electrons' electronic configuration within the atom such as 1s, 2s, 2p, and so on. The number of electrons which are seen in each characteristic peak is proportional to the amount of the element present in the XPS sample volume. For a given photon energy, the kinetic energy can be measured when the electrons are emitted, and the binding energy can be calculated by:

$$E_{binding} = E_{photon} - (E_{kinetic} + \Phi) \qquad \text{Equation 2.20}$$

where, Φ = Work function

This information and the number of electrons striking the detector can help find out the relative composition of the species in the sample. Since, the energy levels for different compounds are different, different peaks will give different oxidation states and hence, we can figure out specific compounds or species in a sample. It is possible that other electron types may be detected by XPS such as Auger electrons. These are secondary electrons. When a core electron is emitted, a higher-energy electron will come and take its place, releasing energy as photon in the process which is equal to the difference between the energy levels. During this process, it is possible for the photon to excite and eject an Auger electron. A typical XPS plot shows the number of electrons detected against their binding energy.

The chamber must always be kept in an ultra-high vacuum and low pressures are needed. The chemical state (local bonding environment) of an atom is affected by numerous things such as its bonding hybridization with its nearest-neighbour atom and between the atom and its next-nearest

neighbour, its formal oxidation state and what its nearest-neighbour atom is. Hence, chemical shifts can give information about the chemical state. The value of chemical shift is dependent upon how much the electron bond is polarised between the nearest neighbour atoms. A specific chemical shift represents the difference in binding energy values of an explicit chemical state against that of the element in its standard state. It is a quantitative technique since the chemical environment of the atom and the cross-section for a photoelectron emission are independent of each other.

In this thesis, the XPS measurements were done by our collaborator Dr Robert Palgrave, at UCL. The samples were put on carbon studs which were stuck to a metal slab (Figure 2.10).
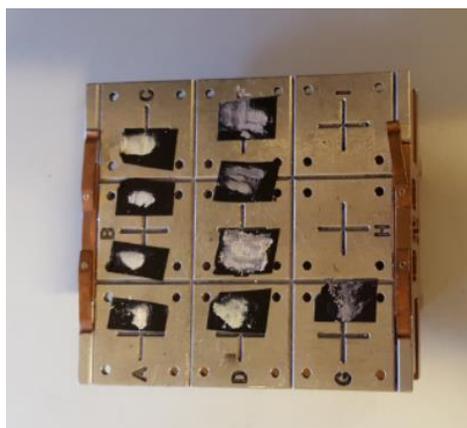
Figure 2.10 Samples prepared for XPS analysis.

2.2.6 SQUID Magnetometry

The Quantum Design Magnetic Property Measurement System (MPMS) consists of a superconducting detection coil, the superconducting quantum interference device (SQUID) and a superconducting magnet. The prepared sample is then put at the bottom of a rod and lowered into the sample chamber which is maintained at a low pressure and surrounded with liquid helium as low temperatures are needed. The detecting coil is a second order gradiometer and is placed outside the sample compartment in a way that the sample's magnetic field combines inductively to the coils as the sample is moved through them. The coil is linked to the SQUID by superconducting wires which permit the current coming from the coils to couple, through induction, to the SQUID sensor. The output voltage recorded is proportional to the amount of current flowing in the input coil, hence, it is a very sensitive current-to-voltage converter. As the sample moves in the coils, an electric current is induced by the sample's magnetic moment in the detection coils. The detection coils,

wires and SQUID form a closed superconducting loop and the slightest change in in the detection coils' magnetic flux causes a change in current and hence, in the output voltage. Therefore, the output voltage of the SQUID is proportional to the current in the detecting coils while the current is in turn proportional to the sample's magnetic moment, thus, causing the output voltage of the SQUID to be proportional to the sample's magnetic moment.

Superconducting Quantum Interference Device (SQUID) is among the most sensitive forms of magnetometry. It utilises a mixture of superconducting materials and Josephson junctions to measure magnetic fields together with resolutions up to 10^{-14} kG. The Josephson junction combines two superconductors via a small insulating slit via which superconducting electrons can go through (Figure 2.11).[29–31] Any magnetic dipole (ferromagnetic or paramagnetic) creates a field of the order of:

$$B_0 = {M}/{d^3}$$ Equation 2.21

Where, M = Dipole moment

d = Distance of the point on the field from the centre of the dipole.

If d is fixed, the measured field tells us about the dipole moment and magnetisation or susceptibility.
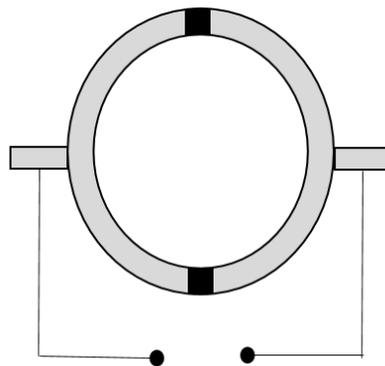
Figure 2.11 Schematic of the SQUID showing the Josephson junctions (in black), the superconductors (in grey) and the wires which connect to the output.

The magnetic coil can operate in 2 modes: oscillate and hysteresis modes. In the oscillate mode, in each cycle, the magnetic field over give/under give the anticipated field in an alternate way with reducing amplitude. This diminishes the quantity of magnetic flux becoming dormant which is typical of a change of field in superconducting magnet. This mode permits very sensitive

measurements to be made quicker. In the hysteresis mode, the tenacious current switch is always left on, hence, the magnet is not run in persistent mode and the power supply forms a frequent part of the magnetic circuit. This mode is very useful for speedy magnetisation (M) against applied magnetic field (H) although large magnetisation is required.

In zero field cooled (ZFC), the sample is first cooled to the desired temperature in the absence of any applied magnetic field and then data is collected while heating in the presence of a magnetic field. In field-cooled (FC), the sample is cooled to the desired temperature in the presence of any applied magnetic field and depending on the field-cooled measurements, the data is collected either during cooling (field-cooled cooling) or during warming (field-cooled warming). In the absence of an applied magnetic field, particles are randomly oriented and depending on the sample, when these particles are cooled, the magnetic domains are frozen and remain oriented. When a magnetic field is applied, any response will occur because of anisotropy of the particles as strong anisotropy increases at low temperatures and hence, the magnetic saturation field becomes huge. Additionally, when the sample is cooled in the presence of any applied magnetic field, the magnetic domains will align with the field and magnetic saturation is attained. ZFC and FC measurements can give information about superconducting properties, spin-glass behaviour and presence of exchange bias.

The behaviour of the magnetic specific heat of a 'simple' antiferromagnet focussing on the singular behaviour where the transition occurs, should closely match the shape of the function $\mathrm{d}(\chi T)/\mathrm{d}T$, where χ is the magnetic susceptibility. The maximum obtained from the $\mathrm{d}(\chi T)/\mathrm{d}T$ v/s T plot, made by using magnetic data, is usually in good agreement with heat capacity data and hence, can be used to confirm the transition temperature, T_N. Hence, the Fisher heat capacity can be used to determine heat capacity indirectly from magnetic susceptibility data. Moreover, the entropy associated with the magnetic transition can be calculated which can suggests the presence of short-range correlations.[32]

In this thesis, the samples were weighed ($La_2O_2Fe_2OSe_2$ = 0.0966g, $La_2O_2Fe_2OSe_2$ = 0.1021g, $La_2O_2Fe_{1.5}Co_{0.5}OSe_2$ = 0.1060g and $La_2O_2Fe_{1.9}Ni_{0.1}OSe_2$ = 0.1335g) and put in half of a gelatine capsule, with the other upturned half of the capsule holding the loose powder in place. They were then inserted in plastic straws in a way so that the samples would be in the centre of the pickup coils. Empty gelatine capsules were inserted into the straws to fill them up. The ends were sealed with special tape and holes were punctured in the straws taking care not to puncture the capsules (Figure

2.12). The data was collected on a Quantum Design SQUID Magnetometer which can collect data between 1.8 K and 400 K in a field strength of up to 5 Tesla. The data was collected on field-cooled and zero-field-cooled from 2 K to 300 K at 5 K min^{-1} in an applied magnetic field of 1000 Oe (for FC only) (Appendix 2.06).

Figure 2.12 Picture of a sample ready for magnetometry measurements

2.2.7 Physical Properties Measurement System

Electrical resistivity is among the most sensitive indicators when the nature of chemical bonding is modified. As a rule, the electrical resistivity is inversely proportional to the carrier density and mobility. Whenever there is a modification in the nature of the chemical binding, the carrier density is changed which in turn changes the carrier mobility. There are many ways to measure electrical resistance and these depend on the contact resistance and the sample shape (crystal, thin film, crystallite). Two probes method can be used for higher resistive samples while four probes method can be used for low resistive samples, small samples and single crystals (Figure 2.13).[33]

In the two-probe method (Figure 2.13a), the voltage drop and current through the sample are measured and the resistivity is calculated as follows:

$$\rho = \frac{VA}{IL} \qquad \text{or} \qquad \rho = \frac{RA}{L} \qquad \qquad \text{Equation 2.22}$$

Where, V = Voltage

I = Current

A = Cross-sectional area of sample

L = Length of sample

R = Resistance

This means that the resistivity of a material increases with cross-sectional area and decreases with length. However, the contact resistance can cause inaccurate resistance to be measured and these can be improved using conductive gels.[34]

In the four-probe method (Figure 2.13b), the current goes though the outer contacts and the voltage is recorded across the inner contacts. The voltage drop and current through the sample are measured and the resistivity is calculated as:

$$\rho = \frac{V_D A}{DI}$$

Equation 2.23

This method is excellent for low and accurate electrical resistance measurements as the effects of contact resistance between the electrical contacts and sample are removed. Even though the contact and lead resistance are eliminated, the contact resistance can still produce an error if they are heated enough and hence, they should have a small resistance. Other errors that can occur are instrument dc and self-induced voltage offsets, and signal noise. However, these can be easily corrected for.[33]
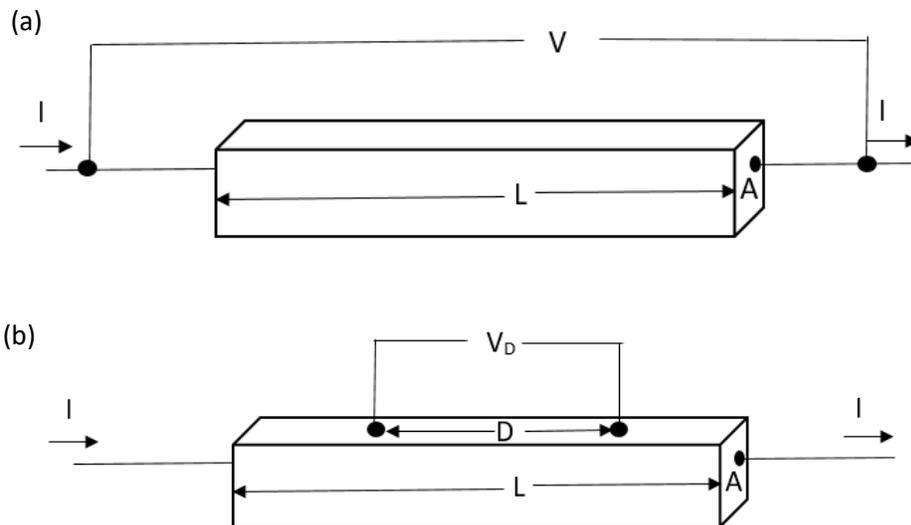
Figure 2.13 Electrical resistivity measurements by the (a) two probe method (b) four probe method.[33]

A band conduction model predicts an Arrhenius temperature dependence of the conductivity as follows:[35]

$$k = Ae^{\left(\frac{-E_a}{RT}\right)}$$

Equation 2.24

Where, k = Rate constant

A = Pre-exponential constant related to the state of the reaction

E_a = Activation energy

R = Universal gas constant

T = Absolute temperature (K)

It has been observed that in some materials, namely semiconductors, the temperature dependence deviates at low temperatures up to room temperature, signifying that there is a different conduction mechanism involved. The electronic conduction processes that are dominant occur in a much narrower energy band around the level of the chemical potential, where the electronic states in semiconductors within the gap are localised. Hence, the charge transportation needs a conduction mechanism through these localised states.[36,37] According to the variable range hopping theory of Mott, for 3-D systems, when conduction between localised states near Fermi level, E_f, happens by hopping, the temperature, T, dependence of the resistivity is as follows:[38]

$$\rho = \rho_0 e^{\left(-\frac{T_0}{T}\right)^{\frac{1}{4}}}$$

Equation 2.25

Where, T = Absolute temperature (K)

T_0 = Constant

ρ = Resistivity

ρ_0 = Prefactor

This above equation includes the assumptions that the density of states is constant over the energy range of hopping. In variable range hopping, there is a strong relation between the level of hopping conductance and the concentration of localized states around the chemical potential. Variable range hopping is the main conductivity mechanism present in disordered media. Phonons stimulate tunnelling processes which allow electrons and holes to move through localised states. This mechanism is analogous to the impurity conductivity, which can be observed in heavily doped semiconductors at low temperatures. The density of states favours the hopping conductivity as it enhances the probability to hop from one site to another.[39–42] Berkovits and Shklovskii suggested other possible hopping mechanisms based on delocalised tightly bound excitons. In this model, in

the strongly disordered regime, the behaviour of the numerous-level spectral statistics is explained as a manifestation of delocalised excitons which in turn suggests that the latter can substitute the phonons as an energy source for the hopping conductance.[43,44]

In this thesis, the samples for PPMS measurements were annealed as 5 mm pellets in a furnace in sealed quartz tubes under vacuum and cut into small rectangles. These pellets were taken to the Materials Characterisation Laboratory at the ISIS Neutron Source where I was trained to do the measurements by Dr Gavin Stenning. The pellets were put on a puck and the contacts were glued onto the pellets using silver conductive paint (Figure 2.14). Their resistance as a function of temperature (2-300 K) was recorded. The instrument used was a Quantum Design PPMS-9.
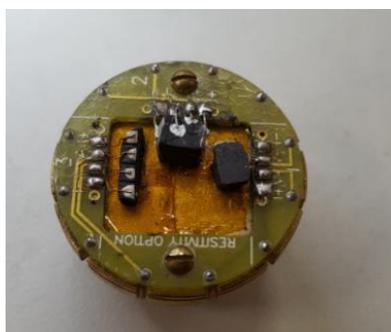
Figure 2.14 Puck with samples ready for electrical resistivity measurements

2.2.8 Diffuse Reflectance Spectroscopy

When light is shone on a powdered sample, it can be absorbed, transmitted or reflected. When the incident light is scattered back from where it came from, it gets reflected and the angle of incidence, θ_i, is the same as the angle of reflection, θ_r (Figure 2.15). Absorption is when light is retained by the medium while transmission is when all the light goes through it.
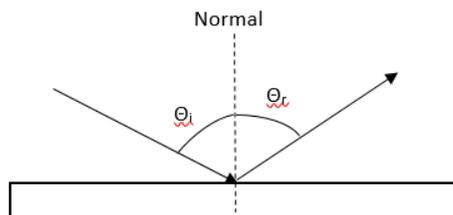
Figure 2.15 Laws of reflection

The reflected light becomes specular reflection at the sample's surface while the rest is refracted as it penetrates the sample where it gets scattered because of internal reflection, surface reflection from powder grains or recurrent refraction when it enters the sample (Figure 2.16). Some of the scattered light is ejected back into the air. As the diffuse reflected light is reflected or goes into the sample, it gets weaker if absorption happens and hence, a diffuse reflectance spectrum is obtained which is similar to the transmission spectrum. However, in parts of the sample where the absorption is strong, the majority of the diffuse reflected light in long light paths is absorbed and the ones from the short light paths are ejected back. Similarly, in weak absorption bands, some light from long light paths is not absorbed and instead is ejected back in air giving stronger peaks than the transmission spectrum. The resulting absorbed wavenumber positions are just like the ones in the transmission spectrum, but the relative intensity of the peaks is different since the weak peaks in transmission spectrum become stronger in the diffuse reflectance spectrum. Diffuse reflection is usually formed by a rough surface and if the latter is similar or bigger than the wavelength of incoming light, the rays will get scattered everywhere (Figure 2.16b). However, the law of reflection still applies but the angle changes. Perfectly diffused light has the same intensity everywhere.[45]
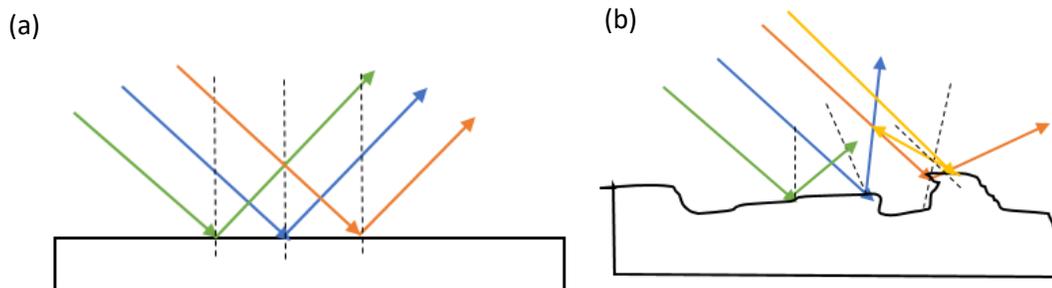
Figure 2.16 (a) Specular reflection (b) diffuse reflection

Kubelka-Munk showed that for an infinitely thick opaque layer, the diffuse reflectance for a specific wavelength is:[46,47]

$$R_\infty = \left[\frac{I}{I_0}\right]_t = \frac{1-\sqrt{\frac{k}{k+2s}}}{1+\sqrt{\frac{k}{k+2s}}}$$

Equation 2.26

Where, R_∞ = Absolute reflectance

K = Absorption coefficient

S = Scattering coefficient

For transmission into a sample with thickness d:[47,48]

$$I = I_0\, exp\left(-\sqrt{k(k+2s)}d\right)$$ Equation 2.27

When s = 0, we get the Beer-Lambert law.

For specular reflection from single crystal, the Fresnel formula is:[49,50]

$$R_{sp} = \left[\frac{I}{I_0}\right]_2 = \frac{(n-1)^2+n^2K^2}{(n+1)^2+n^2K^2}$$ Equation 2.28

Where, n = Refractive index

     K = $k\lambda/4\pi n$ = Absorption index

The above equation shows that when K gets bigger, R_{sp} gets larger which means that there is reflection at the absorption band due to crystal selectivity. Therefore, specular reflection (big for strong absorbing sample) and diffuse reflection (big for non-absorbing sample) are largely complementary.

Equation 2.22 can be changed to give the Kubelka-Munk function, F (R_∞):

$$F(R_\infty) = \frac{(1-R_\infty)^2}{2R_\infty} = \frac{k}{s}$$ Equation 2.29

Where, R_∞ = Absolute reflectance

     k = Absorption coefficient

     s = Scattering coefficient

Light released into the air consists of specular reflection light and diffuse reflected light. For accurate diffuse reflectance spectrum, specular reflection light must be decreased and this is done by diluting the sample with a non-absorbing standard.[45] When measuring diffuse reflectance, the sample distance, surface and spot size are important. Sample distance is important because it governs the amount of reflected light that is measured and since the percentage reflection depends on the standard to sample ratio, both at a precise distance, the alteration in the quantity of total light striking the detector would make the full spectrum and baseline shift. However, this can be rectified using a collimated beam. The spot size needs to be well chosen, especially if the sample is

inhomogeneous, as defects may be missed and if light is wasted, it can add to signal noise. If the sample has an irregular surface, it can affect the distance and the amount of light detected.

In this thesis, an ocean optics DH-2000 UV-Vis light source with a Maya Pro 2000 spectrometer (range is 165 – 1100 nm) was used for the measurements. The samples to be analysed were mixed with NaCl (10 % by weight) thoroughly. The NaCl was dried in the furnace prior to using. They were then put in plastic cuvettes and a cuvette of just NaCl was used as a reference to check for deviations. The measurements were taken at an integration time of 900 ms, boxcar smoothing of 7, an average of 4 scans per sample and in the presence of a dark spectrum. Once the measurements were made and plots of intensity against wavelength were obtained, Kubelka-munk transformation was used to plot the data in terms of $[F(R_\infty)*h\nu]^2$ as a function of energy (eV). The band gaps were calculated by extrapolating the linear part of the data at y = 0.

2.2.9 Scanning Electron Microscopy

A scanning electron microscope (SEM) is a type of microscope which uses electrons rather than light so as to make an image. It is mainly used in medical areas to screen a large range of specimens. Scanning electron microscope is a non-destructive technique.

A scanning electron microscope has a big field depth allowing at least one specimen to be focused at one time. Its resolution is better than that of a traditional microscope which means that specimens close together can be magnified much more. The level of magnification can be managed much more since scanning electron microscopy uses electromagnets rather than lenses.[51] Moreover, it uses a beam which is focused and comprises high energy electrons which releases an array of signals at the solid samples' surfaces. Signals coming from the interactions between the electron and the sample give data about the sample such as morphology, chemical composition, crystallinity and the particles' position in the sample. Normally, the data measured over a unique sample surface area gives out a two-dimensional image showing spatial changes in these properties. SEM can image areas ranging from 1 cm to 5 microns, can magnify from 20-30,000 X and has a spatial resolution of 50-100 nm. It can also analyse unique areas on the sample, which is crucial in qualitative and semi-quantitative analysis of the chemical composition, crystallinity and the crystal position. The same materials can be analysed numerous times. The gathering of data is rapid and is

produced in digital formats. Scanning electron microscopes possess at least one detector and the potential of an instrument depends on its detector.

The sample to be analysed by SEM needs to be prepared with care because SEM uses vacuum conditions and electrons. The sample preparation can be minimal or complicated and this depends on the nature of the sample and what information is required. Minimal preparation means fitting the solid sample into the SEM chamber and preventing a build-up of charge on electrically insulating samples. Water needs to be removed from the sample as it would vapourise under vacuum. Metals conduct electricity and hence, need minimal preparation. On the other hand, non-metals do not conduct electricity and need to be made conductive by laying a thin layer of a conductive substance on the surface of the sample. This is performed by sputter coater. In the sputter coater, the sample is inserted inside a small vacuum chamber. The argon gas has an electron removed by an electric field to produce positive argon ions which are attracted towards a negatively charged gold foil where they dislocate gold atoms from its surface. These gold atoms drop and rest onto the top of the sample to produce a thin gold coating.[51]

The sample is inserted in the column of the instrument's vacuum through a door which is air-tight. Air is pumped out of the column and an electron gun found at the top, shoots an electron beam at the top of the microscope. This beam of electrons moves downwards through the microscope in the electromagnetic fields, and electromagnetic lenses focus the electrons to a very narrow spot. The scanning coils located beneath the magnetic lenses move the focused beam backwards and forwards and row by row across the specimen. The beam smashes into the sample and electrons and X-rays are ejected. Some of the ejected X-rays are of a characteristic nature which is crucial for elemental analysis while the others are of continuum nature. The electrons that are ejected include backscattered electrons which are needed for imaging the samples and showing fast phase discrimination in multiphase samples, diffracted backscattered electrons which are needed for structure determination and position, and secondary electrons which give SEM images and show morphology and topography on samples. Backscattered electrons come from a greater region of the sample and are caused by collisions of electrons with atoms. Secondary electrons are emitted by atoms found on the surface or near the surface of the sample when the electron beam and the atoms in the sample interact. Elements of higher atomic mass appear brighter than those with lower atomic mass in backscattered electron images compared to secondary electron images as scattering is proportional to atomic number and hence, contrast gives information on composition. These X-

rays are collected in detectors where they are converted into signals which are then relayed to a screen to give a final image (Figure 2.17).

The SEM instrument used in this project was a Hitachi S-3OON. The samples were pressed into pellets and stuck on a carbon stud. An overall backscattered electrons image for each sample was taken to get an idea of the homogeneity of the sample. Each sample was divided into 10 sites and energy dispersive X-rays spectra were collected on each site at 10 different points.
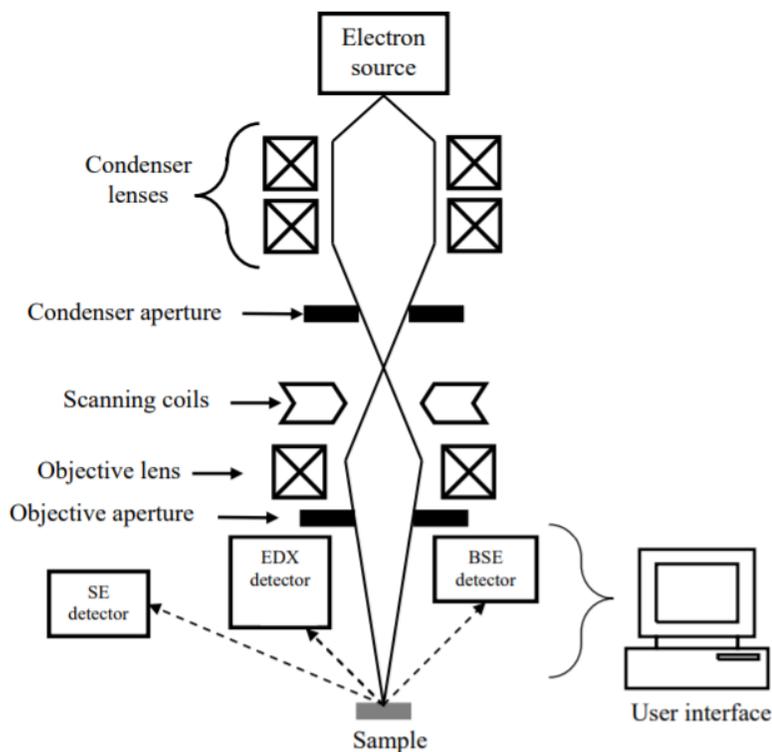
Figure 2.17. Schematic diagram showing inner arrangement of a scanning electron microscope.[51]

2.2.10 Energy Dispersive X-ray microanalysis

Energy-dispersive X-ray microanalysis (EDX) is an analytical technique which is used for elemental analysis of a sample. It relies on the fact that each element has a specific atomic structure and X-rays that are characteristic to such an atomic structure can be identified uniquely. Elements from atomic number 4 to 92 can be detected, although not all instruments can detect light elements which have atomic number less than 10.[52–54] EDX complements SEM.

In EDX, when a high energy electron beam of charged particles hits a sample, it excites an electron in an inner shell, ejecting it and thus creating an electron hole in its place. An electron found in an outer higher binding energy electron level falls into the hole to fill it and an X-ray is emitted with the energy corresponding to the difference between the higher-energy shell and the lower energy shell. The characteristic X-ray energies emitted for elements will usually vary from element to element with only some spectral peaks overlapping owing to the quantisation of electron energy levels. Therefore, if the energy of the X-rays can be measured, the elements found in the sample can be determined. If the conditions of the instrument are monitored with care, the concentrations of the elements can also be found. The excitation source is the normal electron beam of a SEM and the sample is effectively the X-ray source anode.

The three main components of a typical EDX system are the X-ray detector, the pulse processor which records voltage pulses corresponding to the energies of the X-ray, and a computer. The detector is placed so as to catch X-rays released from the sample. When the X-rays go inside the detector, a small current is produced, which is changed into a voltage pulse. The size of the voltage pulse is proportional to the X-ray energy. The computer measures the voltage pulses over a length of time and plots them in the form of a histogram which shows a spectrum of the energies of the X-ray which were measured. By scrutinizing the spectrum, the elements present can be calculated.[52]

The first thing to do in quantitative analysis in SEM is to get homogenous standards for each element that has been found in the qualitative analysis. Both the standards and the sample must be polished flat. Then, the sample's and the standards' X-ray spectrum containing the elements that have been identified in the sample must be obtained at the same dead-time, resolution, calibration, beam current and energy and spectrometer take-off angle. Continuum X-ray background signal must be taken out from the spectra of the standards and of the sample so that the intensities which were measured contain just the characteristic signal.

2.3 References

1   A. R. West, *Solid State Chemistry and its applications*, John Wiley and sons, New Jersey, 1987.

2   P. Moeck, *Topic5a-XRD*, 2004.

3   Scintag, *Chapter 7:Basics of X-ray Diffraction*, 1999.

4   J. Als-Nielsen and D. McMorrow, *Elements of Modern X-ray Physics*, Wiley, West Sussex, 2nd edn., 2011.

5 A. R. West, in *Solid State Chemistry and its applications*, John Wiley and sons, New Jersey, 1987, p. 163.

6 M. Liang, *Int. Union Crystallogr. Teach. Pam.*, 1997.

7 B. D. Cullity, in *Elements of X-ray Diffraction*, ed. M. Cohen, Addison-Wesley, Phllipines, 2nd edn., 1978.

8 H. Berger, *X-ray Spectrom.*, 1986, **15**, 241–243.

9 *Mcgraw-Hill Encyclopedia of Science and Technology*, McGraw-Hill Education, New York, 11th edn., 2012.

10 Oxford Cryosystems, *Cryopad v1.484*, 2007.

11 Bruker AXS, *Diffracplus Basic Evaluation Package: EVA 10.0*, 2004.

12 Bruker AXS, *Diffracplus XRD Commander v2.3: Software for Controlling Bruker Diffractometers*, Karlsruhe, 2000.

13 R. Pynn, *Los Alamos Sci. Summer*, 1990, 1–31.

14 T. Brückel, D. Richter and R. Zorn, in *Neutron Scattering*, Forschungszentrum Jülich GmbH, Germany, 2007.

15 D. Duxbury, D. Khalyavin, P. Manuel, D. Raspino, N. Rhodes, E. Schooneveld and E. Spill, *J. Instrum.*, 2014, **9**, 1–9.

16 L. C. Chapon, P. Manuel, P. G. Radaelli, C. Benson, L. Perrott, S. Ansell, N. J. Rhodes, D. Raspino, D. M. Duxbury, E. Spill and J. Norris, *Neutron News*, 2011, **22**, 22–25.

17 J. M. Carpenter and C. K. Loong, in *Elements of Slow-Neutron Scattering: Basics, Techniques, and Applications*, Cambridge University Press, Cambridge, 2015, pp. 49–86.

18 T. C. Hansen, P. F. Henry, H. E. Fischer, J. Torregrossa and P. Convert, *Meas. Sci. Technol.*, 2008, **19**, 34001.

19 A. A. Coelho, *TOPAS Academic: General profile and Structure Analysis Software for Powder Diffraction Data*, 2010.

20 S. Speakman, *Basics of Rietveld refinement*, 2007.

21 H. H. Rietveld, *J. Appl. Cryst*, 1969, **65**.

22 S. Speakman, *An Introduction to Rietveld Refinement using PANalytical X'Pert HighScore Plus v3.0e*, .

23 K. Shankland and I. Facility, *J. Res. Natl. Inst. Stand. Technol.*, 2004, **I**, 143–154.

24 J. S. O. Evans, *multitopas, FORTRAN 77 routine*, 1999.

25 G. S. Pawley, *J. Appl. Cryst*, 1981, **14**, 357–361.

26 J. Steva, R. Karnatak, J. Fuggle and G. Sawatzky, *Phys. Rev. Lett.*, 1983, **50**, 910–913.

27 M. Alain, M. Jacques, M. B. Diane and P. Karine, *J. Phys. Conf. Ser.*, 2009, **190**, 12034.

28 B. Ravel and M. Newville, *J. Synchrotron Radiat.*, 2005, **12**, 537–541.

29   R. Klingeler, N. Leps, I. Hellmann, A. Popa, U. Stockert, C. Hess, V. Kataev, H. J. Grafe, F. Hammerath, G. Lang, S. Wurmehl, G. Behr, L. Harnagea, S. Singh and B. Büchner, *Phys. Rev. B*, 2010, **81**, 24506.

30   L. Viciu, J. W. G. Bos, H. W. Zandbergen, Q. Huang, M. L. Foo, S. Ishiwata, A. P. Ramirez, M. Lee, N. P. Ong and R. J. Cava, *Phys. Rev. B*, 2006, **73**, 174104.

31   A. R. P. and R. Street, *Proc. Phys. Soc.*, 1966, **87**, 971–973.

32   M. E. Fisher, *Philos. Mag. A J. Theor. Exp. Appl. Phys.*, 1962, **7**, 1731–1743.

33   Y. SINGH, *Int. J. Mod. Phys. Conf. Ser.*, 2013, **22**, 745–756.

34   J. F. Lataste, *Non-Destructive Assessment of Concrete Structures*, Springer, Netherlands, 1st edn., 2012.

35   S. A. Arrhenius, *Z. Phys. Chem.*, 1889, **4**, 96–116.

36   N. F. Mott, *Metal Insulator Transitions*, Taylor & Francis, London, 2nd edn., 1990.

37   B. I. Shklovskii and A. L. Efros, *Electronic Processes in Doped Semiconductors*, Springer-Verlag, Berlin, 1984.

38   N. F. Mott, *J. Non. Cryst. Solids*, 1968, **1**, 1–17.

39   N. F. Mott, *Phil. Mag.*, 1969, **19**, 835.

40   N. F. Mott and E. A. Davis, *Crystal*, 1972, **7**, 55–56.

41   N. F. Mott, *Crystal*, 1991, **26**, 788.

42   A. L. Efros and B. I. Shklovskii, *J. Phys. C Solid State Phys.*, 1975, **8**, L49-51.

43   S. Issai, *Is Hopping A Science?*, World Scientific Publishing, Singapore, 1st edn., 2015.

44   R. Berkovits and B. I. Shklovskii, *J. Phys. Condens. Matter*, 1999, **11**, 779–186.

45   R. Clark, *J. Chem. Educ.*, 1937, **41**, 488–492.

46   P. Kubelka and F. Munk, *Z. Tech. Phys.*, 1931, **12**, 593.

47   P. Kubelka and F. Munk, *J. Opt. Soc. Am.*, 1948, **38**, 1067.

48   G. Kortum and H. Schottler, *Z. Elekfrochem*, 1953, **57**, 353–361.

49   R. W. Ditchburn, *Light*, Interscience Publ. Inc, New York, 1952.

50   F. A. Jenkins and H. E. White, *Fundamentals of Optics*, McGraw-Hill Book Co, New York, 3rd edn., 1957.

51   A. C. Reimschuessel, *J. Chem. Educ.*, 1972, **49**, A413.

52   D. B. Williams and C. B. Carter, *Transmission Electron Microscopy: A Textbook for Materials Science*, Springer, New York, 2nd edn., 2009.

53   M. Head, *Energy Dispersive X-Ray (EDX) Analysis*, New York, 2nd edn., 2006.

54   L. Belkoura, L. Liz-Marzán and J. Crawsha, *Energy Dispersive X-ray Microanalysis (EDX)*, 2006.

Chapter 3: La$_2$O$_2$Fe$_{2-x}$M$_x$OSe$_2$ (*M* = Co, Ni)

3.1 Introduction

La$_2$O$_2$Fe$_2$OSe$_2$ crystallises in the *I*4/*mmm* space group [a = 4.0788(2) Å, c = 18.648(2) Å] (Figure 3.01) and consists of fluorite-like (La$_2$O$_2$)$^{2+}$ layers and anti-CuO$_2$ type (Fe$_2$O)$^{2-}$ layers, separated by Se^{2-} ions. The La$_4$O tetrahedra are edge-shared, where the La^{3+} is in a square antiprismatic coordination with the oxygen and the Se atoms. In the (Fe$_2$O)$^{2-}$ layers, the transition metal is in a distorted octahedron arrangement with the Fe atoms coordinated to two axial O^{2-} ions and 4 equatorial Se^{2-} ions.[1]

La$_2$O$_2$Fe$_2$OSe$_2$ has been reported to be a semiconductor and a Mott insulator and exhibits antiferromagnetic (AFM) ordering at low temperatures.[1,2] La$_2$O$_2$Fe$_2$OSe$_2$ has a 2-*k* magnetic structure (Figure 3.01b) with some 2D-Ising like character and surprisingly weak exchange interactions, consistent with some localization and band narrowing.[2,3] The Fe material could be considered as an intermediate between the Mn and Co analogues. La$_2$O$_2$Mn$_2$OSe$_2$ is the least electronegative so nearest neighbour J$_1$ interactions dominate (AFM1 checkerboard arrangement) while La$_2$O$_2$Co$_2$OSe$_2$ is the most electronegative so next-nearest neighbour J$_{2'}$ interactions dominate.[4]

Doping Mn^{2+} onto the Fe^{2+} sites in *Ln*$_2$O$_2$Fe$_{2-x}$Mn$_x$OSe$_2$ (*Ln* = La, Nd) led to a gradual increase in unit cell parameters *a* and *c* with increasing Mn content due to the bigger ionic radius of Mn^{2+} (0.830 Å) compared to Fe^{2+} (0.780 Å).[5] The electrical resistivity increases with Mn doping in La$_2$O$_2$Fe$_{2-x}$Mn$_x$OSe$_2$, consistent with increased cell volume (and decreased overlap); increased conductivity is observed with Nd analogues in agreement with this in Nd$_2$O$_2$Fe$_{2-x}$Mn$_x$OSe$_2$ (0 ≤ x ≤ 0.5) when compared to La$_2$O$_2$Fe$_{2-x}$Mn$_x$OSe$_2$. They all show semiconducting behaviour. Doping Mn^{2+} onto the Fe^{2+} sites in La$_2$O$_2$Fe$_{2-x}$Mn$_x$OSe$_2$ creates an atomic disorder which lowers the AFM transition temperature and the intermediate alloys display a rich magnetic phase diagram which occurs because of the principal interactions competing in the (Fe/Mn)$_2$OSe$_2$ layer.[6,7] In La$_2$O$_2$FeMnOSe$_2$, direct interaction AFM J$_3$ dominates (similar to J$_1$ on Figure 3.01b) leading to c-type AFM ordering below T_N = 168 K.[4,8] Doping Mn^{2+} onto the Fe^{2+} sites in Nd$_2$O$_2$Fe$_{2-x}$Mn$_x$OSe$_2$ removes the AFM transition T_N. Paramagnetic behaviour dominates at low Mn doping concentration while ferromagnetic behaviour dominates at higher Mn doping concentrations.[7]
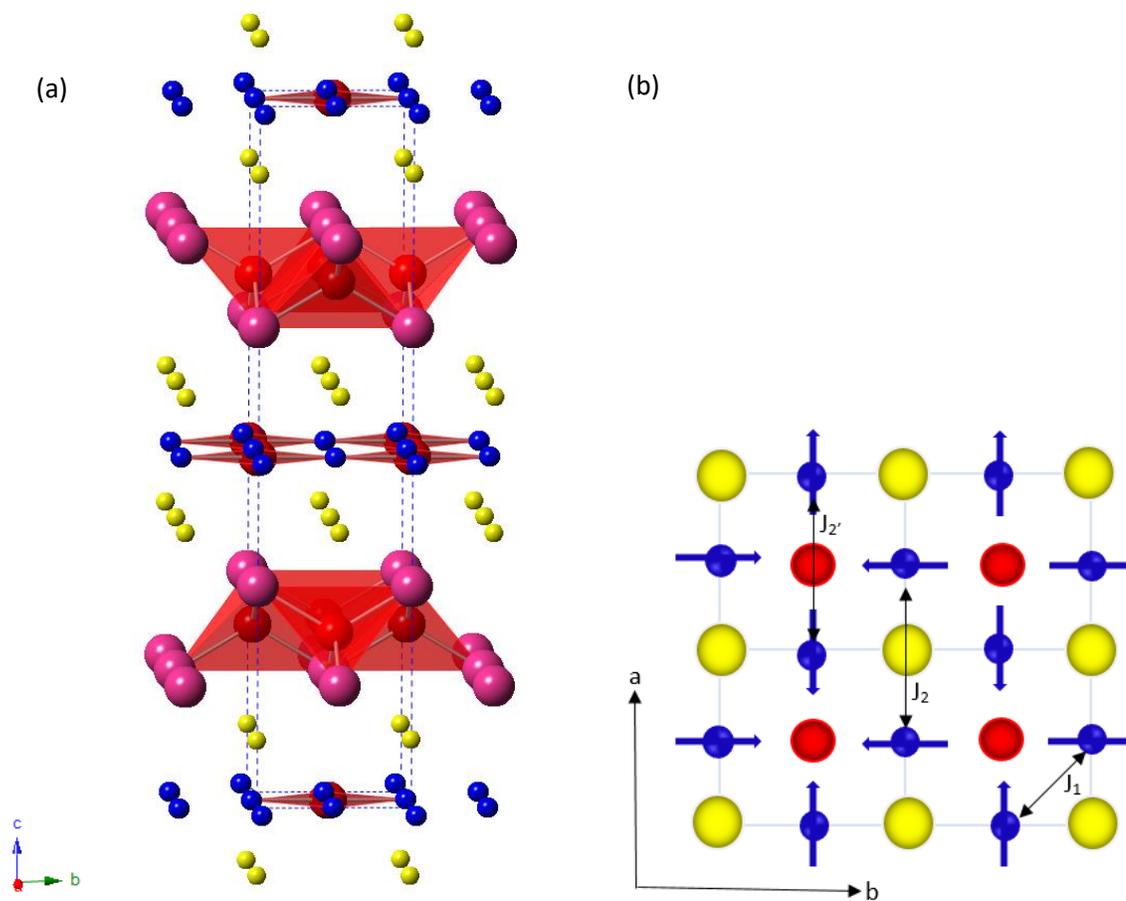
Figure 3.01 (a) Crystal structure of $La_2O_2Fe_2OSe_2$. La atoms are in pink, Fe atoms are in blue, O atoms are in red and Se atoms are in yellow. (b) 2-k magnetic structure

Recent theoretical studies focusing on the Mott insulating character of $La_2O_2Fe_2OSe_2$ (in contrast to the poor metallic parent phases to Fe-based superconductors) suggest that either by applying pressure or by electron doping, $La_2O_2Fe_2OQ_2$ (Q = S, Se) might undergo a Mott transition to a metallic state in which the AFM order is suppressed.[9,10]

The aims of this work are to electron dope $La_2O_2Fe_2OSe_2$ by substituting Co^{2+}/Ni^{2+} ions onto the Fe site and to investigate the resulting changes in structure and physical properties.[11–13]

This chapter deals with the synthesis and properties of $La_2O_2Fe_{2-x}M_xOSe_2$ (M = Co, Ni) series of compounds, focusing on their structures, magnetic properties and conductivity. Structures were characterised using X-ray powder diffraction (XRPD) complemented by Rietveld refinement, SQUID magnetometry for magnetic properties and Physical Property Measurement System (PPMS) for conductivity.

3.2 Results

3.2.1 La$_2$O$_2$Fe$_2$OSe$_2$

3.2.1.1 Synthesis and Structural characterisation

La$_2$O$_2$Fe$_2$OSe$_2$ was prepared from stoichiometric amounts of La$_2$O$_3$ (Sigma-Aldrich, 99.99%), Fe (Alfa-Aesar, 99+%) and Se (Sigma-Aldrich, 99.5+%) as discussed in Chapter 2.1. The starting reagents were weighed in a 1:2:2 ratio and ground using a mortar and pestle in the glovebox. The mixture was then pressed into a 5 mm pellet and placed in a quartz tube. The latter was then sealed under vacuum and heated in a furnace at the following conditions: ramped to 600°C at 1°C/min and dwelled for 12 hours, ramped to 800°C at 0.5°C/min and dwelled for 1 hour, ramped to 1000°C at 1°C/min and dwelled for 12 hours. The furnace was then allowed to cool to room temperature. The mixture was reground, resealed and reheated at the same temperature conditions to ensure crystalline materials. This synthesis gave a highly crystalline sample containing 3.99 ± 0.39 % LaFeO$_3$ impurity phase (Figure 3.02). Search and match software (EVA software) was used to compare diffraction patterns with a database of patterns (ICDD PDF2) for reported structures to identify impurity phases including LaFeO$_3$.[14] Rietveld refinement (using TopasAcademic software) allowed the phase fraction to be refined and it indicated 3.99 ± 0.39 % LaFeO$_3$ by mass.[15,16] The purity of the sample, confirmed by Scanning Electron Microscopy-Energy Dispersive X-ray (SEM-EDX) (Appendix 3.01), suggested La$_2$Fe$_{1.56\pm0.14}$Se$_{1.68\pm0.17}$ (normalised to La).

3.2.1.2 X-ray powder diffraction

The resulting black pellet was then analysed by in-house X-ray powder diffraction (Figure 3.02). The amorphous background seen between 5° and 20° was due to air scattering of the X-rays. A small impurity phase of LaFeO$_3$ was present in the sample. The refinement was performed as described in Chapter 2.2.2. The only deviations applied to the refinement were a 12th order Chebychev polynomial function which was employed to fit the background and 2 atomic positions: z coordinates for La and Se of the main phase. The R_{wp} for the refinement was 6.83 %, the χ^2 was 2.12. Data for some of the relevant parameters are shown in Table 3.01.

Data is in good agreement with literature. The *c* cell parameter value from the parent compound differs from literature, probably due to the $LaFeO_3$ impurity.
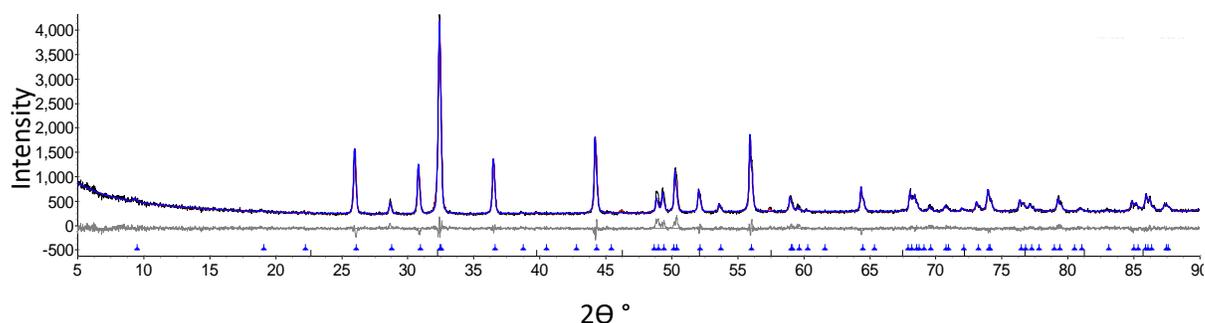
Figure 3.02 Rietveld refinement profiles for $La_2O_2Fe_2OSe_2$ using room temperature XRPD data. R_{wp} is 6.83 %, Rp is 5.29 % and χ^2 is 2.12. The observed data is in black, calculated data is in red and the difference is in grey. The blue vertical tick marks show the predicted peak positions for $La_2O_2Fe_2OSe_2$ (96.01 ± 0.39%) and the black ones show those for $LaFeO_3$ (3.99 ± 0.39%).

Table 3.01 Data for room temperature Rietveld refinement for $La_2O_2Fe_2OSe_2$ together with single crystal values from the literature and $La_2O_2Co_2OSe_2$ for comparison.

$La_2O_2Fe_2OSe_2$		Mayer *et al*[1]	$La_2O_2Co_2OSe_2$[17]
Space group	*I4/mmm*	*I4/mmm*	*I4/mmm*
a cell parameter (Å)	4.085161(6)	4.0788(2)	4.0697(8)
c cell parameter (Å)	18.585159(7)	18.648(2)	18.419(4)
Volume (Å^3)	310.159(3)	310.24	305.06(10)
La *z* coordinate (c)	0.18465(1)	0.18445(5)	
Se *z* coordinate (c)	0.09756(7)	0.09669(9)	

3.2.1.3 Variable temperature X-ray powder diffraction

Variable temperature X-ray powder diffraction (VT-XRPD) data was collected to follow the unit cell parameters on cooling. Refinements were carried out as for the room temperature data but with the peak shape terms fixed. Sequential Rietveld refinements showed a smooth decrease in cell parameters on cooling with a more rapid decrease in *c* around 90 K and very little changes in crystal structure (Figure 3.03) (Appendix 3.02). These are consistent with literature.[18,19]

(a)

(b)

(c)
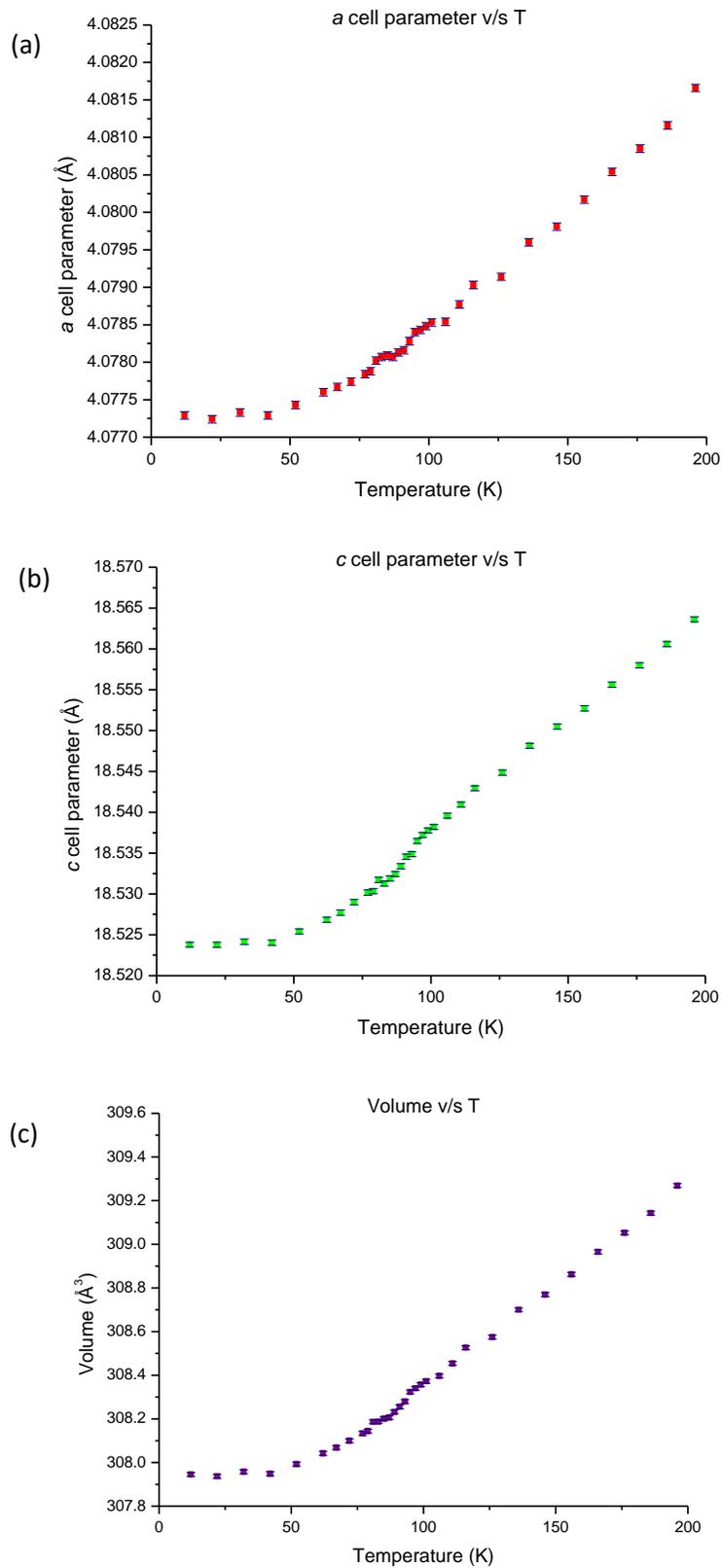
Figure 3.03 (a) *a* cell parameter (b) *c* cell parameter (c) unit cell volume against temperature for $La_2O_2Fe_2OSe_2$. Data is shown in red, green and purple respectively with error bars in blue.

3.2.1.4 SQUID Magnetometry

Field-cooled (FC) and zero-field-cooled (ZFC) magnetic susceptibility measurements were performed on the sample in an applied magnetic field of 1000 Oe, collected on warming from 2 K-300 K at 2 K intervals/ at 5 K min^{-1}.
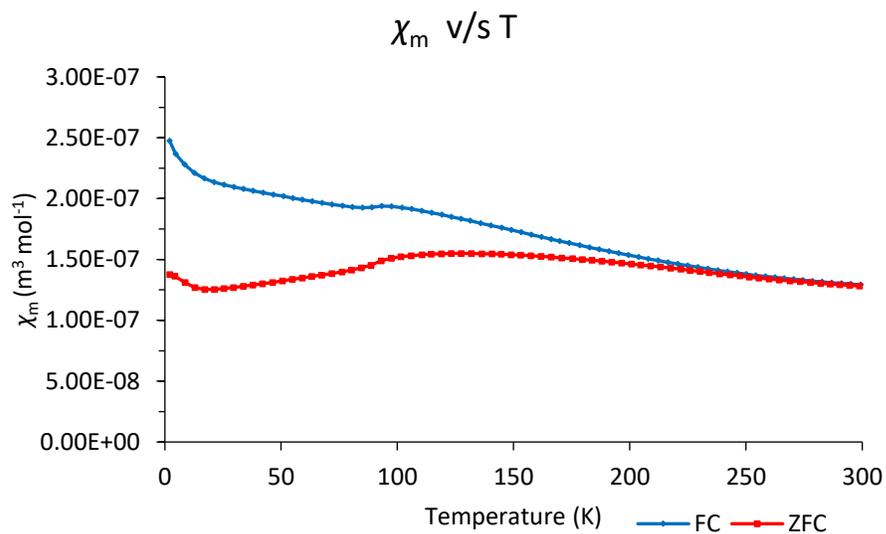
Figure 3.04 χ_m against temperature. ZFC (red) and FC (blue) data for La2O2Fe2OSe2.
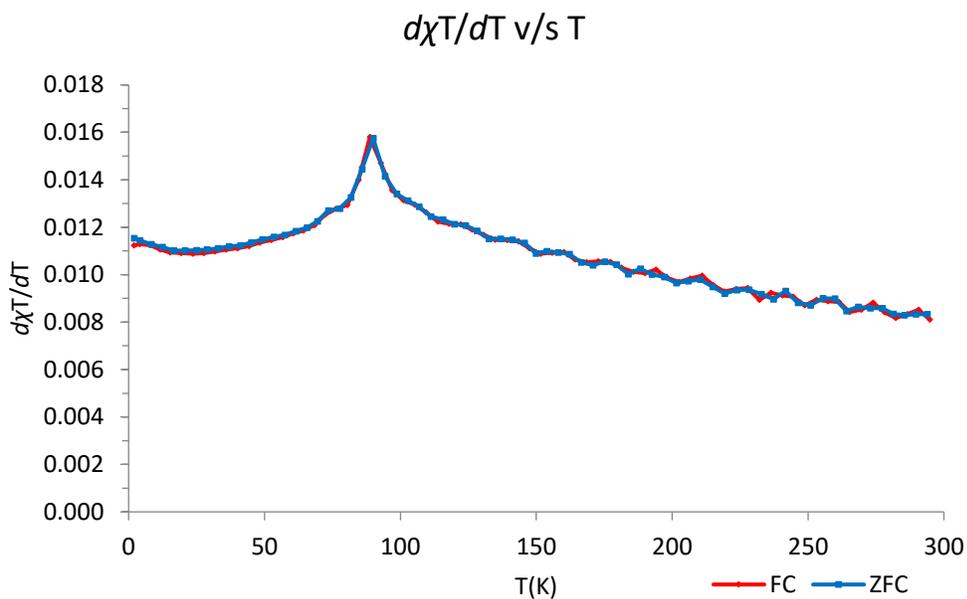
Figure 3.05 $d\chi$T/dT against temperature. ZFC (red) and FC (blue) data for La$_2$O$_2$Fe$_2$OSe$_2$.

There is a broad local maximum at around 90 K, due to low dimensional, 2D order above T_N which is consistent with literature. Moreover, there is AFM ordering below 90 K.[1,3,18] Hence, T_N is more clearly observed in $d\chi T/dT$ plot (Figure 3.05). There is no Curie-Weiss like behaviour up to 300 K and this could be due to short range order within the Fe_2O layers. The feature in the susceptibility at low temperature (Figure 3.04) suggests trace amounts of paramagnetic impurity phases.[20]

3.2.1.5 Conductivity measurements

Conductivity measurements were conducted on $La_2O_2Fe_2OSe_2$ as described in Chapter 2.2.7. Resistance was collected as the pellet was cooled from room temperature to 2 K in a cryostat with readings taken at every 1 K. Temperature readings down to 140 K are shown as any readings below that are unstable due to the sample being too resistive.
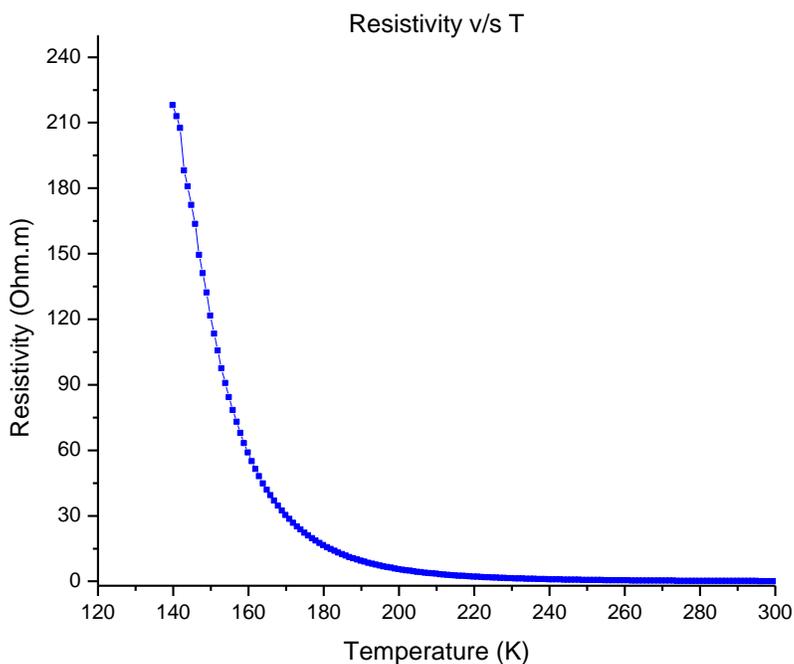
Figure 3.06 Resistivity against temperature. Data is shown in blue
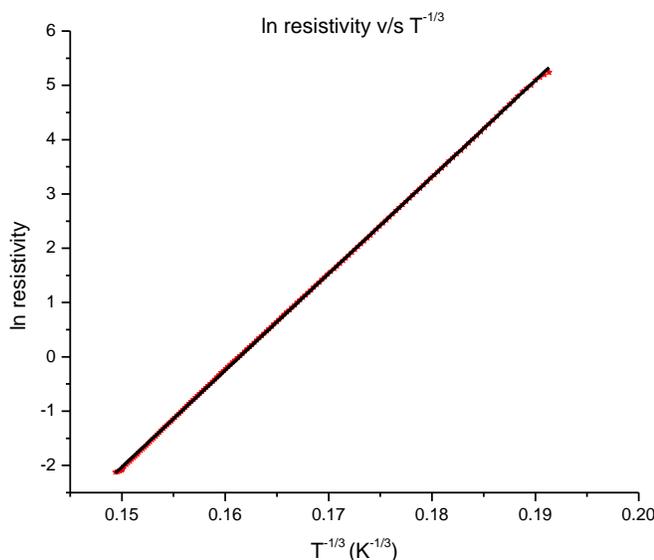
Figure 3.07 ln resistivity vs $T^{-1/3}$ showing linearity with T. Data is shown in red and trendline in black.

The exponential increase in resistivity with decreasing temperature indicates semiconducting behaviour (Figure 3.06) which is consistent with literature.[1,2] The resistivity behaviour at high and low temperatures could not be properly explained using the thermally activated model (Appendix 3.04). However, two-dimensional variable range hopping (2D-VRH) There is a linear behaviour in the ln resistivity vs $T^{-1/3}$ plot (Figure 3.07). [7,21,22] This shows that between 146 K > T > 300 K, the 2D-VRH is obeyed as $\rho = \rho_0 \exp(T_0/T)^{1/3}$ where, ρ_0 and T_0 are prefactors, giving them values of 3.33 x 10^{-13} and 5.64 x 10^6 $K^{1/3}$.

3.2.2 La$_2$O$_2$Fe$_{2-x}$Co$_x$OSe$_2$

3.2.2.1 Synthesis

La$_2$O$_2$Fe$_{2-x}$Co$_x$OSe$_2$ (0 ≤ x ≤ 0.2) was prepared from stoichiometric amounts of La$_2$O$_3$ (Sigma-Aldrich, 99.99%), Fe (Alfa-Aesar, 99+%), Se (Sigma-Aldrich, 99.5+%) and Co (Sigma-Aldrich, 99.9%) using the method described in 3.2.1.1.

3.2.2.2 X-ray powder diffraction

The resulting black pellets were then analysed by Rietveld refinement (Figure 3.08). The amorphous background seen between 5° and 20° was due to air scattering of the X-rays. A small impurity phase

of LaFeO$_3$ was present in the samples. The refinement was performed as described in 3.2.1.2. Data for some of the relevant parameters for La$_2$O$_2$Fe$_{2-x}$Co$_x$OSe$_2$ (0 ≤ x ≤ 0.2) are shown in Table 3.02.
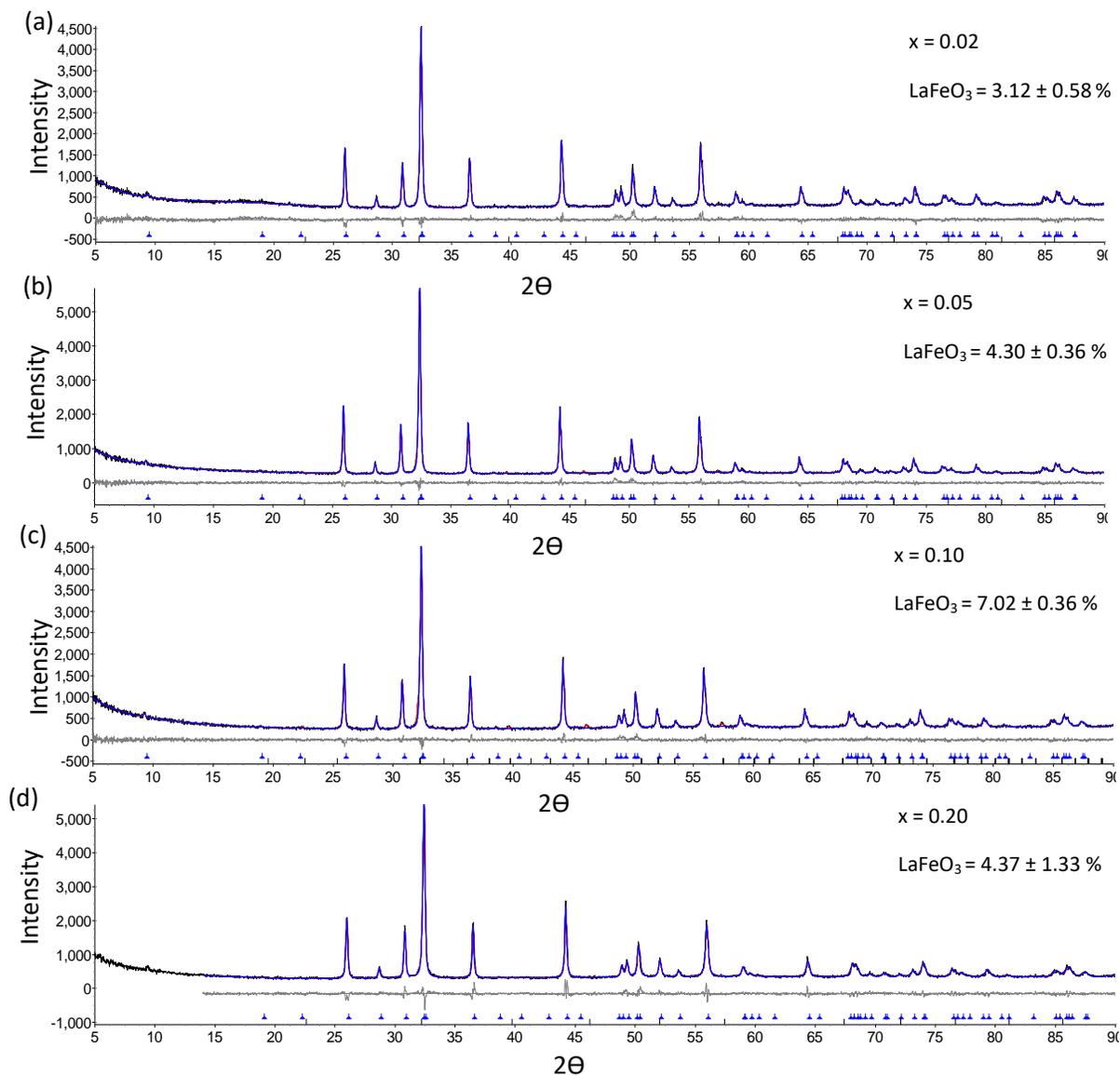
Figure 3.08 Rietveld refinement profiles for La$_2$O$_2$Fe$_{2-x}$Co$_x$OSe$_2$ (0 ≤ x ≤ 0.2) using room temperature XRPD data (a) x = 0.02 (b) x = 0.05 (c) x = 0.1 and (d) x = 0.2. The observed data is in black, the calculated data is in red and the difference is in grey. The blue vertical tick marks show the predicted peak positions for La$_2$O$_2$Fe$_2$OSe$_2$ and the black tick marks show those for LaFeO$_3$. LaFeO$_3$ content, Rwp and the χ2 values are given in table 3.02.

Table 3.02 Data for room temperature Rietveld refinement for $La_2O_2Fe_{2-x}Co_xOSe_2$ ($0 \leq x \leq 0.2$). 32 parameters were used for the refinements.

$La_2O_2Fe_{2-x}Co_xOSe_2$	X = 0	X = 0.02	X = 0.05	X = 0.10	X = 0.20
a (Å)	4.085161 (6)	4.082319 (7)	4.084647 (4)	4.084520 (7)	4.082529 (1)
c (Å)	18.585159 (7)	18.609944 (9)	18.594070 (0)	18.587229 (0)	18.566774 (1)
Volume (Å^3)	310.159 (3)	310.141 (4)	310.230 (7)	310.096 (0)	309.453 (1)
La z coordinate (c)	0.18465 (1)	0.18487 (0)	0.18481 (9)	0.18463 (0)	0.18459 (1)
Se z coordinate (c)	0.09756 (7)	0.09813 (7)	0.09728 (4)	0.09756 (5)	0.09750 (7)
R_{wp} (%)	6.83	6.46	5.59	5.63	6.60
χ^2	2.60	2.54	2.20	2.18	2.72
$LaFeO_3$ (%)	3.99 ± 0.39	3.12 ± 0.58	4.30 ± 0.36	7.02 ± 0.36	4.37 ± 1.33

$La_2O_2Fe_{2-x}Co_xOSe_2$ with higher cobalt content (x > 0.2) were also synthesised but they did not produce high-purity samples and had other impurities (La_2O_2Se and Fe_2O_3) in addition to $LaFeO_3$. The samples were then overlaid on top of one another to check for any differences (Figure 3.09).
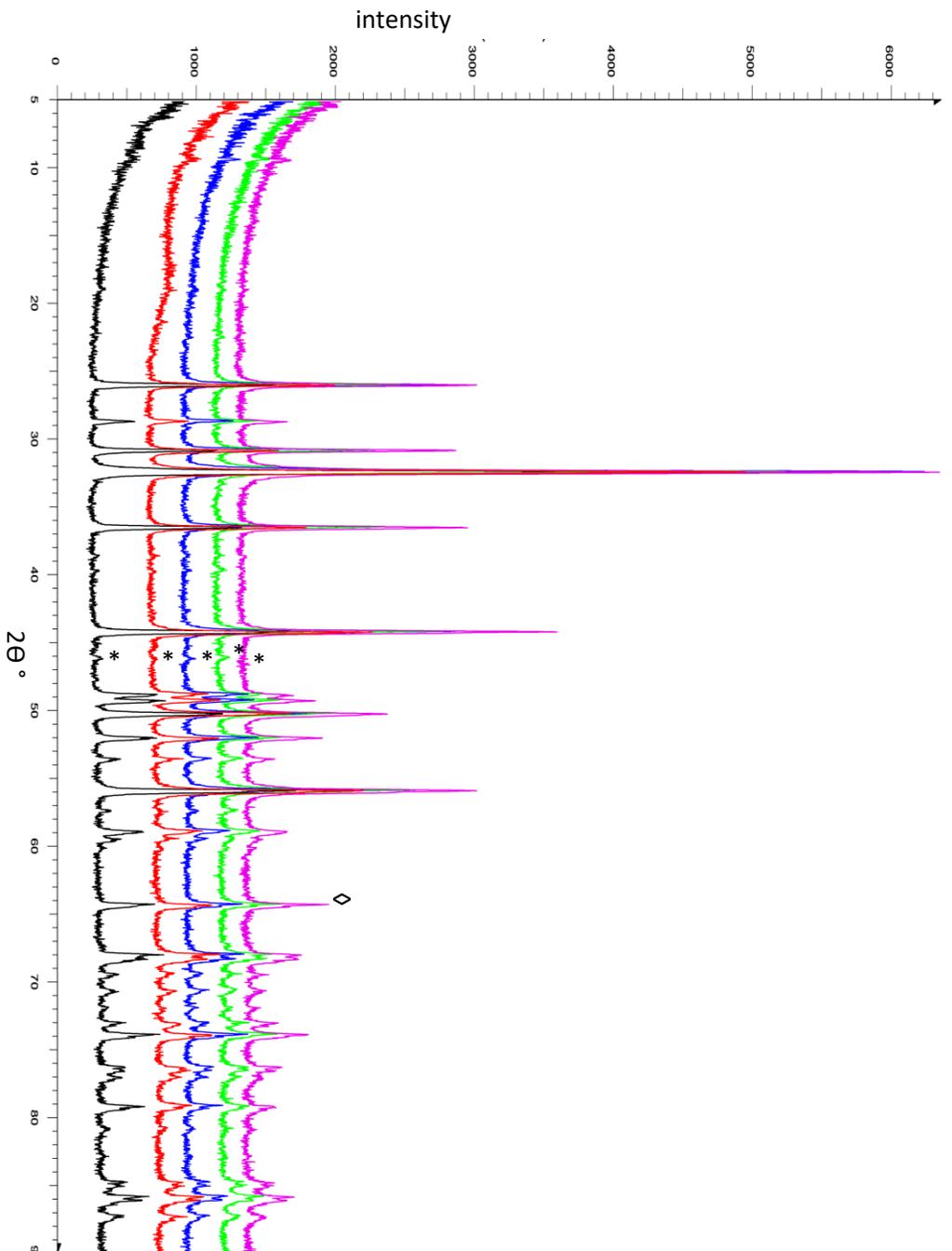
Figure 3.09 Overlay of room temperature XRPD data for $La_2O_2Fe_{2-x}Co_xOSe_2$, $x=0$ (black, bottom) to $x=0.2$ (pink, top). $La_2O_2Fe_2OSe_2$ is in black, $La_2O_2Fe_{1.98}Co_{0.02}OSe_2$ is in red, $La_2O_2Fe_{1.95}Co_{0.05}OSe_2$ is in blue $La_2O_2Fe_{1.9}Co_{0.1}OSe_2$ is in green and $La_2O_2Fe_{1.8}Co_{0.2}OSe_2$ is in pink. * denotes the impurity phase $LaFeO_3$. ◊ denotes the peaks which increase in intensity with increasing Co doping concentrations in $La_2O_2Fe_{2-x}Co_xOSe_2$ (where $0 \leq x \leq 0.2$).

110

(a)

a cell parameter v/s *x* doping concentration number

(b) *c* cell parameter v/s *x* doping concentration

(c) Volume v/s *x* doping concentration
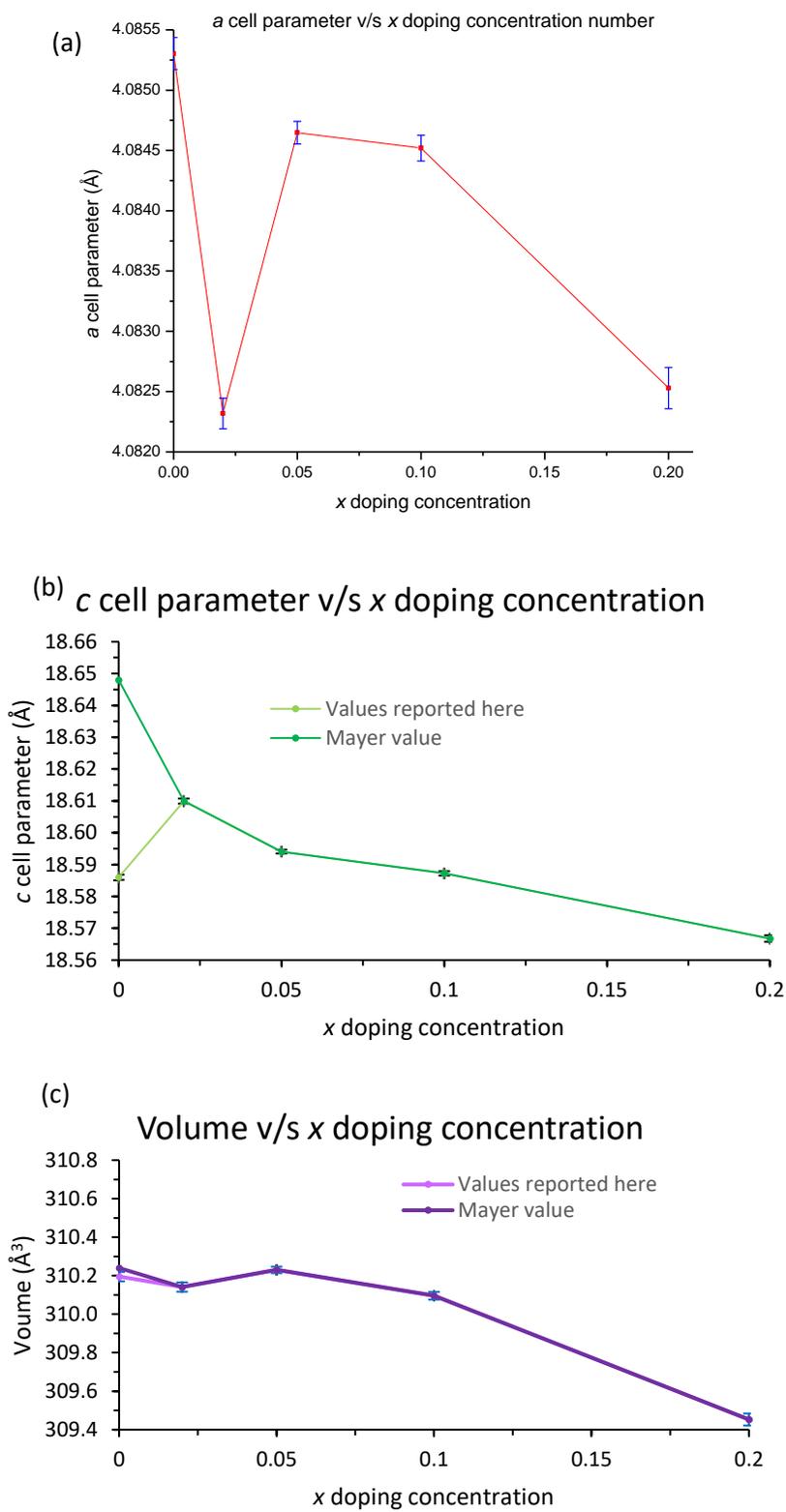
Figure 3.10 (a) Unit cell parameter *a* (red), (b) unit cell parameter *c* (values reported here are in light green and Mayer value in green) and (c) volume (values reported here are in light purple and Mayer value in purple) as a function of *x* for $La_2O_2Fe_{2-x}Co_xOSe_2$ determined from Rietveld refinements using room temperature XRPD data. Error bars in blue.

There are very little other changes in structure with dopant level (Appendix 3.05). The overall trend is slight decrease in unit cell volume with increasing Co content (Figure 3.10c), consistent with the ionic radii of Fe^{2+} (0.780 Å) and Co^{2+} ions (0.745 Å).[5] Room temperature unit cell parameters for $La_2O_2Fe_{2-x}Co_xOSe_2$ (0 ≤ x ≤ 0.2) are in agreement with those of $La_2O_2Fe_2OSe_2$ and are bigger than those of $La_2O_2Co_2OSe_2$ as predicted.[23] The change in c cell parameter with dopant level was larger than that for the a cell parameter (by 0.34%). There is a limited solid solution, with x = 0.02 being the limit, as seen by Vegard's law even though the end members are isostructural.[24]

3.2.2.3 Variable temperature X-ray powder diffraction
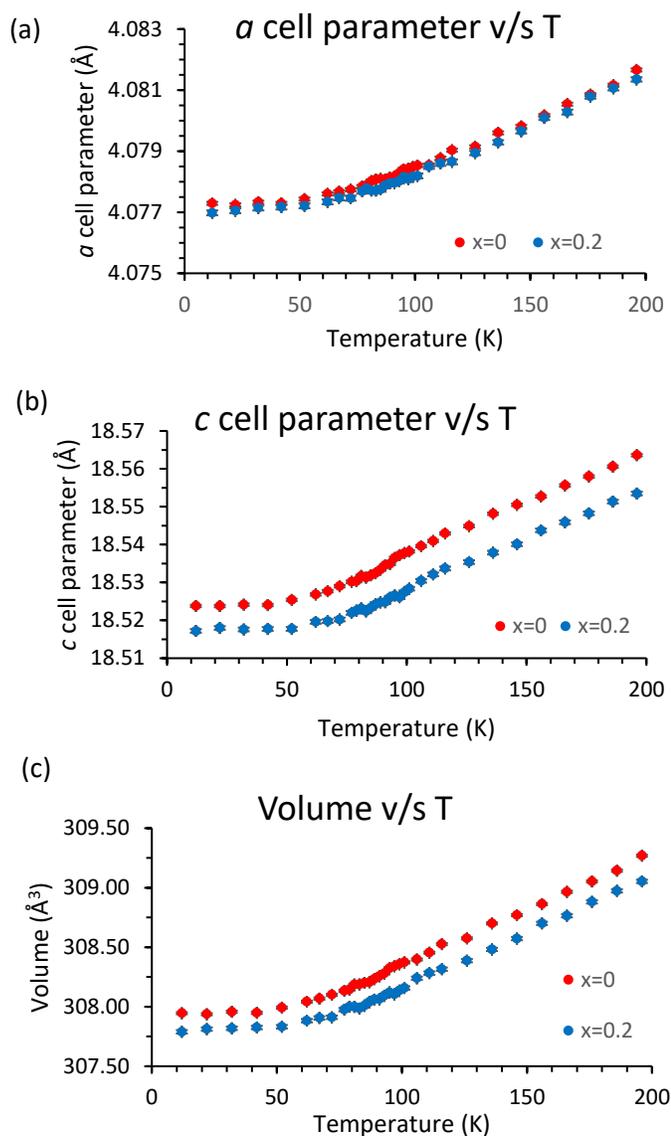
Figure 3.11 (a) a cell parameter (b) c cell parameter (c) unit cell volume against temperature for $La_2O_2Fe_2OSe_2$ (red) and $La_2O_2Fe_{1.8}Co_{0.2}OSe_2$ (blue). Error bars are in black.

Following the same method as outlined for $La_2O_2Fe_2OSe_2$ in section 3.2.1.3. Sequential refinements using variable temperature XRPD data were carried out for $La_2O_2Fe_{1.8}Co_{0.2}OSe_2$. $La_2O_2Fe_{1.8}Co_{0.2}OSe_2$ behaves similarly to $La_2O_2Fe_2OSe_2$ with a smooth decrease in cell parameters on cooling and little changes in structure. The more rapid decrease in c for $T<T_N$ is less pronounced for x = 0.2 (Figure 3.11b) than for the undoped material.

3.2.2.4 SQUID Magnetometry

Field-cooled (FC) and zero-field-cooled (ZFC) magnetic susceptibility measurements were performed on $La_2O_2Fe_{1.8}Co_{0.2}OSe_2$ in an applied magnetic field of 1000 Oe, collected on warming from 2 K-300 K at 2 K intervals at 5 K min^{-1}. Magnetization against applied magnetic field measurements were also performed at 300 K and 10 K. From the $d\chi T/d$T plots, the transition temperature slightly increases slightly from 90 K to 94 K when $La_2O_2Fe_{2-x}Co_xOSe_2$ is doped with 0.2 Co.
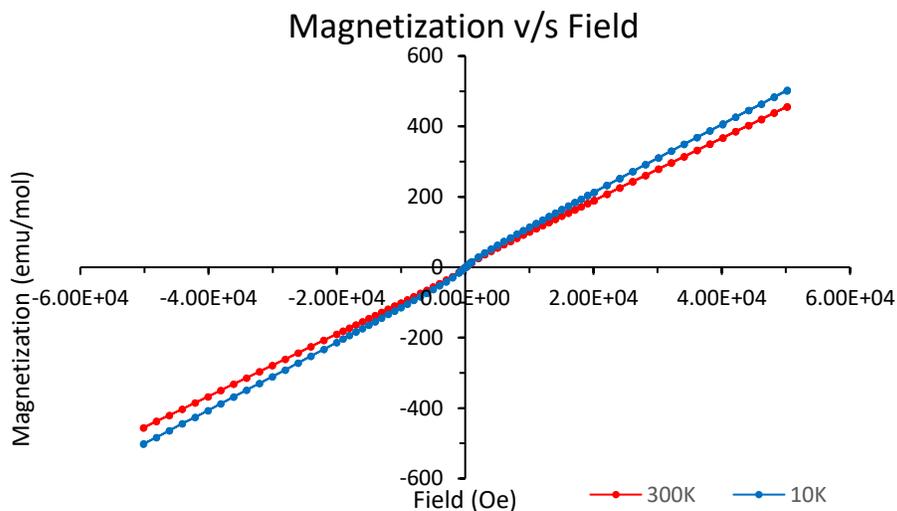
Figure 3.12 Long moment against field. 300K data (red) and 10K data (blue) data for $La_2O_2Fe_{1.8}Co_{0.2}OSe_2$.
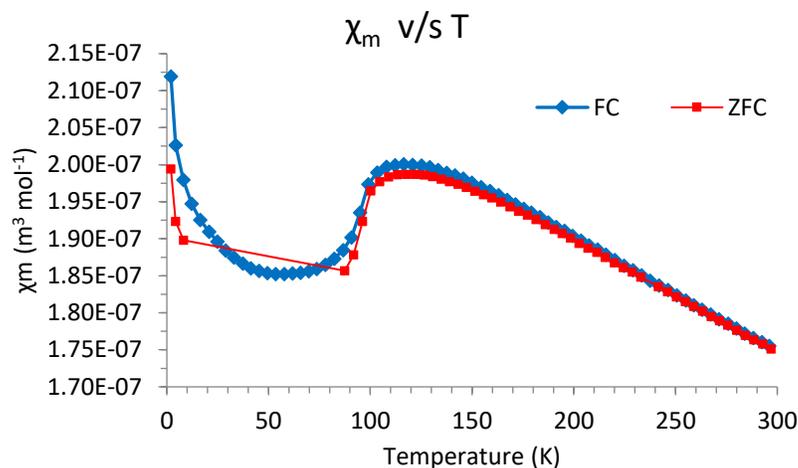
Figure 3.13 χ_m against temperature. ZFC (red) and FC (blue) data for $La_2O_2Fe_{1.8}Co_{0.2}OSe_2$.
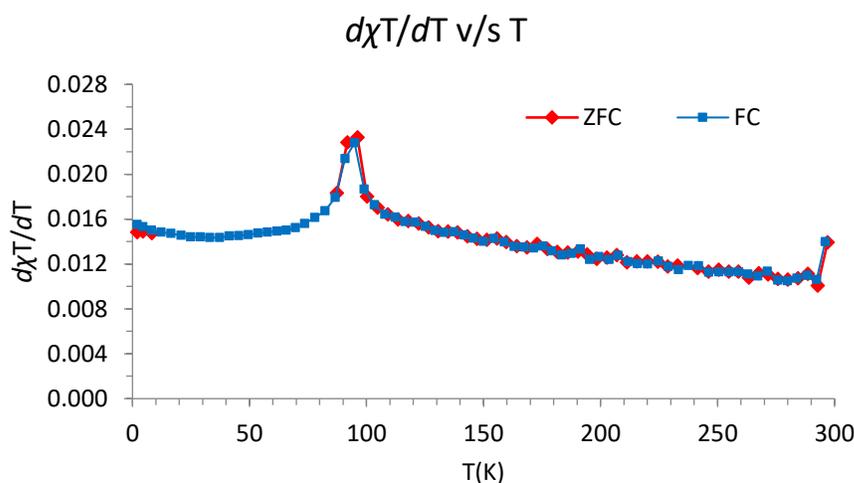
Figure 3.14 $d\chi T/dT$ against temperature. ZFC (red) and FC (blue) data for $La_2O_2Fe_{1.8}Co_{0.2}OSe_2$

3.2.2.5 SEM-EDX

An overall backscattered secondary electrons image for each sample was taken at a magnification between X44-X71 to get an idea of the homogeneity of the sample. An example is given in Appendix 3.08. From the backscattered images and spectra, all the samples were fairly homogenous. For x = 0.02 and x = 0.05, most of the sites had La_2O_3 impurities. The average composition from all the normal points, assuming oxygen content and normalizing the data with respect to La, is $La_2O_2Fe_{1.95\pm0.08}Co_{0.05\pm0.03}OSe_2$ for $La_2O_2Fe_{1.98}Co_{0.02}OSe_2$, $La_2O_2Fe_{1.93\pm0.12}Co_{0.07\pm0.02}OSe_2$ for $La_2O_2Fe_{1.95}Co_{0.05}OSe_2$, $La_2O_2Fe_{1.91\pm0.18}Co_{0.09\pm0.04}OSe_2$ for $La_2O_2Fe_{1.9}Co_{0.1}OSe_2$ and $La_2O_2Fe_{1.85\pm0.02}Co_{0.14\pm0.03}OSe_2$ for $La_2O_2Fe_{1.8}Co_{0.2}OSe_2$.

114

3.2.2.6 Conductivity measurements

Conductivity measurements were conducted on all the doped samples except for $La_2O_2Fe_{1.95}Co_{0.05}OSe_2$. The sintered polished pellets had density between 2.063-4.017 g cm^{-3} (Table 3.03), which were 32.4-62.8 % of the theoretical densities. Resistance measurements were collected as the pellets cooled from room temperature to 2 K in a cryostat with readings taken at every 1 K.
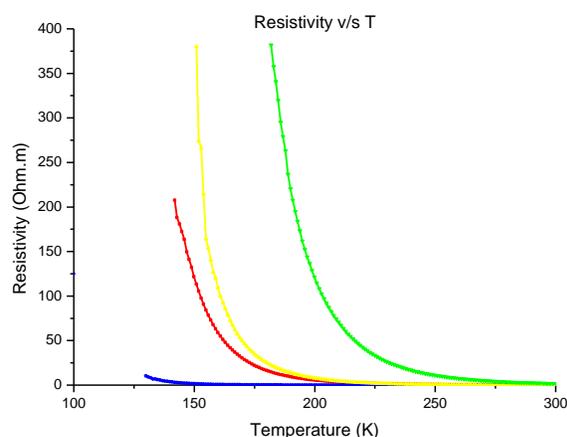
Figure 3.15 Measure of Resistivity (Ohm.m) as a function of temperature for different Co doping in $La_2O_2Fe_{2-x}Co_xOSe_2$. $La_2O_2Fe_2OSe_2$ (RKO024a) is in red, $La_2O_2Fe_{1.98}Co_{0.02}OSe_2$ (RKO024b) is in blue, $La_2O_2Fe_{1.9}Co_{0.1}OSe_2$ (RKO024d) is in yellow and $La_2O_2Fe_{1.8}Co_{0.2}OSe_2$ (RKO024e) is in green.
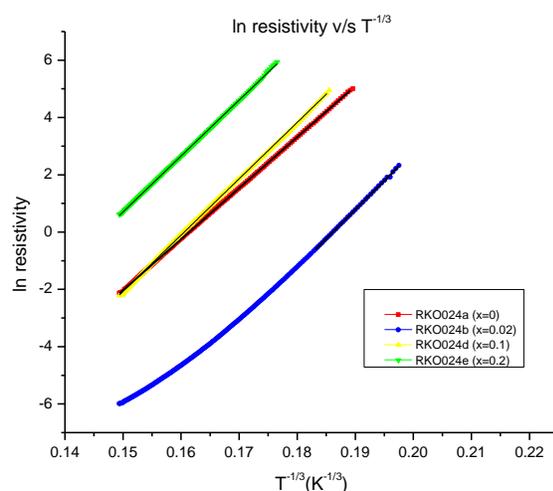
Figure 3.16 Arrhenius plot ln ρ vs T$^{-1/3}$ showing linearity with T for all samples except for x=0.02. $La_2O_2Fe_2OSe_2$ (RKO024a) is in red, $La_2O_2Fe_{1.98}Co_{0.02}OSe_2$ (RKO024b) is in blue, $La_2O_2Fe_{1.9}Co_{0.1}OSe_2$ (RKO024d) is in yellow and $La_2O_2Fe_{1.8}Co_{0.2}OSe_2$ (RKO024e) is in green. The trendlines are shown in black.

The exponential increase with decreasing temperature for all the samples indicates semiconducting behaviour (Figure 3.15). The resistivity behaviour of all the samples at all temperatures could not be

very well explained using the thermally activated model (appendix 3.09), although the resistivity behaviour of x = 0.02 could be explained using that model at high temperatures. Two-dimensional variable range hopping (2D-VRH) could be used to describe the resistivity behaviour at all temperatures for all the samples except x = 0.02, where the model was used at low temperatures. They showed a linear behaviour in the ln resistivity vs $T^{-1/3}$ plot (Figure 3.16). The values of ρ_0 and T_0 are given in table 3.03 together with the activation energy value of $La_2O_2Fe_{1.98}Co_{0.02}OSe_2$ calculated from the slope (Appendix 3.09).

Table 3.03 Resistivity and Activation energy data for $La_2O_2Fe_{2-x}Co_xOSe_2$ $(0 \leq x \leq 0.2)$.

X	0	0.02		0.1	0.2
		2D-VRH **T < 130 K**	**Thermally activated** **T > 200 K**		
ρ_0	3.33×10^{-13}	4.25×10^{-17}	-	1.93×10^{-14}	4.03×10^{-13}
T_0	5.64×10^6	8.30×10^6	-	7.61×10^6	7.41×10^6
E_a (eV)	-	-	0.1619 ± 0.002	-	-
ρ at 298K (Ωm)	0.123	0.0026		0.113	1.945
Pellets theoretical density (%)	32.4	55.8		62.1	62.8

3.2.3 $La_2O_2Fe_{2-x}Ni_xOSe_2$

3.2.3.1 Synthesis

$La_2O_2Fe_{2-x}Ni_xOSe_2$ $(0 \leq x \leq 0.1)$ was prepared from stoichiometric amounts of La_2O_3 (Sigma-Aldrich, 99.99%), Fe (Alfa-Aesar, 99+%), Se (Sigma-Aldrich, 99.5+%) and Ni (Alfa-Aesar, 99.5%) using the method described in 3.1.1.

3.2.3.2 X-ray powder diffraction

The resulting black pellets were then analysed by Rietveld refinement (Figure 3.17). The amorphous background seen between 5° and 20° was due to air scattering of the X-rays. A small impurity phase

of LaFeO$_3$ was present in the samples. The refinement was performed as described in 3.2.1.2. Data for some of the relevant parameters for La$_2$O$_2$Fe$_{2-x}$Ni$_x$OSe$_2$ (0 ≤ x ≤ 0.1) are given in Table 3.04.
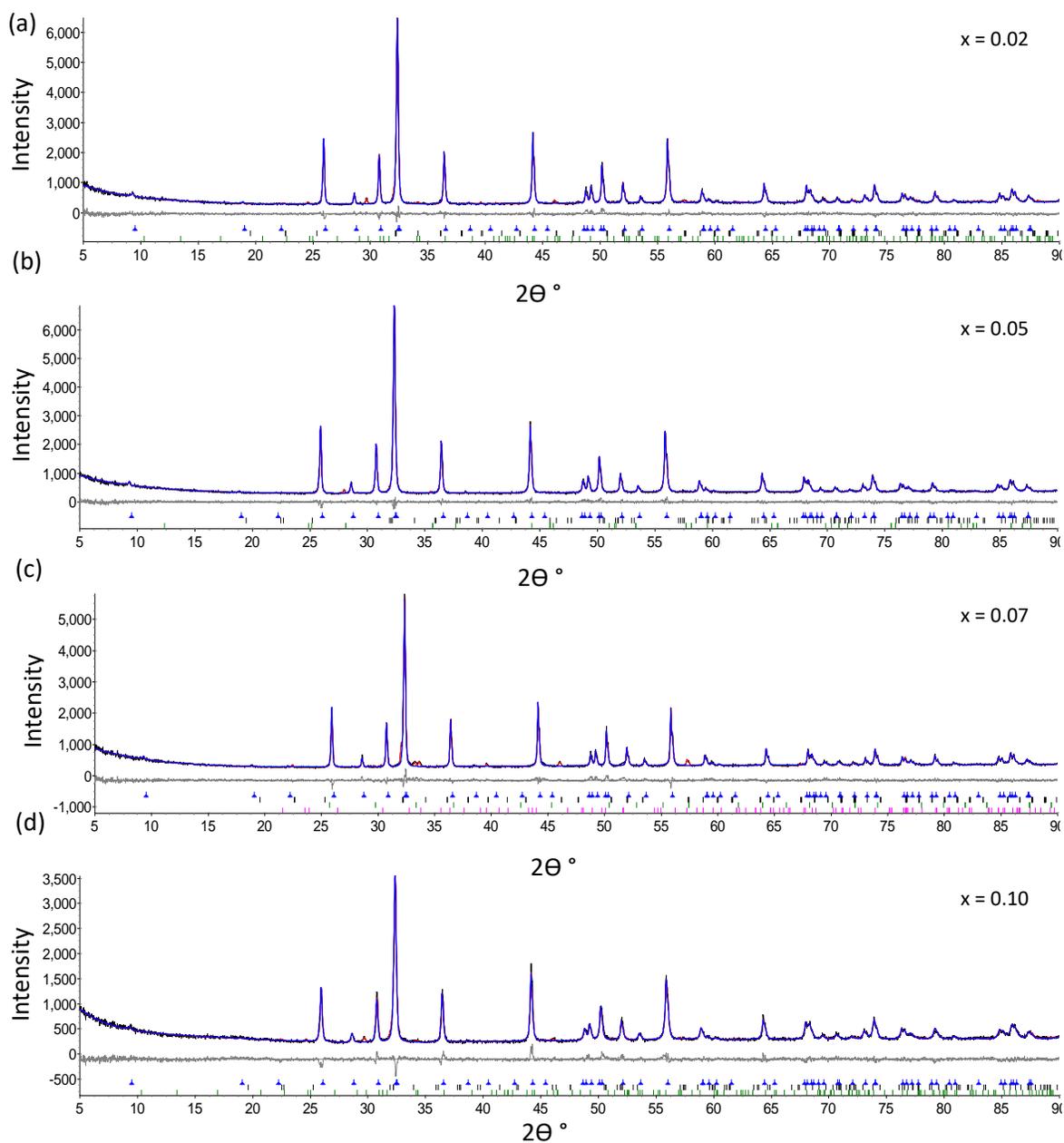
Figure 3.17 Rietveld refinement profiles for La$_2$O$_2$Fe$_{2-x}$Ni$_x$OSe$_2$ (0 ≤ x ≤ 0.1) using room temperature XRPD data (a) x = 0.02 (b) x = 0.05 (c) x = 0.07 and (d) x = 0.1. The observed data is in black, the calculated data is in red and the difference is in grey. The blue vertical tick marks show the predicted peak positions for La$_2$O$_2$Fe$_2$OSe$_2$, the black tick marks show those for LaFeO$_3$, the green tick marks show those for La$_4$O$_4$Se$_3$ or La$_4$O$_4$Se$_2$ or NiSe$_2$ and the pink tick marks show those for NiSeO$_3$. LaFeO$_3$ content, R_{wp} and the χ^2 are given in table 3.4.

Table 3.04 Data for room temperature Rietveld refinement for $La_2O_2Fe_{2-x}Ni_xOSe_2$ ($0 \leq x \leq 0.1$). 32 parameters were used for the refinements.

$La_2O_2Fe_{2-x}Ni_xOSe_2$	X = 0	X = 0.02	X = 0.05	X = 0.07	X = 0.10
a (Å)	4.085161 (6)	4.086688 (4)	4.085113 (4)	4.087126 (2)	4.086418 (4)
c (Å)	18.585159 (7)	18.606953 (0)	18.611882 (2)	18.600668 (1)	18.597592 (1)
Volume ($Å^3$)	310.159 (3)	310.755 (4)	310.598 (4)	310.717 (5)	310.558 (6)
La z coordinate (c)	0.18465 (1)	0.18494 (8)	0.18474 (7)	0.18490 (0)	0.18474 (1)
Se z coordinate (c)	0.09756 (7)	0.09733 (3)	0.09722 (2)	0.09711 (6)	0.09777 (7)
R_{wp} (%)	6.83	5.79	5.29	6.19	6.48
χ^2	2.60	2.43	2.24	2.52	2.50
Main phase (%)	96.01 ± 0.39	94.62 ± 0.27	94.54 ± 1.22	83.16 ± 1.01	89.98 ± 1.14
$LaFeO_3$ (%)	3.99 ± 0.39	3.31 ± 0.24	4.42 ± 1.24	5.80 ± 0.25	7.65 ± 1.15
$La_4O_4Se_3$ (%)	-	2.08 ± 0.14	-	-	2.37 ± 0.20
$La_4O_4Se_2$ (%)	-	-	1.04 ± 0.08	-	-
$NiSe_2$ (%)	-	-	-	4.89 ± 0.66	-
$NiSeO_3$ (%)	-	-	-	6.16 ± 0.91	-

$La_2O_2Fe_{2-x}Ni_xOSe_2$ with higher nickel content (x > 0.1) were also synthesised but they did not produce high-purity samples and the main phases were $La_4O_4Se_3$ and $LaFeO_3$. The samples were then overlaid on top of one another to check for any differences.
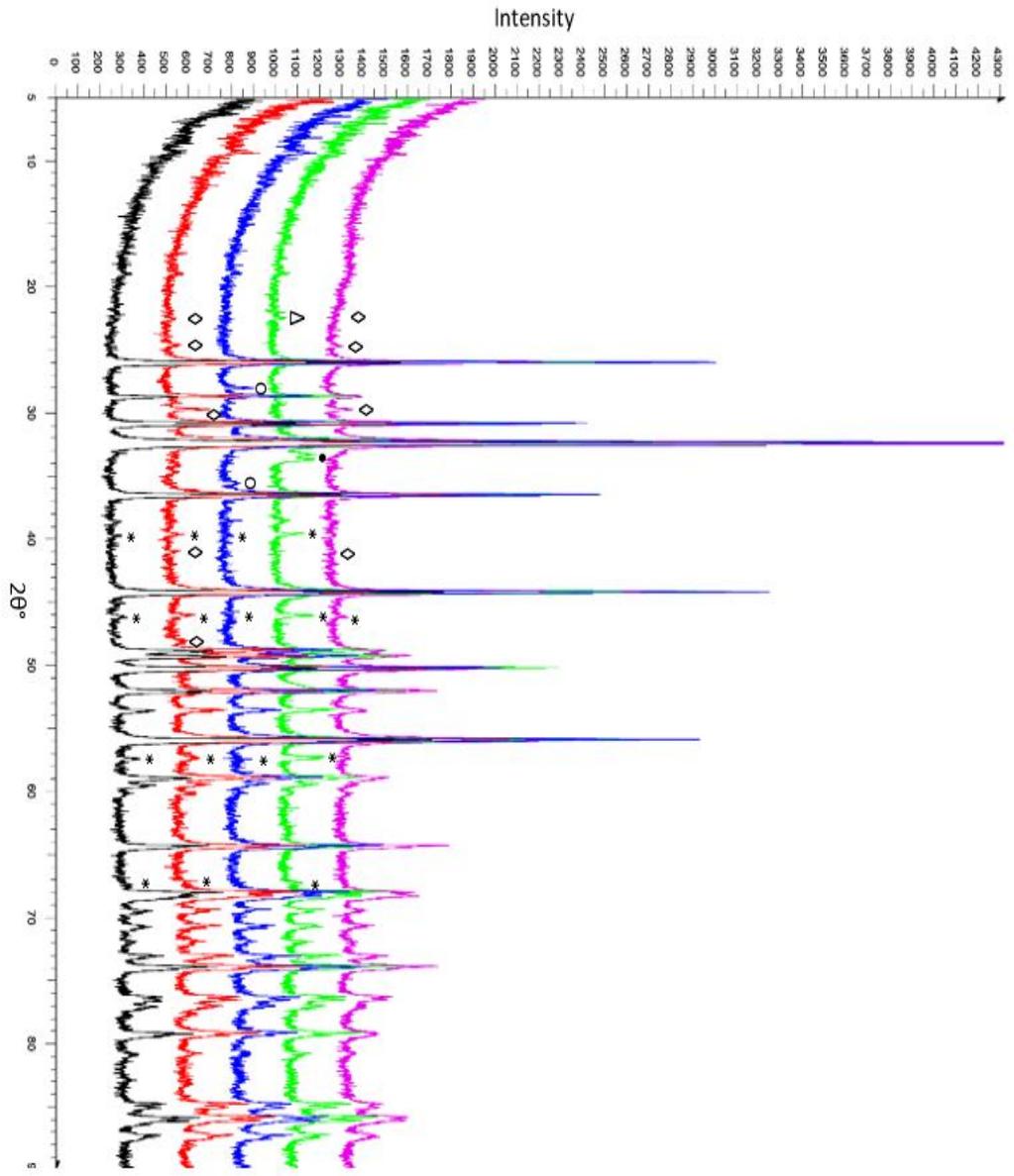
Figure 3.18 Overlay of room temperature XRPD data for $La_2O_2Fe_{2-x}Ni_xOSe_2$ x=0 (black, bottom) to x=0.1 (pink, top). $La_2O_2Fe_2OSe_2$ (RKO024a) is in black, $La_2O_2Fe_{1.98}Ni_{0.02}OSe_2$ (RKO026g) is in red, $La_2O_2Fe_{1.95}Ni_{0.05}OSe_2$ (RKO026b) is in blue, $La_2O_2Fe_{1.93}Ni_{0.07}OSe_2$ (RKO026i) is in green and $La_2O_2Fe_{1.9}Ni_{0.1}OSe_2$ (RKO026c) is in pink. * denotes the impurity phase $LaFeO_3$, ◊ for $La_4O_4Se_3$, o for $La_4O_4Se_2$, • for $NiSe_2$ and Δ for $NiSeO_3$.
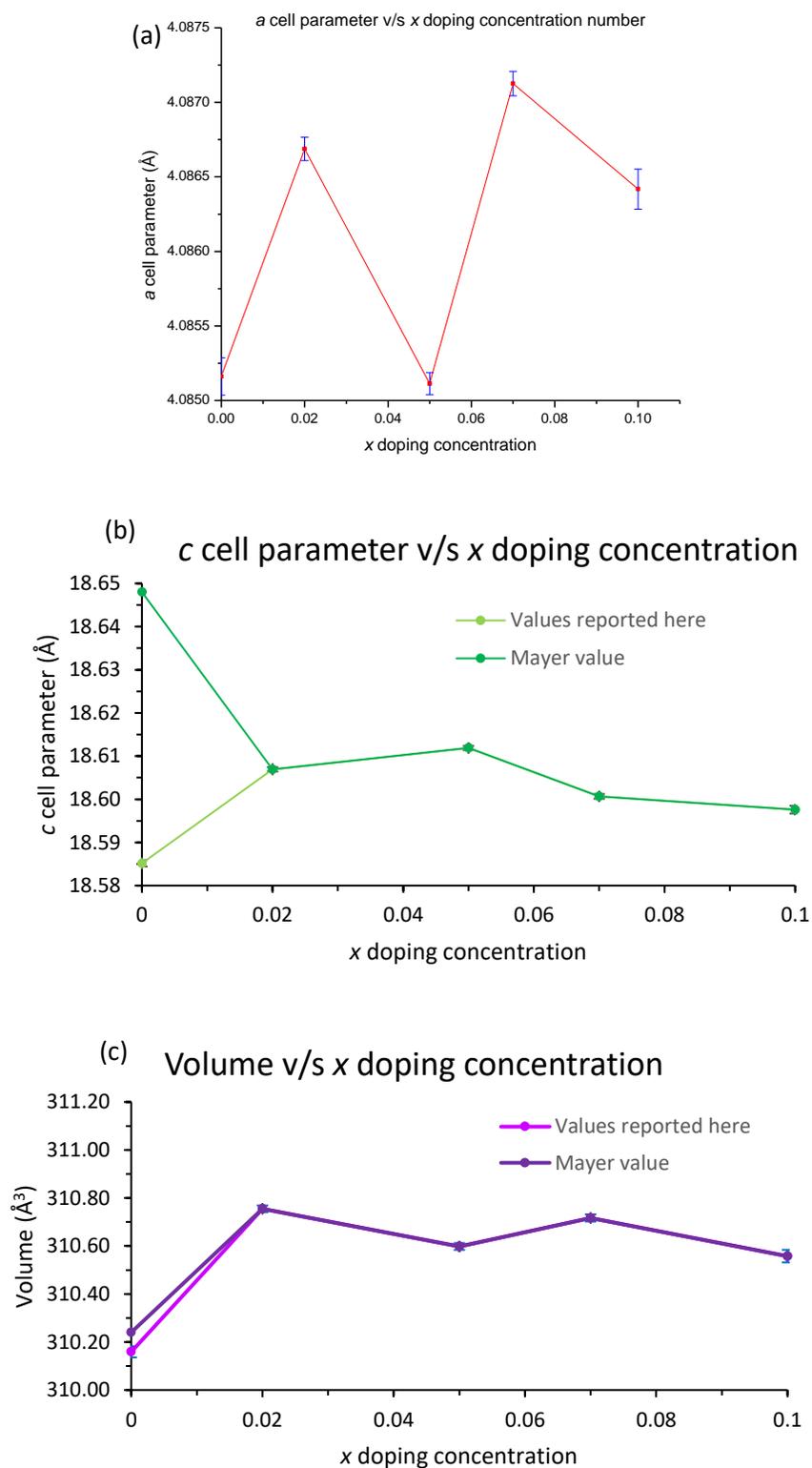
Figure 3.19 (a) Unit cell parameter a (red), (b) unit cell parameter c (values reported here are in light green and Mayer value in green) and (c) volume (values reported here are in light purple and Mayer value in purple) as a function of x for La$_2$O$_2$Fe$_{2-x}$Ni$_x$OSe$_2$ determined from Rietveld refinements using room temperature XRPD data. Error bars in blue.

There are very few other changes in structure with dopant level (Appendix 3.10). Analysis from XRPD indicates no systematic change in unit cell parameters with Ni doping suggesting that none enters the main phase. The change in c cell parameter with dopant level is larger than that for a cell parameter (by 0.22%). Ni impurity phases are only observed in $La_2O_2Fe_{1.93}Ni_{0.07}OSe_2$.

3.2.3.3 Variable temperature X-ray powder diffraction
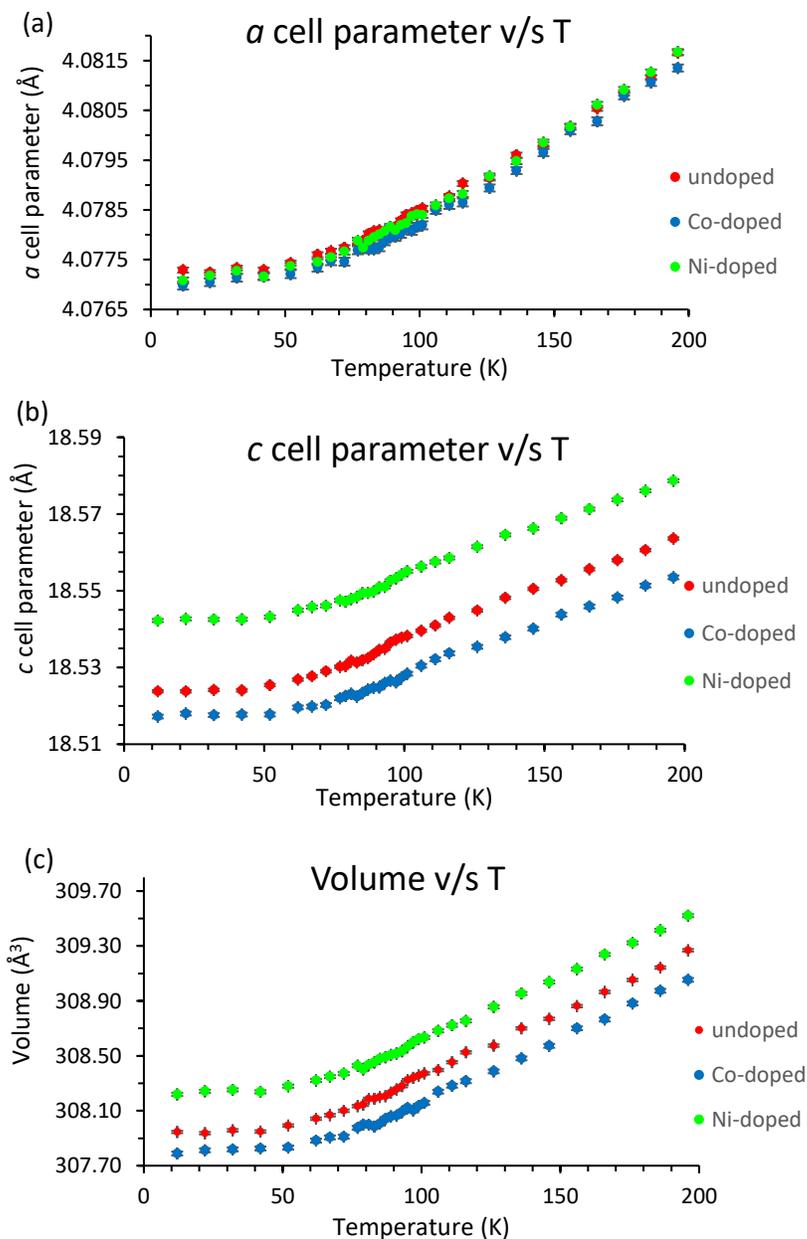
Figure 3.20 (a) a cell parameter (b) c cell parameter (c) unit cell volume against temperature for $La_2O_2Fe_2OSe_2$ (red), $La_2O_2Fe_{1.8}Co_{0.2}OSe_2$ (blue) and $La_2O_2Fe_{1.98}Ni_{0.02}OSe_2$ (green). Error bars are in black.

Following the same method as outlined for $La_2O_2Fe_2OSe_2$ and $La_2O_2Fe_{2-x}Co_xOSe_2$ in Chapter 3.2.1.3 and 3.2.2.3, sequential refinements using variable temperature XRPD data were carried out for $La_2O_2Fe_{1.98}Ni_{0.02}OSe_2$. $La_2O_2Fe_{1.98}Ni_{0.02}OSe_2$ behaves similarly to $La_2O_2Fe_2OSe_2$ with a smooth decrease in cell parameters on cooling and little changes in structure. The more rapid decrease in c for $T<T_N$ is similar for the Ni-doped and undoped materials. (Figure 3.20b).

3.2.3.4 SQUID Magnetometry

Field-cooled (FC) and zero-field-cooled (ZFC) magnetic susceptibility measurements were performed on $La_2O_2Fe_{1.9}Ni_{0.1}OSe_2$ in an applied magnetic field of 1000 Oe, collected on warming from 2 K-300 K at 2 K intervals at 5 K min^{-1}. Magnetization against applied magnetic field measurements were also performed at 300 K and at 10 K. From the $d\chi T/dT$ plots, the transition temperature remains unchanged when $La_2O_2Fe_{2-x}Ni_xOSe_2$ is doped with 0.1 Ni, which is consistent with no Ni entering the main phase.
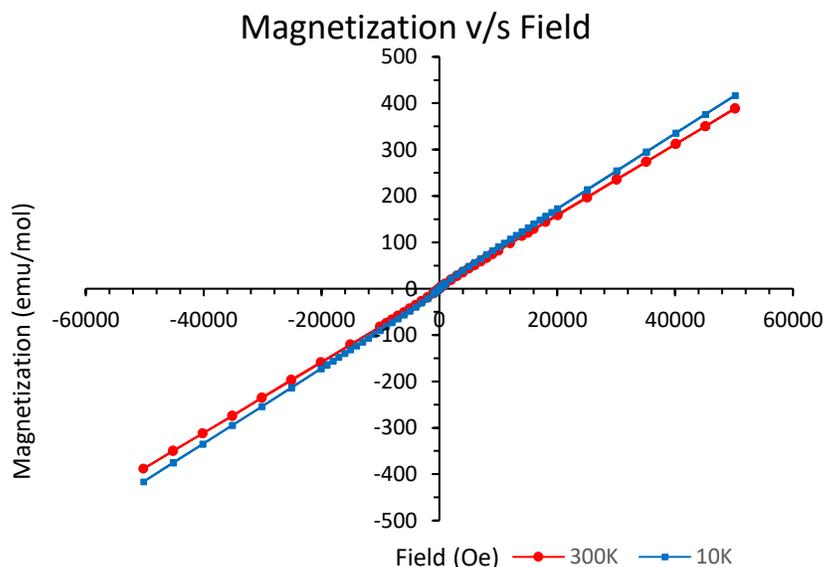
Figure 3.21 Magnetization against field. 300K data (red) and 10K data (blue) data for $La_2O_2Fe_{1.9}Ni_{0.1}OSe_2$.
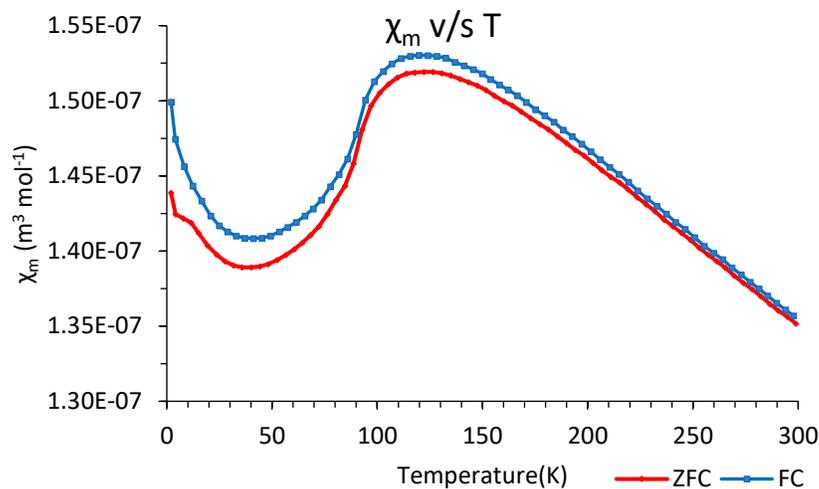
Figure 3.22 χ_m against temperature. ZFC (red) and FC (blue) data for $La_2O_2Fe_{1.9}Ni_{0.1}OSe_2$.
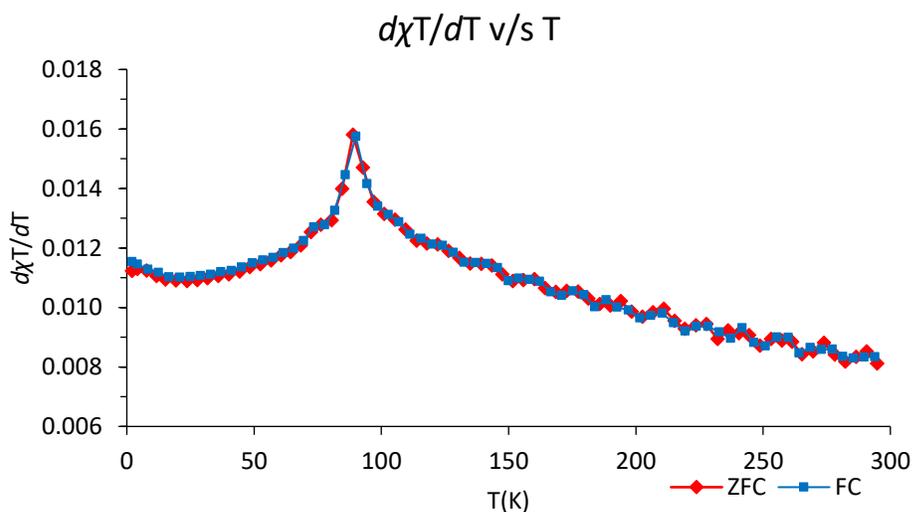
Figure 3.23 $d\chi T/dT$ against temperature. ZFC (red) and FC (blue) data for $La_2O_2Fe_{1.9}Ni_{0.1}OSe_2$

In Figure 3.21, the magnetization at 300 K and 10 K show straight line behaviour crossing the origin indicating absence of any ferromagnetic components, for e.g., any unreacted Fe, Ni reagents or ferromagnetic impurities. The AFM transition temperature stays the same when $La_2O_2Fe_2OSe_2$ is doped with 0.1 Ni.

3.2.3.5 SEM-EDX

An overall backscattered secondary electrons image for each sample was taken at a magnification between X43-X58 to get an idea of the homogeneity of the sample. An example is given in Appendix

3.08. From the backscattered image and spectra, all the samples were fairly homogenous. For x = 0.05 and x = 0.1, most of the sites had La_2O_3 impurities. The average composition from all the normal points, assuming oxygen content and normalizing the data with respect to La, is $La_2O_2Fe_{1.99\pm0.18}Ni_{0.01\pm0.01}OSe_2$ for $La_2O_2Fe_{1.98}Ni_{0.02}OSe_2$, $La_2O_2Fe_{1.98\pm0.14}Ni_{0.02\pm0.02}OSe_2$ for $La_2O_2Fe_{1.95}Ni_{0.05}OSe_2$, $La_2O_2Fe_{1.95\pm0.15}Ni_{0.05\pm0.04}OSe_2$ for $La_2O_2Fe_{1.93}Ni_{0.07}OSe_2$ and $La_2O_2Fe_{1.93\pm0.22}Ni_{0.07\pm0.04}OSe_2$ for $La_2O_2Fe_{1.9}Ni_{0.1}OSe_2$.

3.2.3.6 Conductivity measurements

Conductivity measurements were conducted on all the doped samples except for $La_2O_2Fe_{1.93}Ni_{0.07}OSe_2$. The sintered polished pellets had density between 4.010-4.319 gcm^{-3}, which were 63.0-67.9 % of the theoretical densities. Resistance measurements were collected as the pellets cooled from room temperature to 2 K in a cryostat with readings taken at every 1 K. For x = 0.05, the sample becomes too resistive at low temperatures.
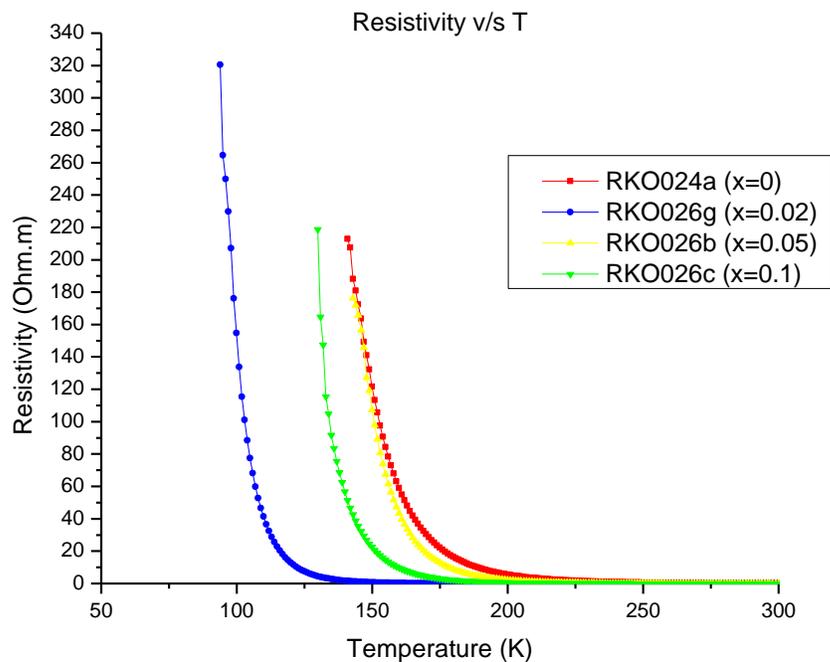
Figure 3.24 Measure of Resistivity (Ohm.m) as a function of temperature for different Ni doping in $La_2O_2Fe_{2-x}Ni_xOSe_2$. $La_2O_2Fe_2OSe_2$ (RKO024a) is in red, $La_2O_2Fe_{1.98}Ni_{0.02}OSe_2$ (RKO026g) is in blue, $La_2O_2Fe_{1.95}Ni_{0.05}OSe_2$ (RKO026b) is in yellow and $La_2O_2Fe_{1.9}Ni_{0.1}OSe_2$ (RKO026c) is in green.
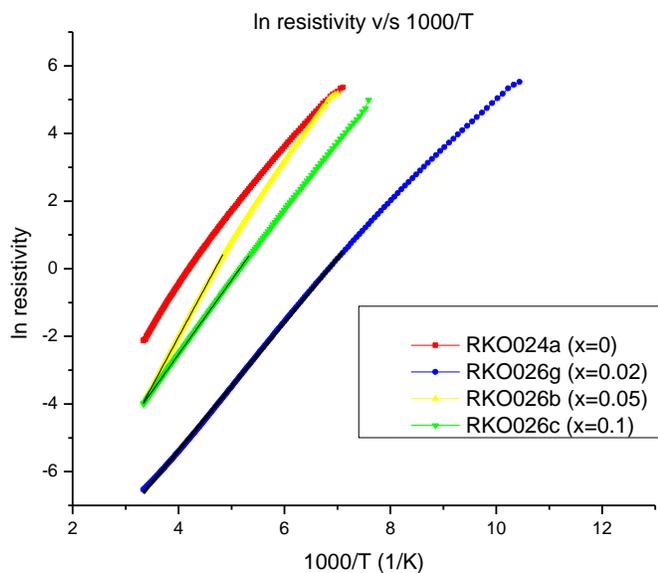
Figure 3.25 Measure of ln resistivity as a function of 1000/T. $La_2O_2Fe_2OSe_2$ (RKO024a) is in red, $La_2O_2Fe_{1.98}Ni_{0.02}OSe_2$ (RKO026g) is in blue, $La_2O_2Fe_{1.95}Ni_{0.05}OSe_2$ (RKO026b) is in yellow and $La_2O_2Fe_{1.9}Ni_{0.1}OSe_2$ (RKO026c) is in green.
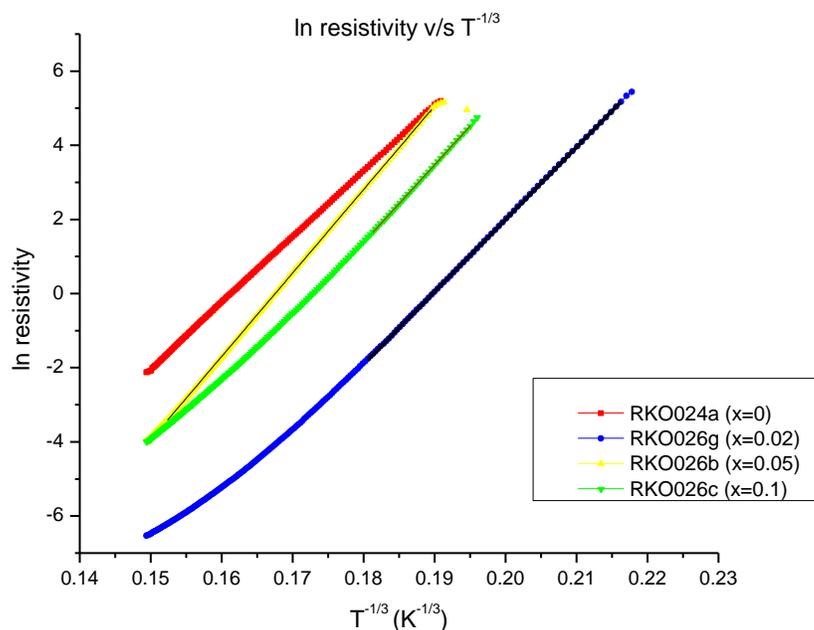
Figure 3.26 Measure of ln resistivity as a function of $T^{-1/3}$. $La_2O_2Fe_2OSe_2$ (RKO024a) is in red, $La_2O_2Fe_{1.98}Ni_{0.02}OSe_2$ (RKO026g) is in blue, $La_2O_2Fe_{1.95}Ni_{0.05}OSe_2$ (RKO026b) is in yellow and $La_2O_2Fe_{1.9}Ni_{0.1}OSe_2$ (RKO026c) is in green.

The exponential increase with decreasing temperature for all the samples indicates semiconducting behaviour (Figure 3.24). The resistivity behaviour of the Ni-doped samples at high temperatures could be explained using the thermally activated model (Figure 3.25) but not at low temperatures, shown by the linear behaviour: T > 140 K (x = 0.02), T > 206 K (x = 0.05) and T > 188 K (x = 0.1).

125

However, two-dimensional variable range hopping (2D-VRH) could be used to describe the resistivity behaviour at low temperatures for those samples, showing a linear behaviour in the ln resistivity vs $T^{-1/3}$ plot (Figure 3.26): 99 K ≤ T ≤ 170 K (x = 0.02), 147 K ≤ T ≤284 K (x = 0.05) and 135 K ≤ T ≤ 168 K (x = 0.1). The values of ρ_0 and T_0 are given in table 3.05 together with the activation energy values of the samples calculated from the slope (Appendix 3.14).

Table 3.05 Resistivity and Activation energy data for $La_2O_2Fe_{2-x}Ni_xOSe_2$ (0 ≤ x ≤ 0.1).

X	0	0.02		0.05		0.1	
Model	**2D-VRH**	**2D-VRH**	**Thermally activated**	**2D-VRH**	**Thermally activated**	**2D-VRH**	**Thermally activated**
T (K)	T < 298	99 ≤ T≤ 170	T > 140	147 ≤ T ≤ 284	T > 206	135 ≤ T ≤ 168	T > 188
ρ_0	3.33×10^{-13}	2.38×10^{-6}	-	1.16×10^{-6}	-	1.25×10^{-5}	-
T_0	5.64×10^6	7.40×10^6	-	1.14×10^7	-	9.16×10^6	-
E_a (eV)	-	-	0.1657 ± 0.007	-	0.1925 ± 0.004	-	0.1901 ± 0.006
ρ at 298K (Ωm)	0.123	0.0015		0.020		0.019	

3.3 Discussion

The *c* cell parameter for $La_2O_2Fe_2OSe_2$ obtained from the room temperature XRPD data is smaller than Mayer's value (Table 3.01) and the SEM-EDX data suggests some Fe deficiency.[1] These may result in anion (e.g. O^{2-}) deficient samples and in some oxidation of Fe^{2+} to smaller Fe^{3+} which might explain the decreased *c* cell parameter.

In $La_2O_2Fe_{2-x}Co_xOSe_2$ (0 ≤ x ≤ 0.2), the overall trend is slight decrease in unit cell volume with increasing Co content (Figure 3.10c). This is consistent with replacing Fe^{2+} with Co^{2+} as the effective ionic radii for high spin ions change from 0.780 Å (Fe^{2+}) to 0.745 Å (Co^{2+})[5] for a coordination number 6. According to Vegard's law, it is expected that since the end members are isostructural, $La_2O_2Fe_2OSe_2$ and $La_2O_2Fe_{2-x}Co_xOSe_2$ (0 ≤ x ≤ 0.2) should form a solid solution limit on mixing. However, linearity is not observed in the unit cell parameters plots with increasing Co doping

concentration (Figure 3.10) which suggests that the Co doping limit is x = 0.02.[24] This maybe is due the presence of LaFeO$_3$ impurity phases in the doped samples. However, La$_2$O$_2$Co$_2$OSe$_2$ was synthesised at 1100°C, 100°C hotter than our synthesis work. Hence, maybe the synthesis conditions could be optimised for higher Co content samples or smaller Ln^{3+} analogues to assess feasibility of a solid solution.[17,23]

In La$_2$O$_2$Fe$_{2-x}$Ni$_x$OSe$_2$ (0 ≤ x ≤ 0.1), no overall trend in unit cell volume with increasing Ni content can be seen (Figure 3.19c). A decrease should have been observed if Fe^{2+} (0.780 Å) was replaced by Ni^{2+} (0.690 Å) in terms of the effective ionic radii for high spin ions for coordination number 6.[5] Although La$_2$O$_2$Ni$_2$OSe$_2$ has not been reported, hypothetically it is assumed that it will be isostructural to La$_2$O$_2$Fe$_2$OSe$_2$ and La$_2$O$_2$Fe$_2$OSe$_2$ and La$_2$O$_2$Fe$_{2-x}$Ni$_x$OSe$_2$ (0 ≤ x ≤ 0.1) would form a solid solution according to Vegard's law.[24] However, no systematic variation in unit cell parameters is observed on Ni-doping and the purity of the samples decreased with increasing Ni doping concentration (Figure 3.19), suggesting that it is not possible to dope Ni^{2+} onto the Fe^{2+} site in La$_2$O$_2$Fe$_2$OSe$_2$. This is maybe due to the presence of various impurity phases in the doped samples, especially those impurity phases which are not observed in La$_2$O$_2$Fe$_{2-x}$Co$_x$OSe$_2$ (0 ≤ x ≤ 0.2). It is possible that Ni^{2+} doping appears to be disfavoured by the electronic effects. The increase observed at x = 0.07 in the unit cell volume and a cell parameter with increasing Ni doping concentration (Figure 3.19a and 3.19c) could be attributed to NiSe$_2$ and NiSeO$_3$ impurities.

In La$_2$O$_2$Fe$_{2-x}$Co$_x$OSe$_2$, the changes in c cell parameters with dopant level are larger than that for a cell parameters. For the same doping percentage, it was expected that the unit cell volume for Ni would have decreased by twice the amount compared to the decrease for Co. Instead, a greater change and a decrease are observed in the unit cell volume for Co suggesting that Ni was not introduced in the sample. The limited solid solution for La$_2$O$_2$Fe$_{2-x}$Ni$_x$OSe$_2$ probably suggests why La$_2$O$_2$Ni$_2$OSe$_2$ does not exist. This is different compared to La$_2$O$_2$Fe$_{2-x}$Mn$_x$OSe$_2$ where a whole solid solution exists which is consistent with the end members being isostructural and with replacing high spin Fe^{2+} with high spin Mn^{2+}.[6] From Ln_2O$_2$Fe$_{2-x}$Mn$_x$OSe$_2$, the dopant content is sensitive to the width of the $[Ln_2O_2]^{2+}$ layer, hence, would be interesting to see if higher Ni content samples could be synthesised for smaller Nd$_2$O$_2$Fe$_{2-x}$Ni$_x$OSe$_2$ series.

From the $d\chi$T/dT plots, the transition temperature increases slightly from 90 K to 94 K when La$_2$O$_2$Fe$_2$OSe$_2$ is doped with 0.2 Co (Figure 3.14) No change in properties was observed for Ni as there

was no change in composition of the main phase due to lack of solid solution. The decrease in lattice parameters for $La_2O_2Fe_{1.8}Co_{0.2}OSe_2$ (Figure 3.10) compared to the undoped material probably reduces the distance between the Fe_2O layers, thus triggering the observed increase in T_N and causing the rapid decrease in c below T_N (Figure 3.11), consistent with the increase in T_N in $La_2O_2Fe_{2-x}Mn_xOSe_2$.[6]

In $La_2O_2Fe_{2-x}Co_xOSe_2$ ($0 \leq x \leq 0.2$), resistivity is largest for x = 0.2 (Table 3.03). This could be due to the impurity present in $La_2O_2Fe_{1.8}Co_{0.2}OSe_2$. T_0 is biggest for x = 0.02 and similar for x = 0.1 and x = 0.2 (Table 3.03). For $La_2O_2Fe_{2-x}Ni_xOSe_2$ ($0 \leq x \leq 0.1$), resistivity is largest for x = 0 and the resistivities in the doped samples don't change much (Table 3.05). This is consistent with no change in composition as there is no solid solution. T_0 is greatest in x = 0.05 (Table 3.05) which could be due to the presence of $La_4O_4Se_2$ in the doped sample. For $La_2O_2Fe_{2-x}Co_xOSe_2$ ($0 \leq x \leq 0.2$), the resistivity behaviour for all the undoped and doped samples, except $La_2O_2Fe_{1.98}Co_{0.02}OSe_2$, at all temperatures could only be explained by the two-dimensional variable range hopping (2D-VRH) (Figure 3.07 and 3.16) and not by the thermally activated model (Appendix 3.04 and 3.09).[7,21,22] For $La_2O_2Fe_{1.98}Co_{0.02}OSe_2$, the resistivity behaviour at high temperatures could be explained by the thermally activated model (Appendix 3.09) and at low temperatures by 2D-VRH (Figure 3.16). This could be due to x = 0.02 being the doping limit and the higher impurity content in those doped samples compared to that in x = 0.02. For $La_2O_2Fe_{2-x}Ni_xOSe_2$, the resistivity behaviour at high temperatures could be explained using the thermally activated model (Figure 3.25) while at low temperatures, the same 2D-VRH model (Figure 3.26) as for the other samples could be used. The 2D-VRH model is typical for systems with localization (e.g. Mott insulators), where the electrons move through localized Fe^{2+} sites with longer distances but closer energy, via a tunneling process stimulated by phonons.[25] There is a transition to different transport mechanisms at higher temperatures where preliminary analysis indicates it is thermally-activated.

3.4 Conclusions

There is a limited solid solution to electron dope $La_2O_2Fe_2OSe_2$ with Co and Ni with Co-doping being successful up to x = 0.02, supported by the thermally-activated model which indicates that $La_2O_2Fe_2OSe_2$ was successfully electron-doped with Co up to x = 0.02. Ni-doping was not successful due to perhaps the small amount used or due to Ni^{2+} being disfavoured by electronic effects. Electron doping $La_2O_2Fe_2OSe_2$ with Co and Ni gave semiconductor materials. The SQUID

Magnetometry analysis showed that electron doping $La_2O_2Fe_2OSe_2$ with x = 0.2 cobalt slightly increased the transition temperature. Other strategies to dope $La_2O_2Fe_2OSe_2$ might be to substitute some O with F in $La_2O_2Fe_2F_xO_{1-x}Se_2$.

3.5 References

1   J. M. Mayer, L. F. Schneemeyer, T. Siegrist, J. V Waszczak and B. Van Dover, *Angew. Chemie Int. Ed.*, 1992, **31**, 1645–1647.

2   J. X. Zhu, R. Yu, H. Wang, L. L. Zhao, M. D. Jones, J. Dai, E. Abrahams, E. Morosan, M. Fang and Q. Si, *Phys. Rev. Lett.*, 2010, **104**, 216405.

3   E. E. McCabe, C. Stock, E. E. Rodriguez, A. S. Wills, J. W. Taylor and J. S. O. Evans, *Phys. Rev. B*, 2014, **89**, 100402.

4   D. G. Free, N. D. Withers, P. J. Hickey and J. S. O. Evans, *Chem. Mater.*, 2011, **23**, 1625–1635.

5   R. D. Shannon, *Acta Crystallogr. Sect. A*, 1976, **32**, 751–767.

6   H. Lei, E. S. Bozin, A. Llobet, V. Ivanovski, V. Koteski, J. Belosevic-Cavor, B. Cekic and C. Petrovic, *Phys. Rev. B*, 2012, **86**, 125122.

7   Y. Liu, S. B. Zhang, W. J. Lu, L. J. Li, S. G. Tan, B. Yuan, J. Chen and Y. P. Sun, *J. Alloys Compd.*, 2015, **618**, 263–268.

8   S. Landsgesell, E. Blumenröther and K. Prokeš, *J. Phys. Condens. Matter*, 2013, **25**, 086004.

9   B. Freelon, Y. H. Liu, J. L. Chen, L. Craco, M. S. Laad, S. Leoni, J. Chen, L. Tao, H. Wang, R. Flauca, Z. Yamani, M. Fang, C. Chang, J. H. Guo and Z. Hussain, *Phys. Rev. B*, 2015, **92**, 155139.

10   G. Giovannetti, L. de Medici, M. Aichhorn and M. Capone, *Phys. Rev. B*, 2015, **91**, 085124.

11   A. S. Sefat, A. Huq, M. A. McGuire, R. Jin, B. C. Sales, D. Mandrus, L. M. D. Cranswick, P. W. Stephens and K. H. Stone, *Phys. Rev. B*, 2008, **78**, 104505.

12   G. Cao, S. Jiang, X. Lin, C. Wang, Y. Li, Z. Ren, Q. Tao, C. Feng, J. Dai, Z. Xu and F. C. Zhang, *Phys. Rev. B*, 2009, **79**, 174505.

13   A. Marcinkova, D. A. M. Grist, I. Margiolaki, T. C. Hansen, S. Margadonna and J. W. G. Bos, *Phys. Rev. B*, 2010, **81**, 064511.

14   Bruker AXS, *Diffracplus Basic Evaluation Package: EVA 10.0*, 2004.

15   A. A. Coelho, *TOPAS Academic: General profile and Structure Analysis Software for Powder Diffraction Data*, 2010.

16   H. H. Rietveld, *J. Appl. Cryst*, 1969, **65**.

17   C. Wang, M. Q. Tan, C. M. Feng, Z. F. Ma, S. Jiang, Z. A. Xu, G. H. Cao, K. Matsubayashi and Y. Uwatoko, *J. Am. Chem. Soc.*, 2010, **132**, 7069–7073.

18   D. G. Free and J. S. O. Evans, *Phys. Rev. B*, 2010, **81**, 214433.

19   K. Horigane, K. Kawashima, S. Ji, M. Yoshikawa, D. Louca and J. Akimitsu, *Proc. Int. Conf. Strongly Correl. Electron Syst.*, 2014, **3**, 015039.

20   M. A. Senaris-Rodriguez and J. B. Goodenough, *J. Solid State Chem*, 1995, **118**, 323–336.

21   D. Yu, C. Wang, B. L. Wehrenberg and P. Guyot-Sionnest, *Phys. Rev. Lett.*, 2004, **92**, 216802.

22   D. Joung and S. I. Khondaker, *Phys. Rev. B*, 2012, **86**, 235423.

23   Y. Fuwa, M. Wakeshima and Y. Hinatsu, *Solid State Commun.*, 2010, **150**, 1698–1701.

24   A. R. Denton and N. W. Ashcroft, *Phys. Rev. A*, 1991, **43**, 3161–3164.

25   F. Han, D. Wang, C. D. Malliakas, M. Sturza, D. Y. Chung, X. Wan and M. G. Kanatzidis, *Chem. Mater.*, 2015, **27**, 5695–5701.

Chapter 4: $Ln_2O_2Fe_2OQ_2$ (Ln= La, Pr and Q= S, Se)

4.1 Introduction to $La_2O_2Fe_2OS_2$

$La_2O_2Fe_2OS_2$ has the same crystal structure as $La_2O_2Fe_2OSe_2$ where fluorite-like $(La_2O_2)^{2+}$ layers and anti-CuO_2 type $(Fe_2O)^{2-}$ layers are separated by S^{2-} ions as described in Chapter 3, although the unit cell is smaller [a = 4.0408(1) Å, c = 17.8985(6) Å for $La_2O_2Fe_2OS_2$ and a = 4.0788(2) Å, c = 18.648(2) Å for $La_2O_2Fe_2OSe_2$].[1] It exhibits antiferromagnetic (AFM) ordering at $T \leq T_N$ (105 K) and the broad maximum in the magnetic susceptibility is ascribed to the magnetic order within layers above T_N.[1] There are three exchange interactions: nearest-neighbour J_1 Fe-Fe, next-nearest-neighbour J_2 Fe – S – Fe exchange and next-nearest-neighbour $J_{2'}$ Fe – O – Fe exchange (Figure 4.01). These interactions compete to produce long range AFM order as shown by theoretical and SQUID studies. Fuwa et al have proposed for $Nd_2O_2Fe_2OSe_2$ that the nearest-neighbour J_1 exchange with Fe^{2+} moments perpendicular to one another in the ab plane, while the next-nearest-neighbour $J_{2'}$ Fe – O – Fe is AFM due to the Goodenough–Kanamori rule and ferromagnetic (FM) next-nearest-neighbour J_2 Fe – Se – Fe exchange.[2,3] This is described as the 2-k magnetic structure (Figure 4.01). Neutron Powder Diffraction (NPD) data of $La_2O_2Fe_2OSe_2$ and $Sr_2F_2Fe_2OS_2$ suggest 2-k magnetic structure. S-substitution work on $Nd_2O_2Fe_2OSe_{2-x}S_x$ has suggested that it enhances FM component.[4–6]
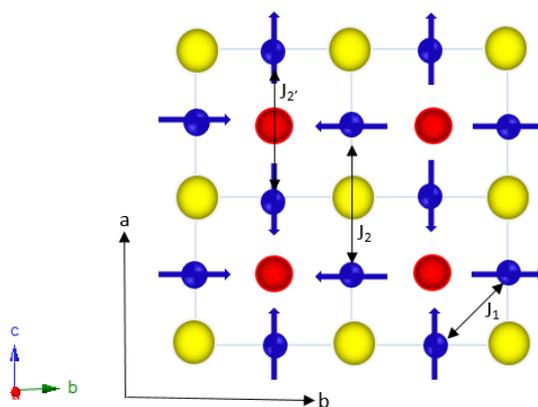
Figure 4.01 2-k magnetic structure showing Fe atoms (blue), oxygen atoms (red) and S atoms (yellow), with Fe^{2+} moments shown by blue arrows.

The aims of this work are to confirm the magnetic structure of $La_2O_2Fe_2OS_2$ using NPD and study the short range magnetic order and magnetic microstructure to compare them to related materials.

4.1.1 Experimental

$La_2O_2Fe_2OS_2$ was prepared from stoichiometric amounts of La_2O_3 (Sigma-Aldrich, 99.99%), Fe (Alfa-Aesar, 99+%) and S (Alfa-Aesar, 99.5%+) as discussed in Chapter 2.1. The starting reagents were weighed and ground using a mortar and pestle in the glovebox. The mixture was then pressed into a 5 mm pellet and placed in a quartz tube. The latter was then sealed under vacuum and heated in a furnace at the following conditions: ramped to 400°C at 1°C/min and dwelled for 12 hours, ramped to 600°C at 0.5°C/min and dwelled for 1 hour, ramped to 850°C at 1°C/min and dwelled for 12 hours. The furnace was then allowed to cool to room temperature. The mixture was reground, resealed and reheated at the same temperature conditions to ensure crystalline materials. This synthesis gave a highly crystalline sample containing 1.67 ± 0.17 % $LaFeO_3$ impurity phase (Figure 4.02). The purity of the sample, confirmed by Scanning Electron Microscopy-Energy Dispersive X-ray (SEM-EDX) (Appendix 4.01), suggested $La_2Fe_{1.61\pm0.15}S_{1.39\pm0.07}$ (normalised to La). Attempts to synthesise other *Ln* analogues were unsuccessful and gave $Ce_2O_2Fe_2OS_2$, FeS, CeO_2 and Ce_2O_2S for $Ce_2O_2Fe_2OS_2$ and Sm_2O_2S, $SmFeO_3$ and Sm_2O_3 for $Sm_2O_2Fe_2OS_2$.[7] Neutron powder diffraction data were collected on the high flux, constant wavelength ($\lambda=2.41$ Å) D20 diffractometer at the ILL on $La_2O_2Fe_2OS_2$. The powder sample of mass 4.44 g was placed in a 10 mm diameter cylindrical vanadium can with a sample height of 2.5 cm. 10 minute scans were collected from 1.8 K to 168 K at 2 K/min, followed by a 40 minute scan at 1.8 K.

4.1.2 Results and discussions

4.1.2.1 X-ray powder diffraction

After synthesis, the resulting black pellet was analysed by in-house X-ray powder diffraction (XRPD) (Figure 4.02). The amorphous background seen between 10° and 18° was due to air scattering of the X-rays. A small impurity phase of $LaFeO_3$ was present in the sample. The refinement was performed as described in Chapter 2.2.2. The only deviations applied to the refinement was a 17th order Chebychev polynomial function to fit the background. The R_{wp} for the refinement was 4.08 %, the χ^2 was 4.22. Data for some of the relevant parameters are shown in Table 4.01.
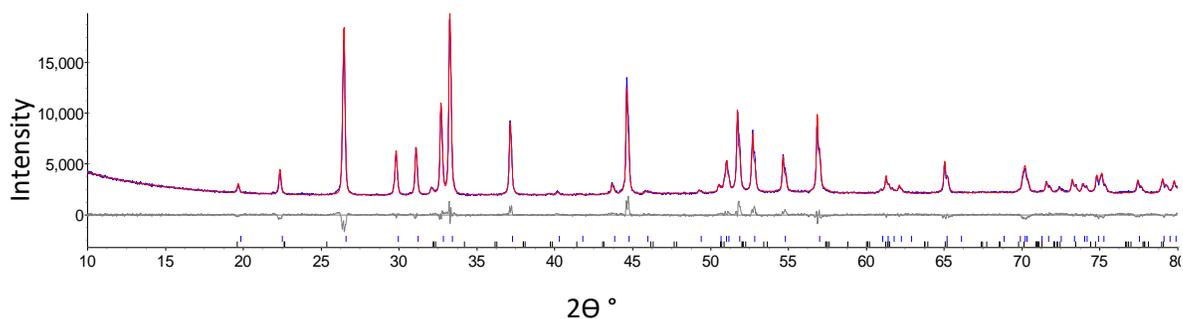
Figure 4.02 Rietveld refinement profiles for $La_2O_2Fe_2OS_2$ using room temperature XRPD data. R_{wp} 4.08 %, Rp 2.89 % and the χ^2 was 4.22. The observed data is in black, the calculated data is in red and the difference is in grey. The blue vertical tick marks show the predicted peak positions for $La_2O_2Fe_2OS_2$ (98.33 ± 0.17 %) and the black tick marks show those for $LaFeO_3$ (1.67 ± 0.17 %).

Table 4.01 Data for room temperature Rietveld refinement for $La_2O_2Fe_2OS_2$ together with values from the literature and $La_2O_2Fe_2OSe_2$ for comparison.

$La_2O_2Fe_2OS_2$		Mayer *et al*[1]	$La_2O_2Fe_2OSe_2$ (Chapter 3)
Space group	*I4/mmm*	*I4/mmm*	*I4/mmm*
a cell parameter (Å)	4.045873 (9)	4.0408 (1)	4.085161 (6)
c cell parameter (Å)	17.884170 (5)	17.8985 (6)	18.585159 (7)
Volume (Å³)	292.747 (2)		310.159 (3)
La *z* (c)	0.18103 (7)		0.18465 (1)
Se *z* (c)	0.09506 (5)		0.09756 (7)

The data is in good agreement with literature.

4.1.2.2 Variable temperature X-ray powder diffraction

Variable temperature X-ray powder diffraction (VT-XRPD) data was collected to follow unit cell parameters on cooling. Refinements were carried out as for the room temperature data but with the peak shape terms fixed. Sequential Rietveld refinements showed a smooth decrease in cell parameters on cooling with a slightly more rapid decrease in *c* around 105 K and very little change in crystal structure (Figure 4.03) (Appendix 4.02).

(a)

(b)

(c)
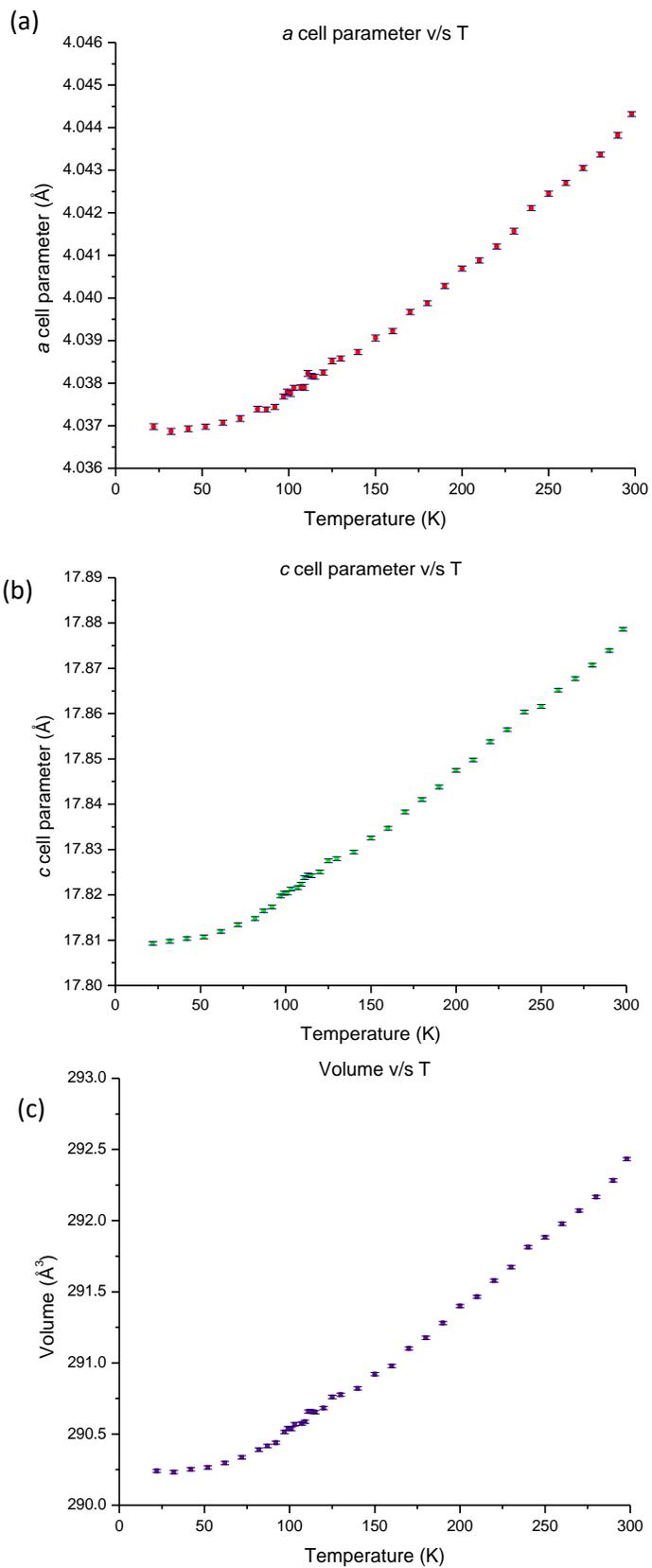
Figure 4.03 (a) *a* cell parameter (b) *c* cell parameter (c) unit cell volume against temperature for $La_2O_2Fe_2OS_2$. Data is shown in red, green and purple respectively with the error bars in blue.

4.1.2.3 SQUID Magnetometry

Field-cooled (FC) and zero-field-cooled (ZFC) magnetic susceptibility measurements were performed on the sample in an applied magnetic field of 1000 Oe, collected on warming from 2 K to 300 K at 2 K intervals at 5 K min^{-1}.
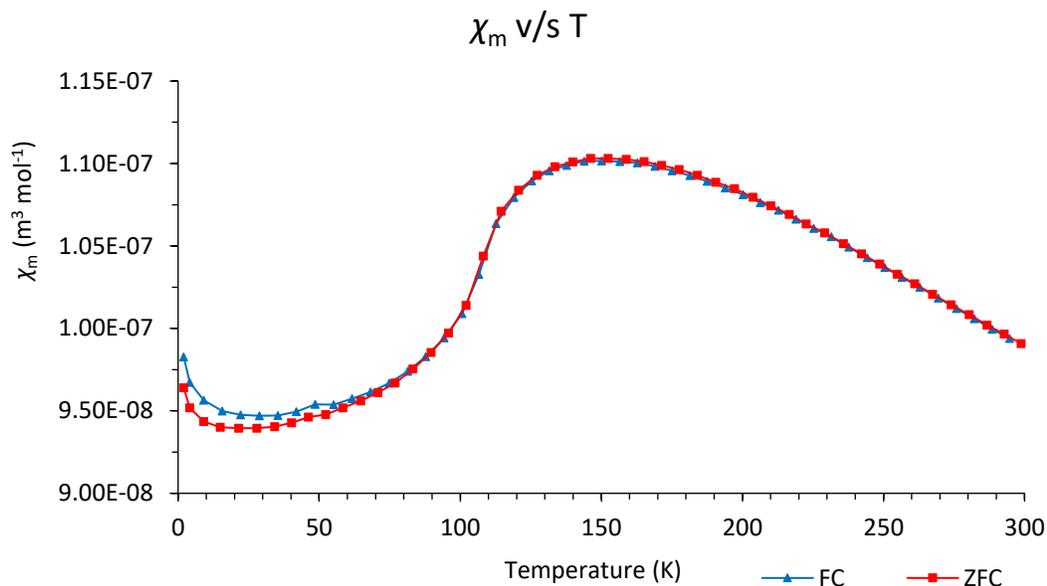
Figure 4.04 χ_m against temperature. ZFC (red) and FC (blue) data for $La_2O_2Fe_2OS_2$.
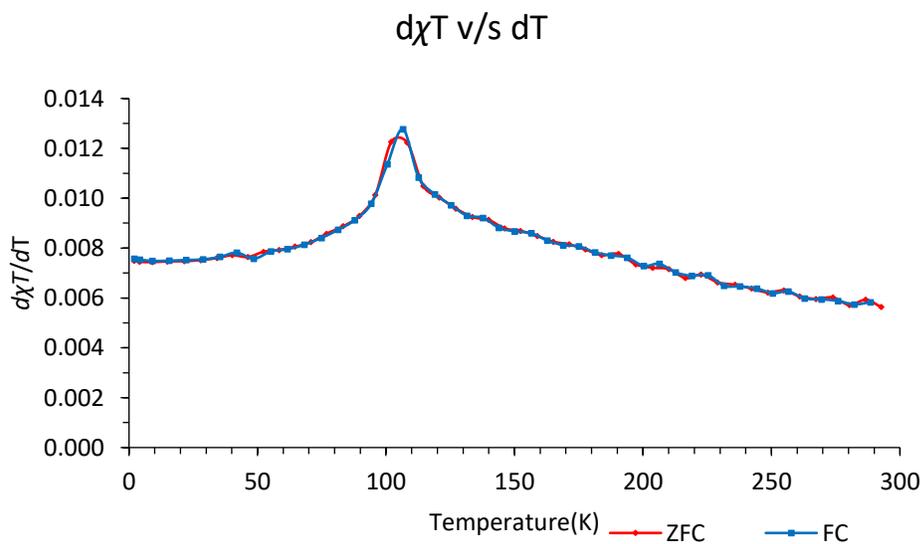
Figure 4.05 $d\chi$T/dT against temperature. ZFC (red) and FC (blue) data for $La_2O_2Fe_2OS_2$.

There is a broad local maximum at around 105 K, due to low dimensional, 2D order above T_N which is consistent with literature.[1] Moreover, there is AFM ordering below 105 K.[1,8] Hence, T_N is more clearly observed in $d\chi T/dT$ plot (Figure 4.05). There is no Curie-Weiss like behaviour up to 300 K and this could be due to short range order within the Fe_2O layers. The feature in the susceptibility at low temperature (Figure 4.04) suggests trace amounts of paramagnetic impurity phases.[9]

4.1.2.4 Neutron powder diffraction

NPD data collected at 168 K (Figure 4.06) are consistent with the *I4/mmm* crystal structure. There is a slight deficiency in Fe and O (2) (Table 4.02) probably due to some Fe^{2+} oxidation. The lattice parameters obtained [a = 4.0321 (3) Å and c = 17.8208 (6) Å] are similar to the room temperature XRPD values [a = 4.045873(9) Å and c = 17.884170(5) Å] and literature.[1]
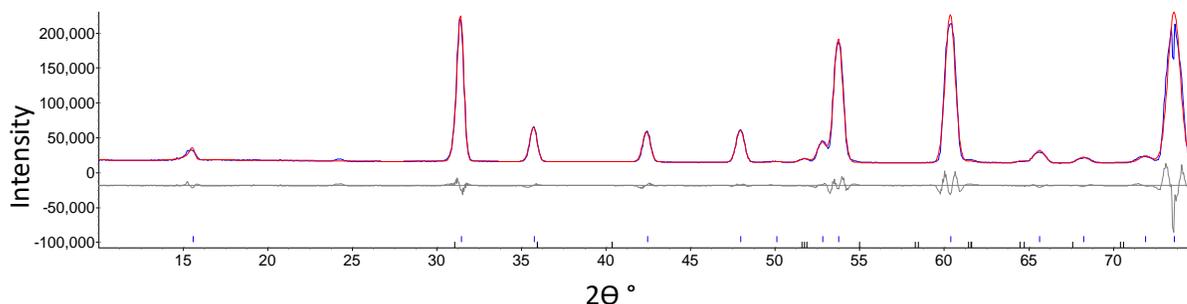
Figure 4.06 Rietveld refinement profile using NPD data at 168 K. The observed data is in blue, the calculated data is in red and the difference is in grey. The blue vertical tick marks show the predicted peak positions for the nuclear $La_2O_2Fe_2OS_2$. R_{wp} 7.20 % and Rp 4.77 %.

Table 4.02 Data for Rietveld refinement using 168 K NPD data. Nuclear structure: I4/mmm space group, a = 4.0321 (3) Å and c = 17.8208 (6) Å

Atom	Site	x	y	z	Site occupancies	U_{iso} x 100 (Å^2)
La	4e	0.5	0.5	0.18033 (7)	1	1.3 (2)
Fe	4c	0.5	0	0	0.97636 (8)	1.3 (2)
S	4e	0	0	0.09458 (9)	0.99568 (8)	1.3 (2)
O (1)	4d	0.5	0	0.25	0.99344 (4)	1.3 (2)
O (2)	2b	0.5	0.5	0	0.97480 (2)	1.3 (2)
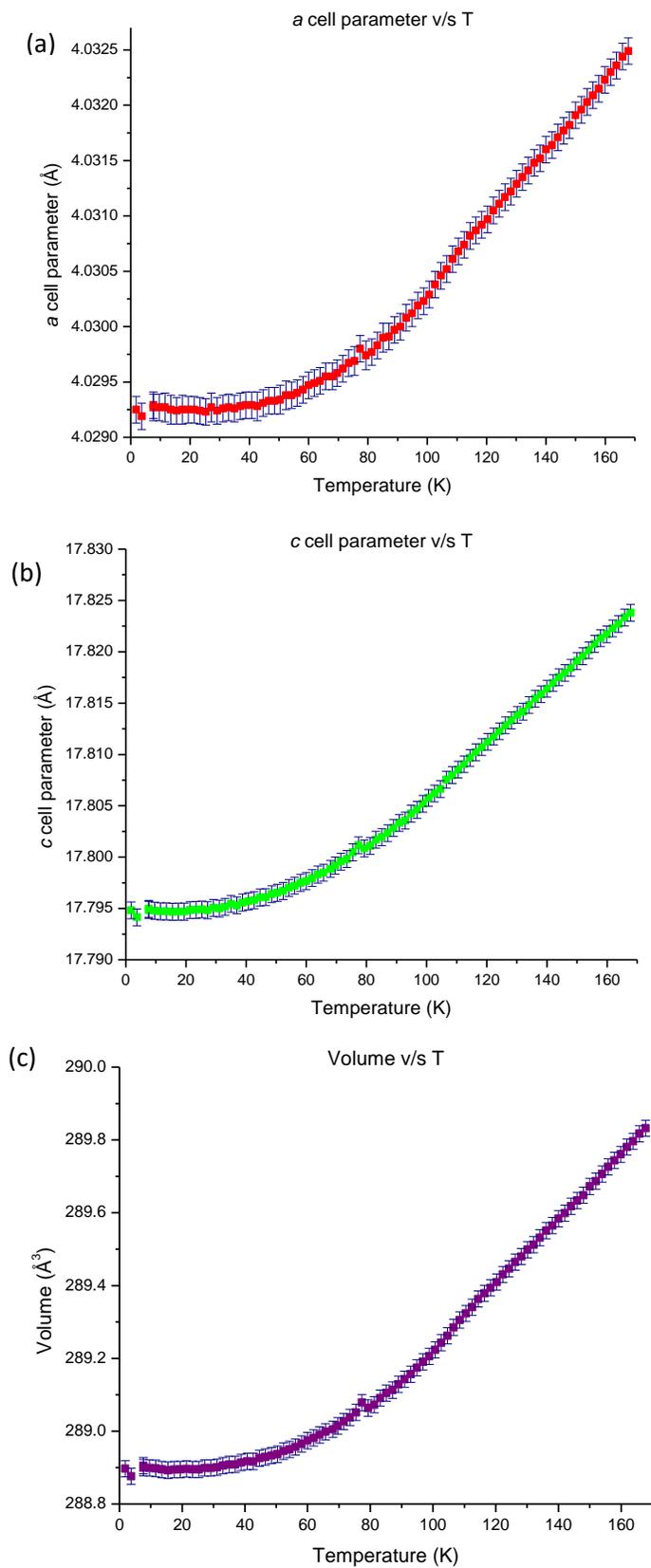
Figure 4.07 NPD data of (a) *a* cell parameter (b) *c* cell parameter (c) unit cell volume against temperature for La$_2$O$_2$Fe$_2$OS$_2$. Data is shown in red for *a* cell parameter, green for *c* cell parameter and purple for unit cell volume with the error bars in blue.

Sequential Rietveld refinements using variable temperature neutron powder diffraction data showed a smooth increase in cell parameters on warming and very little change in crystal structure (Figure 4.07) (Appendix 4.04), consistent with XRPD data. Above T_N, the increase in the c cell parameter is slightly less rapid on warming (after 115 K) (Figure 4.07b). The expansion in the c cell parameter was larger than that for the a cell parameter (by 0.1%). There was a less pronounced decrease in c for $T<T_N$ than for other M_2O materials. $La_2O_2Fe_2OS_2$ showed no marked discontinuity in c cell parameter as in $La_2O_2Fe_2OSe_2$ at T_N (but shows discontinuity in c cell parameter in VT-XRPD data) and the decrease in c cell parameter is less than that in $La_2O_2Fe_2OSe_2$ as its c cell parameter is smaller (Appendix 4.05).[10] This is dissimilar to the rapid decrease in c cell parameter below T_N with larger distance between M_2O layers in $Ln_2O_2M_2OSe_2$ (Ln = La-Pr and M = Mn, Fe, Co) systems.[11,12]

Just above T_N at 106.5 K, a broad asymmetric Warren-peak appearing at around 39.4° 2Θ is observed which decreases in intensity and disappears at around 116.4 K (Figure 4.08a,c).[13] This is similar to that observed in other $Ln_2O_2Fe_2OSe_2$ (Ln = La-Pr) systems and is typical of 2-D short range order and consistent with SQUID measurements (Figure 4.05).[1,5,11] In $La_2O_2Fe_2OSe_2$, the range of temperatures at which the Warren-peak appears is 91 K-103 K, similar to $La_2O_2Fe_2OS_2$.[5] In $La_2O_2Mn_2OSe_2$, the temperature range of the Warren-peak is 200 K-300 K while in $Sr_2F_2Fe_2OSe_2$, the temperature range of the Warren-peak is 16 K-106 K.[6,14] These big ranges could be indicative of frustration in the 2-k magnetic model as the Warren-peak reflects short range 2-D order and maybe frustration. Fitting this peak with a Warren function gave a correlation length of around 100 Å along a (about 25 times the size of the in-plane cell parameter) at 106.5 K which then drops quickly to about 15 Å at 108.5 K (Figure 4.08b). The magnetic correlation length along c is 48 Å at 100 K along c.

Below 105 K, additional magnetic Bragg reflections are observed in $La_2O_2Fe_2OS_2$ NPD data whose intensity increase smoothly on cooling (Appendix 4.06) and these are consistent with a 2-k magnetic structure with a 2a x 2a x 2c unit cell, magnetic propagation vectors $\mathbf{k}$= $(1/2, 0, 1/2)$ and $\mathbf{k}$= $(0, 1/2, 1/2)$ as seen in $Sr_2F_2Fe_2OSe_2$ and $La_2O_2Fe_2OSe_2$.[5,6] $La_2O_2Fe_2OS_2$ has similar unit cell parameters to $Sr_2F_2Fe_2OSe_2$ and $Nd_2O_2Fe_2OSe_{2-x}S_x$ but smaller than for $La_2O_2Fe_2OSe_2$ (Table 4.03).[1,4,15] Fitting the NPD data for $La_2O_2Fe_2OS_2$ with the $I4/mmm$ nuclear phase and a magnetic phase which described the 2-k magnetic structure gave a poor fit in the refinement profile (Figure 4.09a). However, adding anisotropic peak broadening to the magnetic Bragg reflections improved the fit (Figure 4.09b).
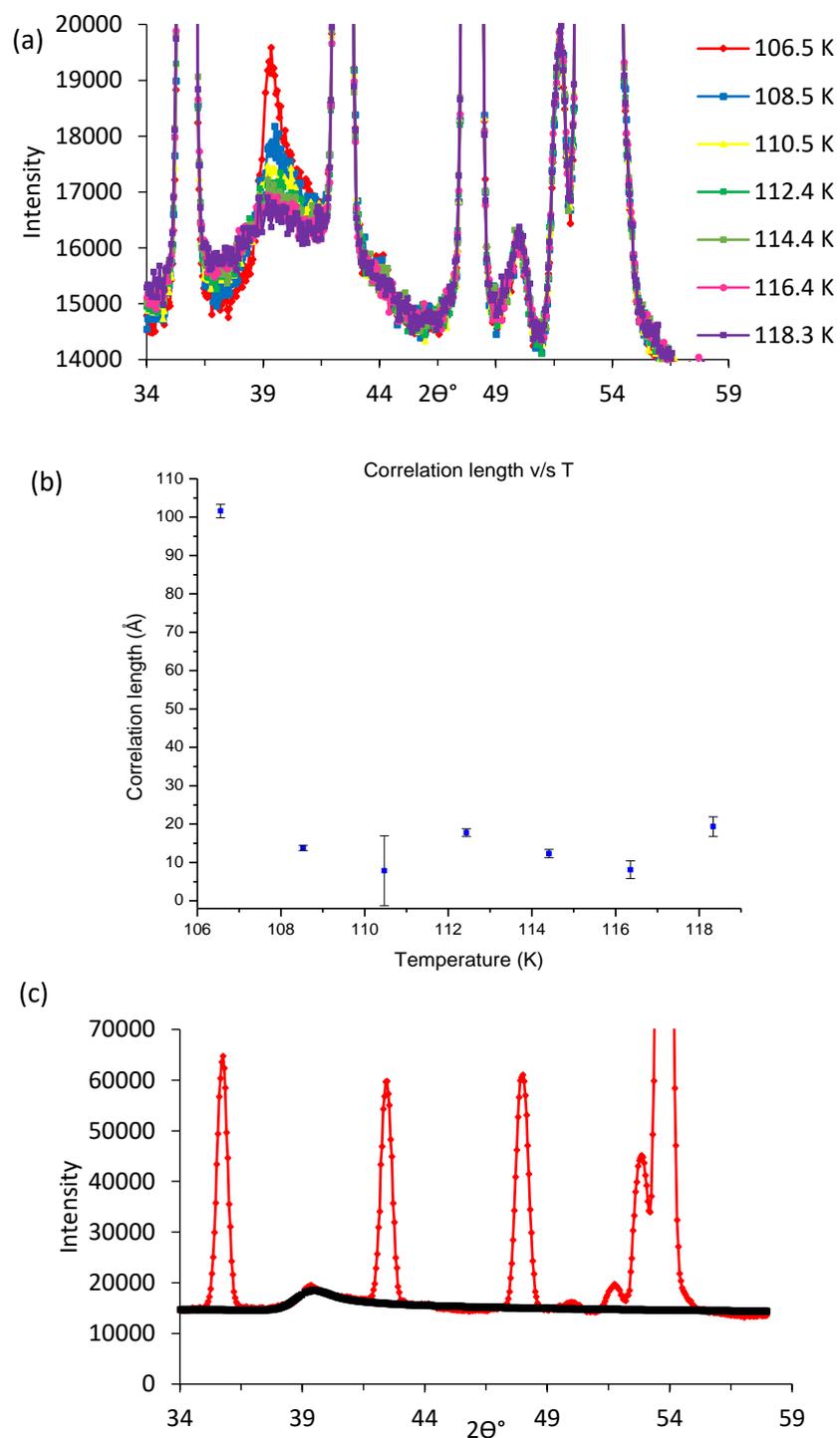
Figure 4.08 NPD data for La$_2$O$_2$Fe$_2$OS$_2$ near T_N showing (a) Intensity against 2Ɵ for various temperatures showing the evolution of the warren peak (b) correlation length against temperature for the warren peaks. Data is shown in blue with the error bars in black (c) Intensity against 2Ɵ for 106.5 K with data in red and calculated warren peak fit and background shown in black.

The *0, k, l* reflections [for e.g. (*0, 1, 0*) at 2Ɵ = 17.2°, (*0, 3, 0*) at 2Ɵ = 53.5°] are broader than the *h, k, 0* ones [for e.g. (*3, 1, 0*) at 2Ɵ = 20.9°, (*5, 1, 0*) at 2Ɵ = 26.1°, (*9, 1, 0*) at 2Ɵ = 39.8°] and hence, the

magnetic correlation length along c (48 Å at 100 K) is shorter than in the ab plane (100 Å at 106.5 K). This improvement model based on Clays describes the stacking faults, similar in $Ln_2O_2Fe_2OSe_2$ (Ln = La-Pr) systems, which are perpendicular to the c-plane.[16] This anisotropic peak broadening is observed in $La_2O_2Fe_2OSe_2$ (magnetic correlation length of 42 Å at 88 K along c and 90 Å at 90 K along ab), $Ce_2O_2Fe_2OSe_2$ (magnetic correlation length of 87 Å at 1.5 K along c), $Nd_2O_2Fe_2OSe_2$ (magnetic correlation length of 86 Å at 1.5 K along c), $Pr_2O_2Fe_2OSe_2$ (magnetic correlation length of 138 Å at 1.5 K along c) and in $Sr_2F_2Fe_2OSe_2$ (magnetic correlation length of 17 Å along c and 310 Å along ab).[5,6,11,17] No anisotropic peak broadening values has been reported yet for nor for the Mn_2O or Co_2O materials.[14,18,19] It seems that the stacking faults are unique to the Fe_2O layers and might be affected by the distance between Fe_2O layers. S^{2-} has a smaller ionic radius than Se hence the separation between Fe_2O layers in $La_2O_2Fe_2OS_2$ is shorter than in $La_2O_2Fe_2OSe_2$ resulting in a longer magnetic correlation length.[2-20] Similarly, La^{3+} has a bigger ionic radius than Ce^{3+}, Nd^{3+} and Pr^{3+}, hence, the separation between Fe_2O layers in $La_2O_2Fe_2OSe_2$ is greater than in $Ln_2O_2Fe_2OSe_2$ (Ln = Ce, Nd, Pr) resulting in a smaller magnetic correlation length.[20] Comparing $La_2O_2Fe_2OS_2$ and $Sr_2F_2Fe_2OSe_2$, since the ionic radius of Sr^{2+} is bigger than La^{3+}, it would be expected that the magnetic correlation length of $Sr_2F_2Fe_2OSe_2$ is smaller than $La_2O_2Fe_2OS_2$.[20] However, that is not the case and this probably means that the fluoride layer is responsible for the difference instead of the oxygen layer.

(a)

(b)
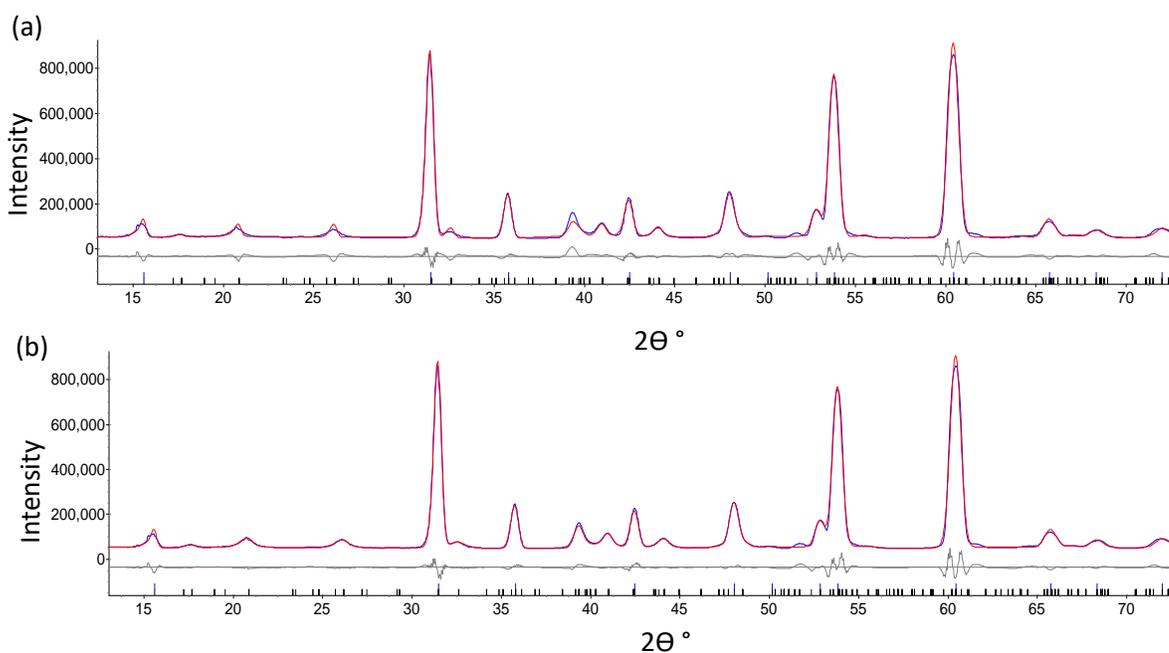
Figure 4.09 Rietveld refinement profiles using 1.8 K NPD data with 2-k magnetic structure (a) Fit using nuclear and magnetic phases (b) the same fit but with stacking faults in the magnetic structure. The observed data is in blue, the calculated data is in red and the difference is in grey. Nuclear phase shown by blue tick marks and magnetic phase in black tick marks.

The Fe^{2+} magnetic moments increase smoothly on cooling below T_N (Appendix 4.07). The Fe^{2+} magnetic moment at 1.8 K was 3.30(3) μ_B (Table 4.04), similar to $Sr_2F_2Fe_2OSe_2$ (3.3[1] μ_B), $La_2O_2Fe_2OSe_2$ (3.5[5] μ_B), $Ce_2O_2Fe_2OSe_2$ (3.32[1] μ_B), $Nd_2O_2Fe_2OSe_2$ (3.18[1] μ_B) and $Pr_2O_2Fe_2OSe_2$ (3.36[1] μ_B).[5,6,11,17]

Table 4.03 Data for room temperature Rietveld refinement for $La_2O_2Fe_2OS_2$ together with values from $La_2O_2Fe_2OSe_2$, $Sr_2F_2Fe_2OSe_2$ and $Nd_2O_2Fe_2OSe_{2-x}S_x$ for comparison.

	$\underline{La_2O_2Fe_2OS_2}$	$\underline{La_2O_2Fe_2OSe_2}$[1]	$\underline{Sr_2F_2Fe_2OSe_2}$[15]	$\underline{Nd_2O_2Fe_2OSe_2}$[4]
a cell parameter (Å)	4.045873 (9)	4.0788 (2)	4.0400 (6)	4.0231 (4)
c cell parameter (Å)	17.884170 (5)	18.648 (2)	17.998 (4)	18.456 (2)
Volume ($Å^3$)	292.747 (2)	310.24	293.75 (9)	298.72 (9)

Table 4.04 Data for Rietveld refinement for $La_2O_2Fe_2OS_2$ using 1.8 K NPD data. Nuclear structure: $I4/mmm$ space group, a = 4.0289 (3) and c = 17.7913 (9). R_{wp} 7.67 % and Rp 5.30 %. ξ_c =50(3) Å.

Atom	**Site**	**x**	**y**	**z**	**U_{iso} x 100 ($Å^2$)**	**Fe^{2+} moment (μ_B))**
La	$4e$	0.5	0.5	0.18043 (7)	1.05 (0)	
Fe	$4c$	0.5	0	0	1.05 (0)	3.30 (3)
S	$4e$	0	0	0.09443 (0)	1.05 (0)	
O (1)	$4d$	0.5	0	0.25	1.05 (0)	
O (2)	$2b$	0.5	0.5	0	1.05 (0)	

Table 4.05 Data for Rietveld refinement for $La_2O_2Fe_2OS_2$ using 1.8 K NPD data showing bond lengths and bond angles.

Bond lengths	**Å**
Fe-Fe	4 x 2.84911 (9)
Fe-O (2)	2 x 2.01463 (6)
Fe-S	4 x 2.62413 (8)
Bond angles	**°**
Fe-O-Fe	180
Fe-S-Fe (1)	100.3 (3)
Fe-S-Fe (2)	65.8 (2)

4.2 Introduction to $Pr_2O_2Fe_2OSe_2$ in applied magnetic field

Ni *et al* reported a peak in heat capacity measurements at around 23 K and the ordering of Pr^{3+} moments at low temperatures for $Pr_2O_2Fe_2OSe_2$.[21] Earlier NPD data in McCabe group gave no evidence for any change in magnetic structure on cooling or for ordering of Pr^{3+} moments.[17] However, these data do indicate anisotropic peak broadening of (*h, 0, 0*) nuclear Bragg reflections below around 23 K, consistent with a subtle orthorhombic distortion. $Pr_2O_2Mn_2OSe_2$ has a similar behaviour but with a larger orthorhombic distortion below a similar temperature and no ordering of Pr^{3+} moments.[12] PrMnSbO and PrMnAsO have similar orthorhombic distortions related to the Pr^{3+} magnetism.[22,23] The Pr^{3+} ion is prone to lower the symmetry in structural distortions partly due to the 4*f* electron degrees of freedom, although it might not always be the case. [22,24] Lanthanide magnetism also has an effect on the magnetism of the transition metal sublattice, where the former orientates the Fe^{2+} spin in PrFeAsO and NdFeAsO.[25,26] In copper oxide superconducting layered materials, the electronic state of Pr^{3+} ions was vital to assess whether these materials will evolve on cooling leading to magnetic or non-magnetic ground states.[27,28] Therefore, research has been done to find different ways to couple the lanthanide and transition metal sublattices in layered systems.

4.2.1 Experimental

Data collected on an existing sample on WISH diffractometer in an applied magnetic field was given.[17]

4.2.2 Results and Discussions

Sequential Rietveld refinements in 5 T applied magnetic field show that the cell parameters decrease on cooling with *c* cell parameter decreasing more quickly and increasing slightly below 26 K (Figure 4.10). The behaviour of the *a* and *b* cell parameters is not similar to that observed in other $Ln_2O_2Fe_2OSe_2$ (*Ln*= La, Ce, Nd) materials.[5,11] Permitting the nuclear phase to undergo a subtle distortion from *I*4/*mmm* to *Immm* symmetry show a subtle orthorhombic distortion on cooling around 23 K (Figure 4.10a) analogous to the structural behaviour in zero-field. No additional peaks or diffraction peaks splitting are observed at low temperatures to support the orthorhombic distortion observed which is more subtle than similar distortions in analogous compounds.[12,22,23] This structural distortion could cause the peak at 23 K to be observed in the heat capacity measurements.[21]
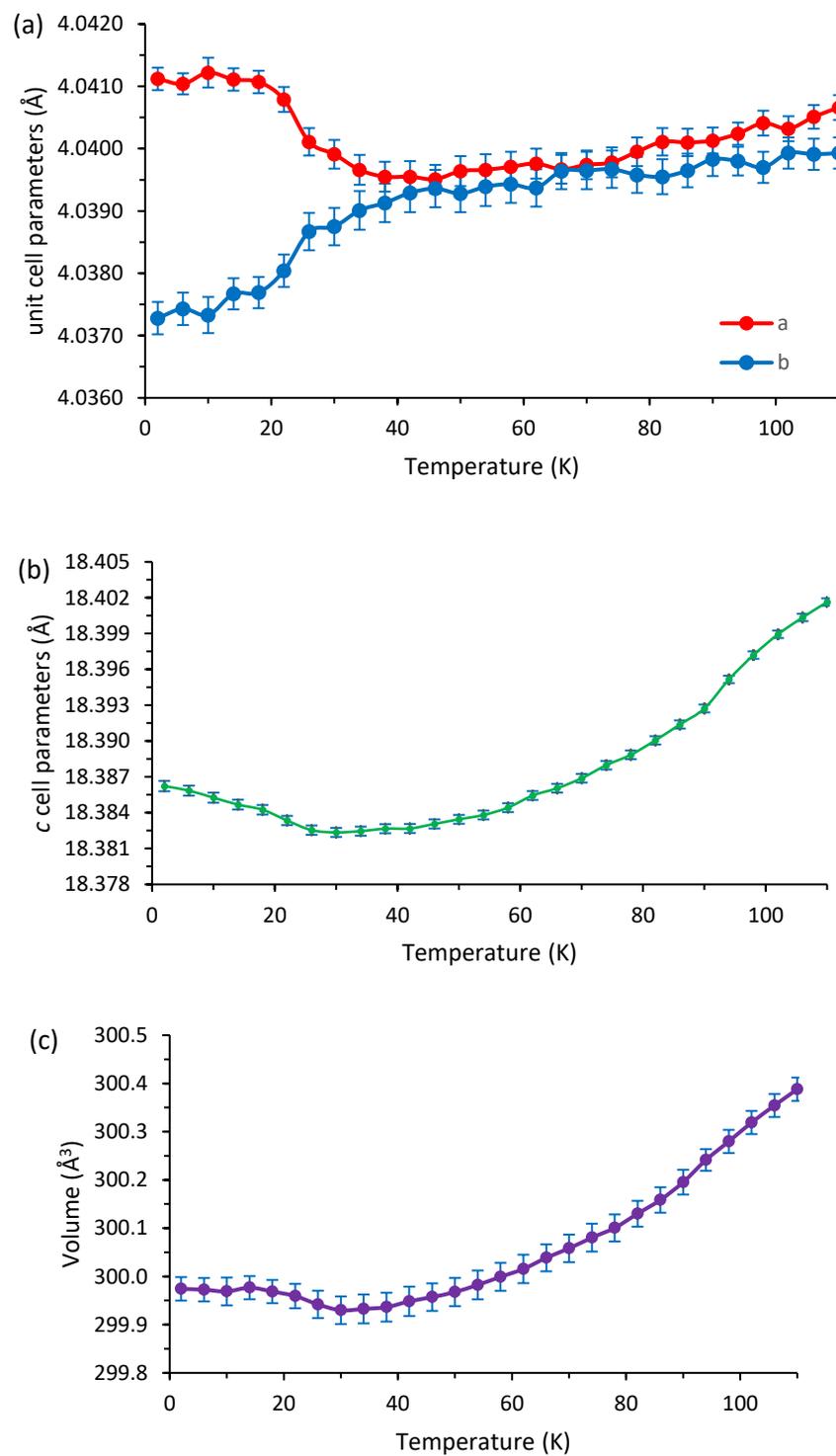
Figure 4.10 Unit cell parameters from sequential refinements using NPD data at 5T using bank 5 collected on warming for Pr$_2$O$_2$Fe$_2$OSe$_2$ showing (a) a (red) and b (blue) cell parameters (b) c cell parameter in green (c) unit cell volume against in purple. Error bars are in blue.

Sequential Rietveld refinements in increasing applied magnetic field at 2 K show *a* and *b* cell parameters approximately constant with applied field (Figure 4.11a) while *c* cell parameter slightly decreases (Figure 4.11b) which suggest that applied field barely changes the structure.
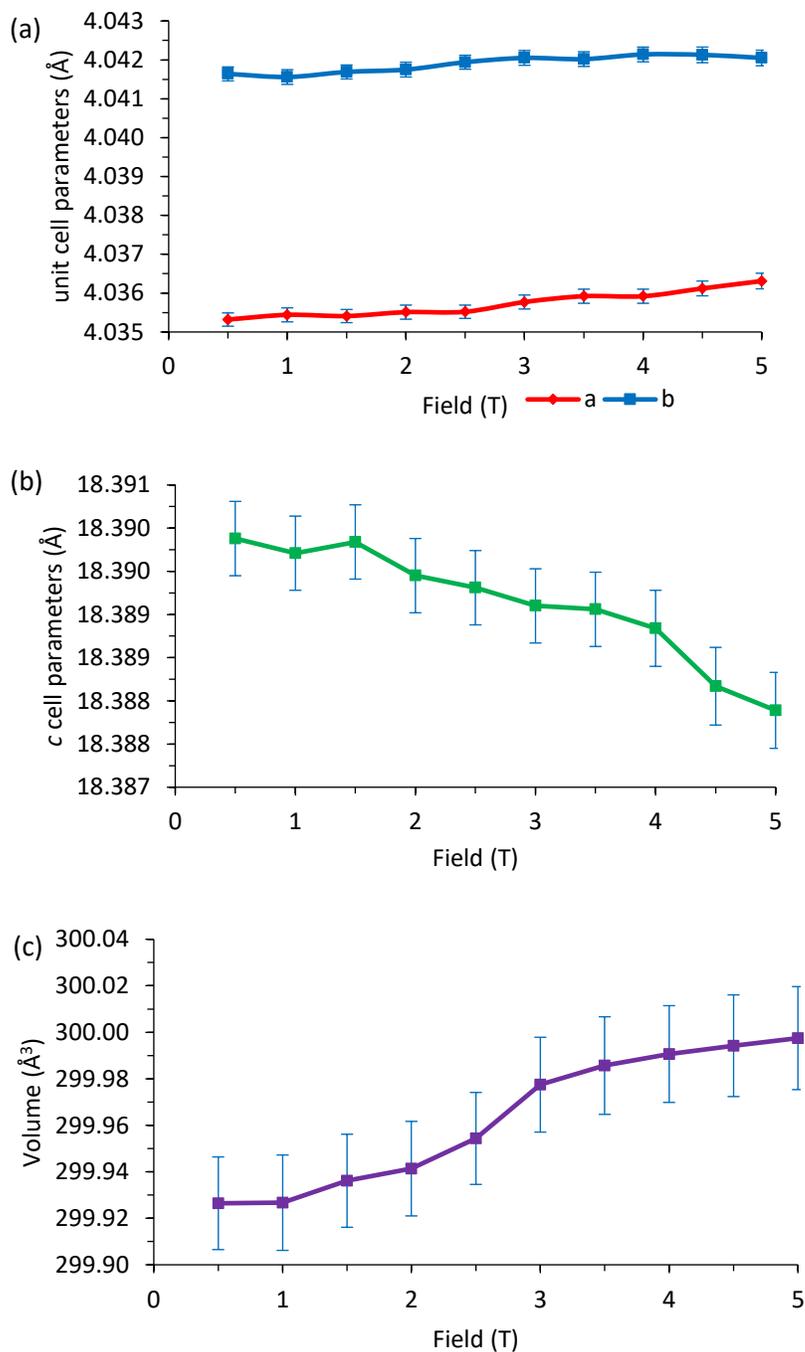
Figure 4.11 Unit cell parameters from sequential refinements using NPD data at 2 K (bank 5) as a function of applied magnetic field for $Pr_2O_2Fe_2OSe_2$ showing (a) *a* (red) and *b* (blue) cell parameters (b) *c* cell parameter (c) unit cell volume against. Error bars are in blue.

Between 23 K < T < T_N, the magnetic Bragg reflections observed on cooling, which increase in intensity, suggest there is 2-k magnetic order on the Fe^{2+} sublattice similar to $Ln_2O_2Fe_2OSe_2$ (Ln= La, Ce, Nd).[5,11] At T ≤ 23, the peak intensities change with some extra peaks appearing at 2 K when the applied magnetic field increases from 0 T to 5 T (Figure 4.12) (Appendix 4.08). The 2-k reflections broaden with applied magnetic field [e.g. (*0, 1, 7*), (*0, 1, 5*), (*0, 1, 3*), (*0, 1, 11*)] (Figure 4.13c) while new peaks appear which have different peak shapes from the other magnetic peaks (Figure 4.12). These new peaks [(*0, 2, 2*), (*0, 2, 6*), (*0, 0, 12*)] can be indexed in the nuclear unit cell at **k**= (0, 0, 0). The reflections and the intensities change with increasing applied magnetic fields (Figure 4.13).
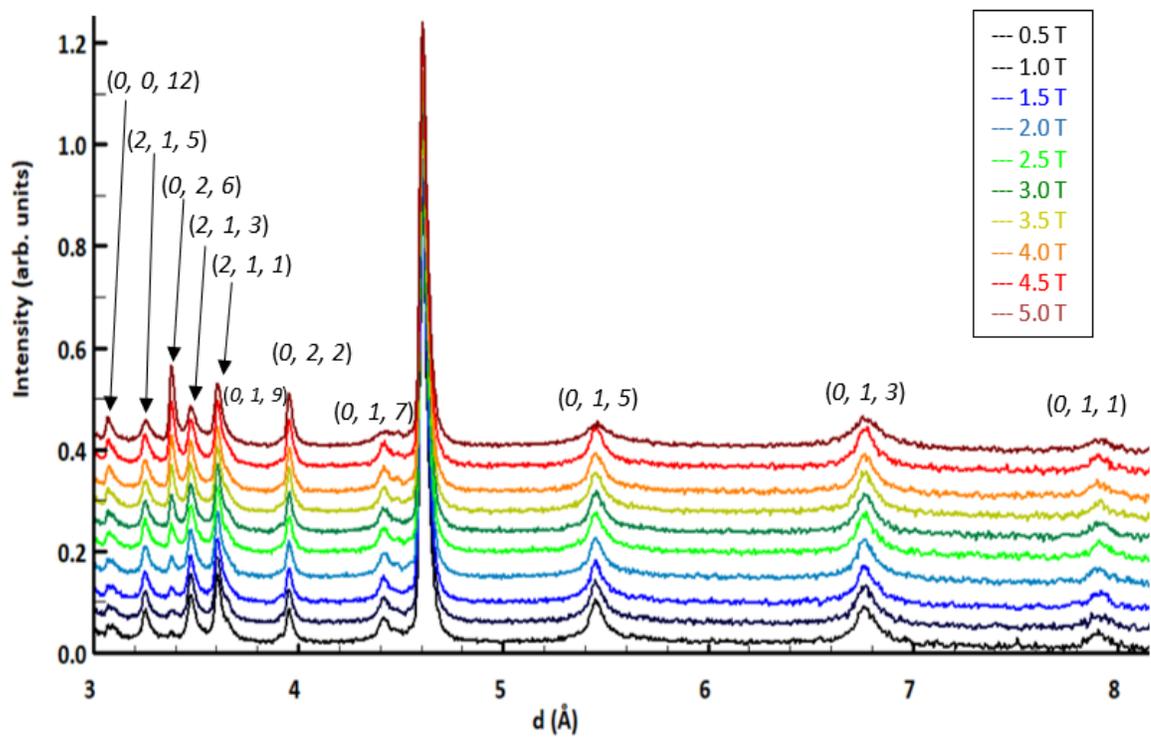
Figure 4.12 NPD data at 2 K using bank 2 showing evolution of new peaks and broadening of existing peaks with applied magnetic field for $Pr_2O_2Fe_2OSe_2$
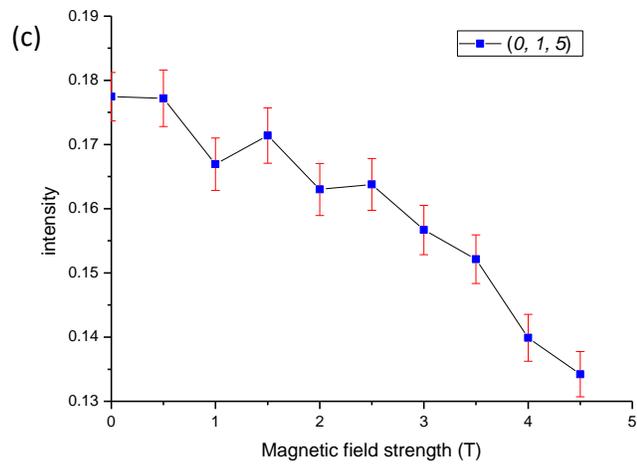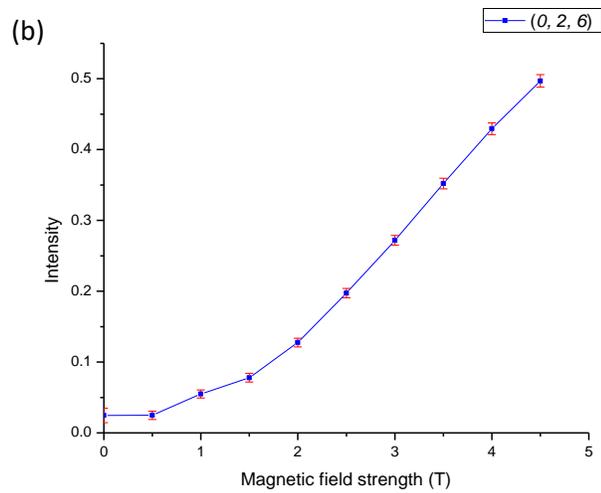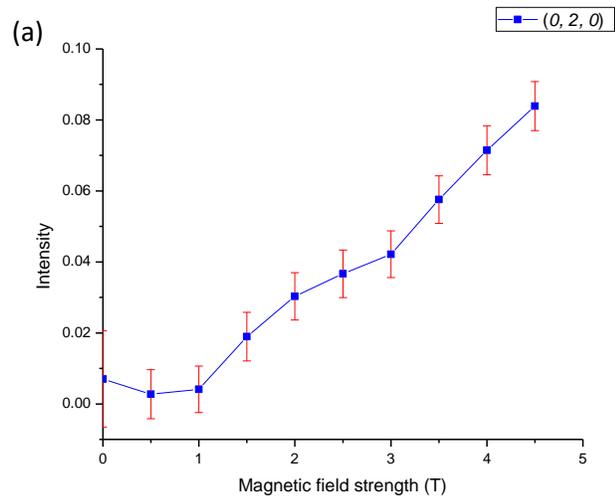
Figure 4.13 NPD data at 2 K using bank 2 showing examples of reflections' behaviours of (a) nuclear (b) new magnetic peaks (c) 2-k Fe with applied magnetic field for $Pr_2O_2Fe_2OSe_2$. Error bars are in red.

To find the magnetic structure of $Pr_2O_2Fe_2OSe_2$, ISODISTORT was used to get a description of the magnetic structure in terms of the nuclear structure with various symmetry-adopted magnetic modes imposed on it. Each imposed mode (displacive, site occupancies or structural distortion) causes a symmetry reduction by distorting the parent structure. The 'mode inclusion method' was used, where each mode is turned on individually and cycles of simulated annealing is performed, to compare the improvement in fit for various magnetic structures.[29] The value of the best result and the corresponding R_{wp} is outputted (Figure 4.14).

From the histogram, the modes with the lowest R_{wp} for Fe (1) are:

➢ mode 123 mS_1^- ($B_{2g(a)}$) (Figure 4.15a)
➢ mode 124 mS_1^- ($B_{2g(b)}$)
➢ mode 129 mR_2^+ ($B_{3g(a)}$) (Figure 4.15b)
➢ mode 130 mR_2^+ ($B_{3g(b)}$)

The modes with the lowest R_{wp} for Fe (2) are:

➢ mode 173 mS_2^+ ($B_{2g(a)}$) (Figure 4.15c)
➢ mode 174 mS_2^+ ($B_{2g(b)}$)
➢ mode 175 mR_1^- ($B_{3g(a)}$) (Figure 4.15d)
➢ mode 176 mR_1^- ($B_{3g(b)}$)

It is hard to differentiate between single k- and multi k- structures using powder neutron diffraction alone. However, it can be expected that the same moment exists per Fe site. Moreover, the magnetic structure can be modelled using either the 2-k model or the collinear model.[10] The former model is less frustrated with J_2 and $J_{2'}$ interactions satisfied (Figure 4.01) as discussed for $La_2O_2Fe_2OSe_2$ and $Sr_2F_2Fe_2OS_2$.[5,6] Hence, the modes 129 mR_2^+ ($B_{3g(a)}$) (Figure 4.15b) for Fe (1) and 173 mS_2^+ ($B_{2g(a)}$) (Figure 4.15c) for Fe (2) were chosen to act on the Fe sites to describe the 2-k magnetic order (Figure 4.01). This suggests no change in the magnetic order on the Fe^{2+} sublattice in an applied magnetic field.
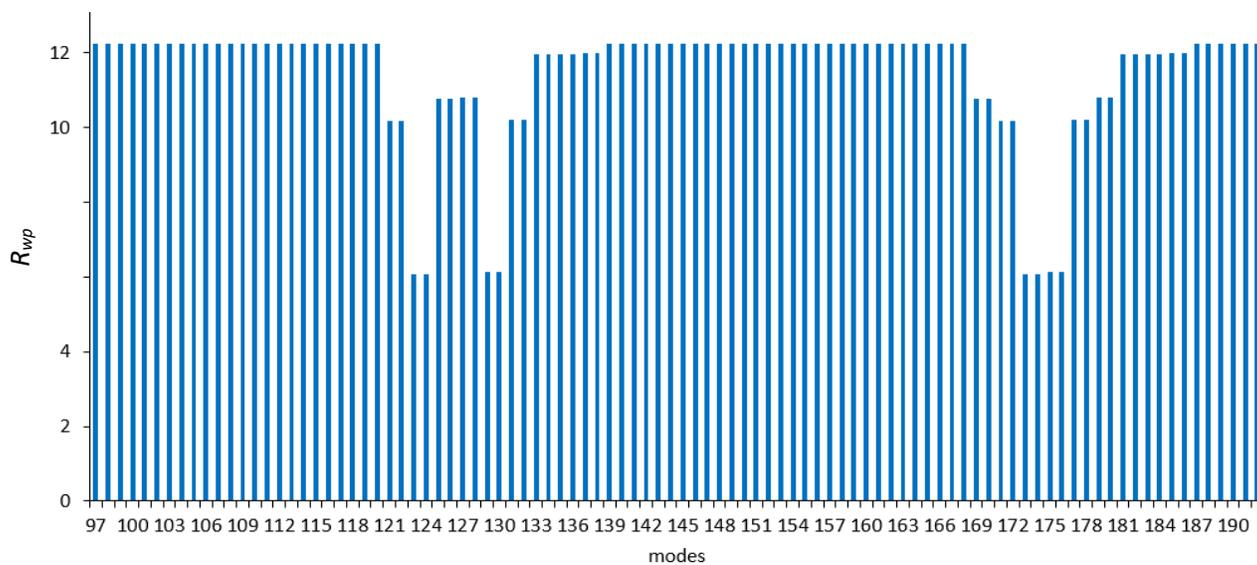
Figure 4.14 NPD data at 2 K in 5 T applied field using bank 2 showing R_{wp} for the different modes for Fe^{2+}.
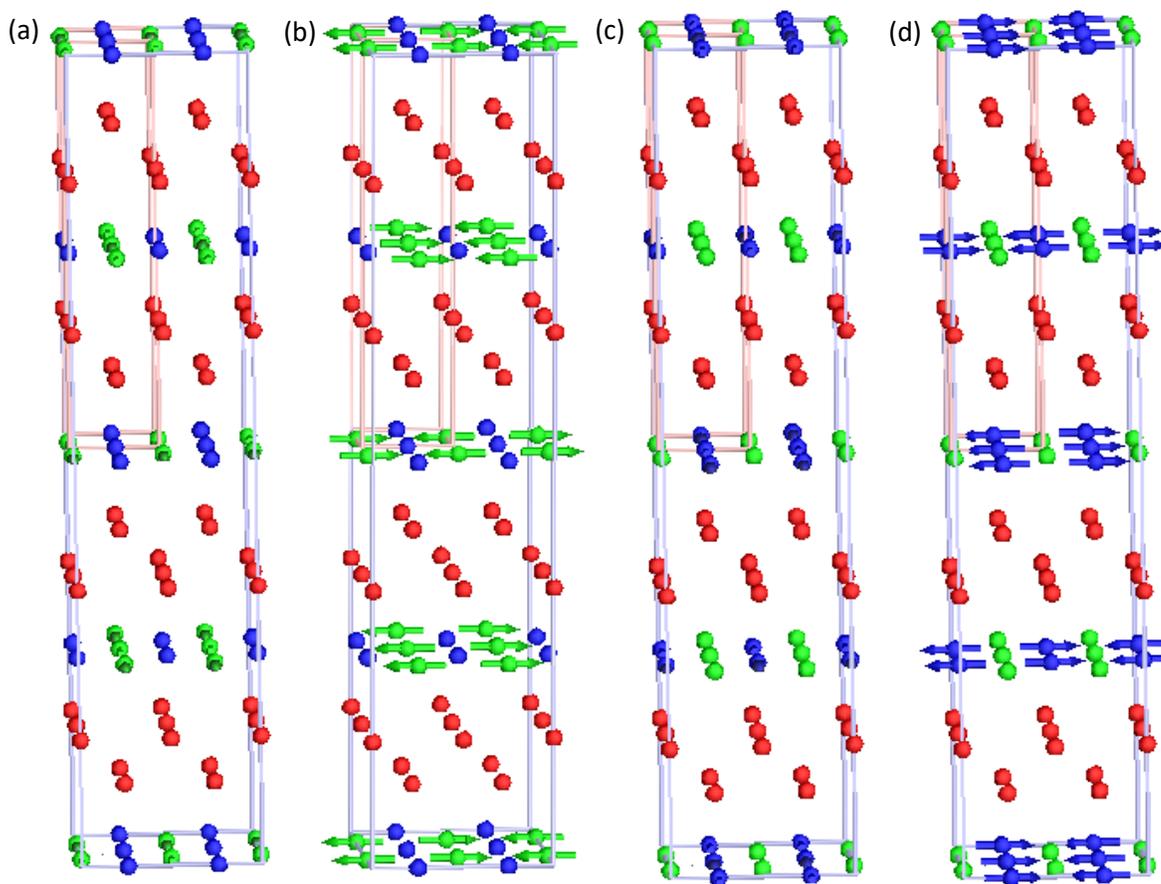
Figure 4.15 NPD data at 2 K 5 T using bank 2 used for Fe^{2+} mode inclusion in ISODISTORT, showing the magnetic moments behaviour when the modes with lowest R_{wp} is activated for Fe (1) (a) mS_1^- (b) mR_2^+ and for Fe (2) (c) mS_2^+ (d) mR_1^-. Pr^{3+}, Fe $(1)^{2+}$, Fe $(2)^{2+}$ magnetic moments shown in red, green and blue respectively.

At T<23 K, in 5 T applied magnetic field, extra peaks are not fitted by this model with the 2-k magnetic order on the Fe^{2+} sublattice (Appendix 4.09). Therefore, similar to the mode inclusion for Fe^{2+} 2-k order, ISODISTORT was used to consider changes to the magnetic structure. The 'mode inclusion method' was then used to compare the improvement in fit for various magnetic structures and the value of the best result and the corresponding R_{wp} is outputted.[29] ISODISTORT was used to get the mode inclusion for Pr^{3+} Gamma modes only (Figure 4.16) (Appendix 4.10). Only the first 6 modes are shown in the histogram. From the histogram, the modes with the lowest R_{wp} for Pr^{3+} are:

➢ 1 mGM_2^+ ($A_{2(a)}$) (Figure 4.17a)

➢ 2 mGM_3^+ ($B_{2(a)}$) (Figure 4.17b)

➢ 3 mGM_4^+ ($B_{1(a)}$) (Figure 4.17c)
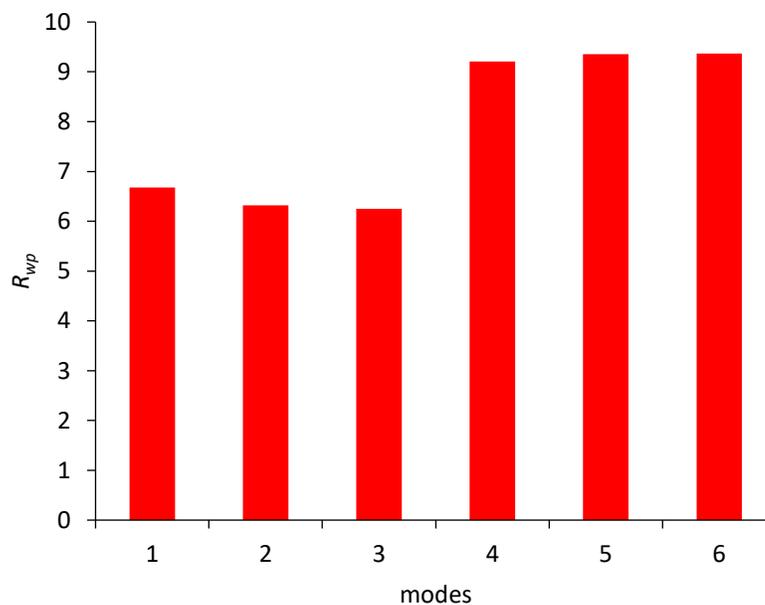
Figure 4.16 NPD data at 2 K 5 T using bank 2 showing R_{wp} for the different modes for Pr^{3+}.
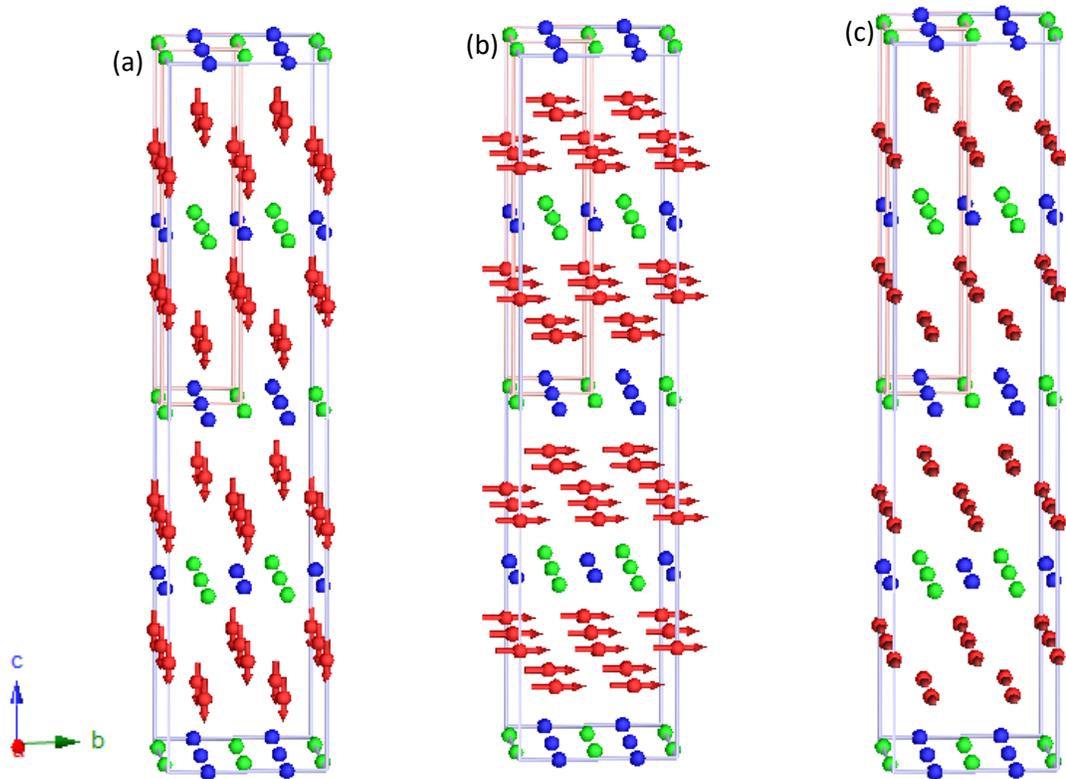
Figure 4.17 NPD data at 2 K 5 T using bank 2 used for Pr^{3+} mode inclusion in ISODISTORT, showing the magnetic moments behaviour when the modes with lowest R_{wp} is activated (a) m$GM2+$ (b) mGM_3^+ and (c) mGM_4^+. Pr^{3+}, Fe $(1)^{2+}$, Fe $(2)^{2+}$ magnetic moments shown in red, green and blue respectively.

The three different magnetic modes were not combined as they belong to different irreps and would not probably mix. The modes Γ_3^+ and Γ_4^+ correspond to Pr^{3+} moments along either the a axis or b axis and there is a very slight preference for one compared with the other due to the subtle orthorhombic distortion. Hence, it is hard to discriminate between these two modes, however, there is a very slight improvement in the fit (1.01 % decrease in R_{wp}) when Pr^{3+} moments are oriented along the shorter in-plane axis corresponding to Γ_3^+. Hence, the mode 2 [mGM_3^+ ($B_{2(a)}$)] (Figure 4.17b) was chosen to act on the Pr sites showing moments along the shorter in-plane axis (Appendix 4.09). Therefore, the modes for Pr^{3+} and Fe^{2+} were activated to give the magnetic structure (Figure 4.18) (Figure 4.19a). The fit to the peak shapes were poor [(*1, 0, 3*) at t.o.f = 70450, (*1, 0, 5*) at t.o.f = 56603, (*1, 0, 7*) at t.o.f = 45624]. Adding anisotropic broadening to the 2-k magnetic peaks improved the fit (Figure 4.19b). This improvement to the fit is similar to that in the above $La_2O_2Fe_2OS_2$, based on Clays and describing the stacking faults perpendicular to the c-plane in the 2-k ordering on the Fe sublattice, similar in $Ln_2O_2Fe_2OSe_2$ (Ln = La-Pr) systems.[5,11,30]
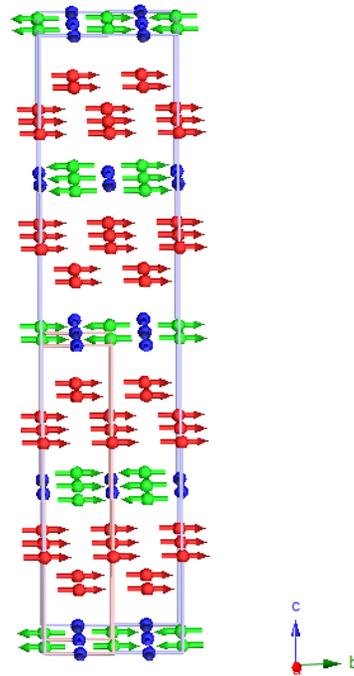
Figure 4.18 Magnetic order for $Pr_2O_2Fe_2OSe_2$ at 2 K in 5 T applied field using bank 2 showing their magnetic moments. Pr^{3+}, Fe $(1)^{2+}$, Fe $(2)^{2+}$ magnetic moments shown in red, green and blue respectively.
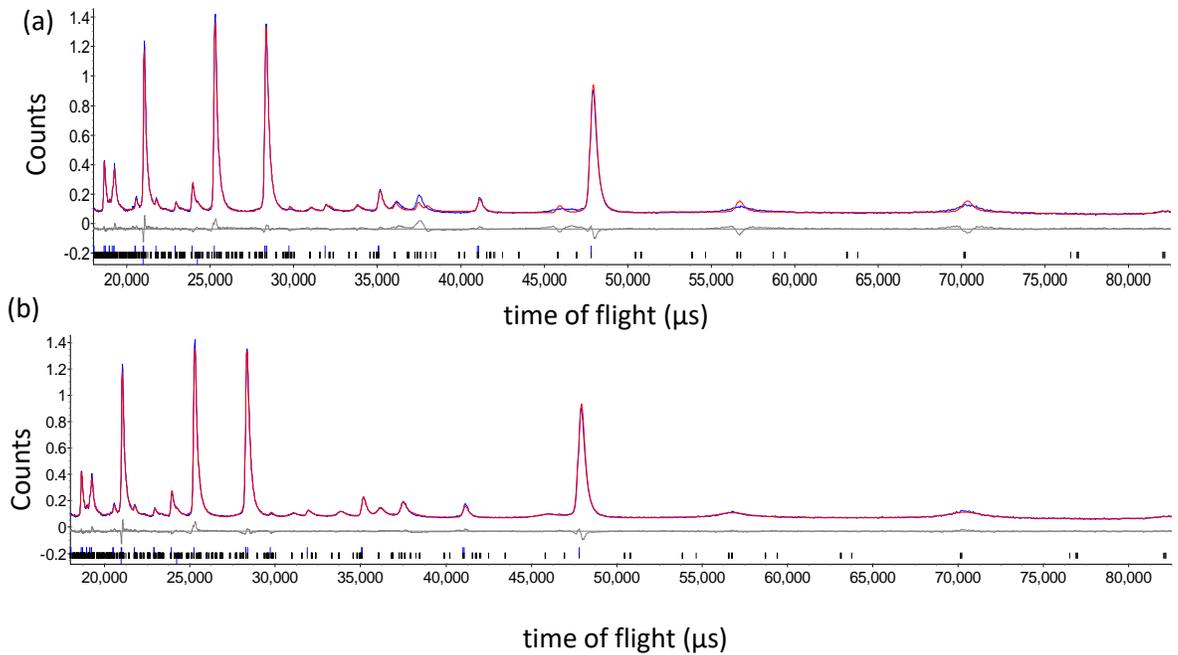
Figure 4.19 Rietveld refinement profiles using 2 K NPD data at 5 T applied magnetic field (a) without anisotropic peak broadening (b) with anisotropic peak broadening to 2-k magnetic peaks. The observed data is in blue, the calculated data is in red and the difference is in grey. Black ticks are magnetic reflections and blue ticks are nuclear reflections.

4.3 Conclusions

$La_2O_2Fe_2OS_2$ was successfully synthesised and characterised by XRPD. VT-NPD data showed a less rapid decrease in c cell parameter for $T<T_N$ than for other $Ln_2O_2M_2OSe_2$ (Ln = La-Pr and M = Mn, Fe, Co) systems but showed a similar broad asymmetric Warren-peak just above T_N as observed in other $Ln_2O_2Fe_2OSe_2$ (Ln = La-Pr) systems, typical of 2D short range order and consistent with SQUID measurements.[1,5,11–13] This Warren peak is shown to appear between both narrow (e.g. $La_2O_2Fe_2OSe_2$) and wide temperature ranges (e.g. $La_2O_2Mn_2OSe_2$ and $Sr_2F_2Fe_2OSe_2$).[5,6,14] VT-NPD data also showed that below T_N, additional magnetic Bragg reflections, whose intensity increase with decreasing temperature are observed. These reflections are consistent with a 2-k magnetic structure with a 2a x 2a x 2c unit cell and magnetic propagation vectors **k** = (*1/2, 0, 1/2*) and **k** = (*0, 1/2, 1/2*), similar to $Sr_2F_2Fe_2OSe_2$ and $La_2O_2Fe_2OSe_2$.[5,6] To obtain a better fit, the magnetic Bragg reflections in the NPD data were adjusted for anisotropic peak broadening, signifying stacking faults in $La_2O_2Fe_2OS_2$ which are similar to these in $Ln_2O_2Fe_2OSe_2$ (Ln = La-Pr) systems and absent in Mn_2O or Co_2O materials suggesting that the stacking faults are exclusive to the Fe_2O layers and might be affected by the separation between Fe_2O layers.[5,6,11,14,17–19]

Sequential Rietveld refinements of VT-NPD data of $Pr_2O_2Fe_2OSe_2$ in a 5 T applied magnetic field showed a rapid decrease in c cell parameter on cooling, similar to that observed in other $Ln_2O_2Fe_2OSe_2$ (Ln = La, Ce, Nd).[5,11] A subtle orthorhombic distortion (from $I4/mmm$ to $Immm$ symmetry) around 23 K was observed on cooling in both applied magnetic field and zero-field, which is less pronounced than in related manganese materials.[12,22,23] VT-NPD data also showed that between 23 K < T < T_N, the magnetic Bragg reflections increase in intensity on cooling suggesting 2-k magnetic order on the Fe^{2+} sublattice similar to $Ln_2O_2Fe_2OSe_2$ (Ln = La, Ce, Nd).[5,11] However, at T ≤ 23, additional peaks appear with increasing applied magnetic field, which can be indexed in the nuclear unit cell at **k** = (*0, 0, 0*) unit cell while the 2-k reflections broaden. ISODISTORT was used to get a description of the magnetic structure of $Pr_2O_2Fe_2OSe_2$ and the fit to the magnetic Bragg peak shapes was improved by adding anisotropic broadening, describing stacking faults in the magnetic ordering on the Fe^{2+} sublattice, common to all Fe_2O materials, but a much longer magnetic correlation length is observed for the Pr^{3+} ordering in applied magnetic field. [5,11]

4.4 References

1   J. M. Mayer, L. F. Schneemeyer, T. Siegrist, J. V Waszczak and B. Van Dover, *Angew. Chemie Int. Ed.*, 1992, **31**, 1645–1647.

2   Y. Fuwa, M. Wakeshima and Y. Hinatsu, *J. Phys. Condens. Matter*, 2010, **22**, 346003.

3   J. Goodenough, *Magnetism and the Chemical Bond*, John Wiley and Sons Inc., New York, 1963.

4   Y. Liu, S. B. Zhang, S. G. Tan, B. Yuan, X. C. Kan, L. Zu and Y. P. Sun, *J. Solid State Chem.*, 2015, **221**, 272–277.

5   E. E. McCabe, C. Stock, E. E. Rodriguez, A. S. Wills, J. W. Taylor and J. S. O. Evans, *Phys. Rev. B*, 2014, **89**, 100402.

6   L. L. Zhao, S. Wu, J. K. Wang, J. P. Hodges, C. Broholm and E. Morosan, *Phys. Rev. B*, 2013, **87**, 020406.

7   D. O. Charkin, V. A. Plotnikov, A. V Sadakov, O. E. Omel'yanovskii and S. M. Kazakov, *J. Alloys Compd.*, 2011, **509**, 7344–7348.

8   J. X. Zhu, R. Yu, H. Wang, L. L. Zhao, M. D. Jones, J. Dai, E. Abrahams, E. Morosan, M. Fang and Q. Si, *Phys. Rev. Lett.*, 2010, **104**, 216405.

9   M. A. Senaris-Rodriguez and J. B. Goodenough, *J. Solid State Chem*, 1995, **118**, 323–336.

10   D. G. Free and J. S. O. Evans, *Phys. Rev. B*, 2010, **81**, 214433.

11   E. E. McCabe, A. S. Wills, L. Chapon, P. Manuel and J. S. O. Evans, *Phys. Rev. B*, 2014, **90**, 165111.

12   D. G. Free, N. D. Withers, P. J. Hickey and J. S. O. Evans, *Chem. Mater.*, 2011, **23**, 1625–1635.

13   B. E. Warren, *Phys. Rev.*, 1941, **59**, 693–698.

14   N. Ni, E. Climent-Pascal, S. Jia, Q. Huang and R. J. Cava, *Phys. Rev. B*, 2010, **82**, 214419.

15   H. Kabbour, E. Janod, B. Corraze, M. Danot, C. Lee, M. H. Whangbo and L. Cario, *J. Am. Chem. Soc.*, 2008, **130**, 8261–8270.

16   J. H. Her, P. W. Stephens, Y. Gao, G. L. Soloveichik, J. Rijssenbeek, M. Andrus and J. C. Zhao, *Acta Crystallogr. Sect. B Struct. Sci.*, 2007, **63**, 561–568.

17   R. K. Oogarah, C. P. J. Stockdale, C. Stock, J. S. O. Evans, A. S. Wills, J. W. Taylor and E. E. McCabe, *Phys. Rev. B*, 2017, **95**, 174441.

18   Y. Fuwa, M. Wakeshima and Y. Hinatsu, *Solid State Commun.*, 2010, **150**, 1698–1701.

19   Y. Fuwa, T. Endo, M. Wakeshima, Y. Hinatsu and K. Ohoyama, *J. Am. Chem. Soc.*, 2010, **132**, 18020–18022.

20   R. D. Shannon, *Acta Crystallogr. Sect. A*, 1976, **32**, 751–767.

21   N. Ni, S. Jia, Q. Huang, E. Climent-Pascual and R. J. Cava, *Phys. Rev. B*, 2011, **83**, 224403.

22   S. A. J. Kimber, A. H. Hill, Y. Z. Zhang, H. O. Jeschke, R. Valentí, C. Ritter, I. Schellenberg, W. Hermes, R. Pöttgen and D. N. Argyriou, *Phys. Rev. B*, 2010, **82**, 100412.

23   E. J. Wildman, F. Sher and A. C. McLaughlin, *Inorg. Chem.*, 2015, **54**, 2536–2542.

24   E. J. Wildman and A. C. Mclaughlin, *Sci. Rep.*, 2016, **6**, 20705.

25   D. Bhoi, P. Mandal, P. Choudhury, S. Pandya and V. Ganesan, *J. Appl. Phys.*, 2011, **110**, 113722.

26   W. Tian, W. Ratcliff, M. G. Kim, J. Q. Yan, P. A. Kienzle, Q. Huang, B. Jensen, K. W. Dennis, R. W. McCallum, T. A. Lograsso, R. J. McQueeney, A. I. Goldman, J. W. Lynn and A. Kreyssig, *Phys. Rev. B*, 2010, **82**, 060514.

27   G. Hilscher, E. Holland-Moritz, T. Holubar, H. D. Jorstarndt, V. Nekvasil, G. Schaudy, U. Walter and G. Fillion, *Phys. Rev. B*, 1994, **49**, 535–550.

28   H. D. Jortardnt, U. Walter, J. Harnischmacher, J. Kalenborn, A. Severing and Hollan, *Phys. Rev. B*, 1992, **46**, 14872–14882.

29   A. J. Tuxworth, E. E. Mccabe, D. G. Free, S. J. Clark and J. S. O. Evans, *Inorg. Chem.*, 2013, **52**, 2078–2085.

30   A. S. Bookin, *Clays Clay Miner.*, 1989, **37**, 297–307.

Chapter 5: La$_{1-x}$$M_x$GaOS$_2$ (M = Nd, Ce)

<u>5.1 Introduction</u>

LaGaOS$_2$ crystallises in the *Pmca* space group [a = 5.5419 (9) Å, b =5.767 (1) Å c =11.443 (1) Å] (Figure 5.01) and has a KVO$_3$-type structure. It consists of double chains of corner linked tetrahedra (GaO$_2$S$_2$) which extend along the *a*-axis with La^{3+} cations separating these chains along the *c*-axis. Ga^{3+} is in distorted tetrahedra coordinated by oxygen and the sulfur atoms. La^{3+} is coordinated by 2 oxygen atoms and 8 sulfur atoms in a high coordination environment. The oxygen atom is at the centre of a distorted tetrahedra consisting of 2 La atoms and 2 Ga atoms.[1]

This structure is different from LaGaOSe$_2$ where the material crystallises in the *P*2$_1$*ab* space group and consists of (LaO) layers and (GaSe$_2$) layers.[2] Other members of the series of *Ln*GaO*X*$_2$ (*Ln* = Lanthanides and *X* = S, Se) have not been reported. LaGaOSe$_2$ adopts a structure similar to La$_4$O$_4$Ga$_{1.72}$S$_{4.58}$, La$_4$O$_4$Ga$_{1.88}$Se$_{4.82}$, Ce$_4$O$_4$Ga$_2$S$_5$ and La$_4$O$_4$As$_2$S$_5$.[3–5] Nd$_4$O$_4$Ga$_2$S$_5$ has a different structure whereby the NdO layers and Ga$_2$S$_5$ layers are distorted thus creating an undulating structure.[6]

LaGaOS$_2$ has been reported to be an n-type semiconductor with an optical band gap of 3.0 eV and a potential photocatalyst for reducing and oxidising water. The optical band gaps in La-Ga based oxysulfides have been shown to decrease with increasing sulfur content.[7] Photocatalysts usually have d^0 or d^{10} electronic configurations and the bottom of the conduction band should be high enough to reduce H$^+$ to H$_2$.[7–11] It is possible for the *Ln* 4f orbitals to mix with the S 3p and O 2p orbitals and contribute to the photocatalytic activities.[10] However, there is no direct link of different lanthanide analogues and their photocatalytic activities and between H$_2$ evolution and the location of the conduction band.[10,12–16] Ga- and In- based compounds have been reported as photocalysts.[7,17–19]

 Recent theoretical studies of LaGaOS$_2$ and similar compounds have shown that the occupied bands are made up of Ga (4s and 4p), O (2p), and S (3p) orbitals in the valence bands and of La (5d) and Ga (4s and 4p) orbitals in the conduction band with a band gap of 2.20 eV (DFT calculations tend to underestimating band gap values).[20] In the valence band, the O 2p and S 3p orbitals overlap with S 3p orbitals at the top of the valence band and O 2p orbitals at the bottom while the valence band maximum is preferably localized on sulfur.[7,10,20] The *Ln* (*Ln* = La-Pr) 4f orbitals can be found at the

top of the valence band and bottom of the conduction band. However, these 4f orbitals are quite localized making the overlap between 4f orbitals relatively small and hence do not mix with O 2p and S 3p orbitals, therefore, lowering the 4f orbital energy.[10] Oxysulfides band structure calculations in Ln_2O_2S have shown that the valence band consists of a mixture of S and O orbitals.[21–23] Density functional theory (DFT) calculations also suggest that oxysulfides are more stable than sulfides in terms of oxidation reactions and this is attributed to differences in the electronic band structure.[10,24]
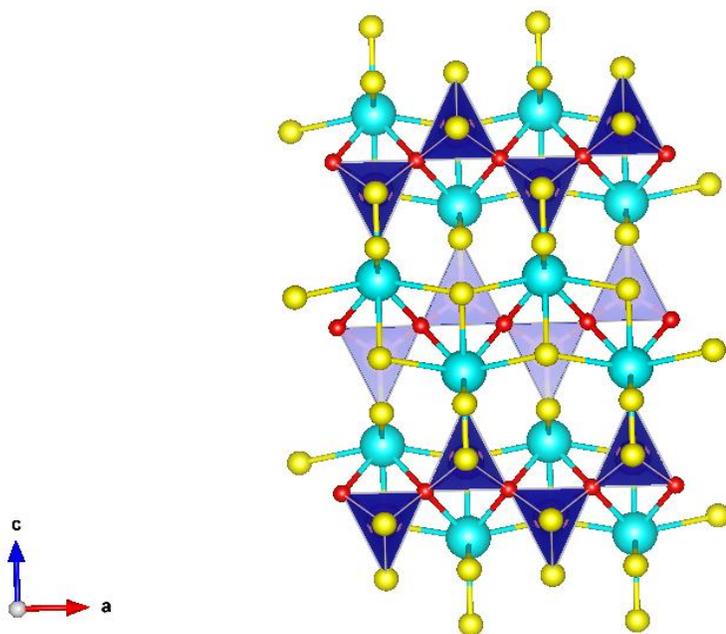
Figure 5.01 KVO$_3$-type structure of LaGaOS$_2$ with lanthanum ions in aqua, gallium ions in pink, oxygen ions in red and sulfur ions in yellow.

The aims of this work are to dope LaGaOS$_2$ by substituting isovalent dopants (Nd^{3+}/Ce^{3+} ions) onto the La site and to investigate the resulting changes in structure and physical properties.

This chapter deals with the synthesis and properties of La$_{1-x}M_x$GaOS$_2$ (M = Nd, Ce) series of compounds, focusing on their structures, optical band gaps and electronic states of the elements. Structures were characterised using X-ray powder diffraction (XRPD) complemented by Rietveld refinement, Scanning Electron Microscopy-Energy Dispersive X-ray (SEM-EDX) for homogeneity, Diffuse Reflectance Spectroscopy (DRS) for band gap measurements and X-ray Photoelectron Spectroscopy (XPS) for the electronic states.

5.2 Results

5.2.1 LaGaOS$_2$

5.2.1.1 Synthesis and Structural characterisation

LaGaOS$_2$ was prepared from stoichiometric amounts of La$_2$O$_3$ (Sigma-Aldrich, 99.99%), Ga$_2$O$_3$ (Sigma-Aldrich, 99.99%) and S (Alfa-Aesar, 99.5%+) as discussed in Chapter 2.1. The starting reagents were weighed in a 1:1:4 ratio and ground using a mortar and pestle in the fume cupboard. The mixture was then put in an alumina crucible and placed in a quartz tube. Titanium powder was used as an oxygen getter and placed in an alumina crucible. The latter was placed on top of the sample crucible, sealed under vacuum and heated in a furnace at the following conditions: ramped to 400°C at 2°C/min and dwelled for 6 hours, ramped to 800°C at 0.5°C/min and dwelled for 1 hour, ramped to 900°C at 1°C/min and dwelled for 12 hours. The sample was then quenched into iced water. This synthesis gave a highly crystalline sample with no impurity phase (Figure 5.02). The purity of the sample, confirmed by SEM-EDX (Appendix 5.01), suggested LaGa$_{1.13\pm0.20}$S$_{1.58\pm0.12}$ (normalised to La).

5.2.1.2 X-ray powder diffraction

The resulting pale-grey pellet was then analysed by in-house X-ray powder diffraction (Figure 5.02). The refinement was performed as described in Chapter 2.2.2. The only deviations applied to the refinement were an 11th order Chebychev polynomial function which was employed to fit the background and 9 atomic positions: y coordinates for O and y and z coordinates for La, Ga, S (1) and S (2) of the main phase. The R_{wp} for the refinement was 11.48 %, the χ^2 was 2.40. Data for some of the relevant parameters are shown in Table 5.01.

When looking at the XRPD pattern, there were some shoulders to the peaks (Figure 5.02a). Impurities were checked for but there were not any present. The pattern was fitted well by a model containing two LaGaOS$_2$-like phases with slightly different lattice parameters (First phase: 91.74 ± 0.87 % and second phase: 8.26 ± 0.87 %) (Figure 5.02b). No composition differences could be observed between the two LaGaOS$_2$ phases. Data is in good agreement with literature (Table 5.01).[1]
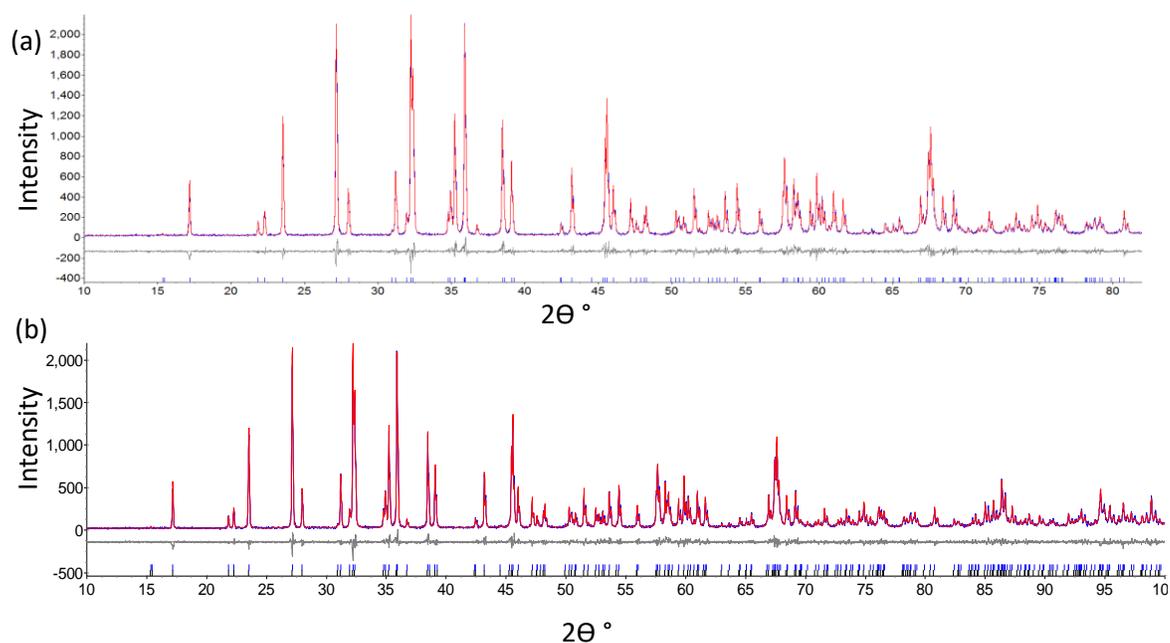
Figure 5.02 Rietveld refinement profiles for LaGaOS$_2$ using room temperature XRPD data using (a) only one LaGaOS$_2$ phase (b) two LaGaOS$_2$-like phases giving R_{wp} = 11.48 %, Rp= 8.72 % and χ^2= 2.40. The observed data is in blue and black, calculated data is in red and the difference is in grey. The blue vertical tick marks show the predicted peak positions for LaGaOS$_2$ (91.74 ± 0.87 %) and the black ones show those for the second LaGaOS$_2$ phase (8.26 ± 0.87 %).

Table 5.01 Data for room temperature Rietveld refinement for LaGaOS$_2$ together with values from the literature and LaGaOSe$_2$ for comparison.

LaGaOS$_2$	This work	Jaulmes[1]	Bénazeth et al[2]
Space group	*Pmca*	*Pmca*	*P21ab*
a cell parameter (Å)	5.552349 (6)	5.5419 (9)	5.951 (3)
b cell parameter (Å)	5.774507 (0)	5.767 (1)	5.963 (3)
c cell parameter (Å)	11.46058 (1)	11.443 (1)	12.256 (7)
Volume (Å^3)	367.450 (6)	365.72	434.9 (7)
La *y* coordinate (c)	0.14894 (7)	0.14976 (7)	
La *z* coordinate (c)	0.10775 (1)	0.10759 (4)	
Ga *y* coordinate (c)	0.52052 (6)	0.5200 (1)	
Ga *z* coordinate (c)	0.33564 (9)	0.33565 (7)	
S (1) *y* coordinate (c)	0.65581 (1)	0.6567 (3)	
S (1) *z* coordinate (c)	0.01162 (5)	0.0112 (2)	
S (2) *y* coordinate (c)	0.09650 (9)	0.0971 (3)	
S (2) *z* coordinate (c)	0.84614 (7)	0.8449 (2)	
O *y* coordinate (c)	0.37854 (6)	0.3771 (8)	

5.2.1.3 Diffuse Reflectance Spectroscopy

Diffuse Reflectance Spectroscopy data were collected, as described in Chapter 2.2.8 to ascertain the optical band gap of the pale-grey powder. A Kubelka–Munk transformation was performed on the data.[25] The band gap value is where the positive gradient of the extrapolated line of the absorption edge crosses the x-axis. Hence, the value obtained for $LaGaOS_2$ is 3.06 ± 0.32 eV (Figure 5.03). This band gap value explains the pale-grey colour of the powder. This is consistent with literature (3.0 eV).[7] This value is similar to that of LaCuOS (3.26 eV) and higher than $LaInOS_2$ (2.73 eV).[26,27]
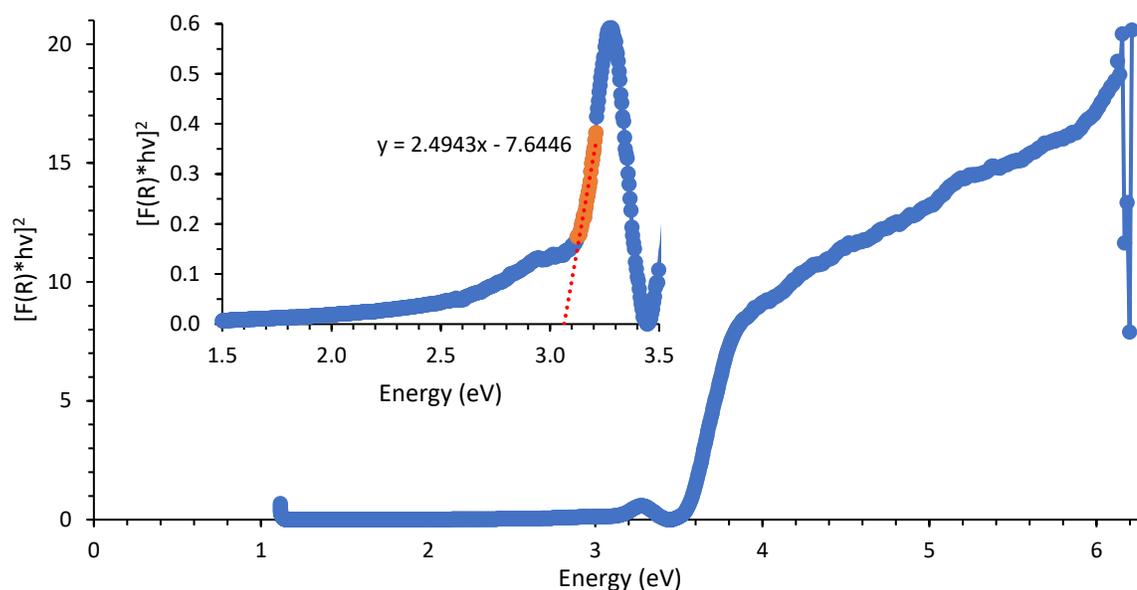
Figure 5.03 Plot of $[F(R)*hv]^2$ against energy for $LaGaOS_2$ giving a band gap value of 3.06 eV. Data is shown in blue. Line of best fit to positive curve is shown in dotted red.

5.2.1.4 X-ray Photoelectron Spectroscopy

XPS data were collected as described in Chapter 2.2.5, in collaboration with Dr R.Palgrave (UCL) to ascertain the electronic states of the elements present in the pale-grey material. The S 2p data (Figure 5.04) shows that nearly all the sulfur is present as sulfide. Moreover, there is more oxygen on the surface than sulfur.
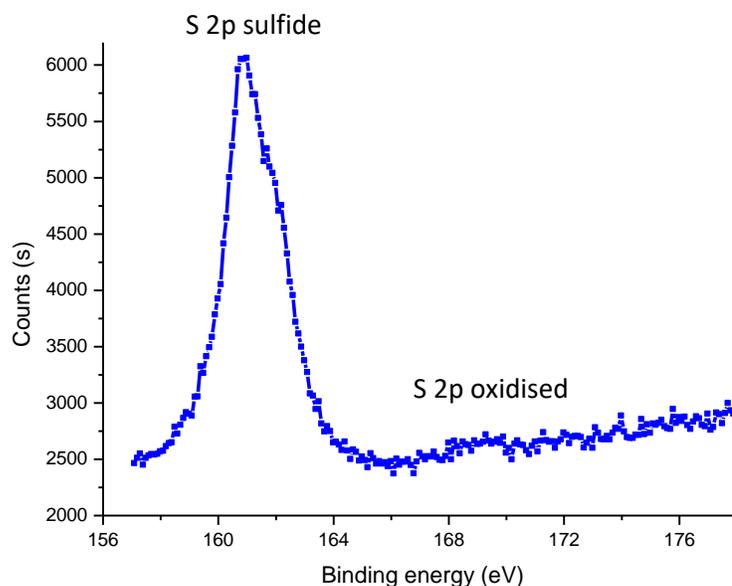
Figure 5.04 Plot of counts against energy for S 2p for LaGaOS$_2$. Data is shown in blue.

5.2.2 La$_{1-x}$Nd$_x$GaOS$_2$

5.2.2.1 Synthesis

La$_{1-x}$Nd$_x$GaOS$_2$ (0 ≤ x ≤ 0.1) was prepared from stoichiometric amounts of La$_2$O$_3$ (Sigma-Aldrich, 99.99%), Ga$_2$O$_3$ (Sigma-Aldrich, 99.99%), S (Alfa-Aesar, 99.5%+) and Nd$_2$O$_3$ (Acros Organics, 99.9%) using the method described in 5.2.1.1. The only deviation was furnace cooling the doped samples instead of quenching (main phase present between 76% - 97% with La$_4$O$_4$Ga$_{1.72}$S$_{4.58}$ present as impurity in every sample when quenched).

5.2.2.2 X-ray powder diffraction

The resulting powders were then analysed by Rietveld refinement (Figure 5.05). The amorphous background seen between 5° and 20° was due to air scattering of the X-rays. A small impurity phase of La$_4$O$_4$Ga$_{1.72}$S$_{4.58}$ was present in the last 2 samples (x = 0.07 and x = 0.10). The refinement was performed as described in 5.2.1.2. The model used for the data fitting only required one LaGaOS$_2$-like phase. Data for some of the relevant parameters for La$_{1-x}$Nd$_x$GaOS$_2$ (0 ≤ x ≤ 0.1) are shown in Table 5.02.
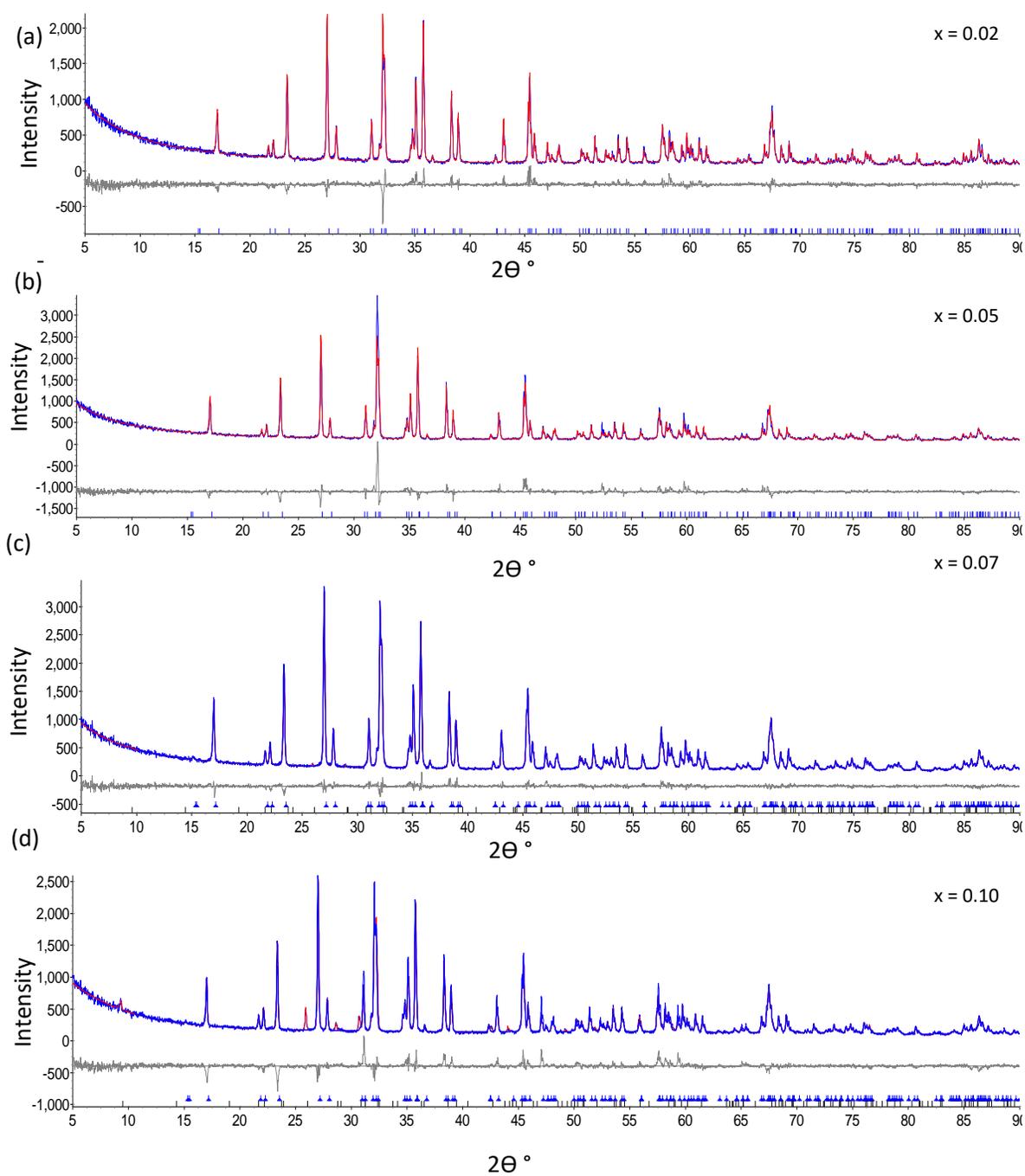
Figure 5.05 Rietveld refinement profiles for $La_{1-x}Nd_xGaOS_2$ ($0 \leq x \leq 0.1$) using room temperature XRPD data (a) x = 0.02 (b) x = 0.05 (c) x = 0.07 and (d) x = 0.10. The observed data is in blue, the calculated data is in red and the difference is in grey. The blue vertical tick marks show the predicted peak positions for $LaGaOS_2$ and the black vertical tick marks show those for $La_4O_4Ga_{1.72}S_{4.58}$. R_{wp} and the χ^2 values are given in table 5.02.

Table 5.02 Data for room temperature Rietveld refinement for $La_{1-x}Nd_xGaOS_2$ ($0 \leq x \leq 0.1$). 36 parameters were used for the refinements.

$La_{1-x}Nd_xGaOS_2$	X = 0	X = 0.02	X = 0.05	X = 0.07	X = 0.10
a (Å)	5.552349 (6)	5.551114 (9)	5.550261 (4)	5.547517 (6)	5.548512 (7)
b (Å)	5.774507 (0)	5.772486 (6)	5.772406 (2)	5.768646 (3)	5.769098 (9)
c (Å)	11.46058 (1)	11.454522 (4)	11.453680 (9)	11.443122 (9)	11.440680 (5)
Volume (Å^3)	367.450 (6)	367.046 (1)	366.957 (8)	366.199 (1)	366.215 (7)
La y coordinate (c)	0.14894 (7)	0.14848 (7)	0.15062 (4)	0.14897 (0)	0.14830 (3)
La z coordinate (c)	0.10775 (1)	0.10630 (8)	0.10883 (2)	0.10774 (3)	0.10835 (3)
Ga y coordinate (c)	0.52052 (6)	0.51949 (6)	0.52218 (8)	0.51887 (0)	0.52002 (9)
Ga z coordinate (c)	0.33564 (9)	0.33478 (0)	0.33745 (8)	0.33603 (2)	0.33639 (7)
S (1) y coordinate (c)	0.65581 (1)	0.65583 (5)	0.66467 (6)	0.65932 (8)	0.66241 (5)
S (1) z coordinate (c)	0.01162 (5)	0.01127 (3)	0.00979 (8)	0.01202 (9)	0.01583 (7)
S (2) y coordinate (c)	0.09650 (9)	0.09282 (6)	0.09000 (0)	0.09036 (7)	0.09018 (1)
S (2) z coordinate (c)	0.84614 (7)	0.84603 (7)	0.85302 (1)	0.84565 (1)	0.84852 (0)
O y coordinate (c)	0.37854 (6)	0.38061 (3)	0.35961 (4)	0.38487 (3)	0.40122 (0)
R_{wp} (%)	11.48	9.10	11.85	7.38	10.69
χ^2	2.40	2.80	3.70	2.44	3.44
$La_4O_4Ga_{1.72}S_{4.58}$ (%)	-	-	-	0.79 ± 0.15	8.22 ± 0.46

$La_{1-x}Nd_xGaOS_2$ with higher Nd content (x > 0.1) were also synthesised but they did not produce the main phase and instead had $La_4O_4Ga_{1.72}S_{4.58}$ as the main phase together with other impurities (GaS, $NdGaO_3$ and $LaGaO_3$). The samples were then overlaid on top of one another to check for any differences (Figure 5.06).
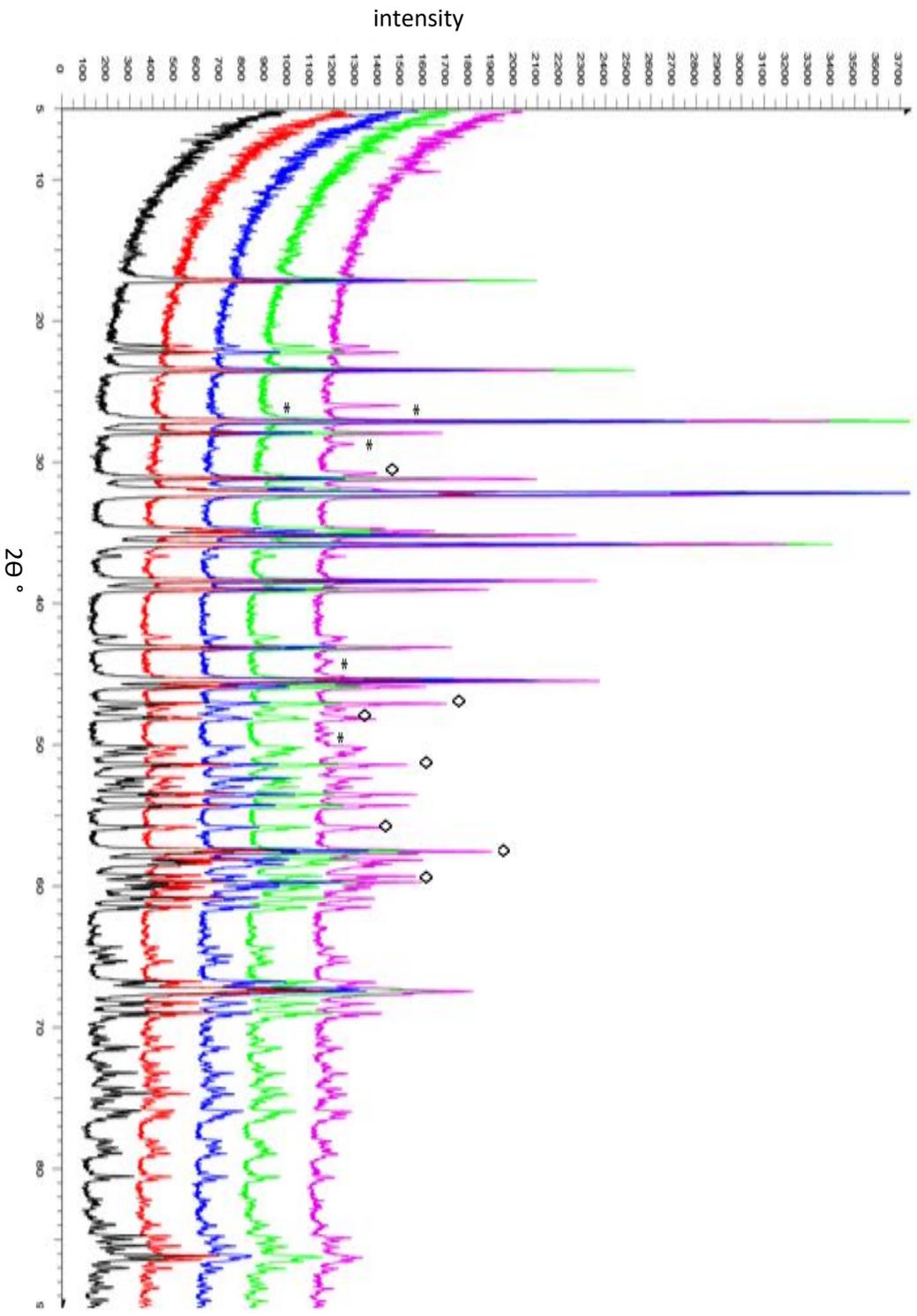
Figure 5.06 Overlay of room temperature XRPD data for $La_{1-x}Nd_xGaOS_2$. x=0 (black, bottom) to x=0.1 (pink, top). $LaGaOS_2$ is in black, $La_{0.98}Nd_{0.02}GaOS_2$ is in red, $La_{0.95}Nd_{0.05}GaOS_2$ is in blue, $La_{0.93}Nd_{0.07}GaOS_2$ is in green and $La_{0.9}Nd_{0.1}GaOS_2$ is in pink. * denotes the impurity phase $La_4O_4Ga_{1.72}S_{4.58}$. ◊ denotes the peaks which increase in intensity with increasing Nd doping concentrations in $La_{1-x}Nd_xGaOS_2$ (0 ≤ x ≤ 0.1).

a cell parameter v/s x doping concentration

a cell parameter (Å)

5.557
5.555
5.553
5.551
5.549
5.547

0   0.02   0.04   0.06   0.08   0.1

x doping concentration

— LaGaOS2 (1)
— LaGaOS2 (2)

(b) **b cell parameter v/s x doping concentration**

b cell parameter (Å)

5.780
5.778
5.776
5.774
5.772
5.770
5.768

0   0.02   0.04   0.06   0.08   0.1

x doping concentration

— LaGaOS2 (1)
— LaGaOS2 (2)

(c)

c cell parameter v/s x doping concentration

c cell parameter (Å)

11.470
11.465
11.460
11.455
11.450
11.445
11.440

0   0.02   0.04   0.06   0.08   0.1

x doping concentration

— LaGaOS2 (1)
— LaGaOS2 (2)

(d)

Volume v/s x doping concentration

Volume (Å^3)

368.5
368.1
367.7
367.3
366.9
366.5
366.1

0   0.02   0.04   0.06   0.08   0.1

x doping concentration

— LaGaOS2 (1)
— LaGaOS2 (2)

Figure 5.07 (a) Unit cell parameter *a* [LaGaOS$_2$ (1) in red and LaGaOS$_2$ (2) in dark red]*,* (b) unit cell parameter *b* [LaGaOS$_2$ (1) in pale pink and LaGaOS$_2$ (2) in dark pink], (c) unit cell paramet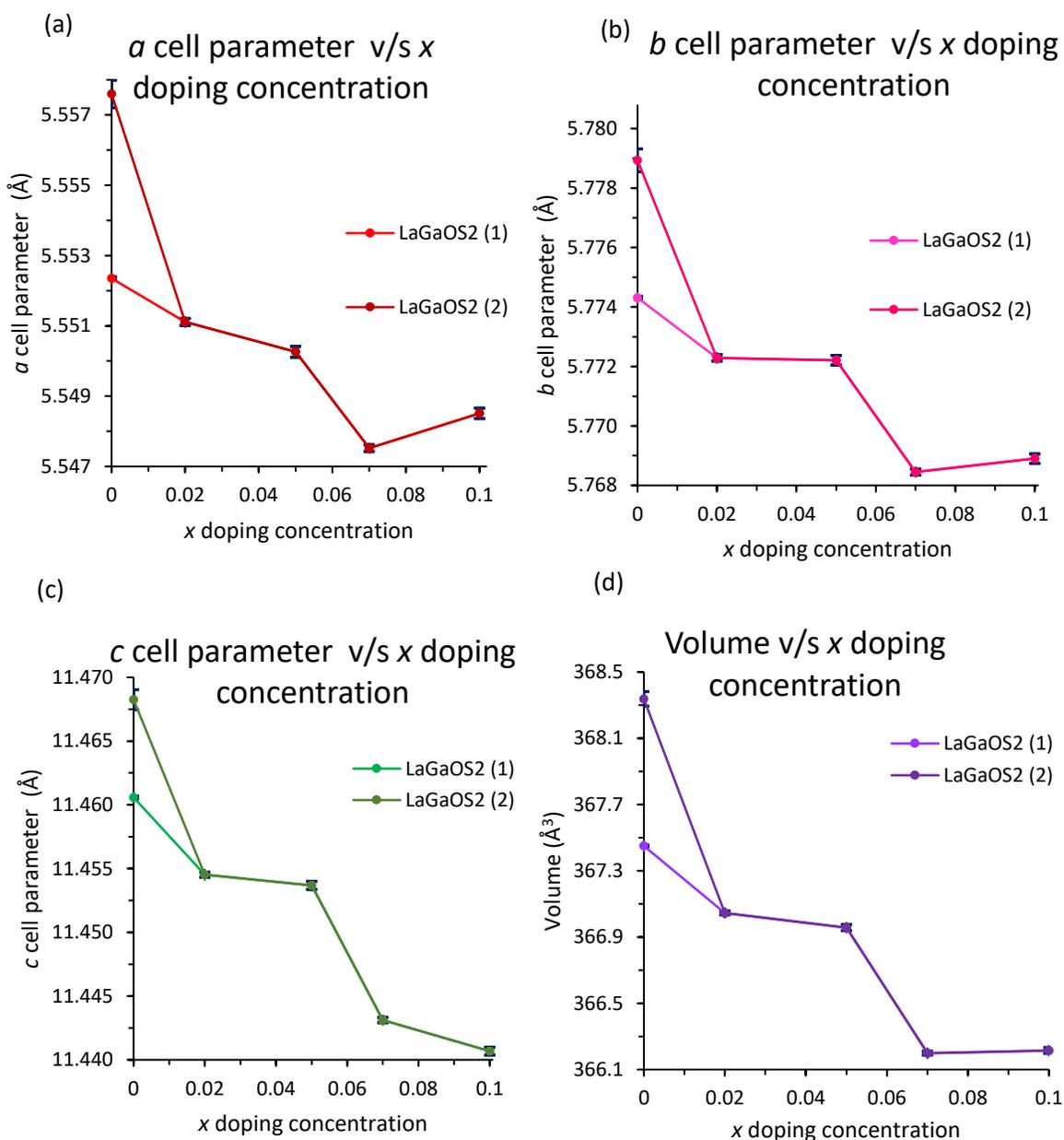er *c* [LaGaOS$_2$ (1) in green and LaGaOS$_2$ (2) in dark green] and (d) volume [LaGaOS$_2$ (1) in pale purple and LaGaOS$_2$ (2) in dark purple] as a function of *x* for La$_{1-x}$Nd$_x$GaOS$_2$ determined from Rietveld refinements using room temperature XRPD data. Error bars in blue. The main primary phase and the secondary phase of the undoped sample are described as LaGaOS$_2$ (1) and LaGaOS$_2$ (2) respectively.

There are few changes in structure with dopant level (Appendix 5.02). The overall trend is a slight decrease in unit cell volume with increasing Nd content (Figure 5.07d), consistent with the ionic radii of La^{3+} (1.032 Å) and Nd^{3+} ions (0.983 Å).[28] Room temperature unit cell parameters for La$_{1-x}$Nd$_x$GaOS$_2$ ($0 \leq x \leq 0.1$) are in agreement with those of LaGaOS$_2$.[1] The change in *c* cell parameter with dopant level was larger than that for the *a* and *b* cell parameters (by 0.08%). There is a limited solid solution

of x = 0.02 according to Vegard's law which probably suggests why NdGaOS$_2$ does not exist.[29] There is little change in unit cell parameter observed for x > 0.07, reflecting no further change in composition.

5.2.2.3 SEM-EDX

An overall backscattered secondary electrons image for each sample was taken at a magnification between X57-X102 to get an idea of the homogeneity of the sample. An example is given in Appendix 5.03. From the backscattered images and spectra, all the samples were fairly homogenous. For all the doped samples, most of the sites that were picked had La$_2$O$_3$ impurities and showed Ga deficiencies. The Ga deficiency could be due to EDX operating at only a thin layer on the sample surface. The average composition from all the normal points, assuming oxygen content and normalizing the data with respect to S, is La$_{0.94\pm0.05}$Nd$_{0.06\pm0.01}$Ga$_{0.75\pm0.16}$OS$_2$ for La$_{0.98}$Nd$_{0.02}$GaOS$_2$, La$_{0.94\pm0.06}$Nd$_{0.06\pm0.01}$Ga$_{0.75\pm0.14}$OS$_2$ for La$_{0.95}$Nd$_{0.05}$GaOS$_2$, La$_{0.91\pm0.12}$Nd$_{0.09\pm0.03}$Ga$_{0.69\pm0.17}$OS$_2$ for La$_{0.93}$Nd$_{0.07}$GaOS$_2$ and La$_{0.90\pm0.14}$Nd$_{0.10\pm0.03}$Ga$_{0.69\pm0.11}$OS$_2$ for La$_{0.9}$Nd$_{0.1}$GaOS$_2$.

5.2.2.4 Diffuse Reflectance Spectroscopy

Before the reaction, the doped samples were blue-green. After the reaction was complete La$_{0.98}$Nd$_{0.02}$GaOS$_2$ and La$_{0.95}$Nd$_{0.05}$GaOS$_2$ became pale-grey, La$_{0.93}$Nd$_{0.07}$GaOS$_2$ became green-grey and La$_{0.9}$Nd$_{0.1}$GaOS$_2$ became apple-green (Figure 5.08). The colours are subjective to the reader.

Figure 5.08 Colour change in each of the different Nd doping concentrations form the initial blue-green colour after reaction. La$_{0.98}$Nd$_{0.02}$GaOS$_2$ (far left) became pale-grey, La$_{0.95}$Nd$_{0.05}$GaOS$_2$ (second from the left) became pale-grey, La$_{0.93}$Nd$_{0.07}$GaOS$_2$ (third from the left) became green-grey and La$_{0.9}$Nd$_{0.1}$GaOS$_2$ (far right) became apple-green.

Colour changes in the samples may suggest changes in the band gap or may reflect the changes in colour with Nd content due to *f-f* transitions. Hence, diffuse reflectance Spectroscopy data was collected to ascertain the optical band gaps of the powders. A Kubelka–Munk transformation was performed on the data.[25] The band gap value is where the positive gradient of the extrapolated line of the absorption edge crosses the *x*-axis (Figure 5.09). In figure 5.09d, the peak at 2.9 eV seems to be comprised of two different features, possibly as a result of the high amount of $La_4O_4Ga_{1.72}S_{4.58}$ impurity compared to the other Nd-doped samples. These values are shown in Table 5.03. There is no significant change (within errors) in the band gap values. The different errors in the band gap values could be due to the *f-f* transitions of Nd ions as well as due to the impurity (for $La_{1.93}Nd_{0.07}GaOS_2$). These band gap values explain the grey colour (408-411 nm) of the powders for $La_{1-x}Nd_xGaOS_2$ ($0 \leq x \leq 0.07$) but not the green colour of $La_{0.9}Nd_{0.1}GaOS_2$ as the band gap obtained suggests a blue colour (475 nm) which could be due to absorption arising from *f-f* transitions.

Table 5.03 Optical band gap values for $La_{1-x}Nd_xGaOS_2$ ($0 \leq x \leq 0.1$)

Sample	Band gap value (eV)
$LaGaOS_2$	3.06 ± 0.32
$La_{1.98}Nd_{0.02}GaOS_2$	3.03 ± 0.00
$La_{1.95}Nd_{0.05}GaOS_2$	3.02 ± 0.01
$La_{1.93}Nd_{0.07}GaOS_2$	3.04 ± 0.53
$La_{1.9}Nd_{0.1}GaOS_2$	2.61 ± 0.02
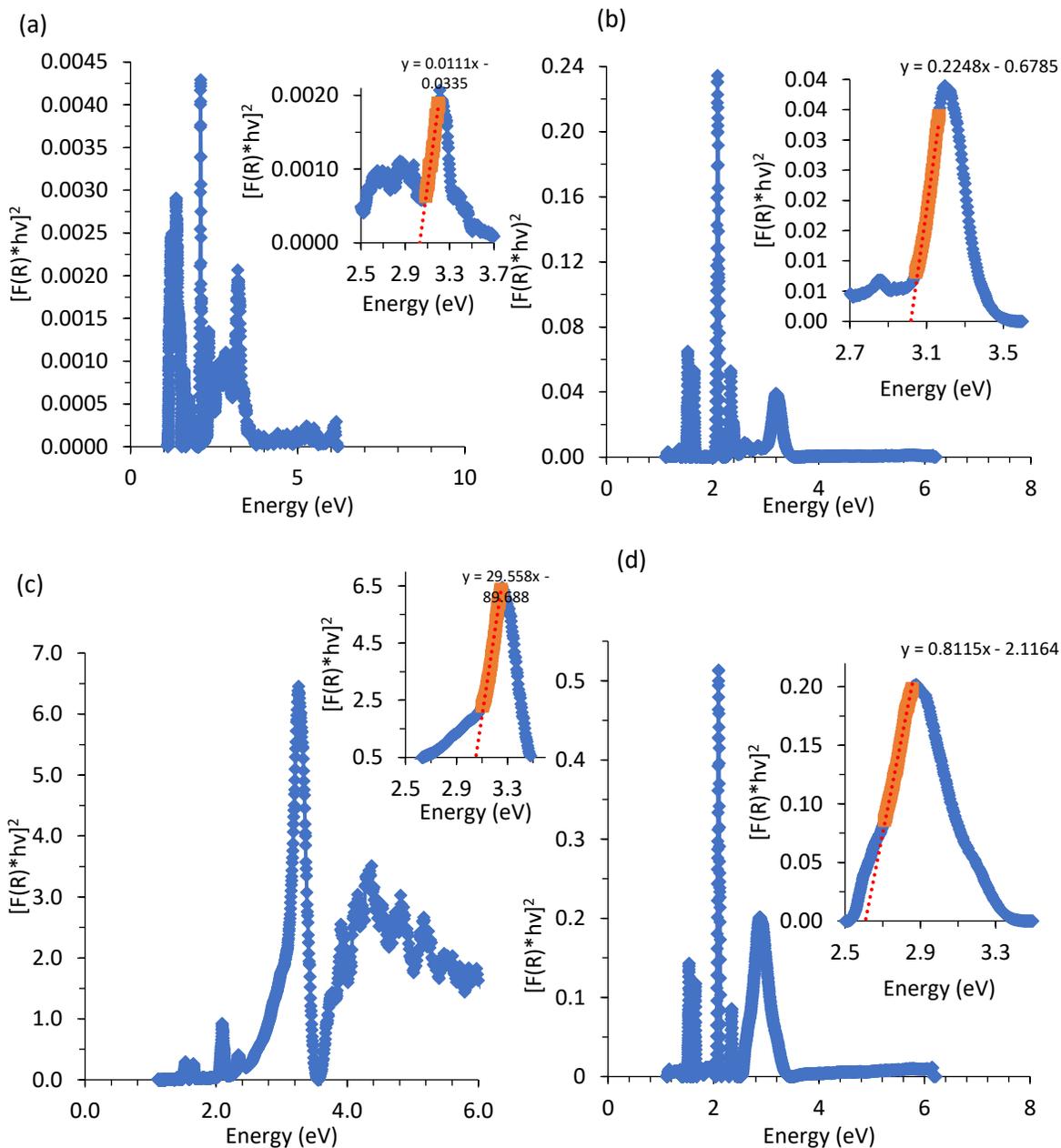
Figure 5.09 Plot of $[F(R)*h\nu]^2$ against energy for (a) $La_{0.98}Nd_{0.02}GaOS_2$ (b) $La_{0.95}Nd_{0.05}GaOS_2$ (c) $La_{0.93}Nd_{0.07}GaOS_2$ and (d) $La_{0.9}Nd_{0.1}GaOS_2$. Data is shown in blue. Line of best fit to positive curve is shown in dotted red.

5.2.2.5 X-ray Photoelectron Spectroscopy

XPS data were collected as described in Chapter 2.2.5, in collaboration with Dr R. Palgrave (UCL), to ascertain the electronic states of the elements present in the materials. The S 2p data (Figure 5.10a) shows that most of the sulfur is present as sulfide. Moreover, there is more oxygen than sulfur on

the surface in all the samples. The shift in binding energy in S 2p in $La_{0.93}Nd_{0.07}GaOS_2$ and $La_{0.9}Nd_{0.1}GaOS_2$ (Figure 5.10a) could be due to the $La_4O_4Ga_{1.72}S_{4.58}$ impurity present in these samples. The Nd 3d data (Figure 5.10b) is inconclusive as the Nd 3d peaks overlap with the O 2p peaks, making them hard to see. The peaks at around 980 eV may suggest metallic Nd–Nd while the peaks at 983.8 eV may suggest Nd oxide components.[30]
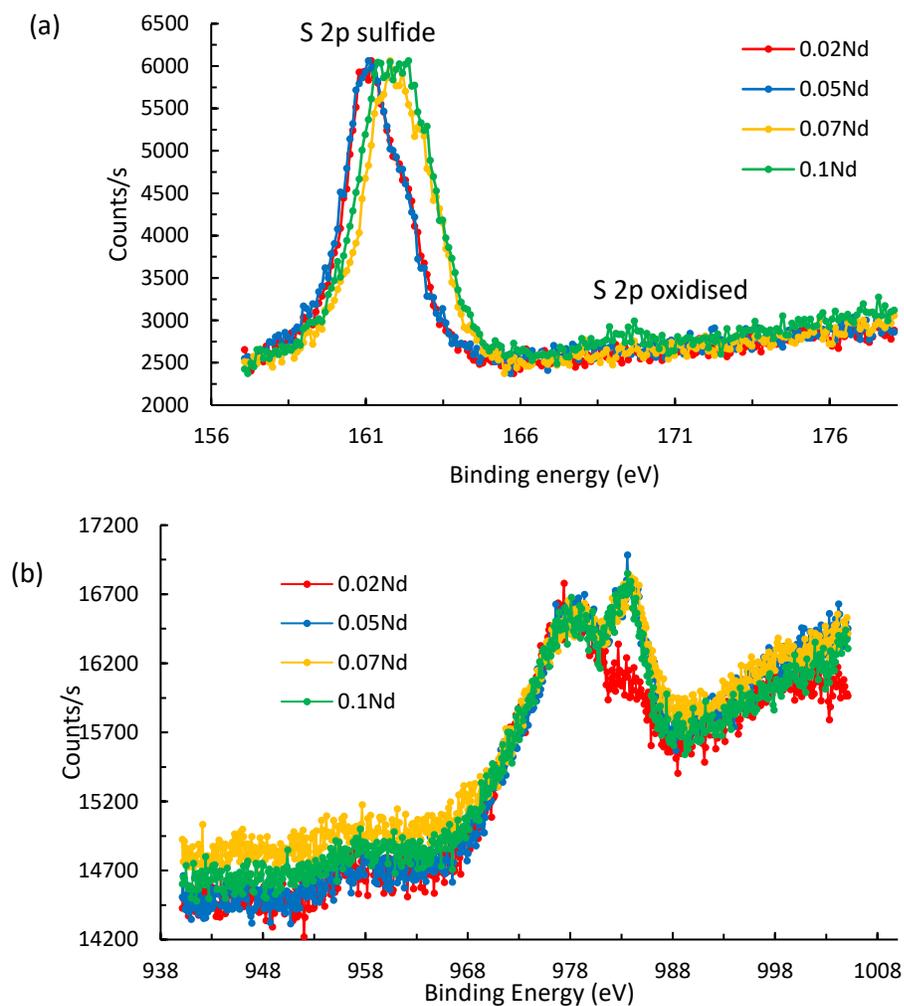

Figure 5.10 Plot of counts against energy for (a) S 2p and (b) Nd 3d for $La_{1-x}Nd_xGaOS_2$.

5.2.3 La$_{1-x}$Ce$_x$GaOS$_2$

5.2.3.1 Synthesis

$La_{1-x}Ce_xGaOS_2$ ($0 \leq x \leq 0.1$) was prepared from stoichiometric amounts of La_2O_3 (Sigma-Aldrich, 99.99%), Ga_2O_3 (Sigma-Aldrich, 99.99%), S (Alfa-Aesar, 99.5%+) and CeO_2 (Acros Organics, 99.9%) using the method described in 5.2.1.1.

5.2.3.2 X-ray powder diffraction

The resulting powders were then analysed by Rietveld refinement (Figure 5.11). A small impurity phase of $La_4O_4Ga_{1.72}S_{4.58}$ was present in $La_{0.9}Ce_{0.1}GaOS_2$. The refinement was performed as described in 5.2.1.2. Data for some of the relevant parameters for $La_{1-x}Ce_xGaOS_2$ ($0 \leq x \leq 0.1$) are shown in Table 5.04. As for $La_{1-x}Nd_xGaOS_2$ ($0 \leq x \leq 0.1$), only one $LaGaOS_2$ phase was needed to fit these data.
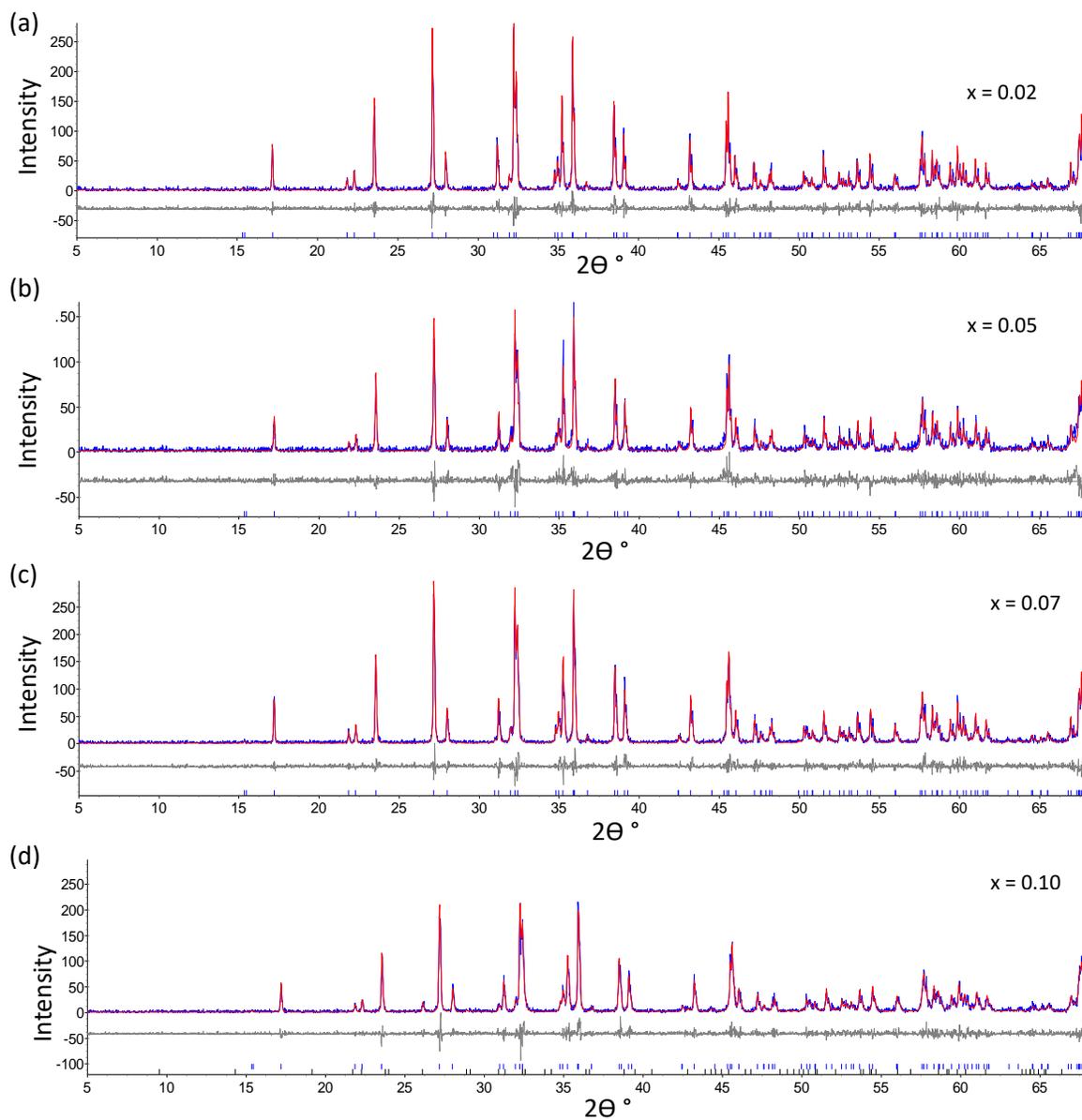

Figure 5.11 Rietveld refinement profiles for $La_{1-x}Ce_xGaOS_2$ ($0 \leq x \leq 0.1$) using room temperature XRPD data (a) x = 0.02 (b) x = 0.05 (c) x = 0.07 and (d) x = 0.1. The observed data is in blue, the calculated data is in red and the difference is in grey. The blue vertical tick marks show the predicted peak positions for $LaGaOS_2$ and the black tick marks show those for $La_4O_4Ga_{1.72}S_{4.58}$. R_{wp} and the χ^2 values are given in table 5.05.

Table 5.04 Data for room temperature Rietveld refinement for $La_{1-x}Ce_xGaOS_2$ ($0 \leq x \leq 0.1$). 36 parameters were used for the refinements.

$La_{1-x}Ce_xGaOS_2$	X = 0	X = 0.02	X = 0.05	X = 0.07	X = 0.10
a (Å)	5.552349 (6)	5.552067 (9)	5.551754 (7)	5.551547 (3)	5.551117 (8)
b (Å)	5.774507 (0)	5.774317 (7)	5.773643 (3)	5.773661 (9)	5.773722 (6)
c (Å)	11.46058 (1)	11.459758 (3)	11.456921 (6)	11.457671 (2)	11.456722 (2)
Volume (Å^3)	367.450 (6)	367.393 (7)	367.238 (6)	367.250 (9)	367.195 (8)
La y coordinate (c)	0.14894 (7)	0.15044 (1)	0.14851 (9)	0.14810 (6)	0.14923 (3)
La z coordinate (c)	0.10775 (1)	0.10716 (7)	0.10744 (8)	0.10725 (5)	0.10779 (9)
Ga y coordinate (c)	0.52052 (6)	0.51895 (6)	0.52068 (3)	0.52103 (9)	0.52061 (1)
Ga z coordinate (c)	0.33564 (9)	0.33602 (4)	0.33333 (2)	0.33504 (8)	0.33617 (3)
S (1) y coordinate (c)	0.65581 (1)	0.65971 (4)	0.65288 (5)	0.65488 (2)	0.65579 (4)
S (1) z coordinate (c)	0.01162 (5)	0.01101 (6)	0.01318 (1)	0.01022 (7)	0.00978 (7)
S (2) y coordinate (c)	0.09650 (9)	0.09848 (8)	0.09704 (3)	0.09567 (1)	0.09754 (1)
S (2) z coordinate (c)	0.84614 (7)	0.84388 (0)	0.84465 (3)	0.84426 (3)	0.84561 (2)
O y coordinate (c)	0.37854 (6)	0.37873 (4)	0.37353 (6)	0.37498 (0)	0.38306 (4)
R_{wp} (%)	11.48	32.37	37.00	31.01	31.10
χ^2	2.40	2.14	2.14	2.16	2.10
$La_4O_4Ga_{1.72}S_{4.58}$ (%)	-	-	-	-	3.77 ± 0.53

$La_{1-x}Ce_xGaOS_2$ with higher Ce content (x > 0.1) were also synthesised but they did not produce the main phase and instead had impurities (Ce_2O_2S, Ga_2S_3 and $LaGaO_3$). The samples were then overlaid on top of one another to check for any differences (Figure 5.12).
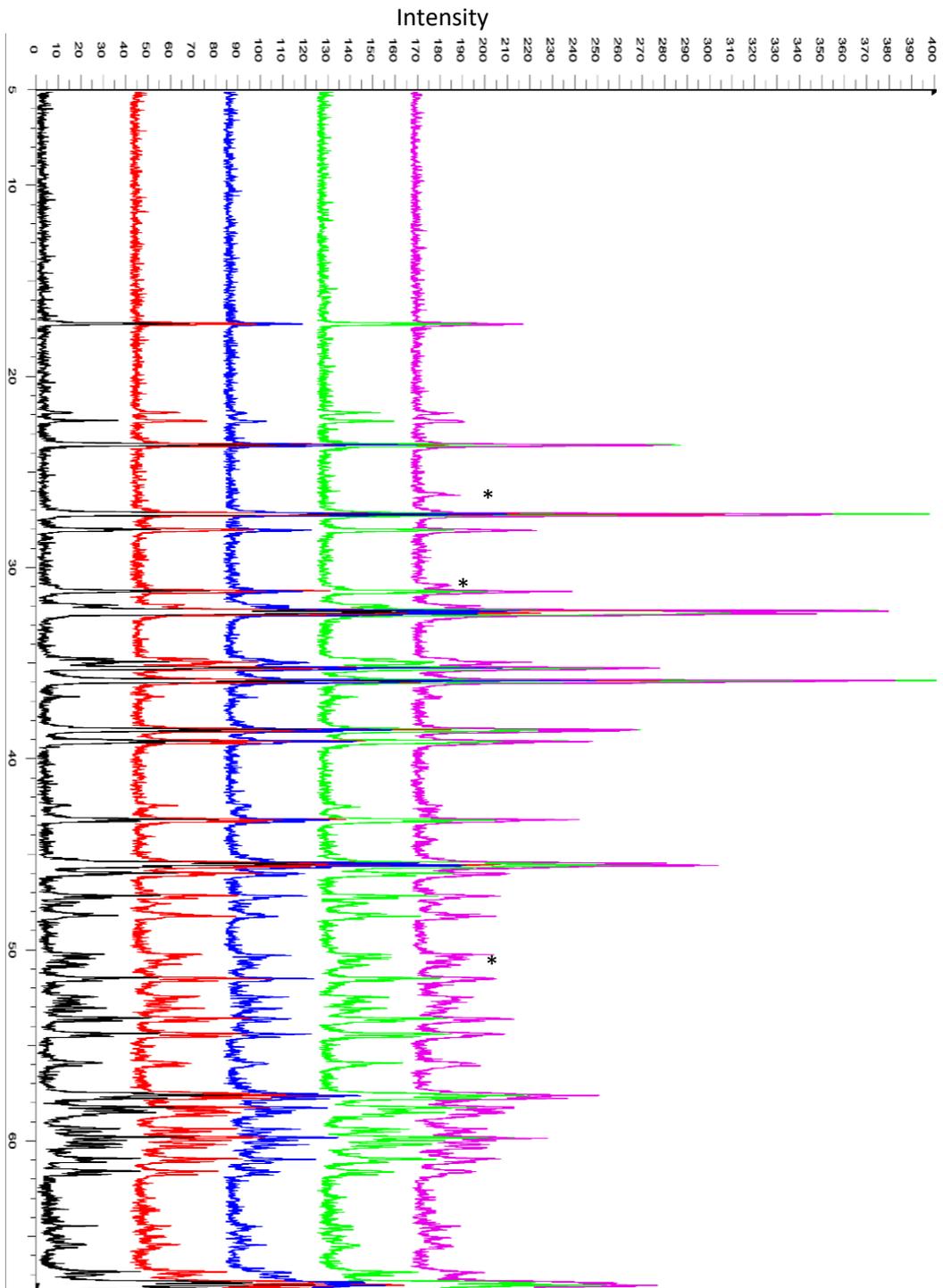
Figure 5.12 Overlay of room temperature XRPD data for $La_{1-x}Ce_xGaOS_2$, $x=0$ (black, bottom) to $x=0.1$ (pink, top). $LaGaOS_2$ is in black, $La_{0.98}Ce_{0.02}GaOS_2$ is in red, $La_{0.95}Ce_{0.05}GaOS_2$ is in blue, $La_{0.93}Ce_{0.07}GaOS_2$ is in green and $La_{0.9}Ce_{0.1}GaOS_2$ is in pink. * denotes the impurity phase $La_4O_4Ga_{1.72}S_{4.58}$.
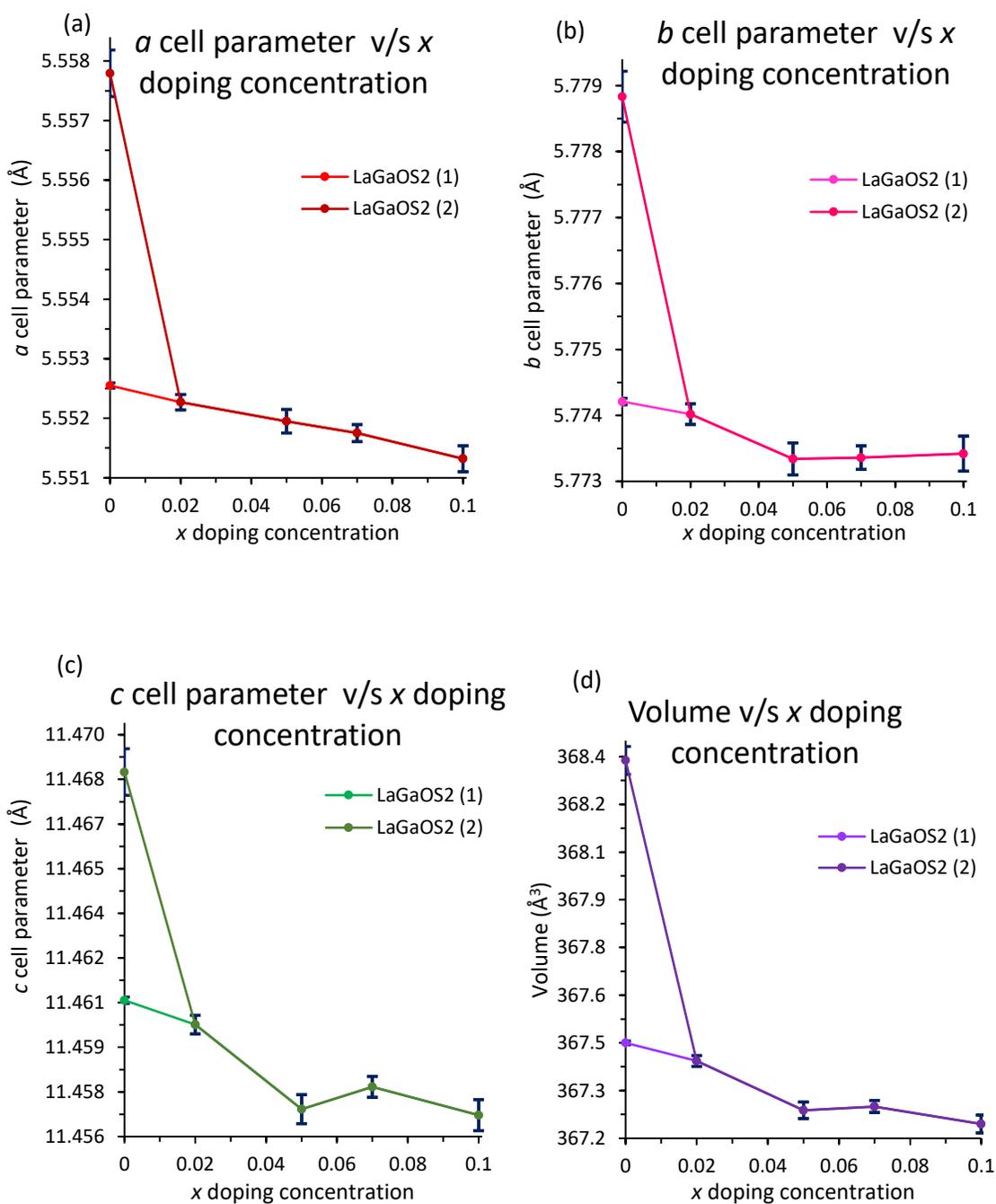
Figure 5.13 (a) Unit cell parameter *a* [LaGaOS₂ (1) in red and LaGaOS₂ (2) in dark red], (b) unit cell parameter *b* [LaGaOS₂ (1) in pale pink and LaGaOS₂ (2) in dark pink], (c) unit cell parameter *c* [LaGaOS₂ (1) in green and LaGaOS₂ (2) in dark green] and (d) volume [LaGaOS₂ (1) in pale purple and LaGaOS₂ (2) in dark purple] as a function of *x* for La₁₋ₓCeₓGaOS₂ determined from Rietveld refinements using room temperature XRPD data. Error bars in blue.

There are few changes in structure with dopant level (Appendix 5.04). The overall trend is a slight decrease in unit cell volume with increasing Ce content (Figure 5.13d), consistent with the ionic radii of La^{3+} (1.032 Å) and Ce^{3+} ions (1.01 Å).[28] Room temperature unit cell parameters for $La_{1-x}Ce_xGaOS_2$ ($0 \leq x \leq 0.1$) are in agreement with those of $LaGaOS_2$.[1] The change in c cell parameter with dopant level was larger than that for the a and b cell parameters (by 0.02%). There is a limited solid solution of x = 0.05 according to Vegard's law which probably suggests why $CeGaOS_2$ does not exist.[29]

5.2.3.3 SEM-EDX

An overall backscattered secondary electrons image for each sample was taken at a magnification between X44-X80 to get an idea of the homogeneity of the sample. An example is given in Appendix 5.05. From the backscattered images and spectra, all the samples were fairly homogenous. For all the doping samples, most of the sites that were picked were La-rich and showed Ga deficiencies which could be due to EDX operating at only a thin layer on the sample surface. The average composition from all the normal points, assuming oxygen content and normalizing the data with respect to S, is $La_{0.94\pm0.11}Ce_{0.06\pm0.01}Ga_{0.68\pm0.09}OS_2$ for $La_{0.98}Ce_{0.02}GaOS_2$, $La_{0.92\pm0.07}Ce_{0.08\pm0.02}Ga_{0.94\pm0.09}OS_2$ for $La_{0.95}Ce_{0.05}GaOS_2$, $La_{0.90\pm0.10}Ce_{0.10\pm0.02}Ga_{0.67\pm0.09}OS_2$ for $La_{0.93}Ce_{0.07}GaOS_2$ and $La_{0.89\pm0.10}Ce_{0.11\pm0.03}Ga_{0.71\pm0.08}OS_2$ for $La_{1.9}Ce_{0.1}GaOS_2$.

5.2.3.4 Diffuse Reflectance Spectroscopy

Before the reaction, the doped samples were pale-yellow. After the reaction was complete $La_{0.98}Ce_{0.02}GaOS_2$ and $La_{0.93}Ce_{0.07}GaOS_2$ became pale-grey while $La_{0.95}Ce_{0.05}GaOS_2$ and $La_{0.9}Ce_{0.1}GaOS_2$ became grey (Figure 5.14). The colours are subjective to the reader.
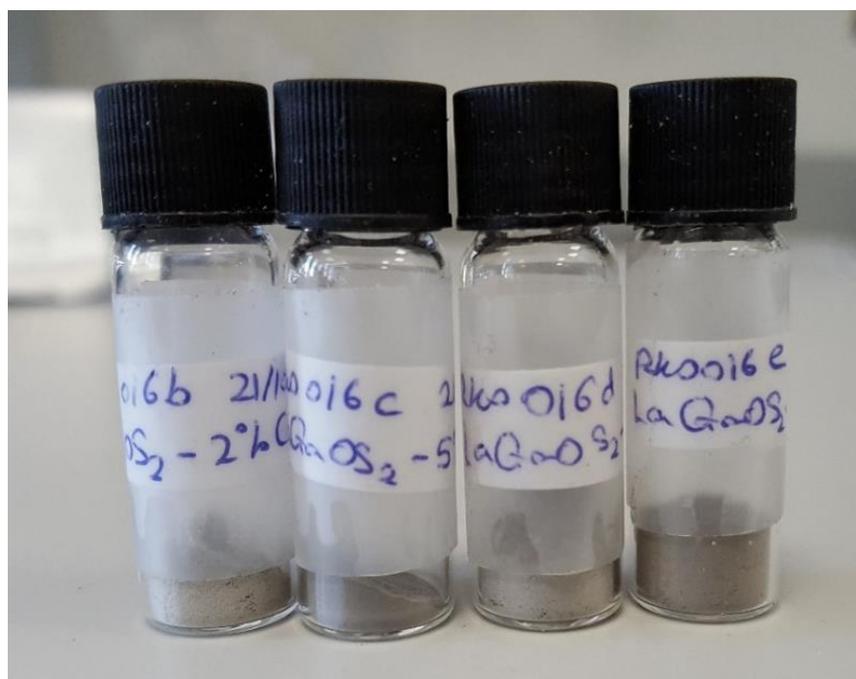
Figure 5.14 Colour change in each of the different Ce doping concentrations form the initial pale-yellow colour after reaction. $La_{0.98}Ce_{0.02}GaOS_2$ (far left) became pale-grey, $La_{0.95}Ce_{0.05}GaOS_2$ (second from the left) became grey, $La_{0.93}Ce_{0.07}GaOS_2$ (third from the left) became pale-grey and $La_{0.9}Ce_{0.1}GaOS_2$ (far right) became grey.

Colour changes in the samples may suggest changes in the band gap or due to f-f transitions similar to the Nd-doped samples, diffuse reflectance spectroscopy data was collected to establish the powders' optical band gap. A Kubelka–Munk transformation was performed on the data.[25] The band gap value is where the positive gradient of the extrapolated line of the absorption edge crosses the x-axis (Figure 5.15). These values are shown in Table 5.05. No significant change (within errors) in band gap values is observed. These band gap values explain the colours of the powders: grey colours (405-412nm) for $La_{1-x}Ce_xGaOS_2$ ($0 \leq x \leq 0.1$).

Table 5.05 Optical band gap values for $La_{1-x}Ce_xGaOS_2$ ($0 \leq x \leq 0.1$)

Sample	Band gap value (eV)
$LaGaOS_2$	3.06 ± 0.32
$La_{1.98}Ce_{0.02}GaOS_2$	3.03 ± 0.05
$La_{1.95}Ce_{0.05}GaOS_2$	3.04 ± 0.04
$La_{1.93}Ce_{0.07}GaOS_2$	3.06 ± 0.03
$La_{1.9}Ce_{0.1}GaOS_2$	3.01 ± 0.06

(a)

(b)

(c)

(d)
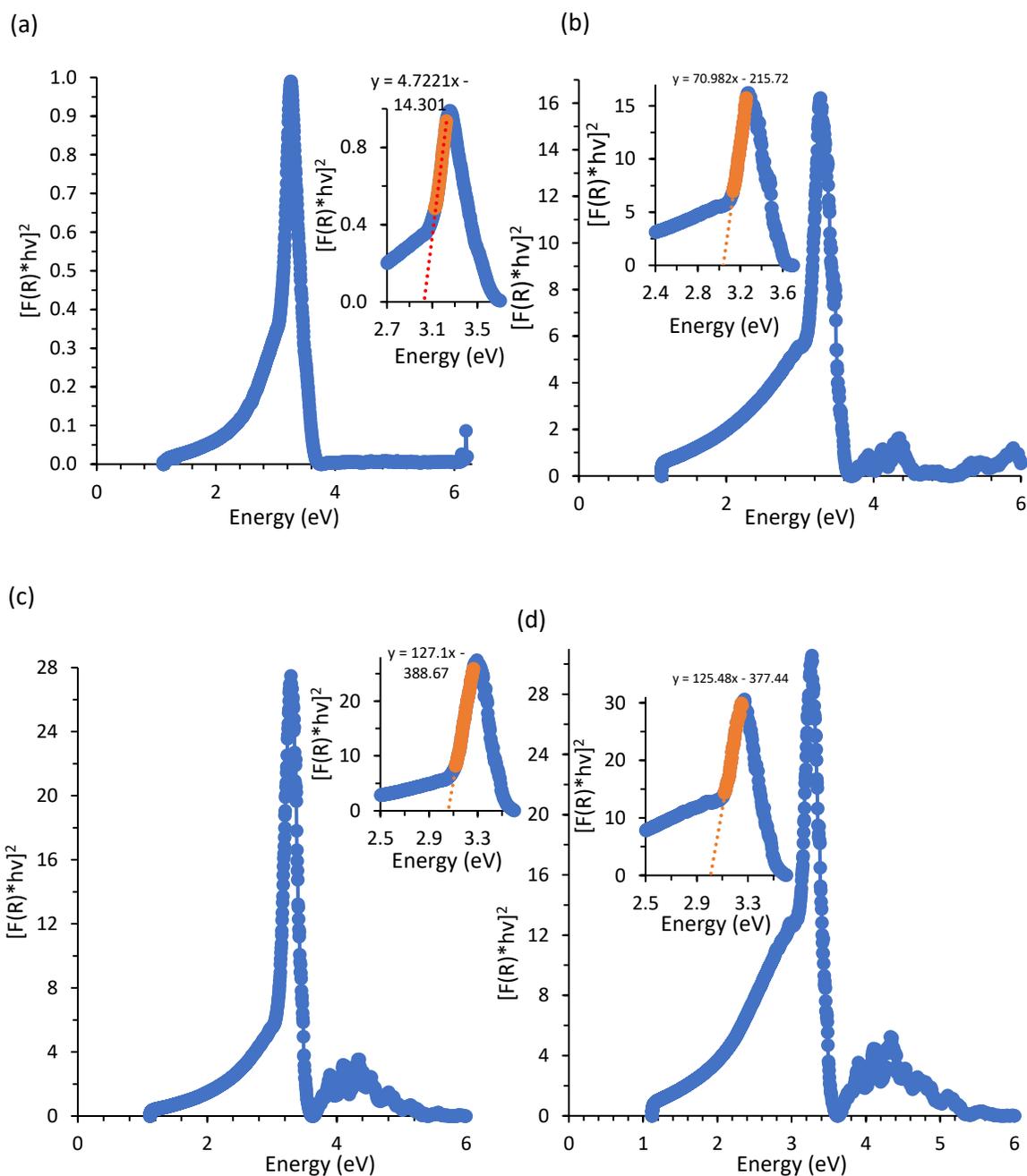
Figure 5.15 Plot of $[F(R)*h\nu]^2$ against energy for (a) $La_{0.98}Ce_{0.02}GaOS_2$ (b) $La_{0.95}Ce_{0.05}GaOS_2$ (c) $La_{0.93}Ce_{0.07}GaOS_2$ and (d) $La_{0.9}Ce_{0.1}GaOS_2$. Data is shown in blue. Line of best fit to positive curve is shown in dotted red.

5.2.3.5 X-ray Photoelectron Spectroscopy

XPS data were collected as described in Chapter 2.2.5, to ascertain the electronic states of the elements present in the materials. The S 2p data (Figure 5.16c) (Appendix 5.06) shows that most of the sulfur was present as sulfide (94 atomic %) and only 4 atomic % S 2p are oxidised. Moreover, according to their atomic %, the oxides are present in a greater content than the sulfides on the

surface in all the samples. The Ce 3d data (Figure 5.16b) shows that peaks increase in intensity with increasing Ce doping concentration and that the doped samples contain only Ce^{3+} ions since only single peaks are observed instead of doublet peaks (Ce^{4+}).
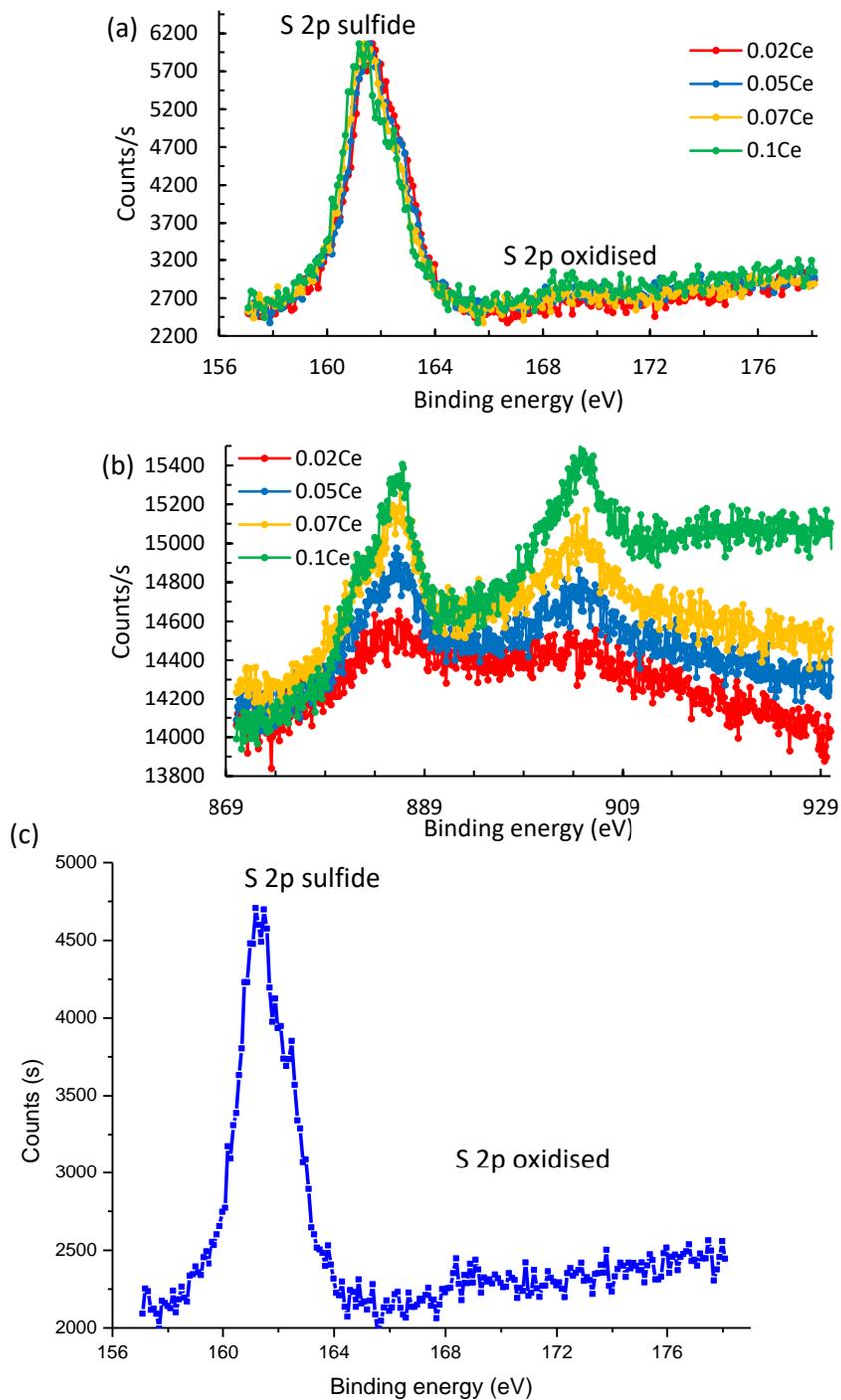

Figure 5.16 Plot of counts against binding energy for (a) S 2p for $La_{1-x}Ce_xGaOS_2$, (b) Ce 3d for $La_{1-x}Ce_xGaOS_2$ and (c) S 2p for $La_{0.9}Ce_{0.1}GaOS_2$

5.3 Discussion

The cell parameters for both the $LaGaOS_2$-like phases obtained from the room temperature XRPD data are bigger than Jaulmes' value (Table 3.01), with the second $LaGaOS_2$-like phase, which is present in a smaller amount (8.26 ± 0.87 %), being slightly bigger than the first one.[1] From the models used to fit the XRPD data of the Nd- and Ce-doped samples, only one $LaGaOS_2$ phase was used for all the doped samples which could probably suggest that doping the parent compound suppresses formation of the second $LaGaOS_2$ phase.

For both $La_{1-x}Nd_xGaOS_2$ ($0 \leq x \leq 0.1$) and $La_{1-x}Ce_xGaOS_2$ ($0 \leq x \leq 0.1$), the overall trend is slight decrease in unit cell volume with increasing x content (Figure 5.07d and 5.13d).[10] This is consistent with ionic radii (replacing La^{3+}[1.032 Å] with Nd^{3+}[0.983 Å] and Ce^{3+} ions [1.01 Å] respectively for a coordination number 6).[28] The decrease in unit cell volume from $La_{0.98}Ce_{0.02}GaOS_2$ to $La_{0.95}Ce_{0.05}GaOS_2$ seems larger than the others. This could be due to replacing La^{3+} (1.032 Å) with Ce^{4+} ions (0.87 Å) for coordination number 6, suggesting a mixture of Ce^{3+}/Ce^{4+} in $La_{0.95}Ce_{0.05}GaOS_2$.[28] In contrast, the XPS Ce 3d data (Figure 5.16b) showed that the doped samples contained purely Ce^{3+} ions, shown by single peaks (Ce^{3+}) ions and no doublet peaks (Ce^{4+}) were present.[31,32] Similarly, comparing the changes in cell parameters with Nd-doping and Ce-doping showed that Ce-doping produces a lesser decrease in the unit cell volume (Appendix 5.07) which suggests that there are no Ce^{4+} ions present in $La_{1-x}Ce_xGaOS_2$. $NdGaOS_2$ and $CeGaOS_2$ have not been reported, yet it was hypothetically assumed that they would be isostructural to $LaGaOS_2$ and there would be a solid solution for $LaGaOS_2$, $La_{1-x}Nd_xGaOS_2$ ($0 \leq x \leq 0.1$) and $La_{1-x}Ce_xGaOS_2$ ($0 \leq x \leq 0.1$) according to Vegard's law.[29] However, linearity is not observed in the unit cell parameters plots with increasing Nd and Ce doping concentration (Figure 5.07 and 5.13) which suggests that the Nd doping limit 0.02 while the Ce doping limit is 0.05. This maybe is due the presence of $La_4O_4Ga_{1.72}S_{4.58}$ impurity phases in the doped samples, reflecting the inflexibility of the $LaGaOS_2$ structure. Increasing amounts of impurities are formed as x is increased to x = 0.07 for Nd and x = 0.10 for Ce. In both $La_{1-x}Nd_xGaOS_2$ and $La_{1-x}Ce_xGaOS_2$, the changes in c cell parameters with dopant level are larger than that for a and b cell parameters.

From the diffuse reflectance plots, the optical band gaps do not change (within errors) when $LaGaOS_2$ was doped with Nd and Ce (Figure 5.09 and 5.15). At $La_{1.9}Nd_{0.1}GaOS_2$, the band gap value corresponds to blue colour (475 nm) which is not consistent with the colour observed for that doped

material and this could be due to f-f transitions. This lack of variation in optical band gaps is different to that observed in M_4O_4Se [Se_2] (M = La-Pr), $Ln_2Ti_2S_2O_5$ (Ln = Sm, Gd, Tb, Dy, Ho and Er)[10], $Ln_2Ti_2O_7$ (Ln = La, Pr, Nd) and $Na_xLa_{1-x}TaO_{1+2x}N_{2-2x}$.[10,33–35] Doping the parent compound with Ce barely changed the colour of the samples (Figure 5.14) which is probably due to low doping concentrations. In contrast, the colour change of the Nd-doped samples could also be due to f-f transitions (Figure 5.09) which are absent in the Ce-doped samples (Figure 5.15). The optical band gaps of $La_{1-x}Nd_xGaOS_2$ ($0 \leq x \leq 0.07$) are similar to $BaTiO_3$ and LaCuOS and can be used in nonlinear optics and uncooled thermal images.[27,36] The optical band gap of $La_{0.9}Nd_{0.1}GaOS_2$ is similar to that of CdS and it can possibly be used in photoresistors, solar cells and quantum dots.[37] The $La_{1-x}Ce_xGaOS_2$ optical band gaps values are similar to ZnSe can be used in blue lasers, LEDs and IR optics.[38]

5.4 Conclusions and Future work

There is a limited solid solution when isovalent-doping $LaGaOS_2$ with Nd and Ce. Other strategies might be to synthesise $LaGaOS_{2-x}Se_x$, p-type dope $LaGaOS_2$ on the Ga-site (such as Zn), n-type dope $LaGaOS_2$ on the Ga-site (such as Ge, Sn, Bi) and investigate the resulting changes in optical band gaps. The DRS measurements showed that the optical band gaps barely decreased when the parent compound was doped with Nd or Ce and presumably the change in colour in Nd-doped samples is due to f-f transitions, which increase with decreasing Nd content. The XPS data showed that all the samples showed barely any sulfur oxidation on the surface and that $La_{1-x}Ce_xGaOS_2$ ($0 \leq x \leq 0.1$) contained only Ce^{3+} ions. It also showed that the surface of the Nd doped samples may contain both metallic Nd-Nd and Nd oxide, however, this could be argued. It would be interesting to see if there are any changes in the photocatalytic properties of the samples. This work suggests that the $LaGaOS_2$ structure has quite limited compositional flexibility and that it is difficult to tune its electronic structure by means of chemical pressure.

5.5 References

1   S. Jaulmes, *Sect. B Struct. Crystallogr. Cryst.*, 1978, **5419**, 2610–2612.

2   S. Bénazeth, M. Guittard and P. Laruelle, *Acta Cryst.*, 1984, **C40**, 345–347.

3   S. Jaulmes, E. Godlewski and M. P. E. T. J. Etienne, *Acta Cryst. B*, 1982, **38**, 1707–1710.

4   S. Jaulmes, D. Carre, M. Palazzi, M. Guittard and J. Flahaut, *C. R. Acad. Sc. Paris*, 1985, **301**, 259.

5   S. Benazeth, P. Laruelle and M. Guittard, *J. Solid State Chem.*, 1989, **78**, 147–153.

6   J. Dugue and M. Guittard, *Acta Cryst.B*, 1982, **B38**, 2368–2371.

7   K. Ogisu, A. Ishikawa, Y. Shimodaira, T. Takata, H. Kobayashi and K. Domen, *J. Phys. Chem. C*, 2008, **112**, 11978–11984.

8   D. E. Scaife, *Sol. Energy*, 1980, **25**, 41–54.

9   K. Ogisu, A. Ishikawa, K. Teramura, K. Toda, M. Hara and K. Domen, *Chem. Lett.*, 2007, **36**, 854–855.

10   A. Ishikawa, T. Takata, T. Matsumura, J. N. Kondo, M. Hara, H. Kobayashi and K. Domen, *J. Phys. Chem. B*, 2004, **108**, 2637–2642.

11   A. Ishikawa, T. Takata, J. N. Kondo, M. Hara, H. Kobayashi and K. Domen, *J. Am. Chem. Soc.*, 2002, **124**, 13547–13553.

12   G. Hitoki, A. Ishikawa, T. Takata, J. N. Kondo, M. Hara and K. Domen, *Chem. Lett.*, 2002, **31**, 736–737.

13   G. Hitoki, T. Takata, J. N. Kondo, M. Hara, H. Kobayashi and K. Domen, *Chem. Commun.*, 2002, **2**, 1698–1699.

14   W. J. Chun, A. Ishikawa, H. Fujisawa, T. Takata, J. N. Kondo, M. Hara, M. Kawai, Y. Matsumoto and K. Domen, *J. Phys. Chem. B*, 2003, **107**, 1798–1803.

15   M. Machida, J. I. Yabunaka and T. Kijima, *Chem Mater*, 2000, **12**, 812–817.

16   M. Machida, S. Murakami and T. Kijima, *J. Phys. Chem. B*, 2001, **105**, 3289–3294.

17   K. Ikarashi, J. Sato, H. Kobayashi, N. Saito, H. Nishiyama and Y. Inoue, *J. Phys. Chem. B*, 2002, **106**, 9048–9053.

18   K. Maeda, K. Teramura, D. Lu, T. Takata, N. Saito, Y. Inoue and K. Domen, *Nature*, 2006, **440**, 295–295.

19   A. Kudo, I. Tsuji and H. Kato, *Chem. Commun.*, 2002, **17**, 1958–1959.

20   G. Trimarchi, K. Lam, A. Freeman, K. Poeppelmeier and A. Zunger, *Am. Phys. Soc.*, 2013, **58**, 16005.

21   R. Vali, *Comput. Mater. Sci.*, 2006, **37**, 300–305.

22   J. Llanosa, V. Sáncheza, C. Mujica and A. Buljan, *Mater. Res. Bull.*, 2002, **37**, 2285–2291.

23   M. Mikami and A. Oshiyama, *Phys. Rev. B*, 1998, **57**, 8939–8944.

24   A. Ishikawa, T. Takata, J. N. Kondo, M. Hara, H. Kobayashi and K. Domen, *J. Am. Chem. Soc.*, 2002, **124**, 13547–13553.

25   W. W. Wendlandt and H. G. Hecht, *Reflectance Spectroscopy*, Interscience Publishers, New York, 1966.

26   H. Kabbour, L. Cario, Y. Moëlo and A. Meerschaut, *J. Solid State Chem.*, 2004, **177**, 1053–1059.

27   H. Hiramatsu, H. Kamioka, K. Ueda, H. Ohta, T. Kamiya, M. Hirano and H. Hosono, *Phys. Status Solidi Appl. Mater. Sci.*, 2006, **203**, 2800–2811.

28   R. D. Shannon, *Acta Crystallogr. Sect. A*, 1976, **32**, 751–767.

29   A. R. Denton and N. W. Ashcroft, *Phys. Rev. A*, 1991, **43**, 3161–3164.

30   B. V Crist, *Handbook of Monocromatic XPS Spectra: The Elements and Native Oxides*, John Willey and Sons Ltd, Chichester, 2000.

31   A. Mehta, S. Patil, H. Bang, H. J. Cho and S. Seal, *Sensors Actuators, A Phys.*, 2007, **134**, 146–151.

32   C. Zhang and J. Lin, *Phys. Chem. Chem. Phys.,* 2011, **13**, 3896–3905.

33   K. Ueda, H. Kato and M. Kobayashi, *J. Mater. Chem. A*, 2013, **1**, 3667–3674.

34   S. Strobel, A. Choudhury, P. K. Dorhout, C. Lipp and T. Schleid, *Inorg. Chem.*, 2008, **47**, 4936–4944.

35   D. W. Hwang, J. S. Lee, W. Li and S. H. Oh, *J. Phys. Chem. B*, 2012, **107**, 4963–4970.

36   H. Matsuda, M. Kuwabara, K. I. Yamada, H. Shimooka and S. Takahashi, *J. Am. Ceram. Soc*, 1998, **81**, 3010–3012.

37   R. B. Kale and C. D. Lokhande, *Semicond. Sci. Technol.*, 2005, **20**, 1–9.

38   M. Cardona, *J. Appl. Phys.*, 1961, **32**, 2151.

Chapter 6: $Bi_{1-x}Ln_xO_{1-x}A_xSe$ (Ln = Ce and A = F)

6.1 Introduction

BiCuOSe crystallises in the $P4/nmm$ space group [a = 3.9213 (1) Å, c = 8.9133 (5) Å] and consists of insulating $(Bi_2O_2)^{2+}$ layers which act like charge reservoirs and anti-CuO_2 type conductive $(Cu_2Se_2)^{2-}$ layers which act as a conduction pathway for carrier transport. These layers alternate along the c axis (Figure 6.01). In the $(Bi_2O_2)^{2+}$ layers, Bi^{3+} is in a distorted square antiprismatic coordination with four oxygen atoms and four Se atoms. In the $(Cu_2Se_2)^{2-}$ layer, the Cu ion is in a distorted tetrahedral arrangement with the Cu ion coordinated to 4 Se^{2-} ions. The Bi_4O and $CuSe_4$ tetrahedra are edge-shared. [1]

BiCuOSe has been reported to be a transparent, p-type semiconductor with a moderate band gap with a promising future as a thermoelectric material.[2] Thermoelectric materials can generate electricity from waste heat and are viewed as a substitute renewable energy solution. The efficiency of these materials is characterised by a dimensionless figure of merit, ZT = ($S^2\sigma$ T)/κ, where S = Seebeck coefficient, σ = electrical conductivity, κ = thermal conductivity, and T = absolute temperature.[3–5] Hence, to have a high ZT, the Seebeck coefficient and the electrical conductivity need to be increased and the thermal conductivity decreased.[5–15]. This can be done through doping, band tuning and introducing Cu vacancies.[2,16–22] BiCuOSe has a high ZT value (0.8) which is greater than polycrystalline oxide systems $Ca_3Co_4O_9$, $NaCo_2O_4$, $SrTiO_3$[23,24], ZnO and In_2O_3 and similar to p-type intermetallic systems PbTe and $Ce_yFe_xCo_{4-x}Sb_{12}$.[2,9,16,23–36] It also has a low thermal conductivity value (0.45 W m^{-1}K^{-1} at 923 K) which is lower than $Ag_{3.9}Mo_9Se_{11}$, Cu_3SbSe_4, $Cu_2Ga_4Te_7$[37], $Cu_{2.1}Zn_{0.9}SnSe_4$, $Cu_2Ga_{0.07}Ge_{0.93}Se_3$, $CsBi_4Te_6$ and $K_2Bi_8Se_{13}$ but bigger than $AgSbTe_2$, Ag_9TlTe_5 and $Ag_{0.95}GaTe_2$.[16,19,37–48] This low value is linked to its low phonon transport speed and Young's modulus. BiCuOSe has a high electrical conductivity (>4000 Sm^{-1}), a large Seebeck coefficient (> 350 μV K^{-1}).[19]

Hole doping BiCuOSe has been shown to increase the electrical conductivity and the thermoelectric power factor, giving high Seebeck coefficients and low thermal conductivity (< 1 W m^{-1}K^{-1} at 873 K) in $Bi_{1-x}Mg_xCuOSe$ (ZT = 0.67), $Bi_{1-x}Ca_xCuOSe$ (ZT = 0.9), $Bi_{1-x}Sr_xCuOSe$ (ZT = 0.76), $Bi_{1-x}Ba_xCuOSe$ (ZT = 1.1), $Bi_{1-x}Pb_xCuOSe$ (ZT = 0.95), $Bi_{1-x}Ni_xCuOSe$ (ZT = 0.39), $Bi_{1-x}K_xCuOSe$ (ZT = 0.6), $Bi_{1-x}Na_xCuOSe$ (ZT = 0.91) and $BiCu_{1-x}SeO$ (ZT = 0.81), though it gave decreased Seebeck

coefficients.[2,16,18–20,49–53] Isovalent doping BiCuOSe has been shown to increase the thermoelectric power factor as hole doping in BiCuOSe$_{1-x}$Te$_x$ (*ZT* = 0.71), BiOCu$_{1-x}$Ag$_x$*Se* (*ZT* = 0.64 and 0.68), Bi$_{1-x}$Sb$_x$CuOSe (*ZT* = 0.73) and Bi$_{1-x}$La$_x$CuOSe (*ZT* = 0.74) while aliovalent doping BiCuOSe has been shown to decrease the electrical conductivity and thermoelectric power factor and give low thermal conductivity and *ZT* values in BiOCu$_{1-x}$*M$_x$*Se (*M* = Cd, Zn) although Ren *et al* showed that Zn doping enhanced the power factor.[21,22,54–58] In contrast, Bi$_{1-x}$Sn$_x$CuOSe (*ZT* = 0.3) showed an increase in the electrical conductivity, thermoelectric power factor and Seebeck coefficients.[59] Moreover, electron doping in BiCuOSe$_{1-x}$Cl$_x$ has been shown to decrease the electrical conductivity and have an effect on thermal transport properties.[60]
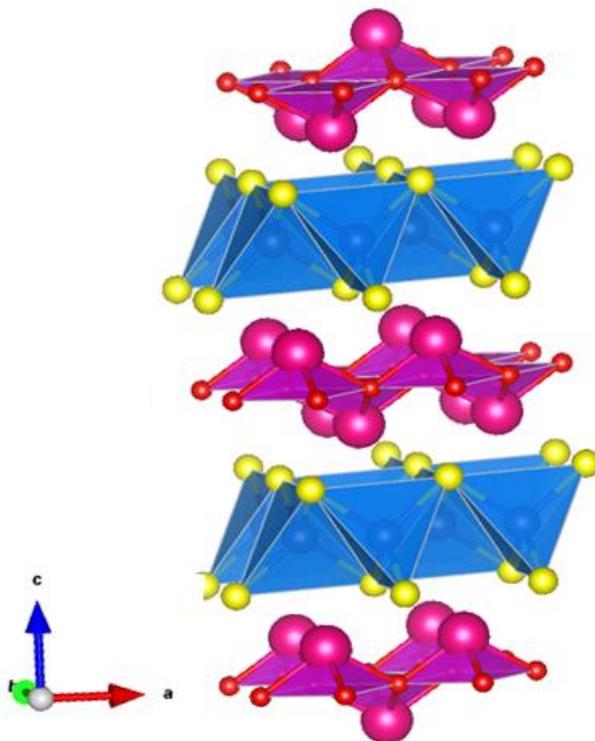
Figure 6.01. Crystal structure of BiCuOSe. Bi atoms are in pink, Cu atoms are in blue, O atoms are in red and Se atoms are in yellow.

Recent theoretical studies of BiCuOSe suggest that its low thermal conductivity is due to the high atomic mass of Bi in the insulating oxide layers which gives rise to lower phonon frequencies.[61] Band structure calculations showed that BiCuOSe is a multiband material and has an indirect band gap.[17,19] The valence bands consist of O 2*s* states (lower level), Se 4*s* and Bi 6*s* states (middle level) and O 2*p*, Cu 3*d* and Se 4*p* states (upper level) while the conduction bands consist of Bi-6*p* states.[19] Zou *et al* showed that the optimal doping level on the Bi site was 12.5 % to give *ZT*= 1.32 at 1000 K and that

the electrical conductivity decreases both with increasing temperature and increasing doping concentrations while exhibiting metallic behaviour.[62]

The aims of this work are to electron dope BiCuOSe and to investigate the resulting changes in structure and physical properties. Even though $Bi_{1-x}La_xCuOSe$ did not improve the thermoelectric properties, Ce-doping on the Bi^{3+} site was chosen because although Ce^{3+} and La^{3+} are similar in size to Bi^{2+}, there is a possibility that Ce^{3+}, with the accessible +4 oxidation state, may be able to electron dope the Cu-Se layers. [22,63]

This chapter deals with the synthesis and properties of $Bi_{1-x}Ln_xCuA_yO_{1-y}Se$ (*Ln* = Ce and *A* = F) series of compounds, focusing on their structures, electrical conductivity properties and chemical states. Structures were characterised using X-ray powder diffraction (XRPD) complemented by Rietveld refinement, Scanning Electron Microscopy-Energy Dispersive X-ray (SEM-EDX) for homogeneity, Physical Property Measurement System (PPMS) for conductivity and X-ray absorption near-edge structure (XANES) for the chemical states.

6.2 Results

6.2.1 BiCuOSe

6.2.1.1 Synthesis and Structural characterization

BiCuOSe was prepared from stoichiometric amounts of Bi_2O_3 (Acros Organics, 99.9%), Bi (Alfa-Aesar, 99.5%), Cu (Fisons) and Se (Sigma-Aldrich, 99.5+%) as discussed in Chapter 2.2.2. The starting reagents were weighed in a 1:1:3:3 ratio and ground using a mortar and pestle in the glovebox. The mixture was then pressed into a 5mm pellet and placed in a quartz tube. The latter was then sealed under vacuum and heated in a furnace at the following conditions: ramped to 300°C at 0.5°C/min and dwelled for 15 hours, ramped to 700°C at 1°C/min and dwelled for 24 hours. The furnace was then allowed to cool to room temperature. The mixture was reground, resealed and reheated at the same temperature conditions to ensure crystalline materials. This synthesis gave a highly crystalline sample containing 0.36 ± 0.04 % Bi impurity phase (Figure 6.02). The purity of the sample, confirmed by SEM-EDX (Appendix 6.01), suggested $BiCu_{0.34\pm0.19}Se_{0.36\pm0.07}$ (normalised to Bi).

6.2.1.2 X-ray powder diffraction

The resulting black pellet was then analysed by in-house X-ray powder diffraction (Figure 6.02). The amorphous background seen between 5° and 10° was due to air scattering of the X-rays. A small impurity phase of Bi was present in the sample. The refinement was performed as described in Chapter 2.2.2. The only deviations applied to the refinement were a 15th order Chebychev polynomial function which was employed to fit the background and 2 atomic positions: z coordinates for Bi and Se of the main phase. The R_{wp} for the refinement was 6.93 %, the χ^2 was 3.04. Data for some of the relevant parameters are shown in Table 6.01.

Data is in somewhat good agreement with literature. The cell parameter and unit cell volume values obtained here differ from literature, probably due to the Bi impurity and are more similar to those of $BiCuO_{1-x}Se$.[16]
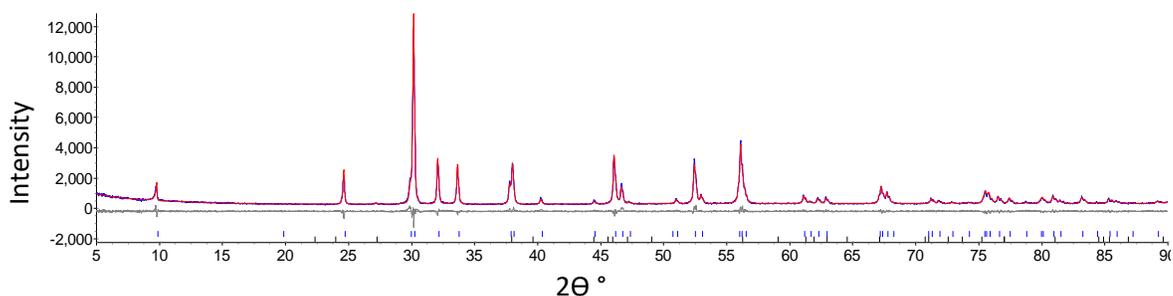
Figure 6.02 Rietveld refinement profiles for BiCuOSe using room temperature XRPD data. R_{wp} is 6.93 %, Rp is 5.43 % and χ^2 is 3.04. The observed data is in black, calculated data is in red and the difference is in grey. The blue vertical tick marks show the predicted peak positions for BiCuOSe (99.64 ± 0.04 %) and the black ones show those for Bi 0.36 ± 0.04%).

Table 6.01 Data for room temperature Rietveld refinement for BiCuOSe together with values from the literature, values from $BiCuO_{1-x}Se$, BiCuOS and CeCuOSe for comparison.

BiCuOSe	This work	Kusainova et al[1]	Liu et al[16] BiCuO$_{1-x}$Se (0≤ x ≤ 0.1)	BiCuOS[1]	CeCuOSe[64]
Space group	P4/nmm	P4/nmm		P4/nmm	P4/nmm
a cell parameter (Å)	3.929187 (9)	3.9213 (1)	3.931-3.926	3.8705 (5)	4.0185 (15)
c cell parameter (Å)	8.932318 (7)	8.9133 (5)	8.964-8.936	8.561 (1)	8.7114 (14)
Volume (Å^3)	137.902 (6)	137.09 (3)		128.25 (1)	
Bi z coordinate (c)	0.14026 (1)	0.1411 (7)			
Se z coordinate (c)	0.67669 (6)	0.680 (2)			

6.2.1.3 Conductivity measurements

Conductivity measurements were conducted on BiCuOSe as described in Chapter 2.2.7. Resistance was collected as the pellet was cooled from room temperature to 2 K in a cryostat with readings taken at every 1 K.
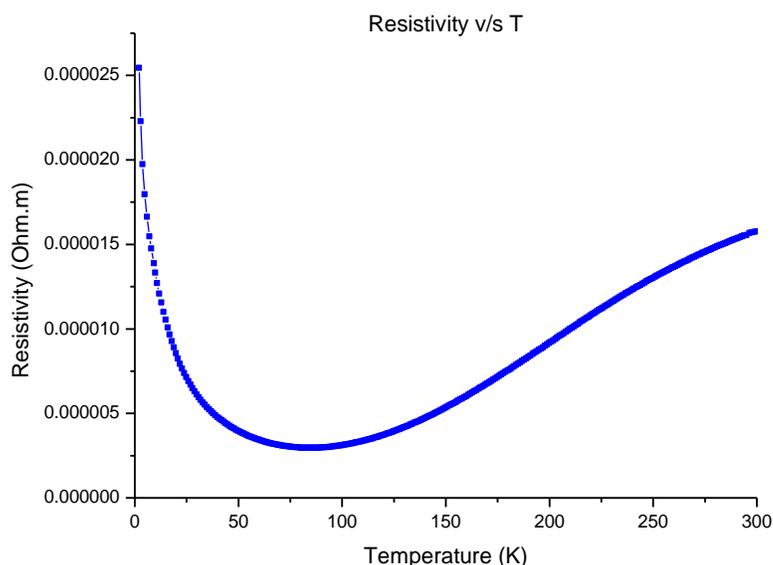
Figure 6.03 Resistivity against temperature. Data is shown in blue

The exponential change in resistivity with temperature is not consistent with literature.[2,16,18,19,65,66] The change instead looks like a semiconductor-metal transition whereby it exhibits metallic behaviour at high temperatures (above 80 K), seen by the decrease in electrical resistivity due to increased electron scattering, and behaves like a semiconductor at low temperatures, seen by the increase in electrical resistivity due to the Fermi level not being in the conduction band. This is not consistent with literature.[19,65] These observations may correspond to Cu deficiencies in the pristine sample.[16]

6.2.2 BiCuO$_{1-x}$F$_x$Se

6.2.2.1 Synthesis

BiCuO$_{1-x}$F$_x$Se was prepared from stoichiometric amounts of Bi$_2$O$_3$ (Acros Organics, 99.9%), Bi (Alfa-Aesar, 99.5%), Cu (Fisons) and Se (Sigma-Aldrich, 99.5+%) and CuF$_2$ (Acros Organics, 98%) using the method described in 6.2.1.1.

6.2.2.2 X-ray powder diffraction

The resulting black pellets were then analysed by Rietveld refinement (Figure 6.04). The amorphous background seen between 5° and 18° was due to air scattering of the X-rays. Al_2O_3 was used as an internal standard. Small impurity phases of Bi_2O_3 and Bi_4Se_3 were present in the samples. The refinement was performed as described in 6.2.1.2. The only deviation was accounting for the internal standard (Al_2O_3). Data for some of the relevant parameters for $BiCuO_{1-x}F_xSe$ ($0 \leq x \leq 0.12$) are shown in Table 6.02.

Table 6.02 Data for room temperature Rietveld refinement for $BiCuO_{1-x}F_xSe$ ($0 \leq x \leq 0.12$). 32 parameters were used for the refinements.

$BiCuO_{1-x}F_xSe$	X = 0	X = 0.02	X = 0.05	X = 0.08	X = 0.10	X = 0.12
a (Å)	3.920874 (6)	3.919275 (7)	3.919876 (8)	3.919386 (1)	3.919671 (4)	3.919921 (0)
c (Å)	8.912630 (2)	8.906457 (1)	8.910356 (5)	8.907517 (2)	8.908800 (6)	8.910069 (6)
Volume (Å³)	137.016 (3)	136.810 (2)	136.911 (0)	136.834 (2)	136.873 (0)	136.910 (3)
Bi z coordinate (c)	0.14034 (1)	0.13893 (9)	0.14088 (1)	0.14108 (2)	0.14151 (1)	0.14137 (9)
Se z coordinate (c)	0.67146 (9)	0.67432 (7)	0.67251 (8)	0.67886 (1)	0.67829 (2)	0.68424 (2)
R_{wp} (%)	18.43	19.67	20.63	22.81	21.58	23.18
χ^2	2.46	2.60	2.80	3.00	2.18	3.04
Bi_2O_3 (%)	-	2.35 ± 0.31	4.07 ± 0.33	8.85 ± 0.55	5.71 ± 0.38	7.66 ± 0.55
Bi_4Se_3 (%)	-	5.76 ± 0.70	9.95 ± 0.59	18.13 ± 0.82	13.38 ± 0.68	11.35 ± 0.71

The samples were then overlaid on top of one another to check for any differences (Figure 6.05).
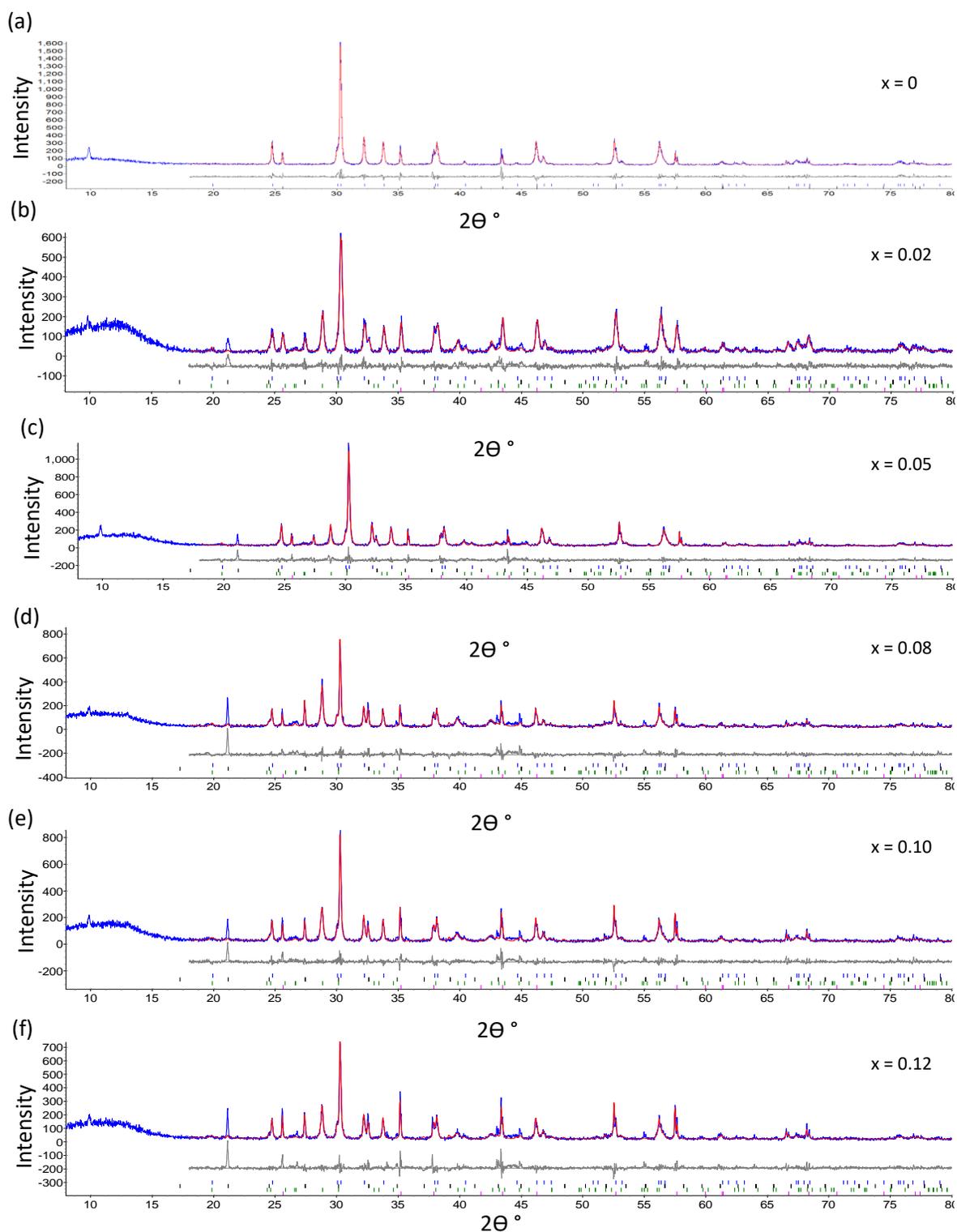
Figure 6.04 Rietveld refinement profiles for BiCuO$_{1-x}$F$_x$Se (0 ≤ x ≤ 0.12) using room temperature XRPD data (a) x = 0 (b) x = 0.02 (c) x = 0.05 (d) x = 0.08 (e) x = 0.10 and (f) x = 0.12. The observed data is in blue the calculated data is in red and the difference is in grey. The blue vertical tick marks show the predicted peak positions for BiCuOSe, the black tick marks show those for Al$_2$O$_3$ in BiCuOSe and for Bi$_2$O$_3$ in the doped samples, the green tick marks show those for Bi$_4$Se$_3$ and the pink tick marks show those for Al$_2$O$_3$. R_{wp} and the χ^2 values are given in table 6.02.
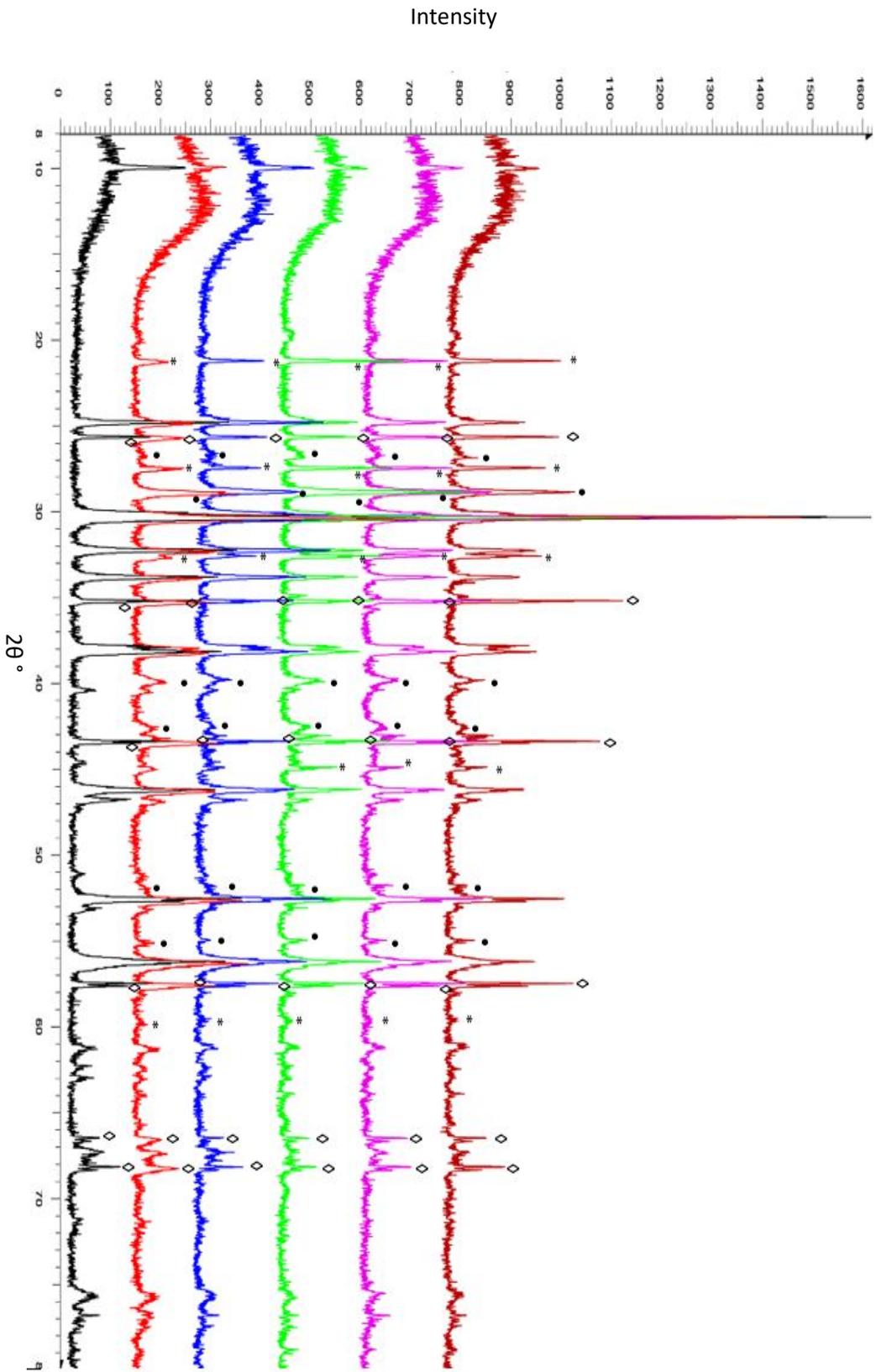
Figure 6.05 Overlay of room temperature XRPD data for $BiCuO_{1-x}F_xSe$ ($0 \le x \le 0.12$), $x=0$ (black, bottom) to $x=0.12$ (brown, top). BiCuOSe is in black, $BiCuO_{0.98}F_{0.02}Se$ is in red, $BiCuO_{0.95}F_{0.05}Se$ is in blue, $BiCuO_{0.92}F_{0.08}Se$ is in green, $BiCuO_{0.9}F_{0.1}Se$ is in pink and $BiCuO_{0.88}F_{0.12}Se$ is in brown. $\Diamond$ denotes the peaks for Al_2O_3. * denotes the impurity phases Bi_2O_3 and • for Bi_4Se_3.
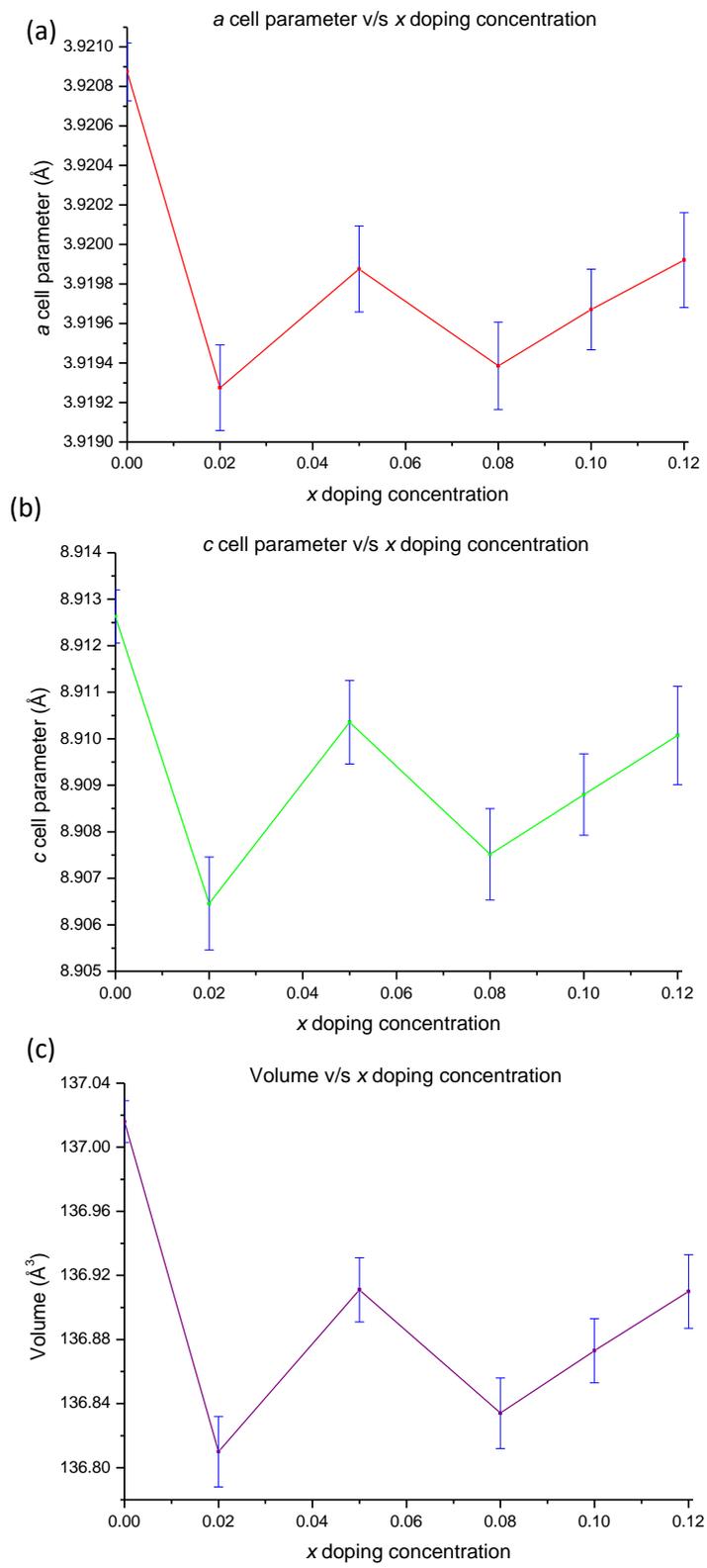
Figure 6.06 (a) Unit cell parameter *a* (red), (b) unit cell parameter *c* (green) and (c) volume (purple) as a function of *x* for BiCuO$_{1-x}$F$_x$Se determined from Rietveld refinements using room temperature XRPD data. Error bars in blue.

There are very few other changes in structure with dopant level (Appendix 6.02). Analysis from XRPD data indicates that there is no systematic change in unit cell parameters with F doping which suggests that none enters the main phase. The change in c cell parameter with dopant level is slightly larger than that for a cell parameter (by 0.01%).

6.2.2.3 SEM-EDX

An overall backscattered secondary electrons image for each sample was taken at a magnification between X43-X50 to get an idea of the homogeneity of the sample. An example is given in Appendix 6.03. From the backscattered image and spectra, all the samples were fairly homogenous. Some of the sites that were picked were rich in Bi. The average composition from all the normal points, assuming oxygen content and normalizing the data with respect to Bi, is $BiCu_{0.86\pm0.16}Se_{0.79\pm0.09}$ for $BiCuO_{0.98}F_{0.02}Se$, $BiCu_{0.93\pm0.21}Se_{0.86\pm0.12}$ for $BiCuO_{0.95}F_{0.05}Se$, $BiCu_{0.88\pm0.23}Se_{0.78\pm0.12}$ for $BiCuO_{0.92}F_{0.08}Se$, $BiCu_{0.93\pm0.28}Se_{0.81\pm0.13}$ for $BiCuO_{0.9}F_{0.1}Se$, and $BiCu_{0.83\pm0.22}Se_{0.84\pm0.15}$ for $BiCuO_{0.88}F_{0.12}Se$.

6.2.2.4 Conductivity measurements

Conductivity measurements were conducted on all the doped samples. The sintered polished pellets had density between 5.470-6.023 g cm^{-3}, which were 61.3-67.5 % of the theoretical densities. Resistance measurements were collected as the pellets cooled from room temperature to 2 K in a cryostat with readings taken at every 1 K.

The exponential decrease in resistivity with decreasing temperature indicates metallic behaviour (Figure 6.07). This could be a result of the various impurities in the doped samples. The resistivity at room temperature decreases slightly when the parent compound is doped with F (Table 6.03), however, this could be due to the impurities present in the doped samples.
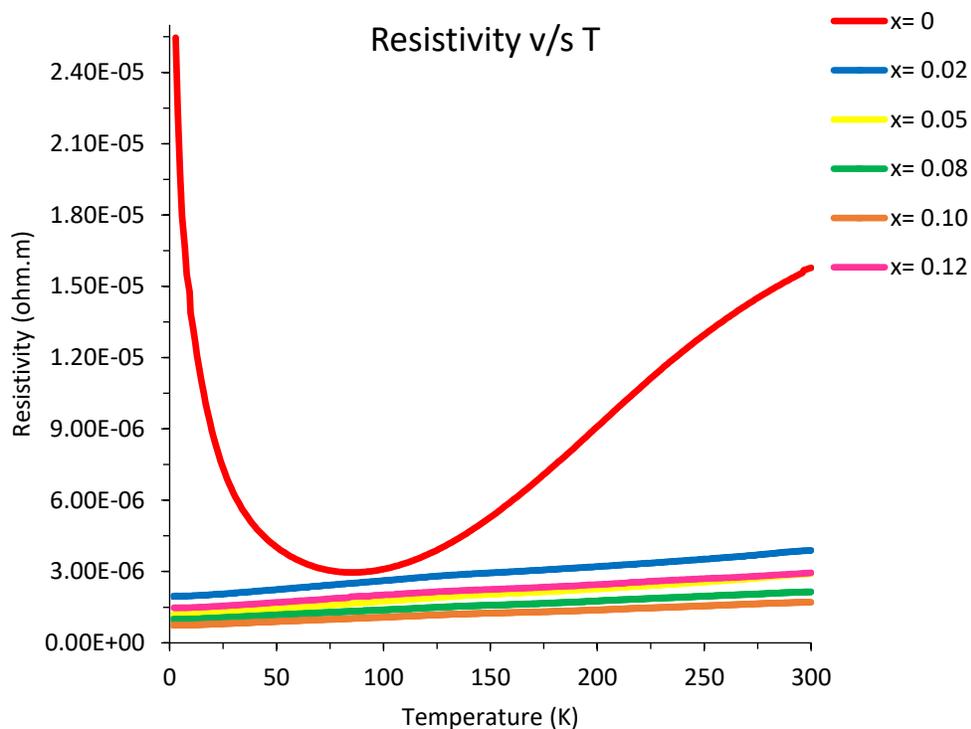
Figure 6.07 Measure of Resistivity (Ohm.m) as a function of temperature for different F doping in $BiCuO_{1-x}F_xSe$, showing metallic behaviour. BiCuOSe is in red, $BiCuO_{0.98}F_{0.02}Se$ is in blue, $BiCuO_{0.95}F_{0.05}Se$ is in yellow, $BiCuO_{0.92}F_{0.08}Se$ is in green, $BiCuO_{0.9}F_{0.1}Se$ is in orange and $BiCuO_{0.88}F_{0.12}Se$ is in pink.

Table 6.03 Resistivity data for $BiCuO_{1-x}F_xSe$ ($0 \leq x \leq 0.12$).

X	ρ at 298K (Ωm)
0	1.57×10^{-5}
0.02	3.88×10^{-6}
0.05	2.90×10^{-6}
0.08	2.14×10^{-6}
0.10	1.71×10^{-6}
0.12	2.94×10^{-6}

6.2.2.5 XANES measurements

XANES measurements were conducted on all the doped samples on B18 at the Diamond Light Source (through the Energy Materials BAG). Similar to the Ce-doped samples, these samples were mixed with PVP as outlined in Absorbix software and pressed into 13 mm pellets.
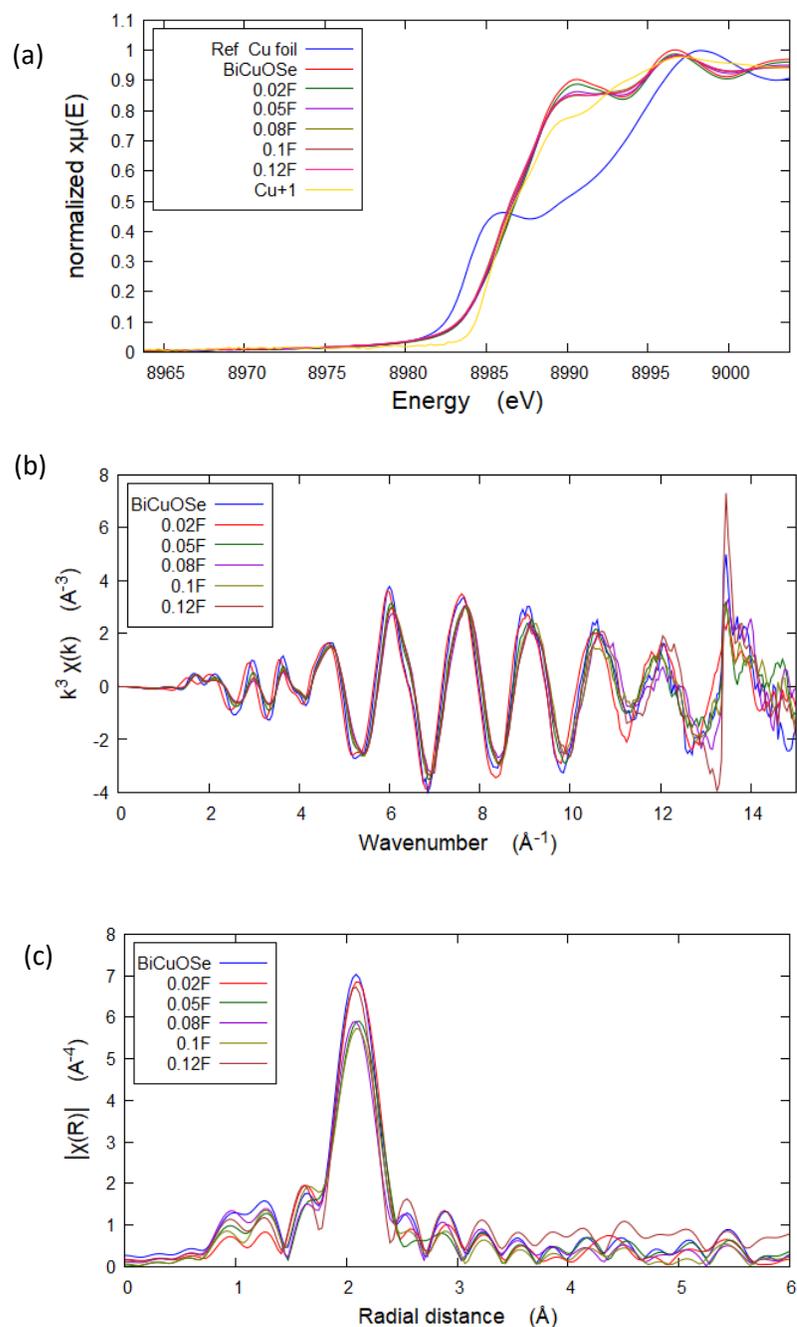
Figure 6.08 (a) Cu-*K* edge normalised energy spectra for the Cu foil (blue), Cu^{+1} standard (yellow), pristine sample (red) and all the Ce-doped samples (b) k^3-weighted derivatives (c) radial distributions surrounding Cu for the undoped and F-doped samples.

The Cu-*K* edge data shows that the samples contain mainly monovalent Cu (Figure 6.08a). The edge does not change since the oxidation state is unchanged which is consistent with no F entering the sample. The EXAFS region suggests a slight increase in disorder in the sample with increased F content (Figure 6.08). These observations could be due to the increased impurities formation when more F is added as dopant in the samples. The shoulder to Cu foil (Figure 6.08a) shows transitions

from 1 s to 4 p of Cu^0. In the Fourier transform spectra (Figure 6.08b), the strongest peak observed around 2 Å arises from the first coordination Cu–Se shell. The weak peaks observed from the second higher coordination shells can be seen in the k^3-weight-amplified spectra (Figure 6.08c). Energy E_0 barely changes with increasing F content, except for x = 0.02, suggesting that the number of unoccupied states remain unchanged with increasing F content (Table 6.04).

Table 6.04 Energy E_0 for $BiCuO_{1-x}F_xSe$ (0 ≤ x ≤ 0.12).

Sample	E_0 (eV)
BiCuOSe	8986.25
$BiCuO_{0.98}F_{0.02}Se$	8988.18
$BiCuO_{0.95}F_{0.05}Se$	8985.96
$BiCuO_{0.92}F_{0.08}Se$	8985.80
$BiCuO_{0.9}F_{0.1}Se$	8985.75
$BiCuO_{0.88}F_{0.12}Se$	8985.69

6.2.3 $Bi_{1-x}Ce_xCuOSe$

6.2.3.1 Synthesis

$Bi_{1-x}Ce_xCuOSe$ was prepared from stoichiometric amounts of Bi_2O_3 (Acros Organics, 99.9%), Bi (Alfa-Aesar, 99.5%), Cu (Fisons) and Se (Sigma-Aldrich, 99.5+%) and CeO_2 (Acros Organics, 99.9%) using the method described in 6.2.1.1.

6.2.3.2 X-ray powder diffraction

The resulting black pellets were then analysed by Rietveld refinement (Figure 6.09). The amorphous background seen between 5° and 10° was due to air scattering of the X-rays. Small impurity phases of Bi, CeO_2 and CeO_{2-x} were present in the samples. The refinement was performed as described in 6.2.1.2. Data for some of the relevant parameters for $Bi_{1-x}Ce_xCuOSe$ (0 ≤ x ≤ 0.1) are shown in Table 6.05.
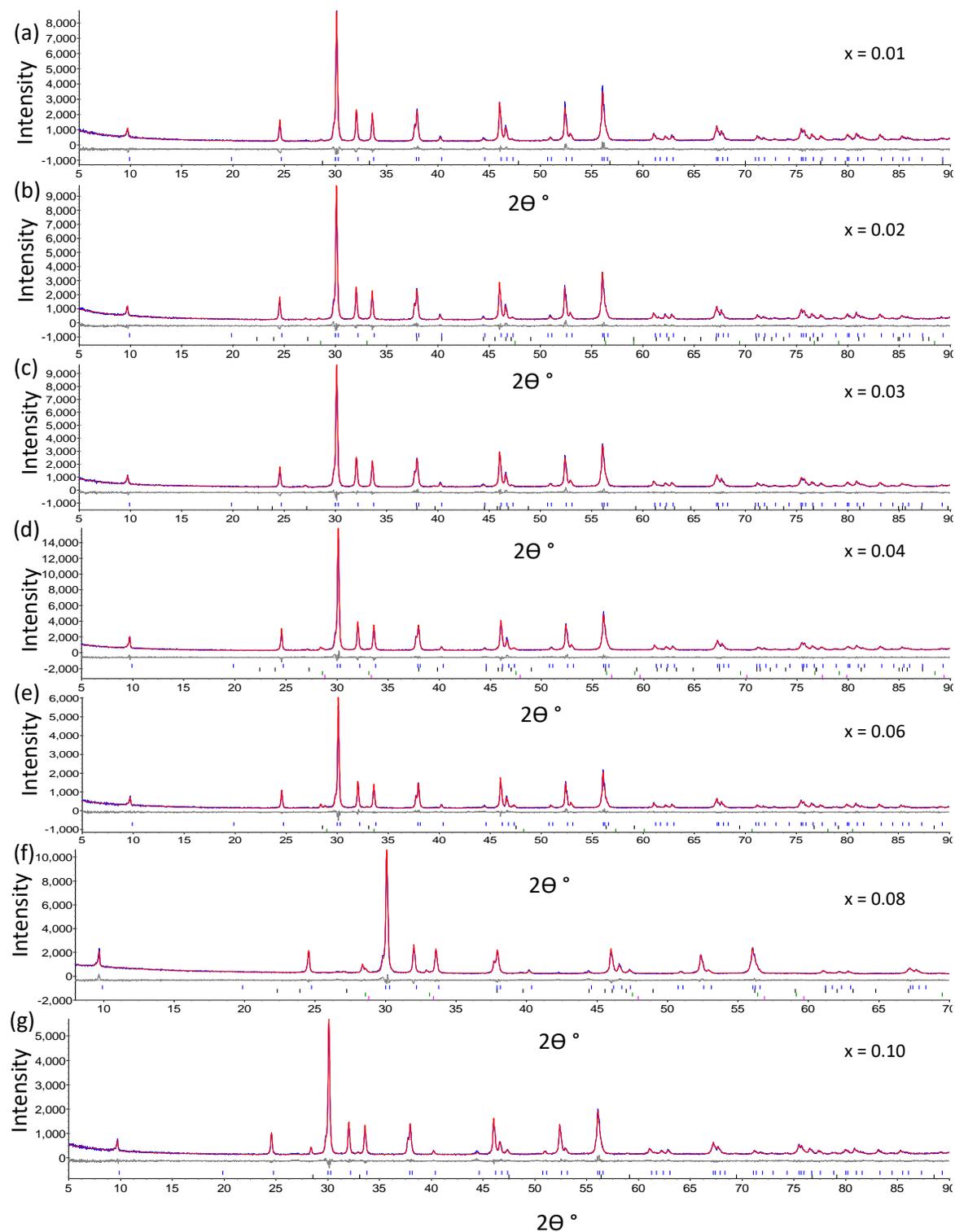
Figure 6.09 Rietveld refinement profiles for Bi$_{1-x}$Ce$_x$CuOSe (0 ≤ x ≤ 0.1) using room temperature XRPD data (a) x = 0.01 (b) x = 0.02 (c) x = 0.03 (d) x = 0.04 (e) x = 0.06 (f) x = 0.08 and (g) x = 0.1. The observed data is in blue the calculated data is in red and the difference is in grey. The blue vertical tick marks show the predicted peak positions for BiCuOSe, the black tick marks show those for Bi in (b-d) and (f), CeO$_2$ in (a) and CeO$_{2-x}$ in (e) and (g), the green tick marks show those for CeO$_{2-x}$ in (b), (d) and (f) and CeO$_2$ in (e) and the pink tick marks show those for CeO$_2$ in (d) and (f). R_{wp} and the χ2 values are given in table 6.05.

Table 6.05 Data for room temperature Rietveld refinement for $Bi_{1-x}Ce_xCuOSe$ ($0 \le x \le 0.1$). 36 parameters were used for the refinements.

$Bi_{1-x}Ce_xCuOSe$	X = 0	X = 0.01	X = 0.02	X = 0.03	X = 0.04	X = 0.06	X = 0.08	X = 0.10
a (Å)	3.929187 (9)	3.929455 (4)	3.927800 (4)	3.929897 (4)	3.926676 (1)	3.927990 (5)	3.927362 (5)	3.926574 (4)
c (Å)	8.932318 (7)	8.932634 (1)	8.928790 (3)	8.933142 (2)	8.927501 (9)	8.928559 (9)	8.928233 (0)	8.926842 (1)
Volume (Å^3)	137.902 (6)	137.925 (7)	137.750 (7)	137.964 (7)	137.651 (7)	137.760 (7)	137.711 (0)	137.634 (9)
Bi z coordinate (c)	0.14026 (1)	0.14008 (0)	0.14025 (4)	0.14003 (9)	0.13983 (4)	0.14018 (2)	0.13962 (7)	0.13977 (3)
Se z coordinate (c)	0.67669 (6)	0.67627 (7)	0.67590 (7)	0.67605 (7)	0.67502 (5)	0.67623 (9)	0.67622 (6)	0.67616 (8)
R_{wp} (%)	6.93	6.83	6.64	6.84	6.33	7.41	6.80	7.31
χ^2	3.04	2.88	2.76	2.82	3.08	2.30	2.90	2.30
Main phase		96.85 ± 1.86	98.68 ± 0.10	99.02 ± 0.11	95.06 ± 1.17	92.96 ± 1.55	89.22 ± 1.18	96.33 ± 0.12
CeO_2 (%)	-	3.15 ± 1.86	-	-	2.82 ± 1.19	4.74 ± 1.58	5.61 ± 1.23	-
CeO_{2-x} (%)	-	-	0.82 ± 0.08	-	1.71 ± 0.09	2.30 ± 0.11	4.65 ± 0.20	3.67 ± 0.12
Bi (%)	0.36	-	0.50 ± 0.06	0.98 ± 0.11	0.41 ± 0.05	-	0.51 ± 0.08	-

The samples were then overlaid on top of one another to check for any differences (Figure 6.10).
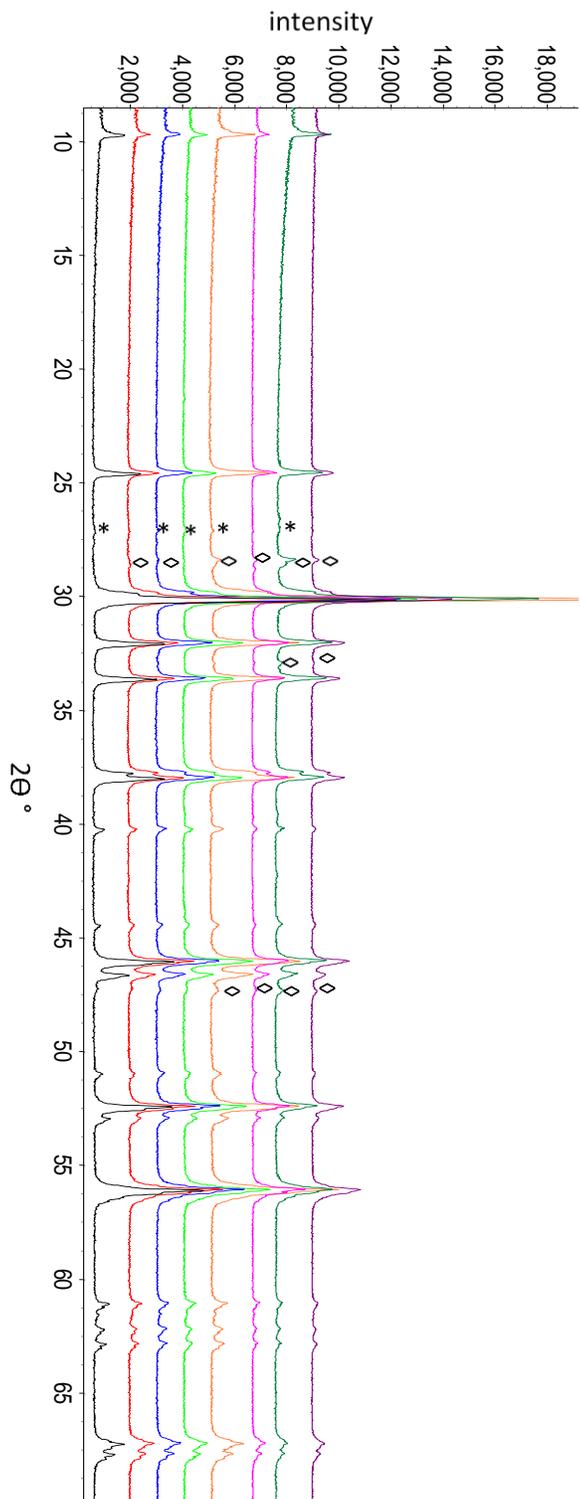
Figure 6.10 Overlay of room temperature XRPD data for $Bi_{1-x}Ce_xCuOSe$ ($0 \leq x \leq 0.1$), $x = 0$ (black, bottom) to $x = 0.1$ (purple, top). BiCuOSe is in black, $Bi_{0.99}Ce_{0.01}CuOSe$ is in red, $Bi_{0.98}Ce_{0.02}CuOSe$ is in blue, $Bi_{0.97}Ce_{0.03}CuOSe$ is in green, $Bi_{0.96}Ce_{0.04}CuOSe$ is in orange, $Bi_{0.94}Ce_{0.06}CuOSe$ is in pink, $Bi_{0.92}Ce_{0.08}CuOSe$ is in dark green and $Bi_{0.9}Ce_{0.1}CuOSe$ is in purple. * denotes the impurity phase Bi. ◊ denotes the impurity phase CeO_2 and CeO_{2-x}.
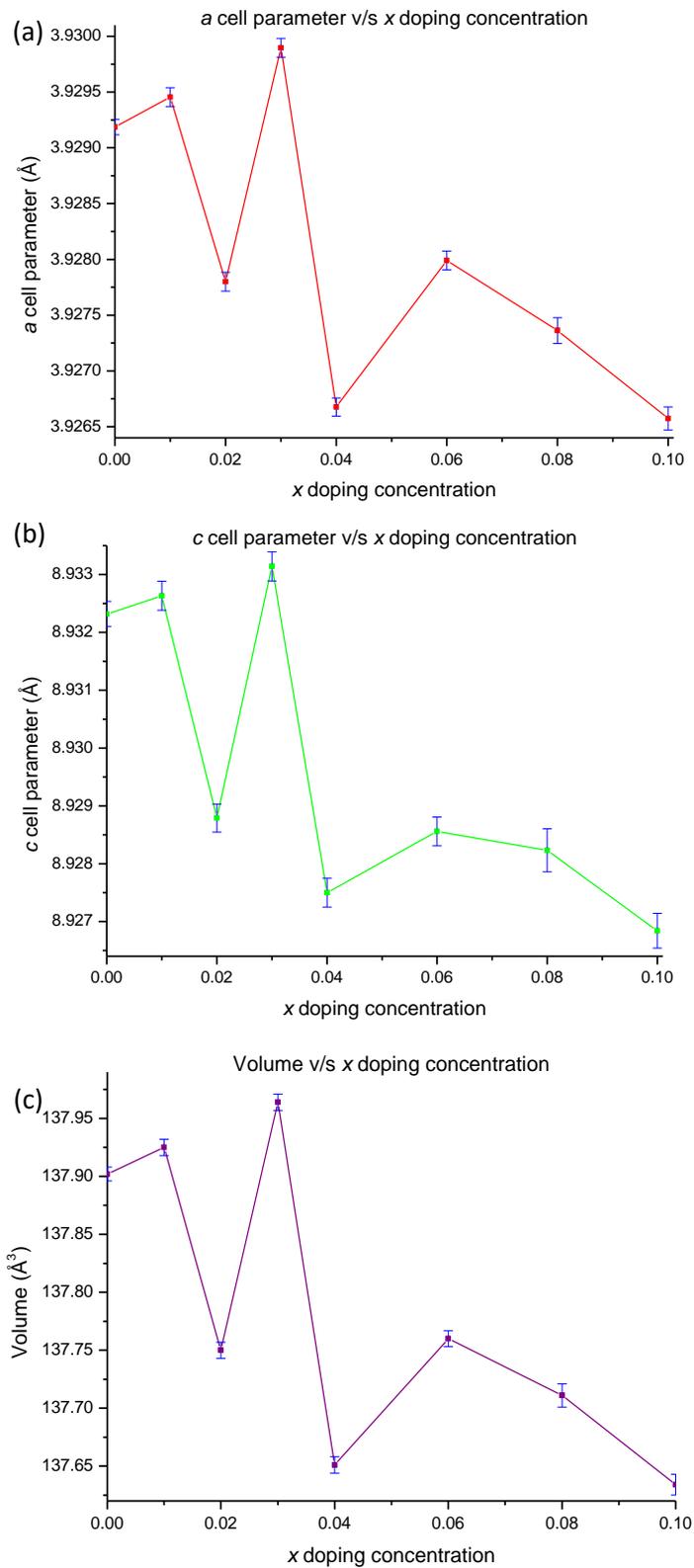
Figure 6.11 (a) Unit cell parameter *a* (red)*,* (b) unit cell parameter *c* (green) and (c) volume (purple) as a function of *x* for Bi$_{1-x}$Ce$_x$CuOSe determined from Rietveld refinements using room temperature XRPD data. Error bars in blue.

There are very few other changes in structure with dopant (Appendix 6.05). The overall trend is slight decrease in unit cell volume with increasing Ce content (Figure 6.11c), consistent with the ionic radii of Bi^{3+} (1.03 Å) and Ce^{3+} ions (1.01 Å).[67] Room temperature unit cell parameters for $Bi_{1-x}Ce_xCuOSe$ (0 ≤ x ≤ 0.1) are in agreement with those of BiCuOSe and are bigger along *c* but smaller along *a* than those of CeCuOSe.[64] The change in *c* cell parameter with dopant level was smaller than that for the *a* cell parameter (by 0.02%). There is a limited solid solution, with x = 0.01 being the limit, as seen by Vegard's law even though the end members are isostructural.[68]

6.2.3.3 SEM-EDX

An overall backscattered secondary electrons image for each sample was taken at a magnification between X44-X194 to get an idea of the homogeneity of the sample. An example is given in Appendix 6.06. From the backscattered images and spectra, all the samples were fairly homogenous. Most of the sites that were picked were rich in Bi and Cu impurities. The average composition from all the normal points, assuming oxygen content and normalizing the data with respect to Se, is $Bi_{1.05\pm0.13}Ce_{0.02\pm0.02}Cu_{1.01\pm0.24}OSe$ for $Bi_{0.99}Ce_{0.01}CuOSe$, $Bi_{1.02\pm0.07}Ce_{0.03\pm0.02}Cu_{1.02\pm0.21}OSe$ for $Bi_{0.98}Ce_{0.02}CuOSe$, $Bi_{1.08\pm0.11}Ce_{0.03\pm0.01}Cu_{1.06\pm0.25}OSe$ for $Bi_{0.97}Ce_{0.03}CuOSe$, $Bi_{1.03\pm0.07}Ce_{0.03\pm0.02}Cu_{1.05\pm0.19}OSe$ for $Bi_{0.96}Ce_{0.04}CuOSe$, $Bi_{0.98\pm0.11}Ce_{0.04\pm0.03}Cu_{1.05\pm0.19}OSe$ for $Bi_{0.94}Ce_{0.06}CuOSe$, $Bi_{0.97\pm0.08}Ce_{0.05\pm0.04}Cu_{1.02\pm0.23}OSe$ for $Bi_{0.92}Ce_{0.08}CuOSe$ and $Bi_{0.93\pm0.10}Ce_{0.07\pm0.04}Cu_{1.05\pm0.15}OSe$ for $Bi_{0.9}Ce_{0.1}CuOSe$.

6.2.3.4 Conductivity measurements

Conductivity measurements were conducted on all the doped samples. The sintered polished pellets had density between 4.922-6.679 g cm^{-3}, which were 56.4-75.9 % of the theoretical densities. Resistance measurements were collected as the pellets cooled from room temperature to 2 K in a cryostat with readings taken at every 1 K.
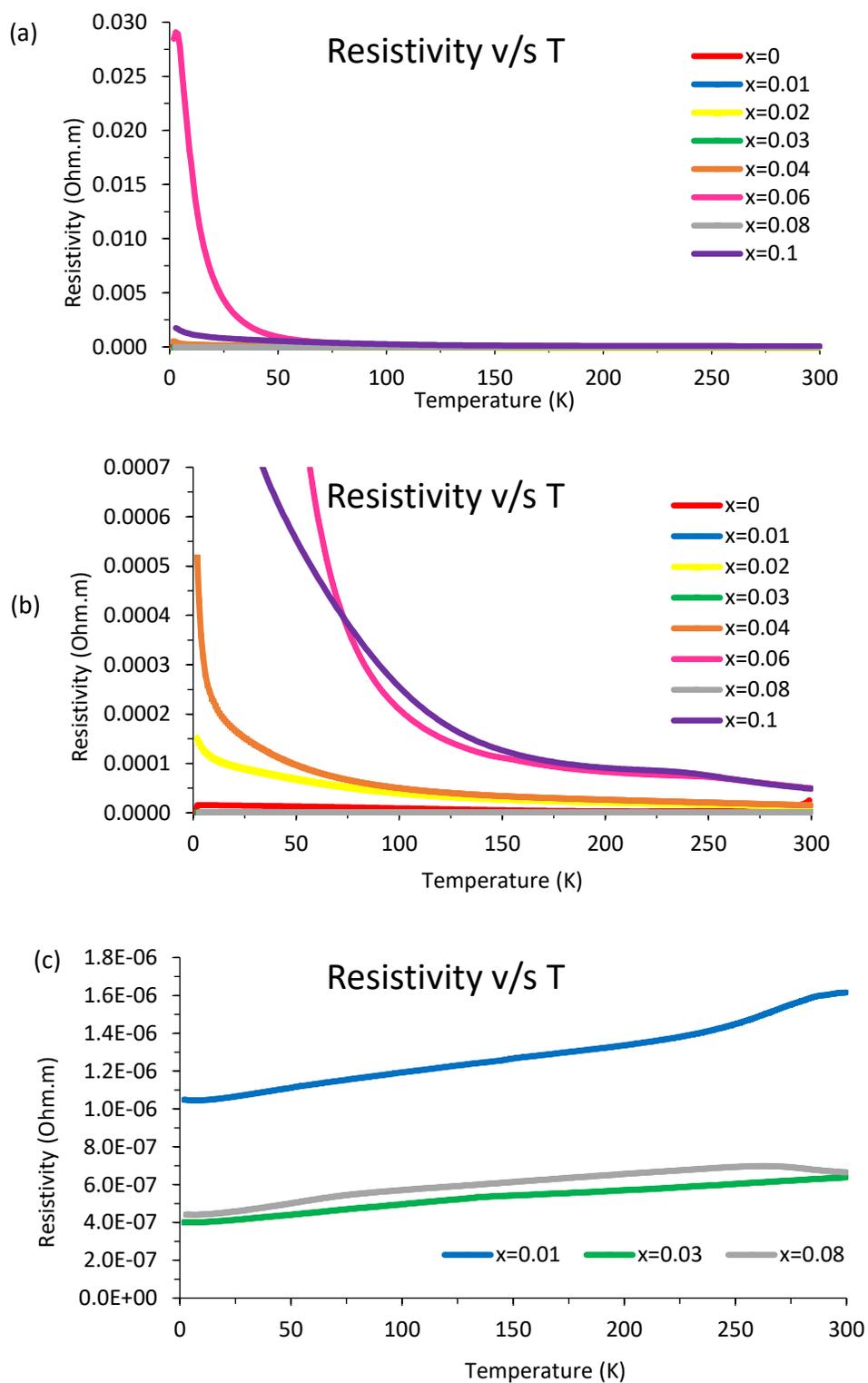
Figure 6.12 Measure of Resistivity (Ohm.m) as a function of temperature for different Ce doping in $Bi_{1-x}Ce_xCuOSe$. $BiCuOSe$ is in red, $Bi_{0.99}Ce_{0.01}CuOSe$ is in blue, $Bi_{0.98}Ce_{0.02}CuOSe$ is in yellow, $Bi_{0.97}Ce_{0.03}CuOSe$ is in green, $Bi_{0.96}Ce_{0.04}CuOSe$ is in orange, $Bi_{0.94}Ce_{0.06}CuOSe$ is in pink, $Bi_{0.92}Ce_{0.08}CuOSe$ is in grey and $Bi_{0.9}Ce_{0.1}CuOSe$ is in purple. (a) shows all the samples (b) shows a zoomed in picture of all the samples (c) shows the samples having metallic behaviour.
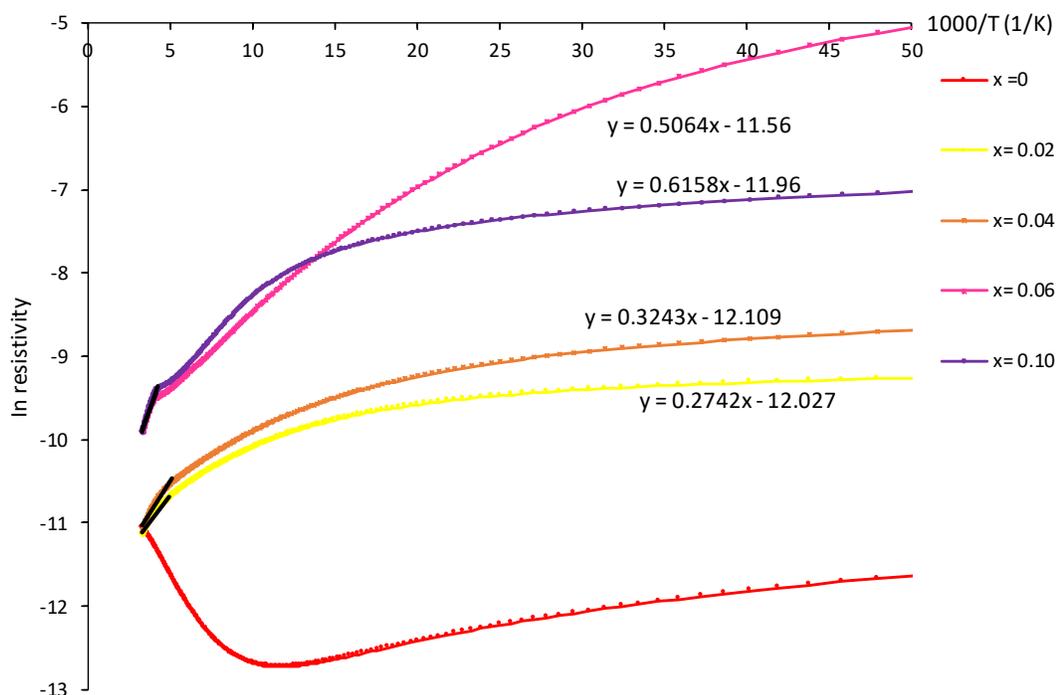
Figure 6.13 Measure of ln resistivity as a function of 1000/T, showing linearity at high temperatures for all samples. BiCuOSe is in red, $Bi_{0.98}Ce_{0.02}CuOSe$ is in yellow, $Bi_{0.96}Ce_{0.04}CuOSe$ is in orange, $Bi_{0.94}Ce_{0.06}CuOSe$ is in pink, and $Bi_{0.9}Ce_{0.1}CuOSe$ is in purple. The trendlines are shown in black.
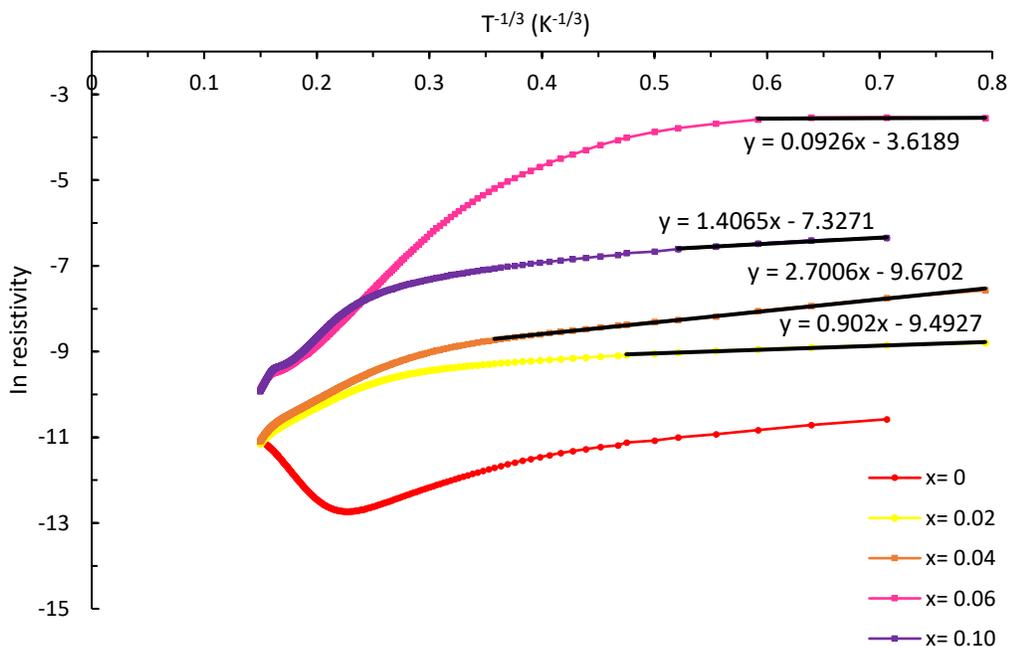
Figure 6.14 Measure of ln resistivity as a function of $T^{-1/3}$, showing linearity at low temperatures for the semiconducting samples. BiCuOSe is in red, $Bi_{0.98}Ce_{0.02}CuOSe$ is in yellow, $Bi_{0.96}Ce_{0.04}CuOSe$ is in orange, $Bi_{0.94}Ce_{0.06}CuOSe$ is in pink and $Bi_{0.9}Ce_{0.1}CuOSe$ is in purple. The trendlines are shown in black.

The exponential increase in resistivity with decreasing temperature for $Bi_{1-x}Ce_xCuOSe$ (x = 0.02, 0.04, 0.06, 0.10) indicates semiconducting behaviour (Figure 6.13b) while the decrease in resistivity with decreasing temperature for $Bi_{1-x}Ce_xCuOSe$ (x = 0.01, 0.03, 0.08) indicates metallic behaviour (Figure 6.13c). The resistivity behaviour of the doped samples at high temperatures could be explained using the thermally activated model (Figure 6.13) but not at low temperatures, shown by the linear behaviour: T > 204 K (x = 0.02), T > 197 K (x = 0.04), T > 239 K (x = 0.06) and T > 236 K (x = 0.10). However, two-dimensional variable range hopping (2D-VRH) could be used to describe the resistivity behaviour at low temperatures for the semiconducting samples, showing a linear behaviour in the ln resistivity vs $T^{-1/3}$ plot (Figure 6.14): 2 K ≤ T ≤ 9 K (x = 0.02), 2 K ≤ T ≤ 22 K (x = 0.04), 2K ≤ T ≤ 4.5 K (x = 0.06), and 2 K ≤ T ≤ 6 K (x = 0.10). The values of ρ_0 and T_0 are given in table 6.06 together with the activation energy values of the samples calculated from the slope (Figure 6.14).

Table 6.06 Resistivity and activation energy data for $Bi_{1-x}Ce_xCuOSe$ (0 ≤ x ≤ 0.1).

X	**Model**	**T (K)**	**ρ_0**	**T_0**	**E_a (eV)**	**ρ at 298K (Ωm)**
0			-	-	-	1.57×10^{-5}
0.01			-	-	-	1.61×10^{-6}
0.02	**2D-VRH**	2 ≤ T ≤ 9	5.98×10^{-6}	7.34×10^{-1}	-	1.45×10^{-5}
	Thermally activated	T > 204	-	-	0.024 ± 0.004	
0.03			-	-	-	6.37×10^{-7}
0.04	**2D-VRH**	2 ≤ T ≤ 22	5.51×10^{-6}	19.7	-	1.54×10^{-5}
	Thermally activated	T > 197	-	-	0.028 ± 0.006	
0.06	**2D-VRH**	2 ≤ T ≤ 4.5	9.54×10^{-6}	7.94×10^{-4}	-	5.05×10^{-5}
	Thermally activated	T > 239	-	-	0.044 ± 0.003	
0.08			-	-	-	6.67×10^{-7}
0.10	**2D-VRH**	2 ≤ T ≤ 6	6.51×10^{-6}	2.78	-	4.94×10^{-5}
	Thermally activated	T > 236	-	-	0.052 ± 0.008	

6.2.3.5 XANES measurements

XANES measurements were conducted on all the doped samples on B18 at the Diamond Light Source (through the Energy Materials BAG). The samples were mixed with PVP according to Absorbix software and pressed into 13 mm pellets.
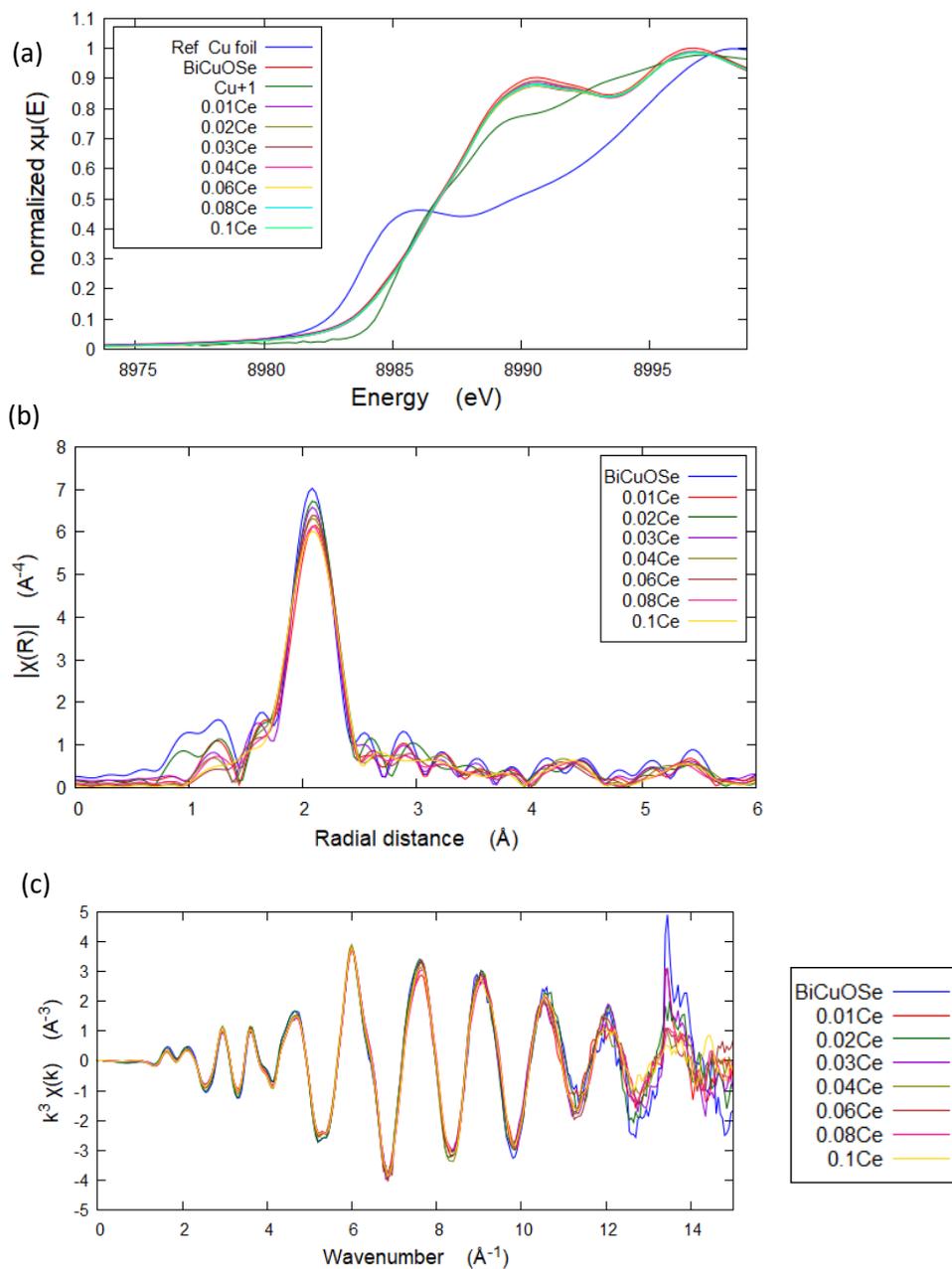
Figure 6.15 (a) Cu-*K* edge normalised energy spectra for the Cu foil (blue), Cu^{+1} standard (dark-green), pristine sample (red) and all the Ce-doped samples (b) k^3-weighted derivatives (c) radial distributions surrounding Cu for the undoped and Ce-doped samples.
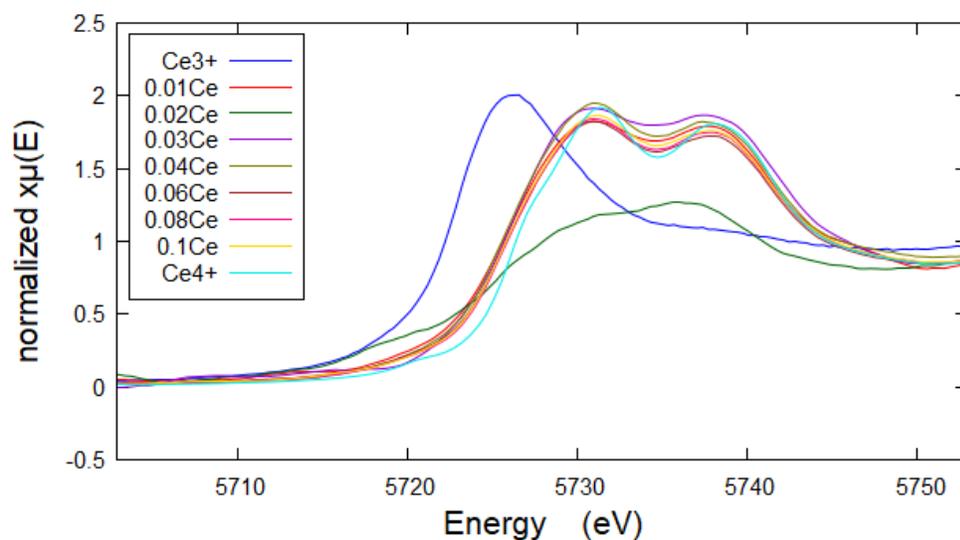
Figure 6.16 Ce-L_3 edge normalised energy spectra for the Ce^{3+} standard (blue), Ce^{4+} standard (aqua) all the Ce-doped samples

The Cu-K edge data shows that when Ce is introduced in the pristine sample, there is no obvious trend in the main edge and no indication of a change in Cu oxidation state in the samples with doping (Figure 6.15a and Appendix 6.07). The shoulder to Cu foil (Figure 6.18a) shows transitions from 1 s to 4 p of Cu^0. In the Fourier transform spectra (Figure 6.15b), the strongest peak observed around 2 Å arises from the first coordination Cu–Se shell. The peaks observed from the second higher coordination shells are hard to see as they are very weak and are concealed in the noisy background. However, the recorded k^3-weight-amplified spectra (Figure 6.15c) shows the input from the higher coordination shells. Energy E_0 for Cu increases very slightly with increasing Ce content (Table 6.07), suggesting that the number of unoccupied states barely changes with Ce content.

The Ce-L_3 edge data shows that the Ce-doped samples contain doublets in their main edge suggesting presence of Ce^{4+} (Figure 6.16 and Appendix 6.07). No clear trend is observed in the main edge (Figure 6.16 and Appendix 6.07). The pre-edge area suggests that the Ce-doped samples contain mainly Ce^{4+} ions as it fits the Ce^{4+} standard used (Figure 6.16 and Appendix 6.07). Energy E_0 for Ce barely changes with increasing Ce content (Table 6.07), suggesting that the number of unoccupied states barely changes with Ce content.

Table 6.07 E_0 values for $Bi_{1-x}Ce_xCuOSe$ ($0 \leq x \leq 0.1$).

Sample	E_0 (eV) for Cu	E_0 (eV) for Ce
BiCuOSe	8986.50	-
$BiCuO_{0.99}Ce_{0.01}Se$	8986.79	5726.14
$BiCuO_{0.98}Ce_{0.02}Se$	8986.82	5725.63
$BiCuO_{0.97}Ce_{0.03}Se$	8986.80	5726.50
$BiCuO_{0.96}Ce_{0.04}Se$	8986.85	5726.00
$BiCuO_{0.94}Ce_{0.06}Se$	8986.81	5725.62
$BiCuO_{0.92}Ce_{0.08}Se$	8986.79	5725.54
$BiCuO_{0.9}Ce_{0.1}Se$	8986.82	5725.65

6.3 Discussion

The cell parameters for BiCuOSe obtained from the room temperature XRPD data are bigger than Kusainova's value (Table 6.01) but similar to Liu's value (Table 6.01) suggesting there might be some Cu vacancies in the pristine sample.[16,69]

In $Bi_{1-x}Ce_xCuOSe$ ($0 \leq x \leq 0.1$), the overall trend is slight decrease in unit cell volume with increasing Ce content (Figure 6.11c). This is consistent with replacing Bi^{3+} with Ce^{3+} or Ce^{4+} as the effective ionic radii change from 1.03 Å (Bi^{3+}) to 1.01 Å (Ce^{3+}) or 0.87 Å (Ce^{4+}) for a coordination number 6.[67] However, the XANES Cu-K edge normalised energy plot (Figure 6.15a) shows that the Ce-doped samples contain Ce^{4+} ions. According to Vegard's law, it is expected that since the end members are isostructural, BiCuOSe and $Bi_{1-x}Ce_xCuOSe$ ($0 \leq x \leq 0.1$), might form a solid solution limit on mixing. However, linearity is not observed in the unit cell parameters plots with increasing Ce doping concentration (Figure 6.11) which suggests that the Ce doping limit is x = 0.01, probably due to the presence of the various impurity phases in the doped samples.[68] However, CeCuOSe was synthesised at 500°C, 200°C less than our synthesis work. Hence, maybe the synthesis conditions could be optimised for higher Ce content samples to assess feasibility of a solid solution.[64] The increase in unit cell parameters at x = 0.01 and x = 0.03 could be due to a change in Cu oxidation state, however, this could be argued. In both $Bi_{1-x}Ce_xCuOSe$ and $BiCuO_{1-x}F_xSe$, the changes in c cell parameters with dopant level are slightly larger than that for the a cell parameters.

In $BiCuO_{1-x}F_xSe$ ($0 \leq x \leq 0.12$), no overall trend in unit cell volume with increasing F content can be seen (Figure 6.06c). A decrease should have been observed if O^{2-} (1.40 Å) was replaced by F^- (1.33 Å) in terms of the effective ionic radii for coordination number 6 as well as because of the expected reduction in copper.[67] Even though BiCuFSe has not been reported, it is hypothetically assumed that it will be isostructural to BiCuOse and together with $BiCuO_{1-x}F_xSe$ ($0 \leq x \leq 0.12$), it would form a solid solution according to Vegard's law.[68] However, there was no systematic variation in unit cell parameters on F-doping (Figure 6.06), suggesting that it is not possible to dope F^- onto the O^{2-} site in BiCuOSe. The increase observed at $x = 0.05$ in the cell parameters and unit cell volume with increasing F doping concentration (Figure 6.06) could be attributed to the greater amount of impurities, when compared to the other doped samples, although this could be argued as it might be within errors. From the SEM-EDX data analysis, it is hard to tell the limit of doping in $BiCuO_{1-x}F_xSe$ as Fluorine is alight element/ low atomic number and is hard to detect by SEM-EDX. Similar to $BiCuO_{1-x}F_xS$, about 20 % impurities was seen when $x \geq 0.05$.[70]

The behaviour of the synthesised BiCuOSe with decreasing temperature is different from what has been reported in the literature.[2,16,18,19,65,66] This may suggest that the sample has Cu vacancies where these point defects traps charge carriers very well at low temperatures. [16,71] The electrical conductivity of BiCuOSe obtained (64648 S/m) is different.[2,16,18–20] $BiCuO_{1-x}F_xSe$ ($0 \leq x \leq 0.12$) showed metallic behaviour as seen by the decrease in resistivities `as a function of decreasing temperatures (Figure 6.07). Berardan *et al* showed a similar decrease in resistivity in $BiCuO_{0.9}F_{0.1}Se$, although the latter showed semiconducting behaviour.[72] It seems that F-doping the pristine sample suppresses the semiconductor-metal transition. Resistivity is largest for $x = 0$ and the resistivities in the doped samples don't change much (Table 6.03). This is consistent with no change in composition as there is no solid solution.

In $Bi_{1-x}Ce_xCuOSe$ ($0 \leq x \leq 0.1$), resistivity is largest for $x = 0.02$ and T_0 is biggest for $x = 0.04$ (Table 6.06). This could be due to the smaller amount of impurity present compared to the other doped samples. For $Bi_{1-x}Ce_xCuOSe$ ($x = 0.02, 0.04, 0.06$ and 0.10), the resistivity behaviour at high temperatures could be explained using the thermally activated model (Figure 6.13) while at low temperatures, the two-dimensional variable range hopping (2D-VRH) (Figure 6.14) could be used. The slight decrease in electrical resistivity at high temperature can be accredited to the thermal excitation of electrons across the band gap into the conduction band.[21] Doping BiCuOSe with Ce gave somewhat similar electrical conductivities as in $Bi_{1-x}Sr_xCuOSe$, $Bi_{1-x}Ba_xCuOSe$[18] and Bi_{1-}

$_x$Pb$_x$CuOSe but were higher than Bi$_{1-x}$Na$_x$CuOSe and BiOCu$_{1-x}$Ag$_x$Se.[2,18,53–55,73,74] In Bi$_{1-x}$Ce$_x$CuOSe ($0 \leq x \leq 0.1$), the overall trend is a slight increase in activation energies (Table 6.06) for those doped samples which showed semiconducting behaviour (x = 0.02, 0.04, 0.06 and 0.10) similar to Bi$_{1-x}$K$_x$CuOSe.[52] This semiconducting behavior was similar to Bi$_{1-x}$Sb$_x$CuOSe, BiOCu$_{1-x}$Ag$_x$Se, BiCu$_{1-x}$OSe and BiCuOSe$_{1-x}$Te$_x$.[16,21,54–56] The Ce-doped samples (x = 0.01, 0.03 and 0.08) showed metallic behaviour as seen by the decrease in resistivities with decreasing temperatures (Figure 6.12c) similar to Bi$_{1-x}$Mg$_x$CuOSe, Bi$_{1-x}$Ca$_x$CuOSe, Bi$_{1-x}$Sr$_x$CuOSe, Bi$_{1-x}$Ba$_x$CuOSe, Bi$_{1-x}$Na$_x$CuOSe and Bi$_{1-x}$Pb$_x$CuOSe.[18,19,53,65,73–75] Since the pristine sample shows metallic behaviour and the fact that the Ce doping limit is x = 0.01 as per Vegard's law and shows metallic behaviour as well suggests that the semiconducting behaviour which is exhibited by the other Ce-doped samples (x = 0.02, 0.04, 0.06, 0.10) is due to the various impurities present in them.[68]

The XANES data for BiCuO$_{1-x}$F$_x$Se and Bi$_{1-x}$Ce$_x$CuOSe show that energy E$_0$ for Cu edge and Ce edge barely change with increasing F and Ce content (Table 6.04 and 6.07) respectively, suggesting that the number of unoccupied states barely changes with F and Ce content, except for BiCuO$_{0.98}$F$_{0.02}$Se which could be due to the impurities. A weak shoulder can be observed for Bi$_{0.98}$Ce$_{0.02}$CuOSe (Figure 6.16) which corresponds to either the 2 $p_{3/2}$ to 4 f forbidden dipole transition or to transitions to the unoccupied delocalized states with d character in the conduction band. [76,77] The first bump in the Ce^{4+} doublet (Figure 6.19) corresponds to transitions to Ce [$2p^54f^15d^1$] O[$2p^5$] while the second bump in the doublet corresponds to those to Ce [$2p^54f^05d^1$] O[$2p^6$].[76–78] The Cu-K edge normalized energy plots for Bi$_{1-x}$Ce$_x$CuOSe and BiCuO$_{1-x}$F$_x$Se (Figure 6.08a and 6.15a) do not have a pre-edge peak at round 8979 eV which suggest that the Ce-doped and F-doped samples have monovalent Cu with no empty d state regardless of the method of doping.[79] Moreover, there is no apparent change in the Cu oxidation states in the Ce- and F-doped samples.

6.4 Conclusions and Future work

There is a limited solid solution to electron dope BiCuOSe with Ce and F being successful up to only x = 0.01 even though CeCuOSe exists. Our synthesised BiCuOSe did not show a semiconducting behaviour which could be attributed to Cu vacancies in the sample. Electron doping BiCuOSe with F causes the sample to become metallic, which is different from Berardan *et al* while doping BiCuOSe with Ce caused both semiconducting and metallic behaviour.[72] The semiconducting behaviour may be due to impurities. The semiconducting Ce-doped BiCuOSe caused a slight increase in activation energy. XANES data for both BiCuO$_{1-x}$F$_x$Se and Bi$_{1-x}$Ce$_x$CuOSe show barely any changes with F or Ce

content for both the Cu edge and the Ce edge. The Cu-k edge plots for both $Bi_{1-x}Ce_xCuOSe$ and $BiCuO_{1-x}F_xSe$ show that Cu^{1+} is dominant in the pristine BiCuOSe and Ce-and F-doped samples while the Ce-L_3 edge plot show that the Ce-doped samples consist of Ce^{4+} ions which would explain the low solution limit. Further work includes spark plasma sintering to produce denser sample pellets to allow the measurement for Seebeck coefficients and thermal conductivity. Other strategies might be to synthesise single crystals of BiCuOSe to increase the power factor, dope an element with valence -1 on the Se site or dope an element with 4+ charge on the Bi or Cu site.

6.5 References

1   A. M. Kusainova, P. S. Berdonosov, L. G. Akselrud, L. N. Kholodkovskaya, V. A. Dolgikh and B. A. Popovkin, *J. Solid State Chem.*, 1994, **112**, 189–191.

2   L. D. Zhao, D. Berardan, Y. L. Pei, C. Byl and L. Pinsard-Gaudart, *Appl. Phys. Lett.*, 2010, **97**, 092118.

3   C. Wood, *Energy Convers. Manag.*, 1984, **24**, 317–329.

4   M. G. Kanatzidis, *Chem. Mater.*, 2010, **22**, 648–659.

5   G. J. Snyder and E. S. Toberer, *Nat Mater*, 2008, **7**, 105–114.

6   L. D. Zhao, B. P. Zhang, J. F. Li, M. Zhou, W. S. Liu and J. Liu, *J. Alloys Compd.*, 2008, **455**, 259–264.

7   J. P. Heremans, V. Jovovic, E. S. Toberer, A. Saramat, K. Kurosaki, A. Charoenphakdee, S. Yamanaka and G. J. Snyder, *Science.*, 2008, **321**, 554–557.

8   L. D. Zhao, S. H. Lo, J. He, H. Li, K. Biswas, J. Androulakis, C. I. Wu, T. P. Hogan, D. Y. Chung, V. P. Dravid and M. G. Kanatzidis, *J. Am. Chem. Soc.*, 2011, **133**, 20476–20487.

9   K. F. Hsu, S. Loo, F. Guo, W. Chen, J. S. Dyck, C. Uher, T. Hogan, E. K. Polychroniadis and M. G. Kanatzidis, *Science.*, 2004, **303**, 818–821.

10   B. Poudel, Q. Hao, Y. Ma, Y. Lan, A. Minnich, B. Yu, X. Yan, D. Wang, A. Muto, D. Vashaee, X. Chen, J. Liu, M. S. Dresselhaus, G. Chen and Z. Ren, *Science.*, 2008, **320**, 634–638.

11   L. D. Zhao, J. He, S. Hao, C. I. Wu, T. P. Hogan, C. Wolverton, V. P. Dravid and M. G. Kanatzidis, *J. Am. Chem. Soc.*, 2012, **134**, 16327–16336.

12   K. Biswas, J. He, Q. Zhang, G. Wang, C. Uher, V. P. Dravid and M. G. Kanatzidis, *Nat Chem*, 2011, **3**, 160–166.

13   K. Biswas, J. He, I. D. Blum, C. I. Wu, T. P. Hogan, D. N. Seidman, V. P. Dravid and M. G. Kanatzidis, *Nature*, 2012, **489**, 414–418.

14   T. C. Harman, P. J. Taylor, M. P. Walsh and B. E. LaForge, *Science.*, 2002, **297**, 2229–2232.

15   J. P. Heremans, C. M. Thrush and D. T. Morelli, *Phys. Rev. B*, 2004, **70**, 115334.

16   Y. Liu, L. D. Zhao, Y. Liu, J. Lan, W. Xu, F. Li, B. P. Zhang, D. Berardan, N. Dragoe, Y. H. Lin, C.

W. Nan, J. F. Li and H. Zhu, *J. Am. Chem. Soc.*, 2011, **133**, 20112–20115.

17   C. Barreteau, D. Beardan, E. Amzallag, L. Zhao and N. Dragoe, *Chem. Mater.*, 2012, **24**, 3168–3178.

18   J. Li, J. Sui, Y. Pei, C. Barreteau, D. Berardan, N. Dragoe, W. Cai, J. He and L. D. Zhao, *Energy Environ. Sci.*, 2012, **5**, 8543–8547.

19   Y. L. Pei, J. He, J. F. Li, F. Li, Q. Liu, W. Pan, C. Barreteau, D. Berardan, N. Dragoe and L. D. Zhao, *NPG Asia Mater.*, 2013, **5**, 1–9.

20   J. Li, J. Sui, C. Barreteau, D. Berardan, N. Dragoe, W. Cai, Y. Pei and L. D. Zhao, *J. Alloys Compd.*, 2013, **551**, 649–653.

21   Y. Liu, J. Lan, W. Xu, Y. Liu, Y. L. Pei, B. Cheng, D. B. Liu, Y. H. Lin and L. D. Zhao, *Chem. Commun.*, 2013, **49**, 8075–8077.

22   Y. Liu, J. Ding, B. Xu, J. Lan, Y. Zheng, B. Zhan, B. Zhang, Y. Lin and C. Nan, *Appl. Phys. Lett.*, 2015, **106**, 233903.

23   S. Ohta, T. Nomura, H. Ohta, M. Hirano, H. Hosono and K. Koumoto, *Appl. Phys. Lett.*, 2005, **87**, 92108.

24   H. C. Wang, C. L. Wang, W. B. Su, J. Liu, Y. Zhao, H. Peng, J. L. Zhang, M. L. Zhao, J. C. Li, N. Yin and L. M. Mei, *Mater. Res. Bull.*, 2010, **45**, 809–812.

25   M. Ohtaki, T. Tsubota, K. Eguchi and H. Arai, *J. Appl. Phys.*, 1996, **79**, 1816–1818.

26   E. Guilmeau, D. Bérardan, C. Simon, A. Maignan, B. Raveau, D. O. Ovono and F. Delorme, *J. Appl. Phys.*, 2009, **106**, 053715.

27   D. Bérardan, E. Guilmeau, A. Maignan and B. Raveau, *Solid State Commun.*, 2008, **146**, 97–101.

28   Z. H. Dughaish, *Phys. B Condens. Matter*, 2002, **322**, 205–223.

29   C. Wood, *Reports Prog. Phys.*, 1988, **51**, 459–539.

30   M. Zhou, J. F. Li and T. Kita, *J. Am. Chem. Soc.*, 2008, **130**, 4527–4532.

31   A. D. LaLonde, Y. Pei and G. J. Snyder, *Energy Environ. Sci.*, 2011, **4**, 2090–2096.

32   X. Tang, L. Chen, T. Goto and T. Hirai, *J. Mater. Res.*, 2001, **16**, 837–843.

33   W. Zhang, Z. Zhong, Y. Wang and R. Xu, *J. Phys. Chem. C*, 2008, **112**, 17635–17642.

34   Y. Masuda, D. Nagahama, H. Itahara, T. Tani, W. S. Seo and K. Koumoto, *J. Mater. Chem.*, 2003, **13**, 1094–1099.

35   Y. Wang, N. S. Rogado, R. J. Cava and N. P. Ong, *Nature*, 2003, **423**, 425–428.

36   F. Kenjiro, T. Mochida and K. Nakamura, *Jpn. J. Appl. Phys.*, 2001, **40**, 4644–4647.

37   T. Plirdpring, K. Kurosaki, A. Kosuga, M. Ishimaru, A. Harnwunggmoung, T. Sugahara, Y. Ohishi, H. Muta and S. Yamanaka, *Appl. Phys. Lett.*, 2011, **98**, 172104.

38   D. Y. Chung, K. S. Choi, L. Iordanidis, J. L. Schindler, P. W. Brazis, C. R. Kannewurf, B. Chen, S. Hu, C. Uher and M. G. Kanatzidis, *Chem. Mater.*, 1997, **9**, 3060–3071.

39   H. Wang, J. F. Li, M. Zou and T. Sui, *Appl. Phys. Lett.*, 2008, **93**, 202106.

40   D. T. Morelli, V. Jovovic and J. P. Heremans, *Phys. Rev. Lett.*, 2008, **101**, 035901.

41   K. Kurosaki, A. Kosuga, H. Muta, M. Uno and S. Yamanaka, *Appl. Phys. Lett.*, 2005, **87**, 061919.

42   A. Yusufu, K. Kurosaki, A. Kosuga, T. Sugahara, Y. Ohishi, H. Muta and S. Yamanaka, *Appl. Phys. Lett.*, 2011, **99**, 61902.

43   F. Li, J. F. Li, L. D. Zhao, K. Xiang, Y. Liu, B. P. Zhang, Y. H. Lin, C. W. Nan and H. M. Zhu, *Energy Environ. Sci.*, 2012, **5**, 7188–7195.

44   T. Zhou, B. Lenoir, M. Colin, A. Dauscher, R. A. R. Al Orabi, P. Gougeon, M. Potel and E. Guilmeau, *Appl. Phys. Lett.*, 2011, **98**, 162106.

45   E. J. Skoug, J. D. Cain and D. T. Morelli, *Appl. Phys. Lett.*, 2011, **98**, 261911.

46   M. L. Liu, I. W. Chen, F. Q. Huang and L. D. Chen, *Adv. Mater.*, 2009, **21**, 3808–3812.

47   J. Y. Cho, X. Shi, J. R. Salvador, G. P. Meisner, J. Yang, H. Wang, A. A. Wereszczak, X. Zhou and C. Uher, *Phys. Rev. B*, 2011, **84**, 085207.

48   D. Y. Chung, T. Hogan, P. Brazis, M. Rocci-Lane, C. Kannewurf, M. Bastea, C. Uher and M. G. Kanatzidis, *Science.*, 2000, **287**, 1024–1027.

49   G. K. Ren, J. Le Lan, S. Butt, K. J. Ventura, Y. H. Lin and C. W. Nan, *RSC Adv.*, 2015, **5**, 69878–69885.

50   L. Pan, D. Bérardan, L. Zhao, C. Barreteau and N. Dragoe, *Appl. Phys. Lett.*, 2013, **102**, 023902.

51   Y. C. Liu, J. F. Liu, B. P. Zhang and Y. H. Lin, *Key Eng. Mater.*, 2014, **602**, 906–909.

52   J. Le Lan, W. Ma, C. Deng, G. K. Ren, Y. H. Lin and X. Yang, *J. Mater. Sci.*, 2017, **52**, 11569–11579.

53   J. Li, J. Sui, Y. Pei, X. Meng, D. Berardan, N. Dragoe, W. Cai and L. D. Zhao, *J. Mater. Chem. A*, 2014, **2**, 4903–4906.

54   M. U. Farooq, S. Butt, K. Gao, X. L. Pang, X. Sun, Asfandiyar, F. Mohmed, A. Ahmad, A. Mahmood and N. Mahmood, *J. Alloys Compd.*, 2017, **691**, 572–577.

55   Y. C. Liu, Y. H. Zheng, B. Zhan, K. Chen, S. Butt, B. Zhang and Y. H. Lin, *J. Eur. Ceram. Soc.*, 2015, **35**, 845–849.

56   B. Feng, G. Li, Y. Hou, C. Zhang, C. Jiang, J. Hu, Q. Xiang, Y. Li, Z. He and X. Fan, *J. Alloys Compd.*, 2017, **712**, 386–393.

57   S. D. N. Luu and P. Vaqueiro, *Semicond. Sci. Technol.*, 2014, **29**, 064002.

58   G. Ren, S. Butt, C. Zeng, Y. Liu, B. Zhan, J. Lan, Y. Lin and C. Nan, *J. Electron. Mater.*, 2015, **44**, 1627–1631.

59   Y. Yang, X. Liu and X. Liang, *Dalt. Trans.*, 2017, **46**, 2510–2515.

60   Z. Zhou, X. Tan, G. Ren, Y. Lin and C. Nan, *J. Electron. Mater.*, 2017, **46**, 2593–2598.

61   S. K. Saha, *Phys. Rev. B*, 2015, **92**, 041212.

62   D. Zou, S. Xie, Y. Liu, J. Lin and J. Li, *J. Mater. Chem. A*, 2013, **1**, 8888–8896.

63   M. J. Pitcher, C. F. Smura and S. J. Clarke, *Inorg. Chem.*, 2009, **48**, 9054–9056.

64   T. Ohtani, M. Hirose, T. Sato, K. Nagaoka and M. Iwabe, *Jpn. J. Appl. Phys.*, 1993, **32**, 316–318.

65   C. Barreteau, D. Berardan and N. Dragoe, *J. Solid State Chem.*, 2015, **222**, 53–59.

66   J. Sui, J. Li, J. He, Y. L. Pei, D. Berardan, H. Wu, N. Dragoe, W. Cai and L. D. Zhao, *Energy Environ. Sci.*, 2013, **6**, 2916–2920.

67   R. D. Shannon, *Acta Crystallogr. Sect. A*, 1976, **32**, 751–767.

68   A. R. Denton and N. W. Ashcroft, *Phys. Rev. A*, 1991, **43**, 3161–3164.

69   A. M. Kusainova, P. S. Berdonosov, L. G. Akselrud, L. N. Kholodkosvkaya, V. A. Dolgikh and B. A. Popovkin, *J. Solid State Chem.*, 1994, **112**, 189–191.

70   A. Ubaldini, E. Giannini, C. Senatore and D. Van Der Marel, *Phys. C Supercond. its Appl.*, 2010, **470**, S356–S357.

71   T. L. Chou, G. C. Tewari, T. S. Chan, Y. Y. Hsu, J. M. Chen, H. Yamauchi and M. Karppinen, *Eur. J. Inorg. Chem.*, 2015, **15**, 2574–2578.

72   D. Berardan, L. D. Zhao, C. Barreteau and N. Dragoe, *Phys. Status Solidi Appl. Mater. Sci.*, 2012, **209**, 2273–2276.

73   S. D. N. Luu and P. Vaqueiro, *J. Mater. Chem. A*, 2013, **1**, 12270–12275.

74   J. Le Lan, Y. C. Liu, B. Zhan, Y. H. Lin, B. Zhang, X. Yuan, W. Zhang, W. Xu and C. W. Nan, *Adv. Mater.*, 2013, **25**, 5086–5090.

75   C. Barreteau, D. Bérardan, L. D. Zhao and N. Dragoe, *J. Mater. Chem. A*, 2013, **1**, 2921–2926.

76   M. Balasubramanian, C. A. Melendresa and A. N. Mansour, *Thin Solid Films*, 1999, **347**, 178–183.

77   A. M. Shahin, F. Grandjean, G. J. Long and T. P. Schuman, *Chem. Mater.*, 2005, **17**, 315–321.

78   J. El Fallah, S. Boujana, H. Dexpert, A. Kiennemann, J. Majerus, O. Touret, F. Villain and F. Le Normand, *J. Phys. Chem.*, 1994, **98**, 5522–5533.

79   T. L. Chou, G. C. Tewari, T. S. Chan, Y. Y. Hsu, H. Yamauchi and M. Karppinen, *Solid State Commun.*, 2015, **206**, 12–16.

Chapter 7: Conclusions and Future work

This thesis has reported the synthesis of new complex oxychalcogenides. To investigate further the role of electron-doping in quarternary oxychalcogenides, similar to that in $Ln_2O_2Fe_{2-x}Mn_xOSe_2$ (Ln=La, Nd), $La_2O_2Fe_2OSe_2$ was electron-doped with Co^{2+}/Ni^{2+} ions onto the Fe site and the resulting changes in structure and physical properties were investigated.[1-4] The SEM-EDX data of the parent compound suggests some Fe deficiency which can produce anion deficient compounds as well as oxidation of Fe^{2+} to smaller Fe^{3+}. The results showed that a limited solid solution exists when the parent compound was electron doped with Co and Ni. Co-doping was successful up to x = 0.02. However, since $La_2O_2Co_2OSe_2$ was synthesised at 100°C hotter than our synthesis temperature, the latter could be optimised for higher Co content samples to evaluate the possibility of a solid solution.[5,6] Ni-doping was not successful as the amount used was probably too small or perhaps due to Ni^{2+} being not compatible with electronic effects. Hence, it would be interesting to see if the $Nd_2O_2Fe_{2-x}Ni_xOSe_2$ series could be synthesised using higher Ni content. The SQUID Magnetometry analysis showed that electron doping $La_2O_2Fe_2OSe_2$ with x = 0.2 cobalt slightly increased the transition temperature and causes a rapid decrease in c below T_N, which is probably due to the decrease in the distance between the Fe_2O layers with Co doping, similar to $La_2O_2Fe_{2-x}Mn_xOSe_2$.[7] Due to the lack of solid solution, no alteration in properties (magnetic and resistivity) was seen for Ni since no change of the main phase composition occurred. Electron doping $La_2O_2Fe_2OSe_2$ with Co and Ni gave semiconductor materials. From the thermally-activated model, it can be seen that electron-doping $La_2O_2Fe_2OSe_2$ with Co was successful. Other work which could be done include introducing F on the oxygen site in $La_2O_2Fe_2F_xO_{1-x}Se_2$.

The magnetic structure of $La_2O_2Fe_2OS_2$ using NPD has been determined and the short range magnetic order and magnetic microstructure have been studied. VT-NPD data showed a less rapid decrease in c cell parameter for $T<T_N$ than when compared with other $Ln_2O_2M_2OSe_2$ (Ln = La-Pr and M = Mn, Fe, Co) systems.[8,9] However, a similar broad asymmetric Warren-peak just above T_N was seen, similar to $Ln_2O_2Fe_2OSe_2$ (Ln = La-Pr) systems, which shows 2-D short range order.[8,10,11] This Warren peak could indicate frustration in the 2-k magnetic model as it is seen at narrow (e.g. $La_2O_2Fe_2OSe_2$) and wide temperature ranges (e.g. $La_2O_2Mn_2OSe_2$ and $Sr_2F_2Fe_2OSe_2$).[10,12,13] Moreover, the VT-NPD data showed that additional magnetic Bragg reflections, whose intensity increase with decreasing temperature, are observed below T_N and these are consistent with a 2-k magnetic structure, similar to $Sr_2F_2Fe_2OSe_2$ and $La_2O_2Fe_2OSe_2$.[10,12] The NPD data showed stacking

faults in the magnetic ordering on the Fe^{2+} sublattice, similar to $Ln_2O_2Fe_2OSe_2$ (Ln = La-Pr) systems[8,10,12,14] and absent in Mn_2O or Co_2O materials suggesting that the stacking faults are solely to the Fe_2O layers and might be affected by the distance between Fe_2O layers.[6,8,10,12–15]

The magnetic structure of $Pr_2O_2Fe_2OSe_2$ using NPD has been further analysed to better understand the additional peak in specific heat capacity at 23 K seen by Ni et $al.$[16] Sequential Rietveld refinements of VT-NPD data in a 5 T applied magnetic field showed a rapid decrease in c cell parameter on cooling, as observed in other $Ln_2O_2Fe_2OSe_2$ (Ln = La, Ce, Nd) systems.[8,10] The peak at 23 K was seen to be the result of a subtle orthorhombic distortion (from $I4/mmm$ to $Immm$ symmetry) on cooling in both applied magnetic field and zero-field, which is less noticeable as seen in analogous compounds.[9,17,18] VT-NPD data for $Pr_2O_2Fe_2OSe_2$ (23 K < T < T_N) showed, the magnetic Bragg reflections increase in intensity on cooling suggesting 2-k magnetic order on the Fe^{2+} sublattice similar to $La_2O_2Fe_2OS_2$. Moreover, at T ≤ 23, we can see more peaks appearing at 2 K when the applied magnetic field is increased while the 2-k reflections broaden. These new peaks were indexed in the nuclear unit cell at $\mathbf{k}$ = (0,0,0) with a 2a x 2a x 2c unit cell. ISODISTORT was used to get a description of the magnetic structure of $Pr_2O_2Fe_2OSe_2$ and stacking faults are observed as in $La_2O_2Fe_2OS_2$.

In this thesis, isovalent-doping in quaternary oxychalcogenides was also investigated by doping $LaGaOS_2$ with Nd^{3+} and Ce^{3+} ions and resulting changes in structure and physical properties were investigated. There is a limited solid solution when electron doping $LaGaOS_2$ with Nd and Ce. The XPS data showed that the samples showed barely any sulfur oxidation on the surface and that maybe the surface of the Nd-doped samples contains metallic Nd-Nd and Nd oxide. Moreover, XPS data showed that $La_{1-x}Ce_xGaOS_2$ (0 ≤ x ≤ 0.1) contained only Ce^{3+} ions, as confirmed when comparing the changes in cell parameters for both Nd-doping and Ce-doping.[19,20] From the diffuse reflectance plots, Nd-doping and Ce-doping the parent compound gave no significant change (within errors) in optical band gaps. The change in colour in Nd-doped samples are presumably due to f-f transitions, which increase with decreasing Nd content while Ce-doping the parent compound barely changed the colour of the samples, probably due to low doping concentrations. The optical band gap values suggest potential applications in nonlinear optics, uncooled thermal images and photoresistors (for Nd-doped samples) and in blue lasers, LEDs and IR optics (for Ce-doped samples).[21–23] It would be interesting to investigate their photocatalytic activities. Other strategies include synthesising $LaGaOS_{2-x}Se_x$, p-type dope $LaGaOS_2$ on the Ga-site (such as Zn), n-type dope $LaGaOS_2$ on the Ga-site (such as Ge, Sn, Bi) and investigate the resulting changes in optical band gaps.

In addition to electron doping $La_2O_2Fe_2OSe_2$, more quaternary oxychalcogenides were electron doped, specifically BiCuOSe with Ce^{3+} and F^- ions and the resulting changes in structure and properties were investigated. There is a limited solid solution to electron dope BiCuOSe with Ce. However, since our Ce-doped samples were synthesised at higher temperatures than CeCuOSe, maybe decreasing the synthesis temperatures might be used to create a solid solution.[24] Our synthesised BiCuOSe showed no semiconducting behaviour and has a semiconductor-metal transition, which suggests Cu vacancies in the pristine sample. Electron doping BiCuOSe with F causes the sample to become metallic, different from Berardan *et al* and the resistivity remained unchanged with increasing F content which suggests no change in composition as no solid solution is present.[25] Interestingly, Ce-doped BiCuOSe showed both semiconducting (may be due to impurities) and metallic behaviour and an increase in activation energy. The slight decrease in electrical resistivity in Ce-doped sample could be due to the thermal excitation of electrons across the band gap into the conduction band.[26] XANES data for $BiCuO_{1-x}F_xSe$ and $Bi_{1-x}Ce_xCuOSe$ show that the unoccupied states remain unchanged with increasing dopants level. The Cu-*k* edge plots for Cu^{1+} is dominant in the undoped and all the Ce- and F-doped samples while the Ce-*L₃* edge plot show that Ce^{4+} ions are present in the Ce-doped samples, which would probably explain the low solution limit. The Cu oxidation state does not seem to alter in the Ce-doped samples or F-doped samples. Further work includes using spark plasma sintering to make denser sample pellets and perform Seebeck coefficients and thermal conductivity measurements on them. Other strategies include synthesising single crystals of BiCuOSe to increase the thermoelectric power, dope an element with valence -1 on the Se site or dope an element with 4+ charge on the Bi or Cu site.

7.1 References

1   A. S. Sefat, A. Huq, M. A. McGuire, R. Jin, B. C. Sales, D. Mandrus, L. M. D. Cranswick, P. W. Stephens and K. H. Stone, *Phys. Rev. B*, 2008, **78**, 104505.

2   G. Cao, S. Jiang, X. Lin, C. Wang, Y. Li, Z. Ren, Q. Tao, C. Feng, J. Dai, Z. Xu and F. C. Zhang, *Phys. Rev. B*, 2009, **79**, 174505.

3   A. Marcinkova, D. A. M. Grist, I. Margiolaki, T. C. Hansen, S. Margadonna and J. W. G. Bos, *Phys. Rev. B*, 2010, **81**, 064511.

4   Y. Liu, S. B. Zhang, W. J. Lu, L. J. Li, S. G. Tan, B. Yuan, J. Chen and Y. P. Sun, *J. Alloys Compd.*, 2015, **618**, 263–268.

5   C. Wang, M. Q. Tan, C. M. Feng, Z. F. Ma, S. Jiang, Z. A. Xu, G. H. Cao, K. Matsubayashi and Y. Uwatoko, *J. Am. Chem. Soc.*, 2010, **132**, 7069–7073.

6   Y. Fuwa, M. Wakeshima and Y. Hinatsu, *Solid State Commun.*, 2010, **150**, 1698–1701.

7   H. Lei, E. S. Bozin, A. Llobet, V. Ivanovski, V. Koteski, J. Belosevic-Cavor, B. Cekic and C. Petrovic, *Phys. Rev. B*, 2012, **86**, 125122.

8   E. E. McCabe, A. S. Wills, L. Chapon, P. Manuel and J. S. O. Evans, *Phys. Rev. B*, 2014, **90**, 165111.

9   D. G. Free, N. D. Withers, P. J. Hickey and J. S. O. Evans, *Chem. Mater.*, 2011, **23**, 1625–1635.

10   E. E. McCabe, C. Stock, E. E. Rodriguez, A. S. Wills, J. W. Taylor and J. S. O. Evans, *Phys. Rev. B*, 2014, **89**, 100402.

11   B. E. Warren, *Phys. Rev.*, 1941, **59**, 693–698.

12   L. L. Zhao, S. Wu, J. K. Wang, J. P. Hodges, C. Broholm and E. Morosan, *Phys. Rev. B*, 2013, **87**, 020406.

13   N. Ni, E. Climent-Pascal, S. Jia, Q. Huang and R. J. Cava, *Phys. Rev. B*, 2010, **82**, 214419.

14   R. K. Oogarah, C. P. J. Stockdale, C. Stock, J. S. O. Evans, A. S. Wills, J. W. Taylor and E. E. McCabe, *Phys. Rev. B*, 2017, **95**, 174441.

15   Y. Fuwa, T. Endo, M. Wakeshima, Y. Hinatsu and K. Ohoyama, *J. Am. Chem. Soc.*, 2010, **132**, 18020–18022.

16   N. Ni, S. Jia, Q. Huang, E. Climent-Pascual and R. J. Cava, *Phys. Rev. B*, 2011, **83**, 224403.

17   S. A. J. Kimber, A. H. Hill, Y. Z. Zhang, H. O. Jeschke, R. Valentí, C. Ritter, I. Schellenberg, W. Hermes, R. Pöttgen and D. N. Argyriou, *Phys. Rev. B*, 2010, **82**, 100412.

18   E. J. Wildman, F. Sher and A. C. McLaughlin, *Inorg. Chem.*, 2015, **54**, 2536–2542.

19   A. Mehta, S. Patil, H. Bang, H. J. Cho and S. Seal, *Sensors Actuators, A Phys.*, 2007, **134**, 146–151.

20   C. Zhang and J. Lin, *Phys. Chem. Chem. Phys.,* 2011, **13**, 3896–3905.

21   H. Matsuda, M. Kuwabara, K. I. Yamada, H. Shimooka and S. Takahashi, *J. Am. Ceram. Soc*, 1998, **81**, 3010–3012.

22   R. B. Kale and C. D. Lokhande, *Semicond. Sci. Technol.*, 2005, **20**, 1–9.

23   M. Cardona, *J. Appl. Phys.*, 1961, **32**, 2151.

24   T. Ohtani, M. Hirose, T. Sato, K. Nagaoka and M. Iwabe, *Jpn. J. Appl. Phys.*, 1993, **32**, 316–318.

25   D. Berardan, L. D. Zhao, C. Barreteau and N. Dragoe, *Phys. Status Solidi Appl. Mater. Sci.*, 2012, **209**, 2273–2276.

26   Y. Liu, J. Lan, W. Xu, Y. Liu, Y. L. Pei, B. Cheng, D. B. Liu, Y. H. Lin and L. D. Zhao, *Chem. Commun.*, 2013, **49**, 8075–8077.

Appendix 2.01

```
□ RKO024a_021115_1hr30_riet_02.inp (G:\Results for thesis chapters\CHPT3_La2O2Fe2OSe2\La2O2Fe2OSe2\XRPD\)
1  ' Input file for simple Rietveld Refinement
2  ' Use save/set current button then run with F6 in topas
3  ' Replace @ and # symbols with text/numbers as needed
4
5
6  r_wp 6.8338382 r_exp 5.23482835 r_p 5.28694909 r_wp_dash 20.9872152 r_p_dash 26.0937358 r_exp_dash 16.0763018 weighted_Durbin_Watson 1.05888354 gof 1.30547532
7
8
9
10 ' General information about refinement here
11 ' Remove comments as required
12
13 iters 100000
14 chi2_convergence_criteria 0.001
15 do_errors
16
17 ' Information on datafile etc here
18 ' Check that default weighting is appropriate for your data
19
20 xdd RKO024a_021115_1hr30.raw
21 x_calculation_step = Yobs_dx_at(Xo); convolution_step 4
22 bkg @ 347.442871 0.62631889 -127.799978 1.08905425 138.845346 0.99913634 -103.795771 0.973186 64.731647 0.910746243 -28.3890102 0.907000914 22.5201132 0.84627073 -11.8943562 0.84411268 12.2536045 0.76475376 -3.14821892
23 'd8 Lynx Eye Cu Ra1/a2 5 line emission
24 LP_Factor(!th2_monochromator, 0)
25 CuKa2(0.0001)
26
27 Zero_Error(zero, -0.10534_0.00240)
28
29 ' Information on structure
30 ' Type in phase/space group/cell etc
31 ' Comment in/out sections as needed
32
33 str phase_name La2O2Fe2OSe2
34 a lpa 4.085161_0.000126
35 b lpa 4.085161_0.000126
36 c lpc 18.585159_0.000747
37 al 90.
38 be 90.
39 ga 90.
40 volume 310.159_0.023
41 space_group "I4/mmm"
42 site Fe1 x 0.5 y 0   z 0    occ Fe 1. beq bval -1.81319_0.04528
43 site O1  x 0.5 y 0   z 0.25 occ O 1.  beq bval -1.81319_0.04528
44 site O2  x 0.5 y 0.5 z 0    occ O 1.  beq bval -1.81319_0.04528
45 site La1 x 0.5 y 0.5 z 1la1 0.18465_0.00011 occ La 1. beq bval -1.81319_0.04528
46 site Se1 x 0   y 0   z se1 0.09756_0.00017 occ Se 1. beq bval -1.81319_0.04528
47 scale @ 5.74234919e-005_3.81e-007
48 r_bragg 3.38241967
49 TCHZ_Peak_Type(!pku,-0.08515_0.01211,!pkv, 0.13118_0.01208,!pkw, -0.04793_0.00297,!pkz, 0.0000,!pky, 0.22935_0.00458,!pkx, 0.0000)
50 Simple_Axial_Model(axial, 9.49746_0.40523)
51 Phase_Density_g_on_cm3( 6.37555_0.0047)
```

Appendix 2.01 Example of a XRPD refinement file with variables refined

215

Appendix 2.02

```
 7  r_wp 8.48974005 r_exp 6.80920481 r_p 6.64505525 r_wp_dash 22.5748862 r_p_dash 27.5067966 r_exp_dash 18.1062109 weighted_Durbin_Watson 1.44258487 gof 1.24680345
 8
 9  'General information about refinement here
10
11  iters 100000
12  chi2_convergence_criteria 0.001
13  do_errors
14  #ifdef !GUI_LINES 'use these lines when in gui mode
15     macro filename {12K,xy}
16     macro information [prm :te 12  prm :time 2 ]
17  #else
18  #define writeout
19  #endif
20  information
21  information
22  'Information on datafile etc here
23  'Check that default weighting is appropriate for your data
24
25  xdd filename
26     x_calculation_step = Yobs_dx_at(Xo); convolution_step 4
27     bkg @ 159.902469  80.2819626 -24.297599_0.50838305  6.69200984_0.49853421  2.13943142_0.47807325 -2.80578009_0.47227318  0.19558379_0.46164295  0.37166556_0.45716791  0.44335192_0.43581574  0.85090
28     'd8 Ge(111) Monochromator Vantec Cu Ka1
29     LP_Factor(!th2_monochromator, 27.26)
30     CuKa1(0.0001)
31     Specimen_Displacement(height, 0.33439_0.00090)
32     start_X 14
33
34  'Information on structure
35  'Type in phase/space group/cell etc
36  'Comment in/out sections as needed
37
38     str phase_name La2O2Fe2OSe2
39        a lpa 4.085501_0.000050
40        b lpa 4.085501_0.000050
41        c lpc 18.587533_0.00031
42        al 90.
43        be 90.
44        ga 90.
45        volume vol 310.250_0.009
46
47        space_group "I4/mmm"
48        site Fe1  x 0.5  y 0    z 0               occ Fe 1.    beq bval 0.73482_0.04269
49        site O1   x 0.5  y 0    z 0.25            occ O 1.     beq bval 0.73482_0.04269
50        site O2   x 0.5  y 0.5  z 0               occ O 1.     beq bval 0.73482_0.04269
51        site La1  x 0.5  y 0.5  z zla 0.18453_0.00010 occ La 1. beq bval 0.73482_0.04269
52        site Se1  x 0    y 0    z zse 0.09636_0.00016 occ Se 1. beq bval 0.73482_0.04269
53        scale @ 8.45083678e-005_5.598e-007
54        r_bragg 4.63946338
55        TCHZ_Peak_Type(!pku,-0.01536_0.00353,!pkv, 0.00635_0.00344,!pkw, -0.01216_0.00078,!pkz, 0.0000,!pky, 0.15612_0.00264,!pkx, 0.0000)
56        Simple_Axial_Model(!axial, 2.50918_1.6866)
57        Phase_Density_g_on_cm3( 6.37368_0.0019)
           Surface_Roughness_Pitschke_et_al1(!a1c, 0.16248_0.03125, !a2c, 0.01993_0.03135)
```

Appendix 2.02 Example of a seed refinement file with variables refined for VT-XRPD

Appendix 2.03

```
files_sweep1.list (G:\Res
 1 12K.xy
 2 22K.xy
 3 32K.xy
 4 42K.xy
 5 52K.xy
 6 62K.xy
 7 67K.xy
 8 72K.xy
 9 77K.xy
 0 79K.xy
 1 81K.xy
 2 83K.xy
 3 85K.xy
 4 87K.xy
 5 89K.xy
 6 91K.xy
 7 93K.xy
 8 95K.xy
 9 97K.xy
 0 99K.xy
 1 101K.xy
 2 106K.xy
 3 111K.xy
 4 116K.xy
 5 126K.xy
 6 136K.xy
 7 146K.xy
 8 156K.xy
 9 166K.xy
 0 176K.xy
 1 186K.xy
 2 196K.xy
 3 206K.xy
 4 216K.xy
 5 226K.xy
 6 236K.xy
 7 246K.xy
 8 256K.xy
 9 266K.xy
 0 276K.xy
 1 286K.xy
 2 298K.xy
```

Appendix 2.03 Example of a list of data files for VT-XRPD

Appendix 2.04

Appendix 2.04 Example of an information list containing required information about the relevant data files for VT-XRPD

Appendix 2.05

```
66          a lp2a   5.543886`_0.002470
67          b lp2b   5.554366`_0.002429
68          c lp2c   7.846471`_0.004731
69          al 90.
70          be 90.
71          ga 90.
72          volume   241.615`_0.210
73          space_group "Pbnm"
74          site La1     x -.00614        y 0.02840
75          site Fe1     x 0              y 0.5
76          site O1      x 0.0731         y 0.4875
77          site O2      x -.2809         y 0.2815
78          scale @   1.22206073e-006`_1.055e-007
79          r_bragg   2.14963891
80          TCHZ_Peak_Type(!pku,-0.01526_0.00353,!pkv,
81          Simple_Axial_Model(!axial, 2.50918_1.68656
82          Phase_Density_g_on_cm3( 6.67334`_0.00579)
83
84          #ifdef writeout
85 out "RKO024a_seed04.res " append
86      Out(te, "%11.5f")
87      'Out(time, " %11.5f")
88      Out(Get (r_wp), "%11.5f")
89      'Out(Get (weighted_Durbin_Watson), "%11.5f")
90      Out(Get (gof), "%11.5f")
91      Out(height, "%11.5f", " %11.5f")
92      Out(lpa, "%11.5f", " %11.5f")
93      Out(lpc, "%11.5f", " %11.5f")
94      Out(vol, "%11.5f", " %11.5f")
95      Out(zla, "%11.5f", " %11.5f")
96      Out(zse, "%11.5f", " %11.5f")
97      'Out(bfe1, "%11.5f", " %11.5f")
98      'Out(bo_1, "%11.5f", " %11.5f")
99      'Out(bo_2, "%11.5f", " %11.5f")
100     'Out(bla1, "%11.5f", " %11.5f")
101     'Out(bse1, "%11.5f", " %11.5f")
102     Out(pku, "%11.5f", " %11.5f")
103     Out(pkv, "%11.5f", " %11.5f")
104     Out(pkw, "%11.5f", " %11.5f")
105     Out(pky, "%11.5f", " %11.5f")
106     Out(axial, "%11.5f", " %11.5f\n")
107
108         #endif
```

Appendix 2.05 Example of seed file asking for a.res file to be outputted for VT-XRPD

Appendix 2.06

Hysteresis measurements:

- ➢ Sample at room temperature
- ➢ Measurement from 0 to 200 Oe in 50 Oe increments
- ➢ Measurement from 400 to 1000 Oe in 200 Oe increments
- ➢ Measurement from 2000 to 20000 Oe in 1000 Oe increments
- ➢ Measurement from 22000 to 50000 Oe in 2000 Oe increments
- ➢ Measurement from 50000 to 22000 Oe in -2000 Oe increments
- ➢ Measurement from 20000 to 1000 Oe in -1000 Oe increments
- ➢ Measurement from 800 to 400 Oe in -200 Oe increments
- ➢ Measurement from 200 to -200 Oe in -50 Oe increments
- ➢ Measurement from -400 to -1000 Oe in -200 Oe increments
- ➢ Measurement from -2000 to -20000 Oe in -1000 Oe increments
- ➢ Measurement from -22000 to -50000 Oe in -2000 Oe increments
- ➢ Measurement from -50000 to -22000 Oe in -2000 Oe increments
- ➢ Measurement from -20000 to -1000 Oe in 1000 Oe increments
- ➢ Measurement from -800 to -400 Oe in 200 Oe increments
- ➢ Measurement from -200 to 200 Oe in 50 Oe increments
- ➢ Measurement from 400 to 1000 Oe in 200 Oe increments
- ➢ Measurement from 2000 to 20000 Oe in 1000 Oe increments
- ➢ Measurement from 20000 to 50000 Oe in 2000 Oe increments

Field cooled (FC) measurement:

- ➢ Applied field of 1000 Oe is switched on and sample is cooled to 2 K
- ➢ Measurement from 2 to 300 K at 5 K/min in 2 K increments with an applied field of 1000 Oe

Zero-field cooled (ZFC) measurement:

- ➢ Sample cooled to 2 K with an applied field of 0 Oe
- ➢ Measurement from 2 to 300 K at 5 K/min in 2 K increments with an applied field of 1000 Oe

Hysteresis measurements:

- ➢ Sample at 10 K
- ➢ Measurement from 0 to 200 Oe in 50 Oe increments

- ➢ Measurement from 400 to 1000 Oe in 200 Oe increments
- ➢ Measurement from 2000 to 20000 Oe in 1000 Oe increments
- ➢ Measurement from 22000 to 50000 Oe in 2000 Oe increments
- ➢ Measurement from 50000 to 22000 Oe in -2000 Oe increments
- ➢ Measurement from 20000 to 1000 Oe in -1000 Oe increments
- ➢ Measurement from 800 to 400 Oe in -200 Oe increments
- ➢ Measurement from 200 to -200 Oe in -50 Oe increments
- ➢ Measurement from -400 to -1000 Oe in -200 Oe increments
- ➢ Measurement from -2000 to -20000 Oe in -1000 Oe increments
- ➢ Measurement from -22000 to -50000 Oe in -2000 Oe increments
- ➢ Measurement from -50000 to -22000 Oe in -2000 Oe increments
- ➢ Measurement from -20000 to -1000 Oe in 1000 Oe increments
- ➢ Measurement from -800 to -400 Oe in 200 Oe increments
- ➢ Measurement from -200 to 200 Oe in 50 Oe increments
- ➢ Measurement from 400 to 1000 Oe in 200 Oe increments
- ➢ Measurement from 2000 to 20000 Oe in 1000 Oe increments
- ➢ Measurement from 20000 to 50000 Oe in 2000 Oe increments

Appendix 2.06 Example of magnetic susceptibility measurements sequence

Appendix 3.01
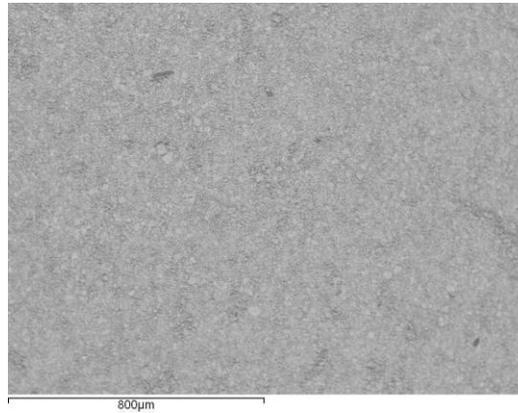
Appendix 3.01 Backscattered secondary electrons image of La2O2Fe2OSe2 taken at X78 magnification.

The sample was pressed into a pellet and divided into 10 sites. Each site was subjected to X201 magnification. Energy dispersive X-rays spectra were collected on each site at 10 different points
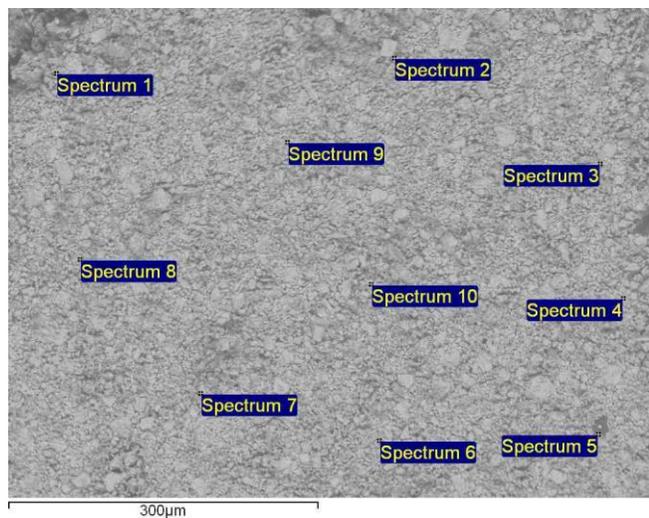
Appendix 3.01 Energy dispersive X-ray spectra collected at 10 different points on a site of $La_2O_2Fe_2OSe_2$ taken at X201 magnification.
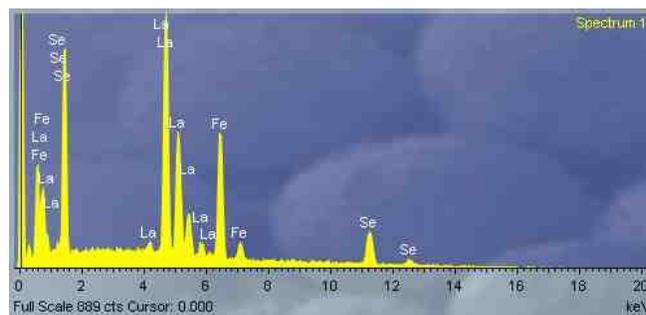
Appendix 3.01 Energy dispersive X-ray spectrum 1 showing the elements present at that point.

Appendix 3.02
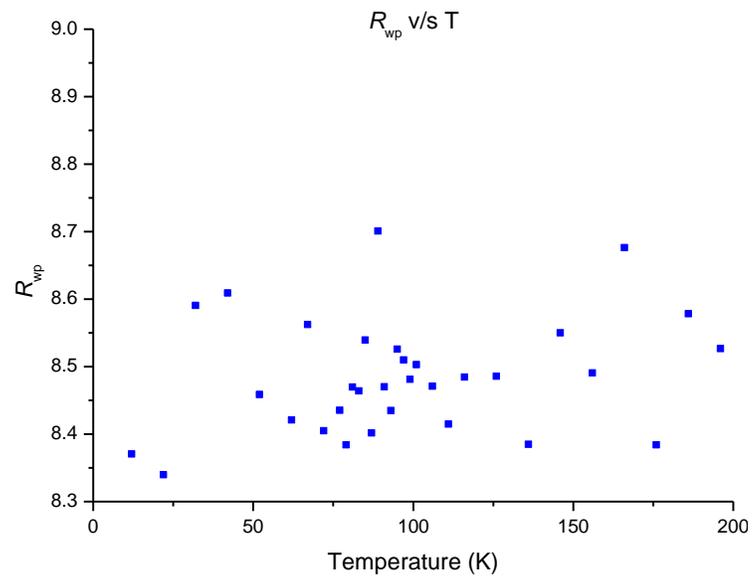
Appendix 3.02 R_{wp} against temperature. Data is shown in blue.
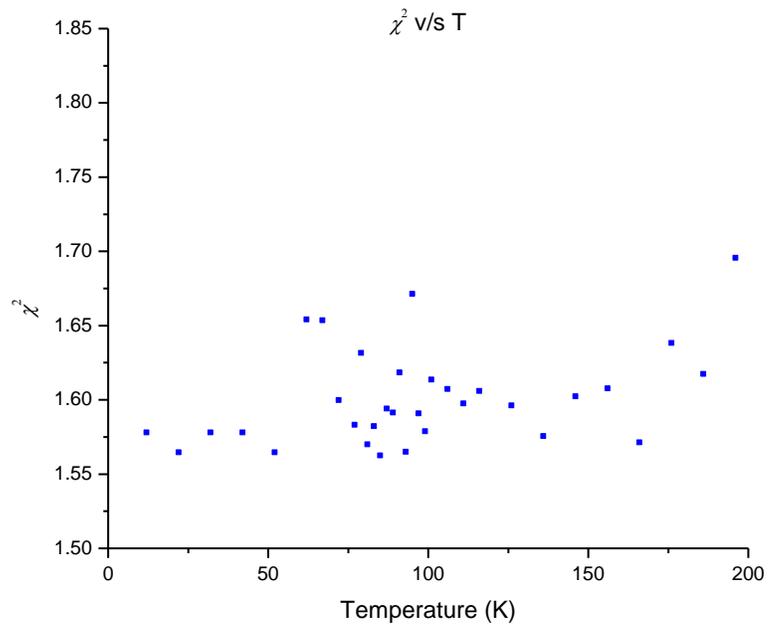
Appendix 3.02 χ^2 against temperature. Data is shown in blue.
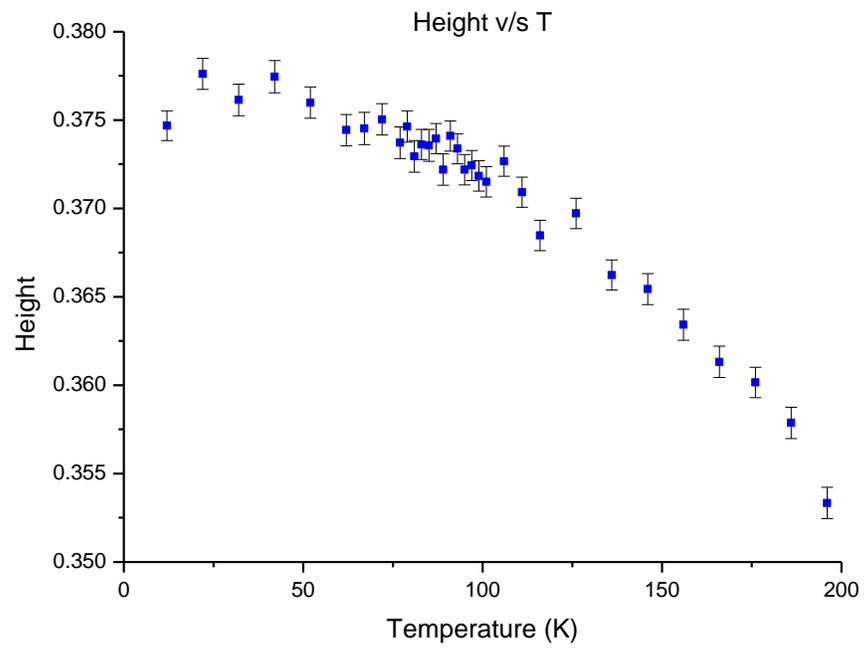
Appendix 3.02 Height against temperature. Data is shown in blue with the error bars in black.

Appendix 3.03
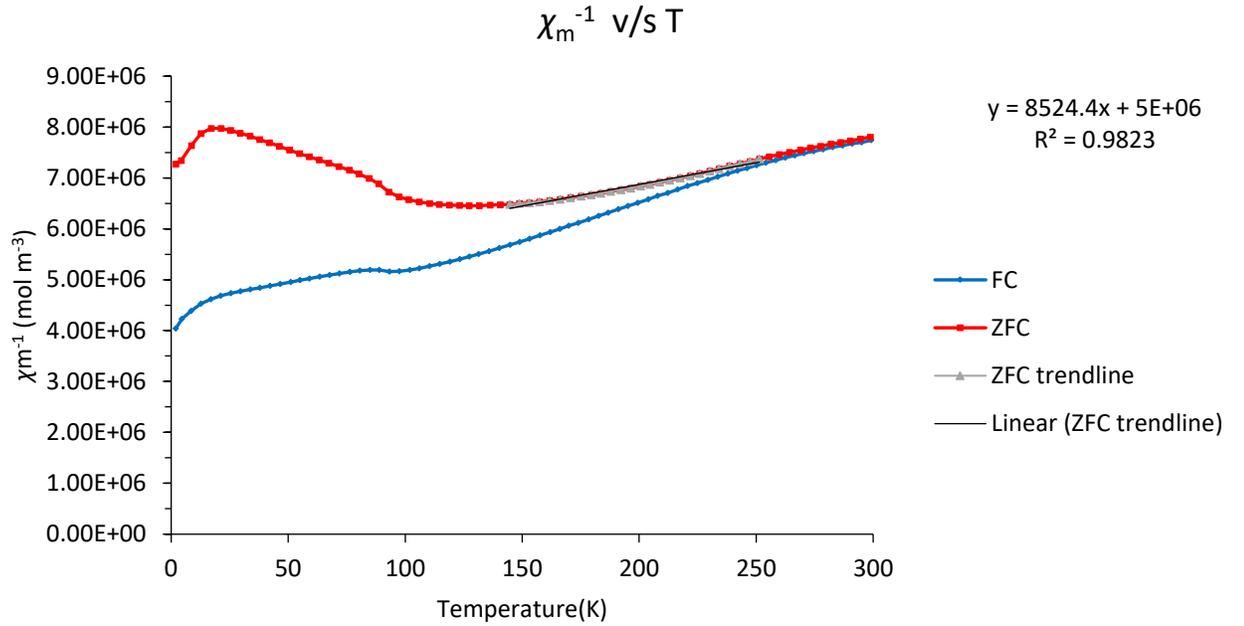
Appendix 3.03 Curie-Weiss plot showing χ_m^{-1} against temperature. ZFC (red) and FC (blue) data for $La_2O_2Fe_2OSe_2$.

Appendix 3.04
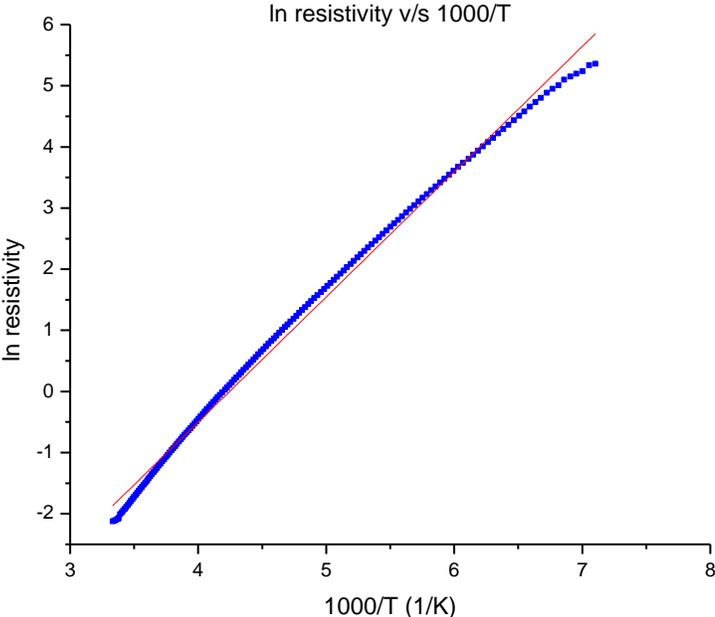
Appendix 3.04 Arrhenius plot ln ρ vs 1000/T showing no linear behaviour. Data is shown in blue and the trendline shown in red.

Appendix 3.05
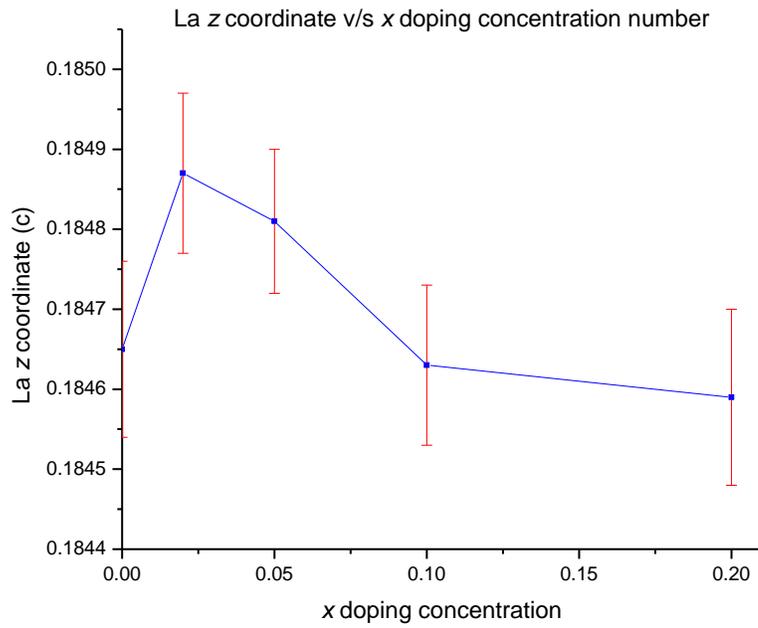
Appendix 3.05 La *z* coordinate against *x* doping concentration. Data is shown in blue and error bars in red
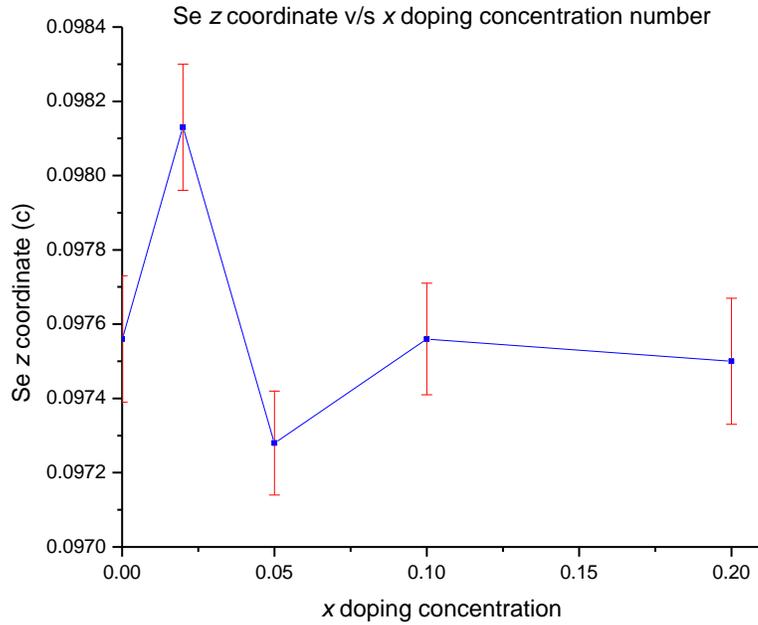
Appendix 3.05 Se *z* coordinate against *x* doping concentration. Data is shown in blue and error bars in red
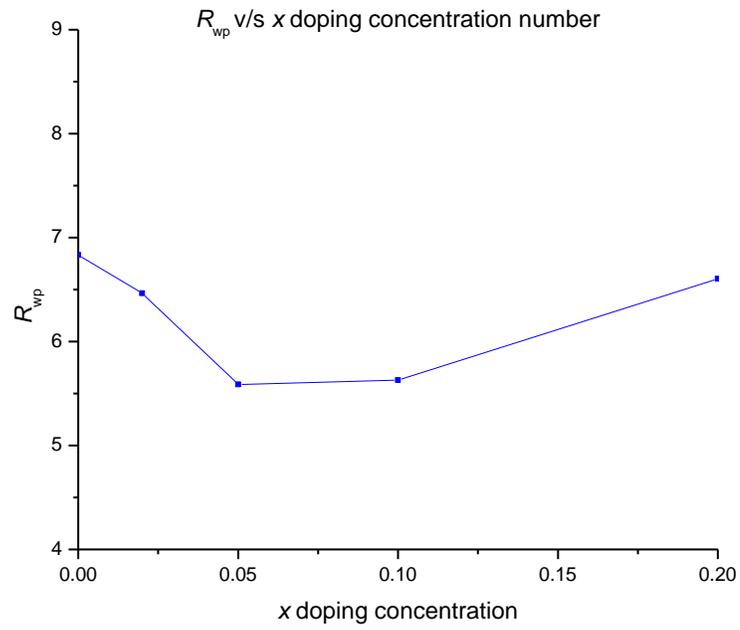
Appendix 3.05 R_{wp} against x doping concentration. Data is shown in blue.
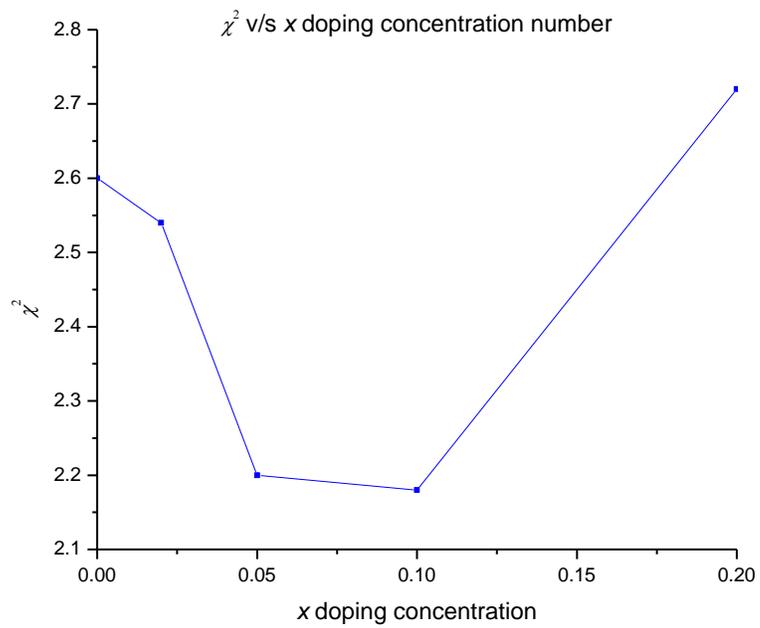
Appendix 3.05 χ^2 against x doping concentration. Data is shown in blue.
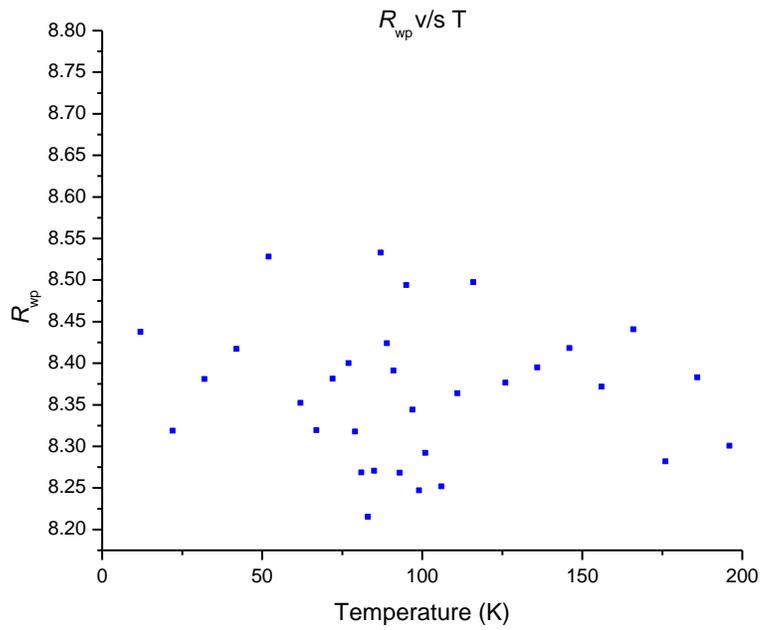
Appendix 3.06 R_{wp} against temperature. Data is shown in blue.
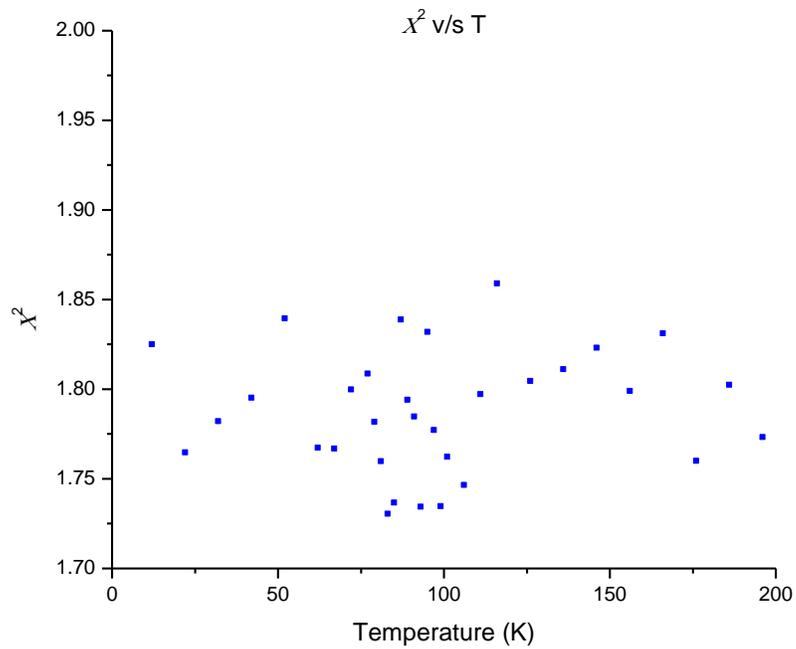
Appendix 3.06 χ^2 against temperature. Data is shown in blue.
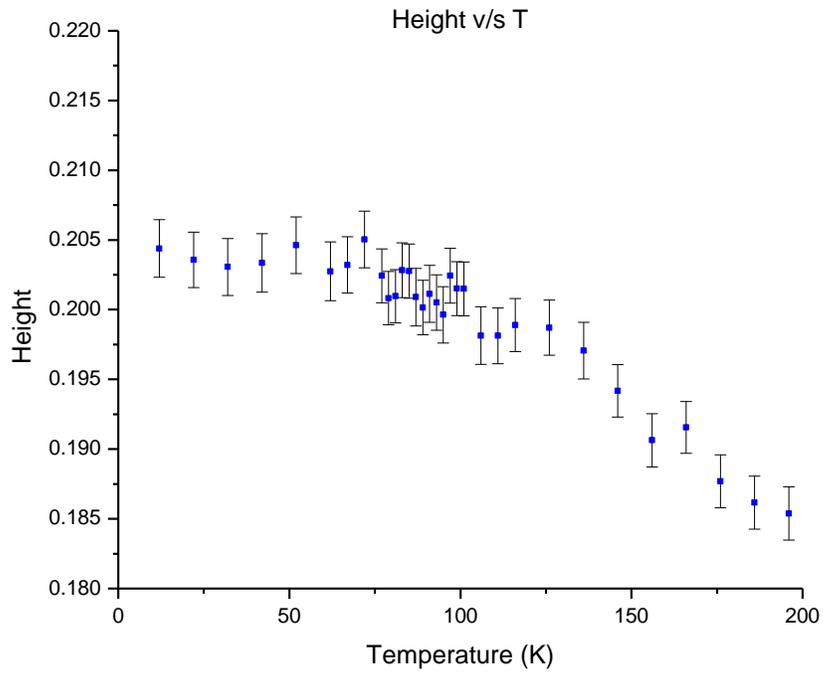
Appendix 3.06 Height against temperature. Data is shown in blue with the error bars in black.
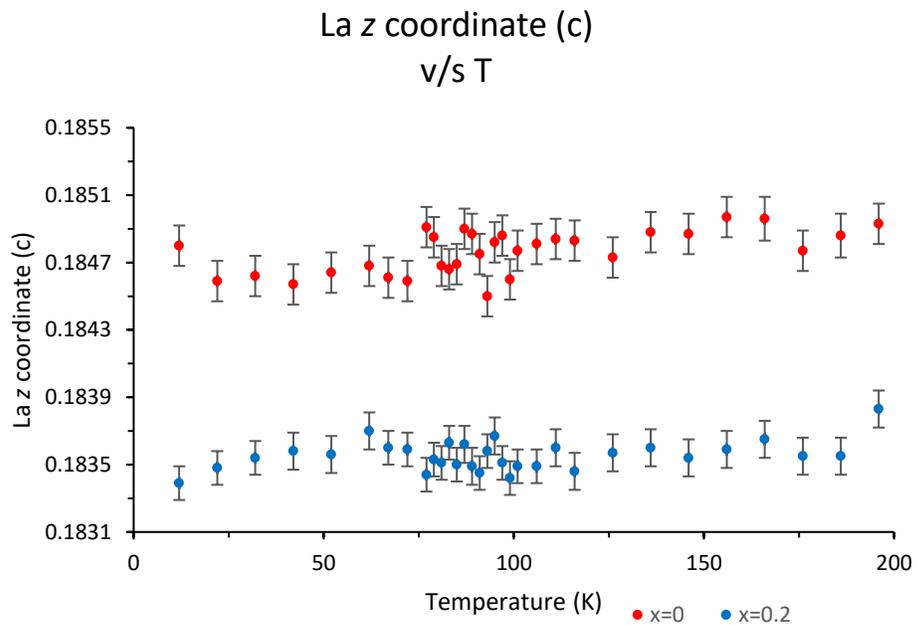
Appendix 3.06 La z coordinate against temperature. $La_2O_2Fe_2OSe_2$ is in red, $La_2O_2Fe_{1.8}Co_{0.2}OSe_2$ is in blue and the error bars in black.
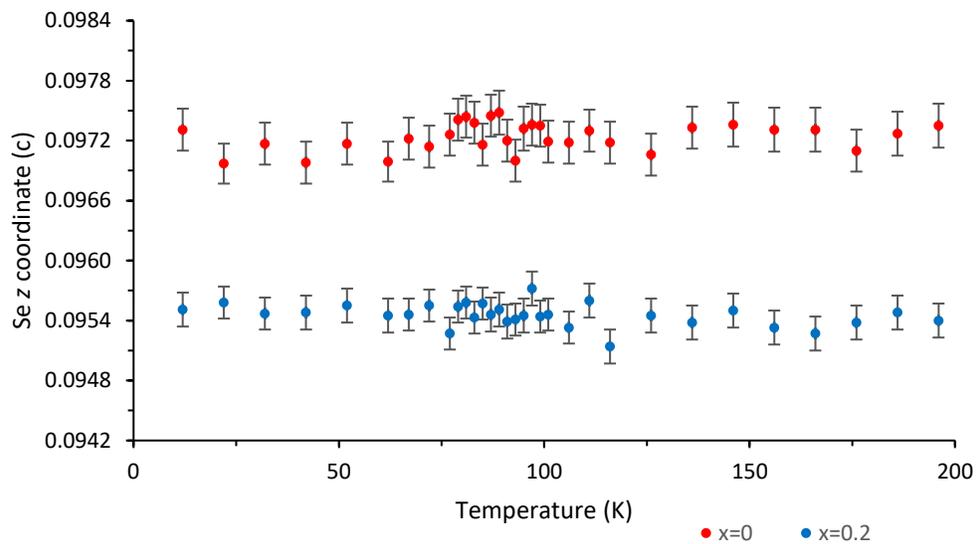
Appendix 3.06 Se z coordinate against temperature. $La_2O_2Fe_2OSe_2$ is in red, $La_2O_2Fe_{1.8}Co_{0.2}OSe_2$ is in blue and the error bars in black.

Appendix 3.07
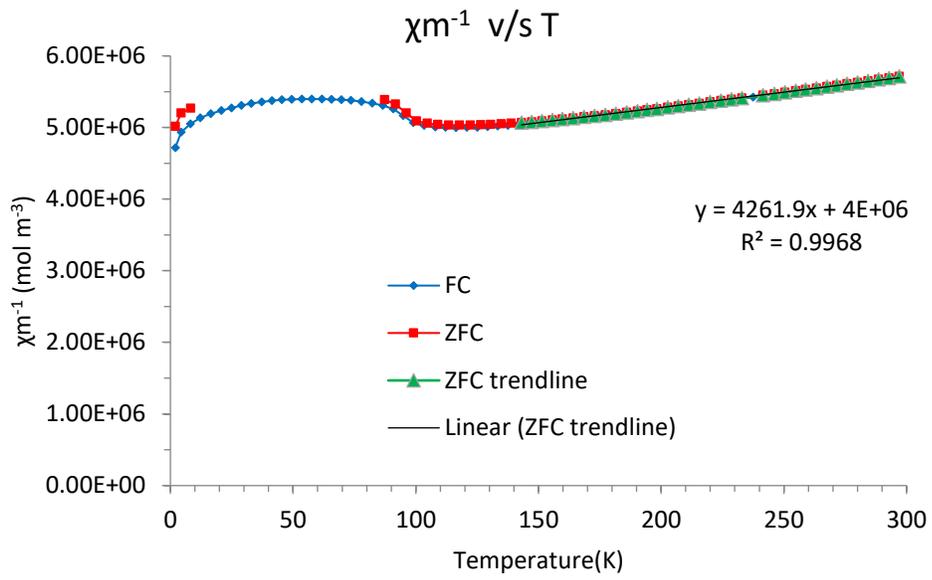
Appendix 3.07 Curie-Weiss plot showing χ_m^{-1} against temperature. ZFC (red) and FC (blue) data for $La_2O_2Fe_{1.8}Co_{0.2}OSe_2$. Trendline data (green) and trendline (black)

Appendix 3.08
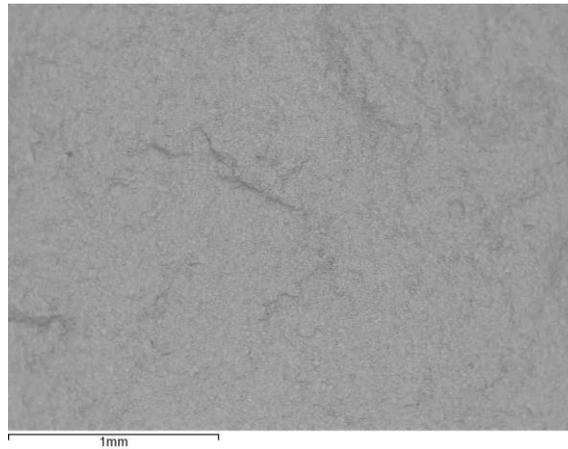
Appendix 3.08 Backscattered secondary electrons image of $La_2O_2Fe_{1.95}Co_{0.05}OSe_2$ taken at X44 magnification.

Each sample site was subjected to a magnification between X199-X202. Energy dispersive X-rays spectra were collected on each site at 10 different points.
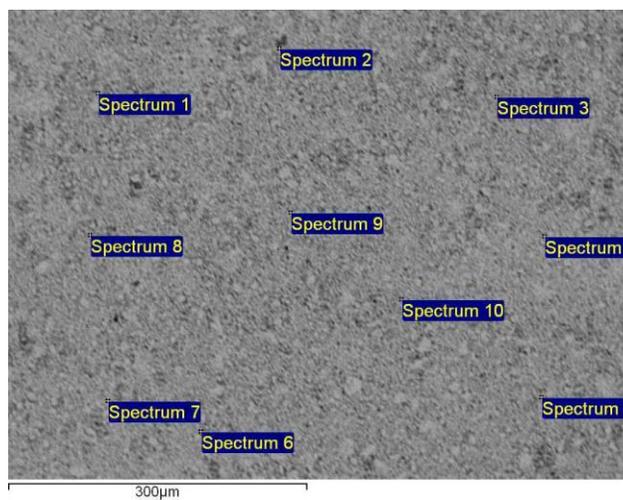
Appendix 3.08 Energy dispersive X-ray spectra of 10 different points on a site of $La_2O_2Fe_{1.95}Co_{0.05}OSe_2$ taken at X202 magnification.
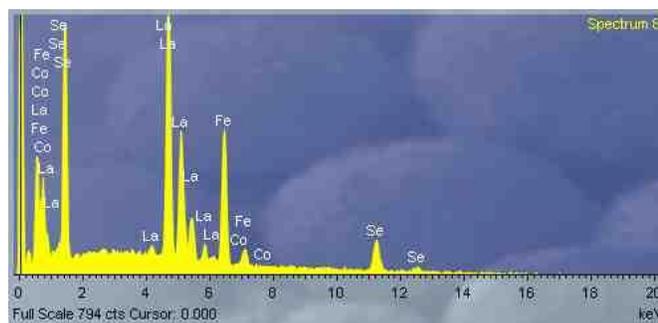
Appendix 3.08 Energy dispersive X-ray spectrum 8 of $La_2O_2Fe_{1.95}Co_{0.05}OSe_2$ showing the elements present at that point.

Appendix 3.09

In resistivity v/s 1/T

x=0.02		Value	Standard
ln resistivi	Intercept	-12.321	0.02128
ln resistivity	Slope	1878.27 761	5.20462

Legend:
- RKO024a (x=0)
- RKO024b (x=0.02)
- RKO024d (x=0.1)
- RKO024e (x=0.2)
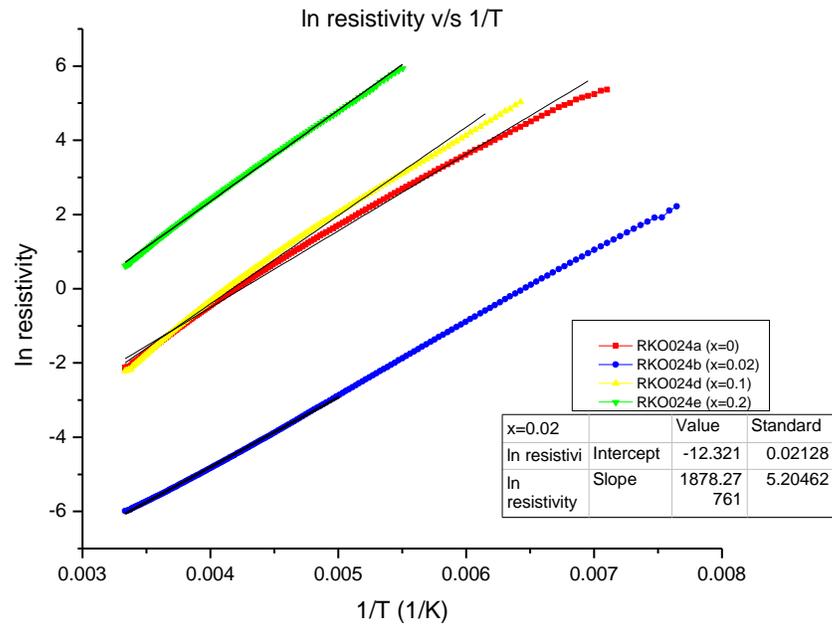
Appendix 3.09 Arrhenius plot ln ρ vs 1/T with the calculated slope and intercept. $La_2O_2Fe_2OSe_2$ (RKO024a) is in red, $La_2O_2Fe_{1.98}Co_{0.02}OSe_2$ (RKO024b) is in blue, $La_2O_2Fe_{1.9}Co_{0.1}OSe_2$ (RKO024d) is in yellow and $La_2O_2Fe_{1.8}Co_{0.2}OSe_2$ (RKO024e) is in green. Trendlines are shown in black.

Appendix 3.10
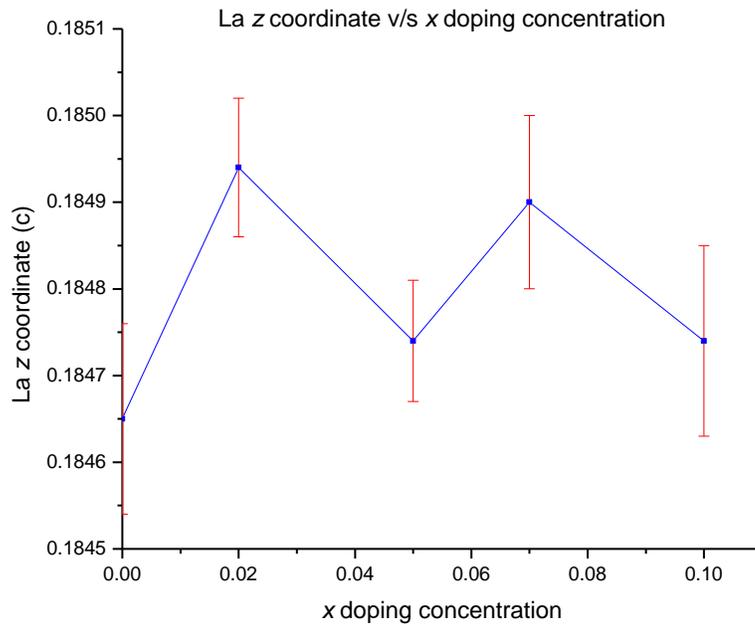
Appendix 3.10 La z coordinate against x doping concentration. Data is shown in blue and error bars in red
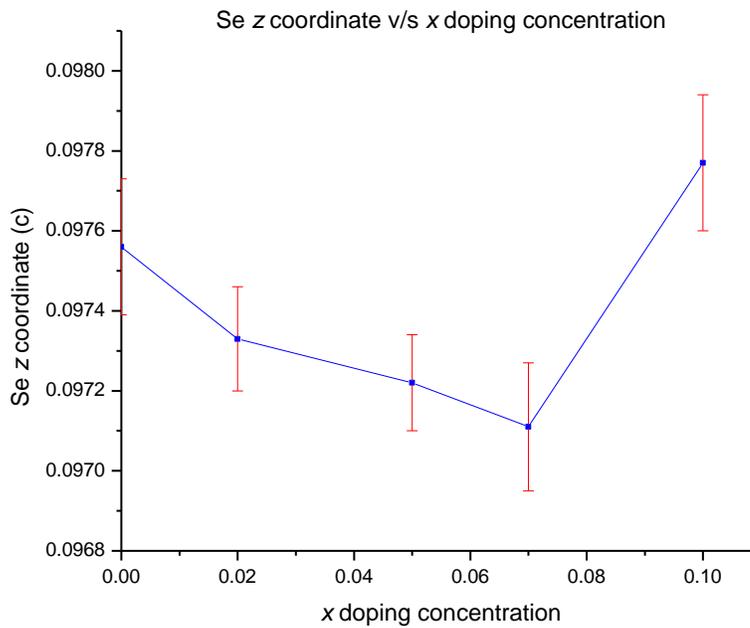
Appendix 3.10 Se z coordinate against x doping concentration. Data is shown in blue and error bars in red
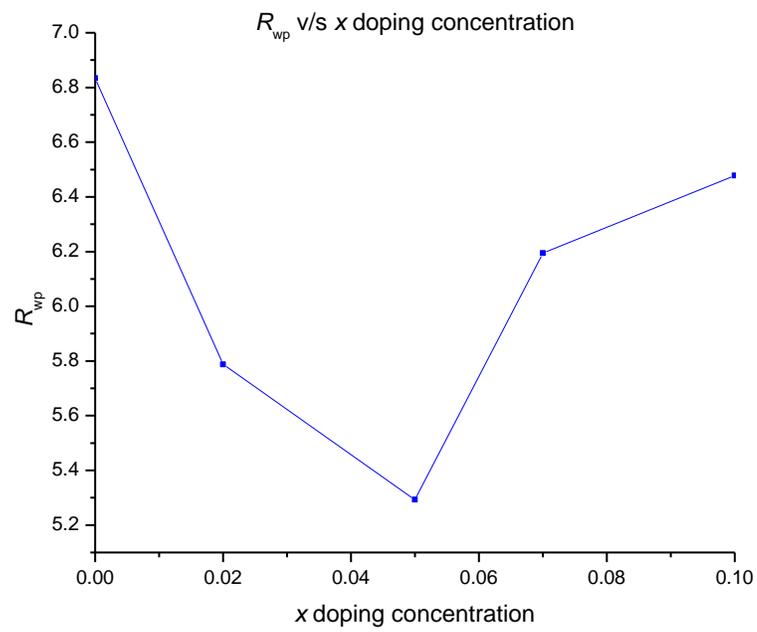
Appendix 3.10 R_{wp} against x doping concentration. Data is shown in blue.
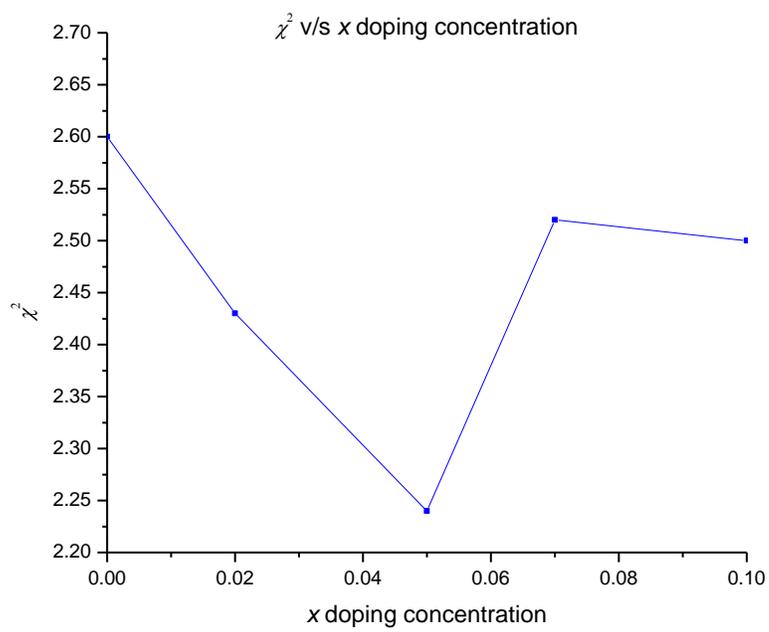
Appendix 3.10 χ^2 against x doping concentration. Data is shown in blue.
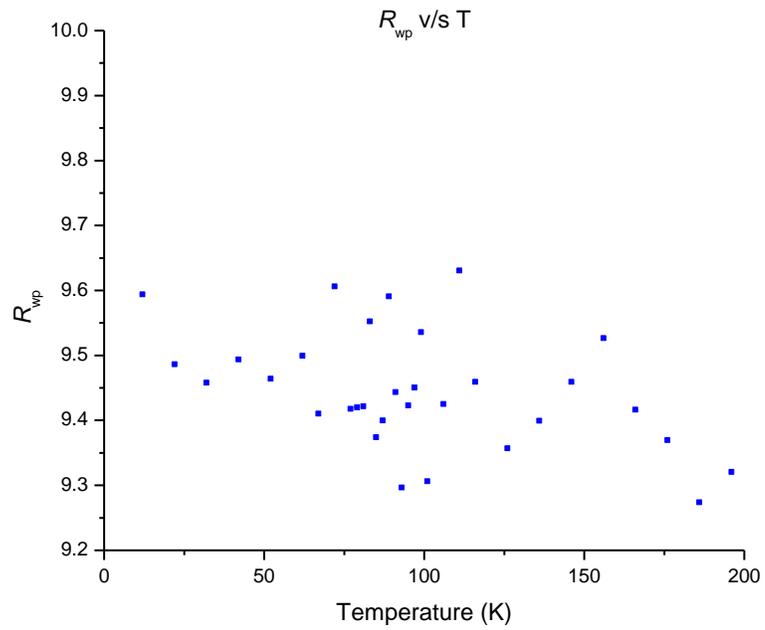
Appendix 3.11

Appendix 3.11 R_{wp} against temperature. Data is shown in blue.
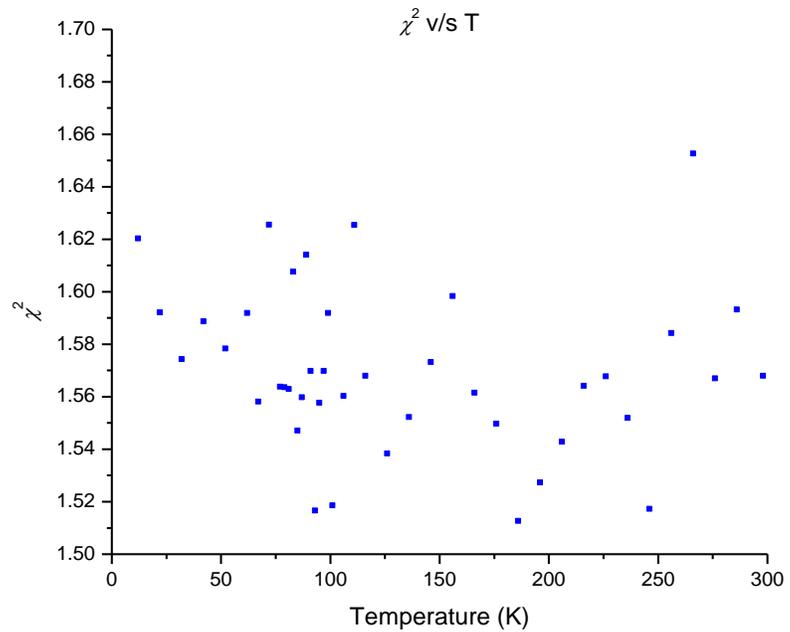
Appendix 3.11 χ^2 against temperature. Data is shown in blue.
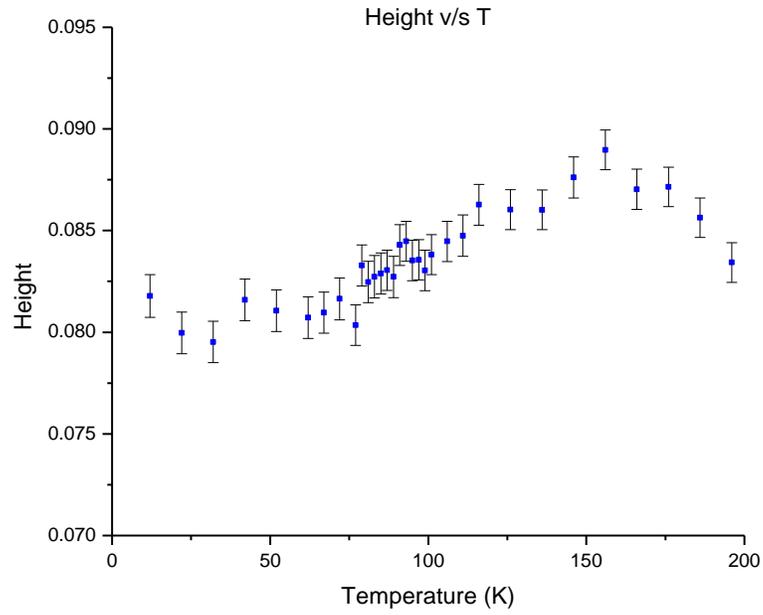
Appendix 3.11 Height against temperature. Data is shown in blue with the error bars in black.
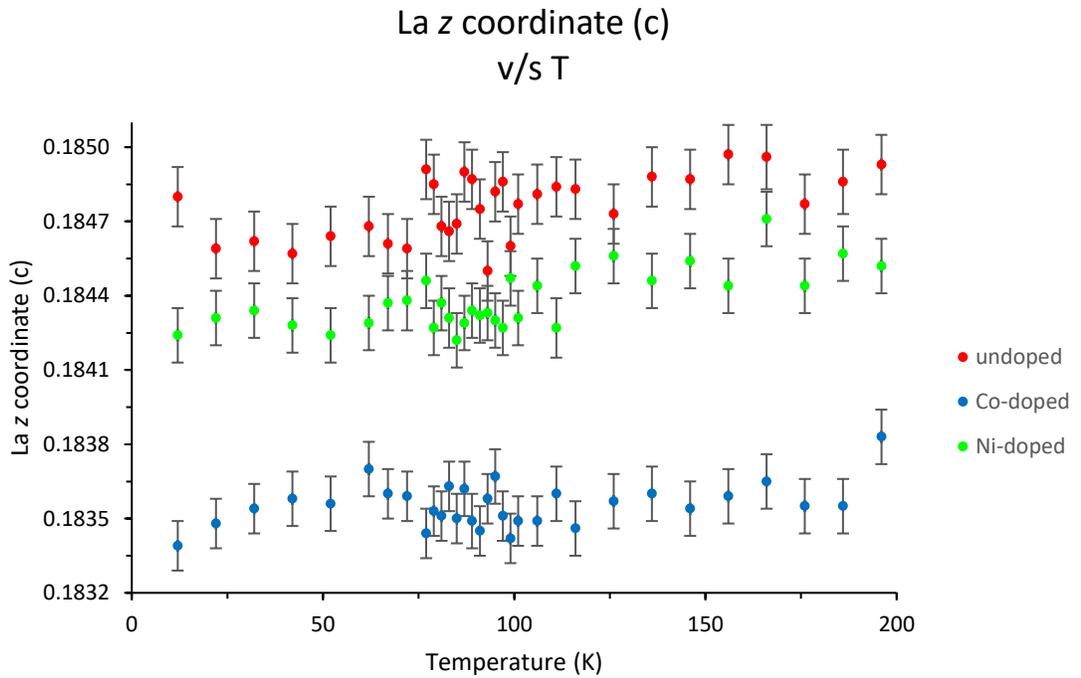
Appendix 3.11 La z coordinate against temperature. $La_2O_2Fe_2OSe_2$ is in red, $La_2O_2Fe_{1.8}Co_{0.2}OSe_2$ is in blue, $La_2O_2Fe_{1.98}Ni_{0.02}OSe_2$ is in green and the error bars in black.
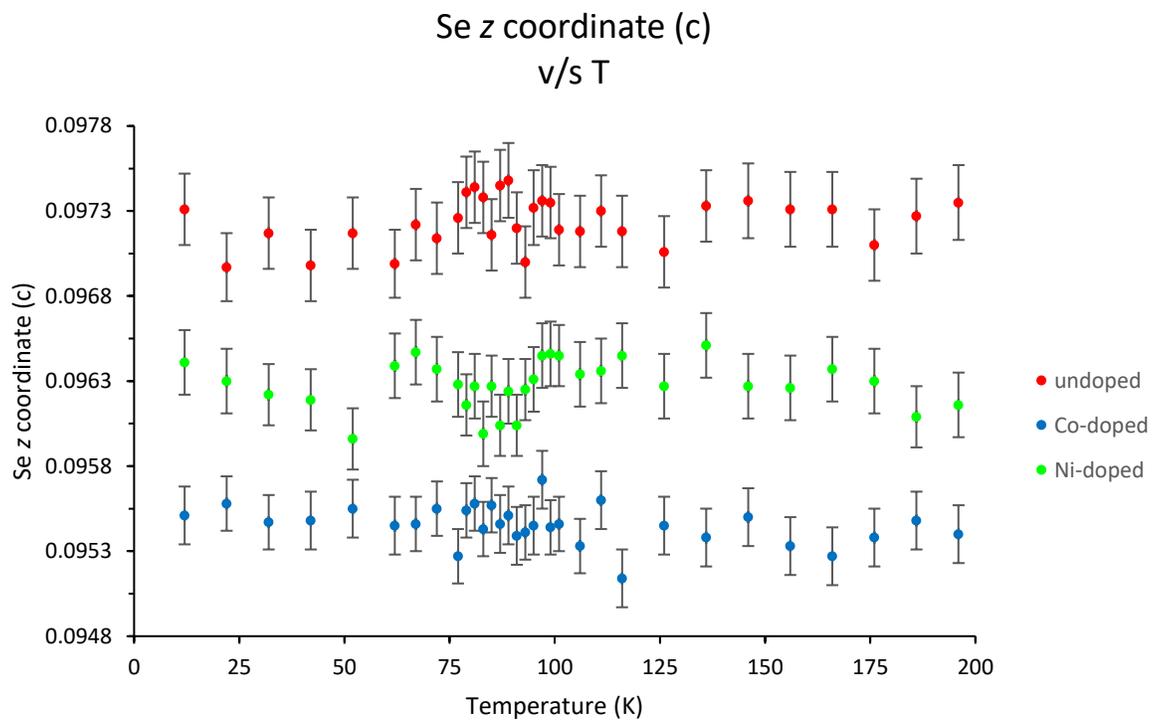
Appendix 3.11 Se z coordinate against temperature. $La_2O_2Fe_2OSe_2$ is in red, $La_2O_2Fe_{1.8}Co_{0.2}OSe_2$ is in blue, $La_2O_2Fe_{1.98}Ni_{0.02}OSe_2$ is in green and the error bars in black.

χm^{-1} (mol m^{-3}) v/s T

y = 5712.9x + 6E+06
R² = 0.9997
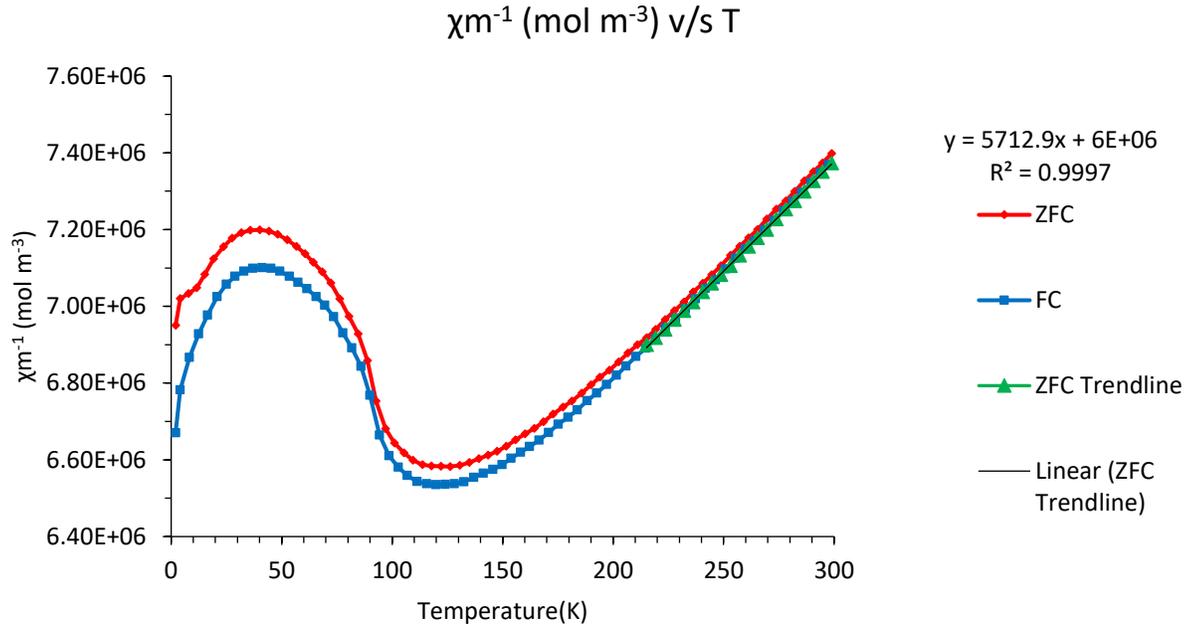
Appendix 3.12 Curie-Weiss plot showing χ_m^{-1} against temperature. ZFC (red) and FC (blue) data for $La_2O_2Fe_{1.9}Ni_{0.1}OSe_2$

Appendix 3.13
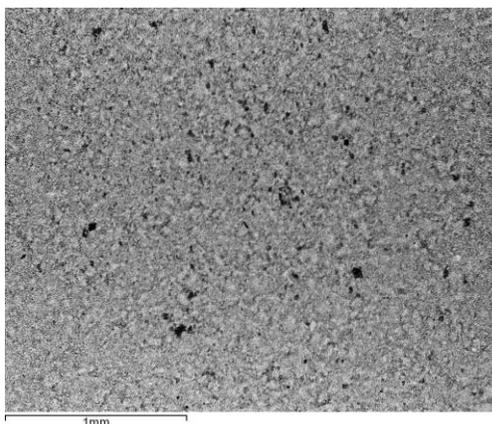
Appendix 3.13 Backscattered secondary electrons image of $La_2O_2Fe_{1.9}Ni_{0.1}OSe_2$ taken at X43 magnification.

The pelletised samples were divided into 10 sites. Each site was subjected to a magnification between X200. Energy dispersive X-rays spectra were collected on each site at 10 different points.
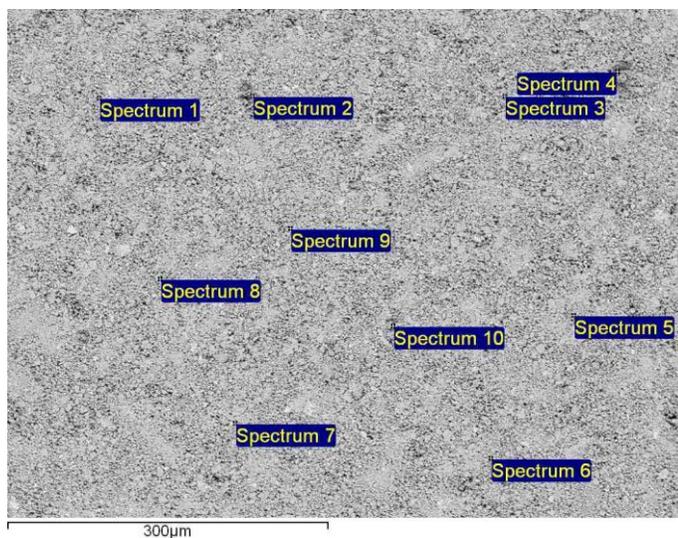
Appendix 3.13 Energy dispersive X-ray spectra at 10 different points on a site of $La_2O_2Fe_{1.9}Ni_{0.1}OSe_2$ taken at X200 magnification.
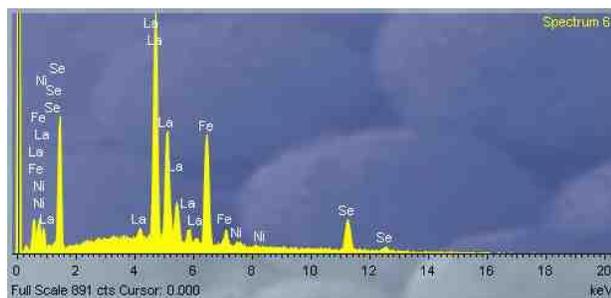
Appendix 3.13 Energy dispersive X-ray spectrum 6 of $La_2O_2Fe_{1.9}Ni_{0.1}OSe_2$ showing the elements present at that point.

Appendix 3.14
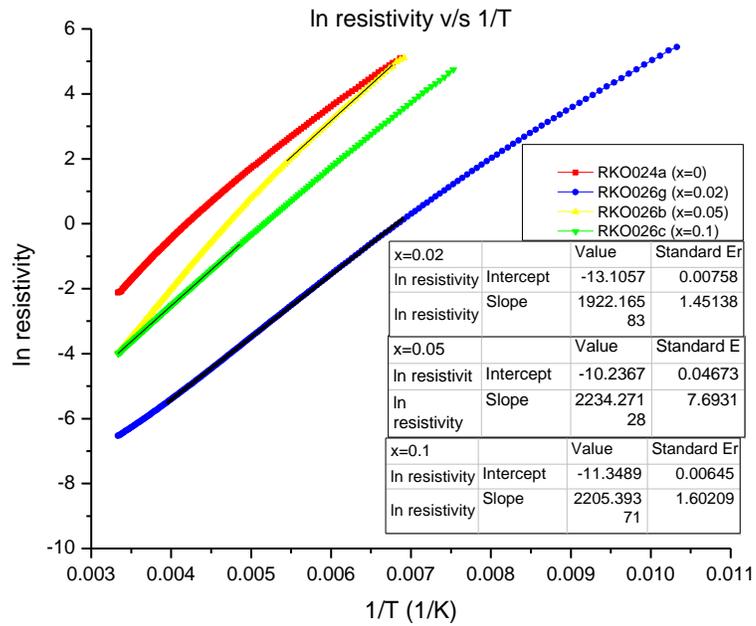
Appendix 3.14 Arrhenius plot ln ρ vs 1/T with the calculated slope and intercept. $La_2O_2Fe_2OSe_2$ (RKO024a) is in red, $La_2O_2Fe_{1.98}Ni_{0.02}OSe_2$ (RKO026g) is in blue, $La_2O_2Fe_{1.95}Ni_{0.05}OSe_2$ (RKO026b) is in yellow and $La_2O_2Fe_{1.9}Ni_{0.1}OSe_2$ (RKO026c) is in green. Trendlines are shown in black.

Appendix 4.01
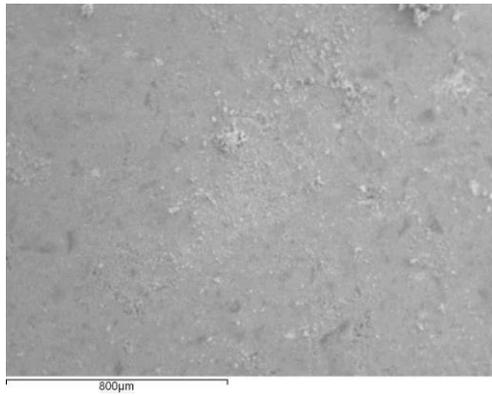
Appendix 4.01 Backscattered secondary electrons image of $La_2O_2Fe_2OS_2$ taken at X67 magnification.

The sample was pressed into a pellet and divided into 10 sites. Each site was subjected to X904 magnification. Energy dispersive X-rays spectra were collected on each site at 10 different points
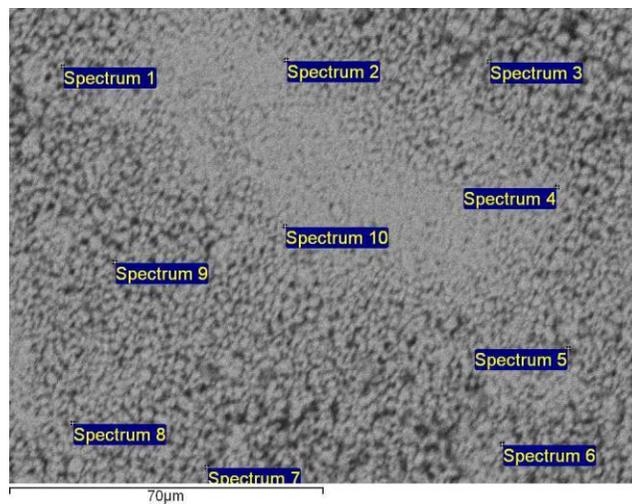
Appendix 4.01 Energy dispersive X-ray spectra collected at 10 different points on a site of $La_2O_2Fe_2OS_2$ taken at X904 magnification.
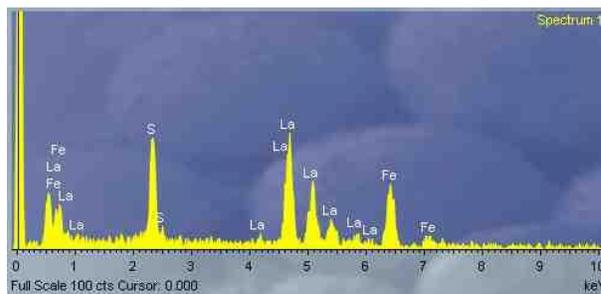
Appendix 4.01 Energy dispersive X-ray spectrum 1 showing the elements present at that point.

Appendix 4.02
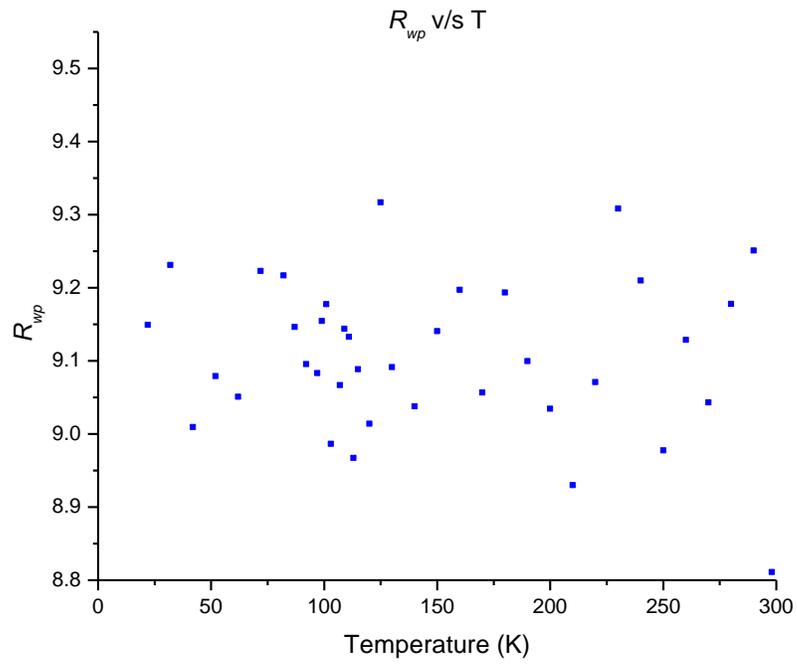
Appendix 4.02 R_{wp} against temperature. Data is shown in blue.
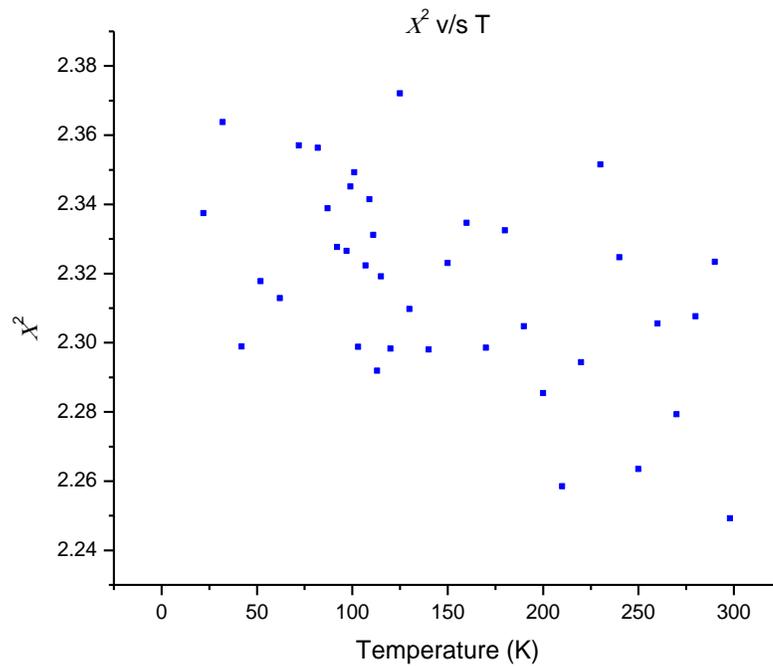
Appendix 4.02 χ^2 against temperature. Data is shown in blue.
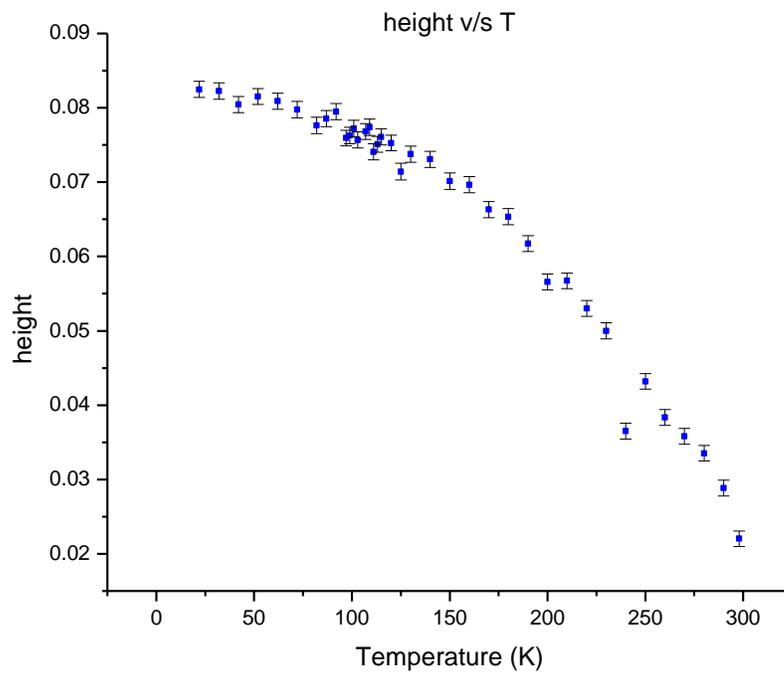
Appendix 4.02 Height against temperature. Data is shown in blue with the error bars in black.

Appendix 4.03
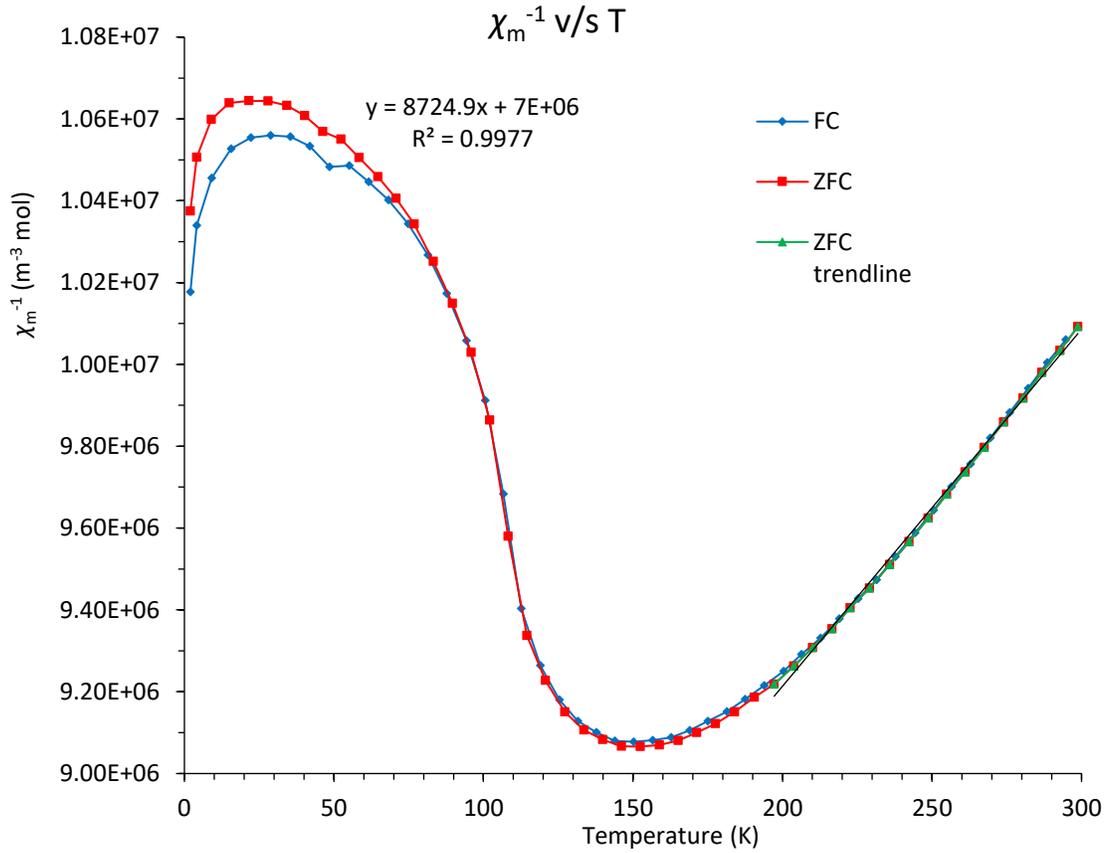
Appendix 4.03 Curie-Weiss plot showing χ_m^{-1} against temperature. ZFC (red) and FC (blue) data for $La_2O_2Fe_2OS_2$.

Appendix 4.04
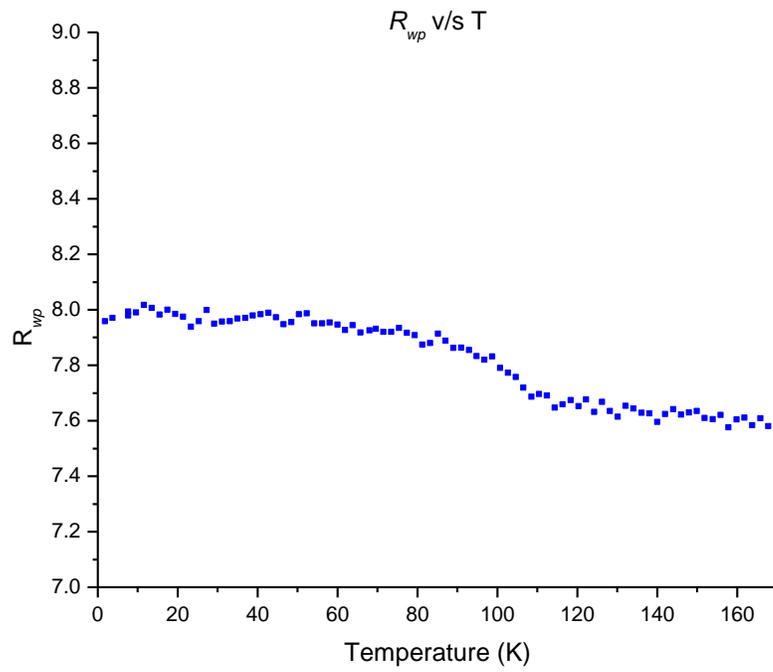
Appendix 4.04 R_{wp} against temperature. Data is shown in blue.
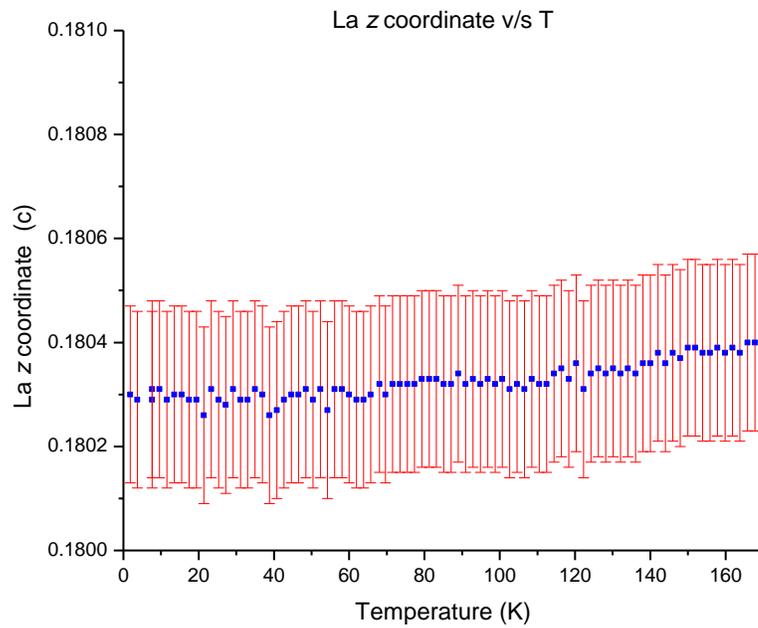
Appendix 4.04 La z coordinate against temperature. Data is shown in blue and error bars in red
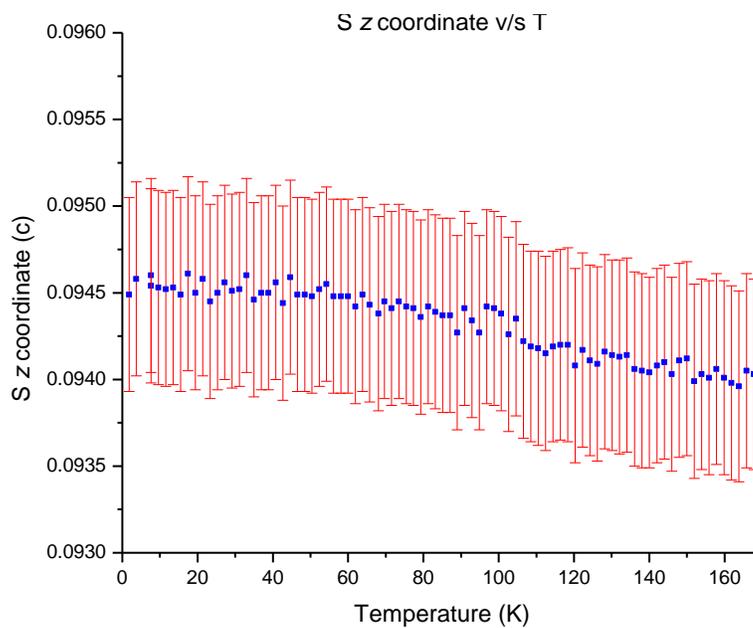
Appendix 4.04 S z coordinate against temperature. Data is shown in blue and error bars in red
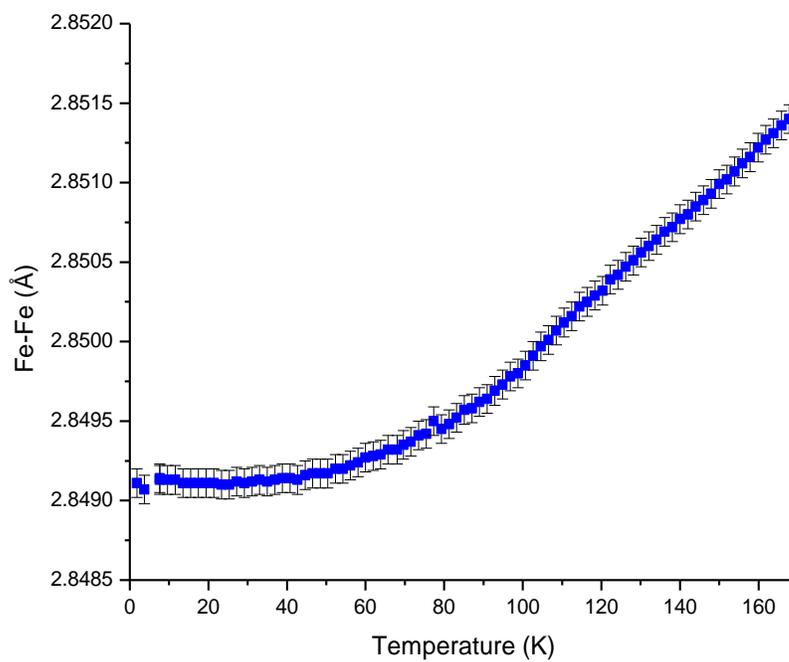
Appendix 4.04 Fe-Fe bond lengths against temperature. Data is shown in blue and error bars in black
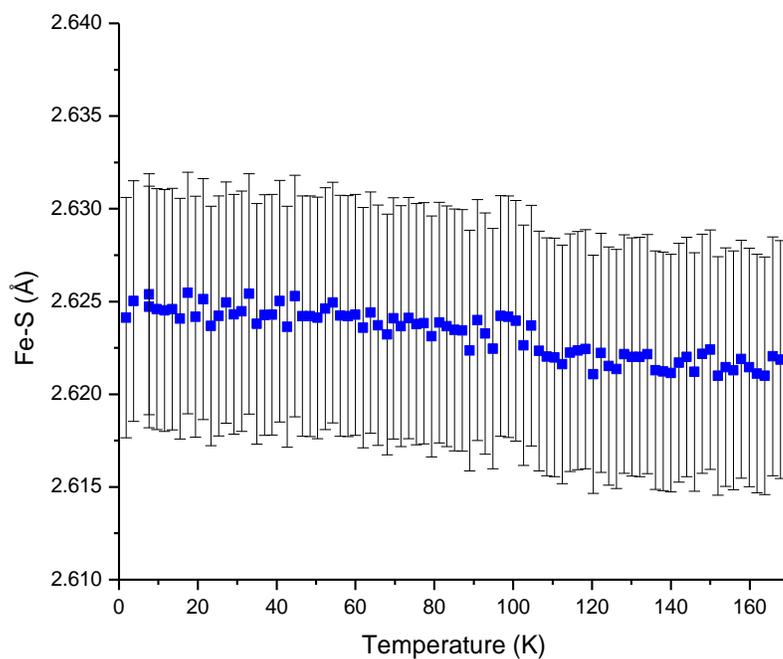
Appendix 4.04 Fe-S bond lengths against temperature. Data is shown in blue and error bars in black
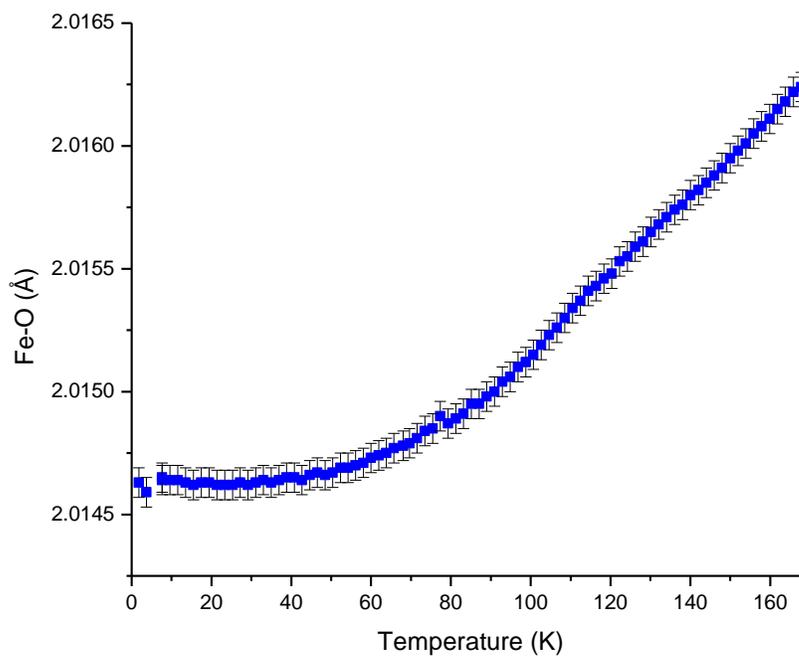
Appendix 4.04 Fe-O bond lengths against temperature. Data is shown in blue and error bars in black
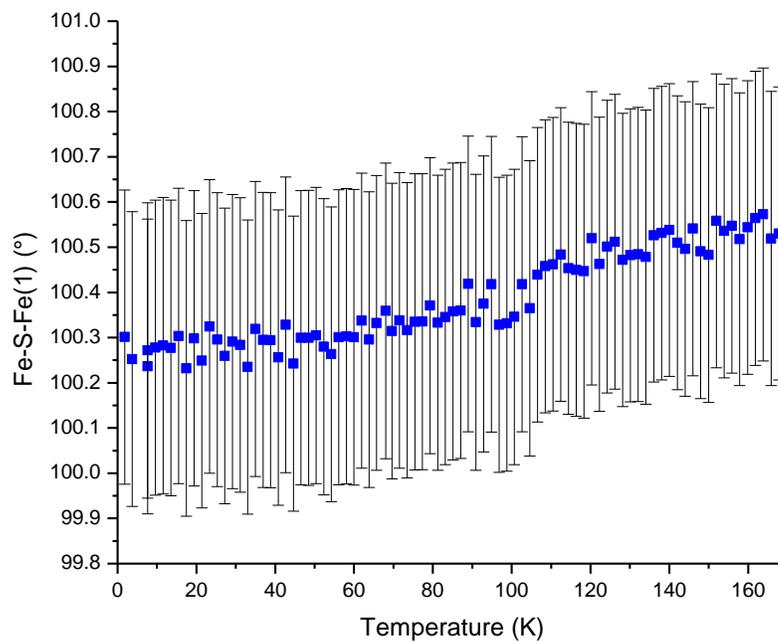
Appendix 4.04 Fe-S-Fe (1) bond angles against temperature. Data is shown in blue and error bars in black
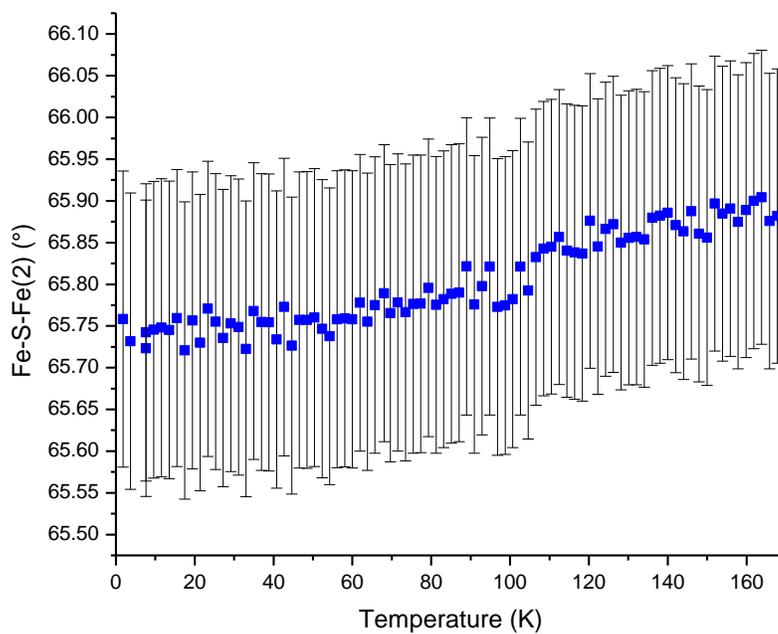
Appendix 4.04 Fe-S-Fe (2) bond angles against temperature. Data is shown in blue and error bars in black

Appendix 4.05
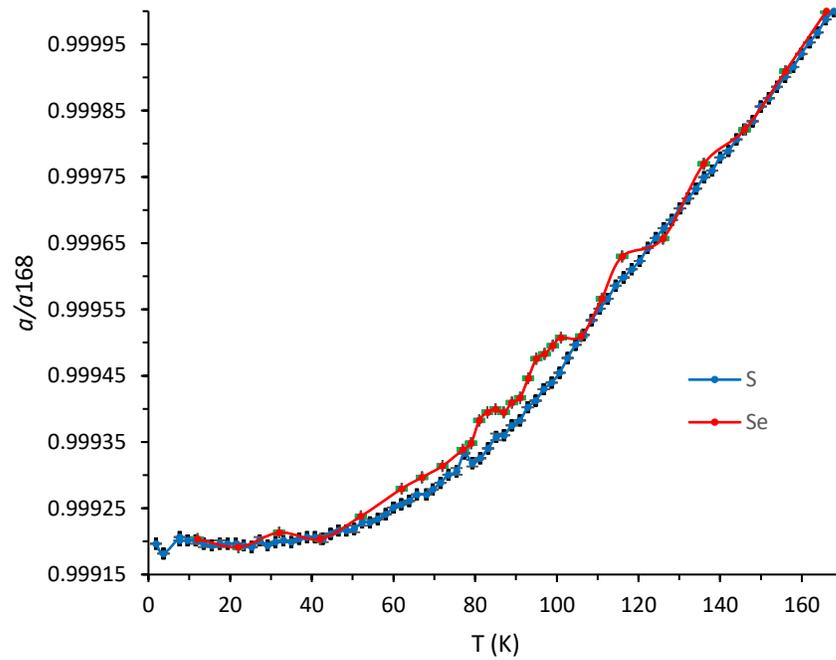
Appendix 4.05 a/a168 against temperature for La$_2$O$_2$Fe$_2$OS$_2$ (blue) with black error bars and La$_2$O$_2$Fe$_2$OSe$_2$ (red) with green error bars
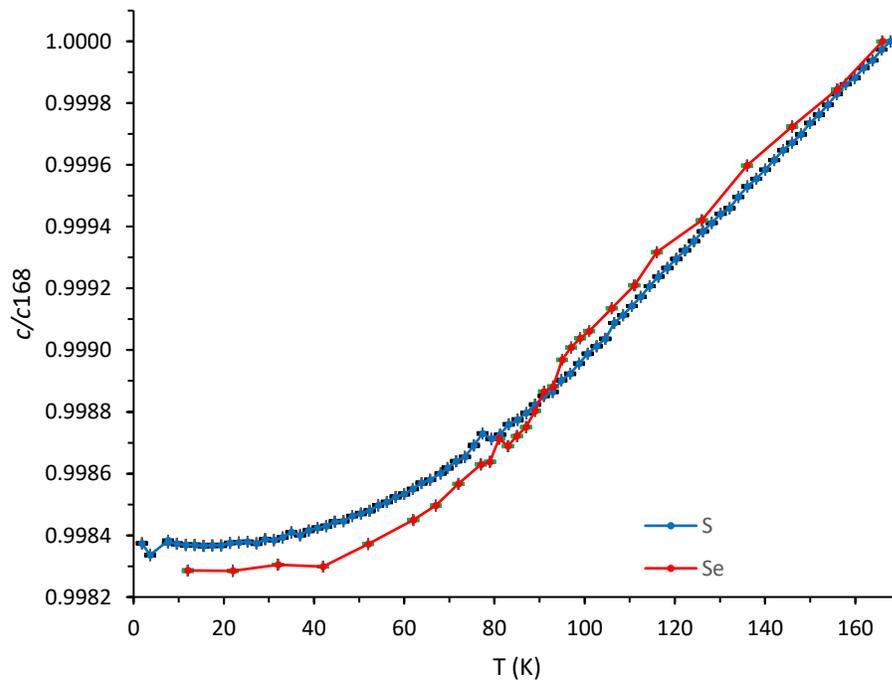
Appendix 4.05 c/c168 against temperature for La$_2$O$_2$Fe$_2$OS$_2$ (blue) with black error bars and La$_2$O$_2$Fe$_2$OSe$_2$ (red) with green error bars

Appendix 4.06

Appendix 4.06 Intensities of magnetic Bragg reflections on cooling from sequential NPD refinements using a Pawley phase to fit the peak intensities. Data is shown in blue and error bars in black.
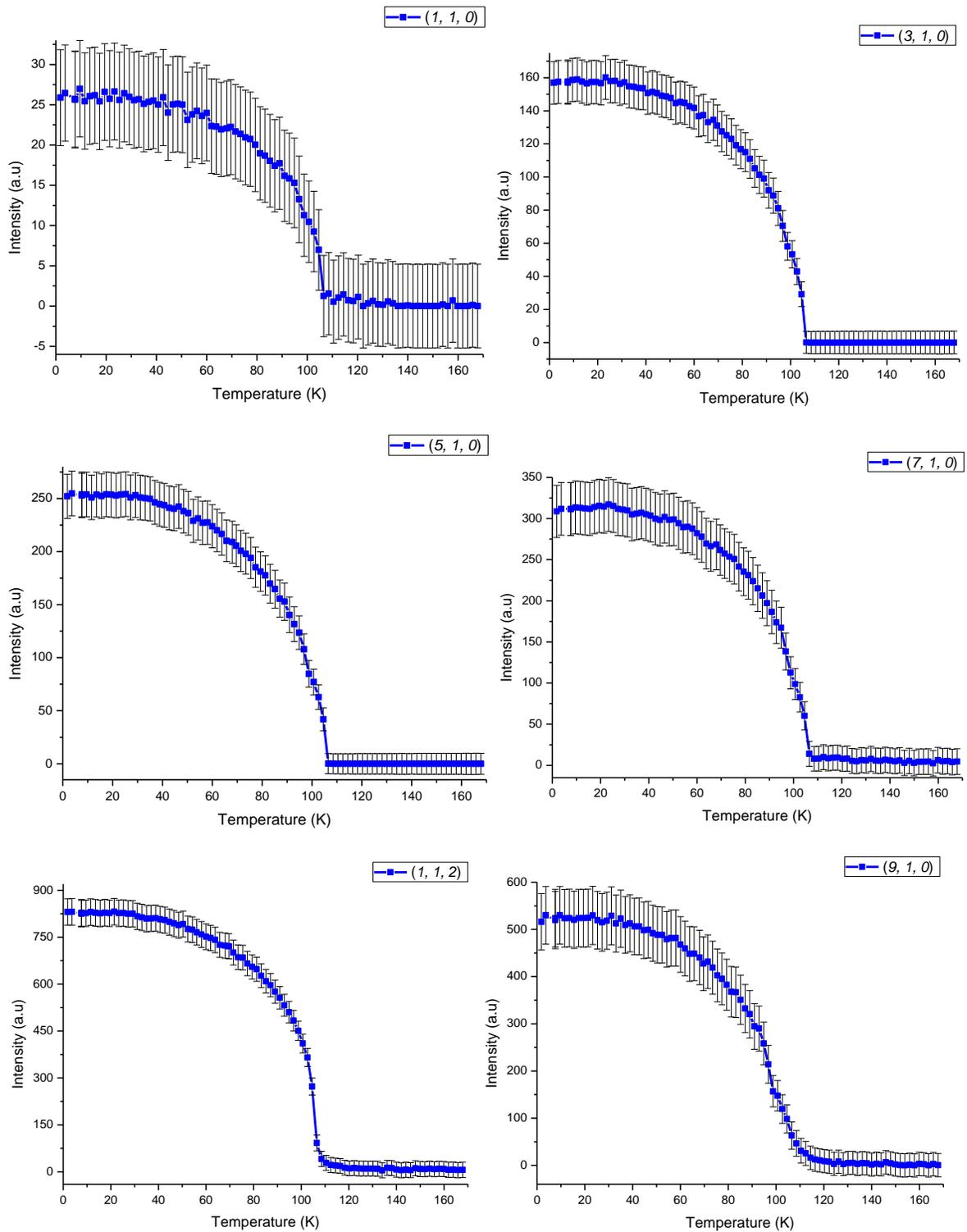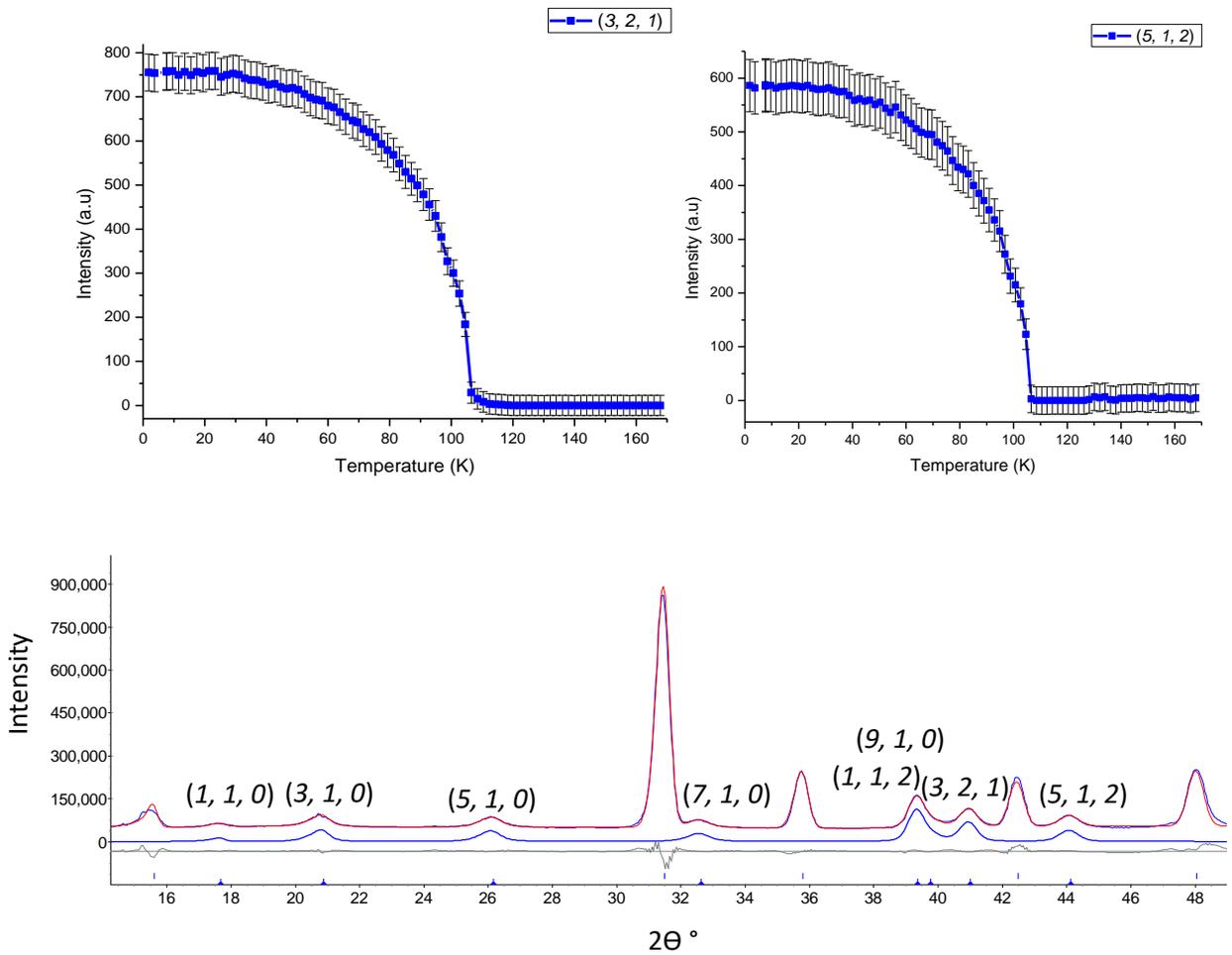
Appendix 4.06 Rietveld refinement profile using 1.8 K NPD data with a pawley fit showing the reflections of the magnetic Bragg intensities. The observed data is in blue, the calculated data is in red and the difference is in grey. Magnetic phase is shown as a solid blue line (just above the difference line)

Appendix 4.07
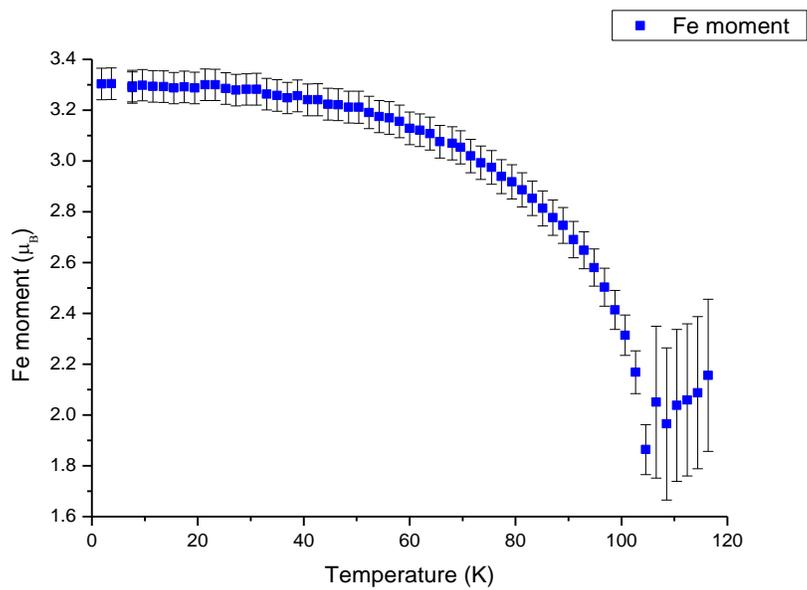
Appendix 4.07 Fe^{2+} moments as a function of temperature (K). data is in blue and error bars in black.

Appendix 4.08
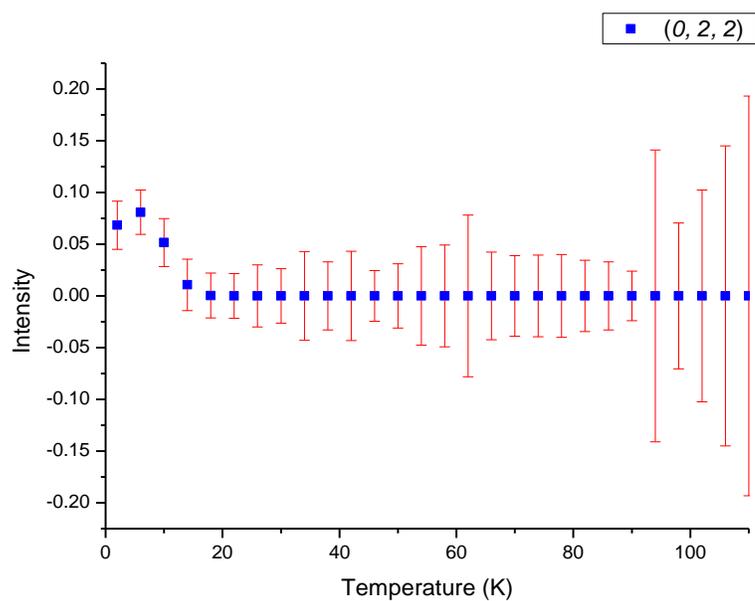
Appendix 4.08 Magnetic Bragg reflection intensity on cooling from sequential NPD refinements using a Pawley phase to fit the peak intensities and using bank 2 data. Error bars are in red and data is in blue.

Appendix 4.09
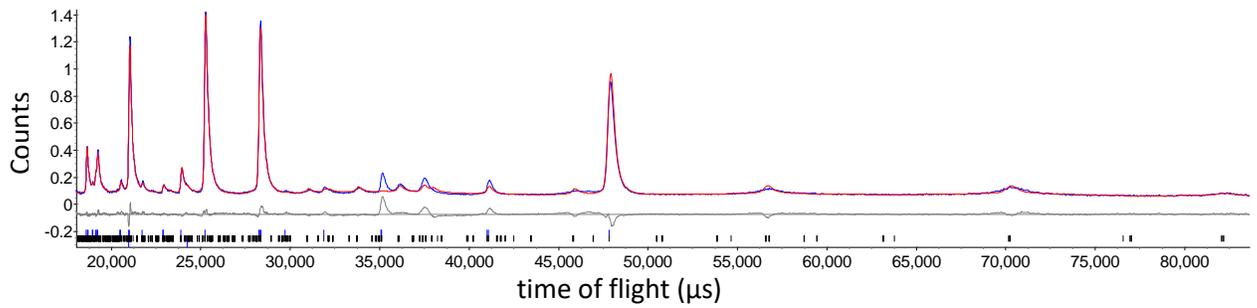
Appendix 4.09 Rietveld refinement profile using 2 K NPD data at 5 T applied magnetic field with Fe^{2+} mode inclusion activated. The observed data is in blue, the calculated data is in red and the difference is in grey. Black ticks are magnetic reflections and blue ticks are nuclear reflections.
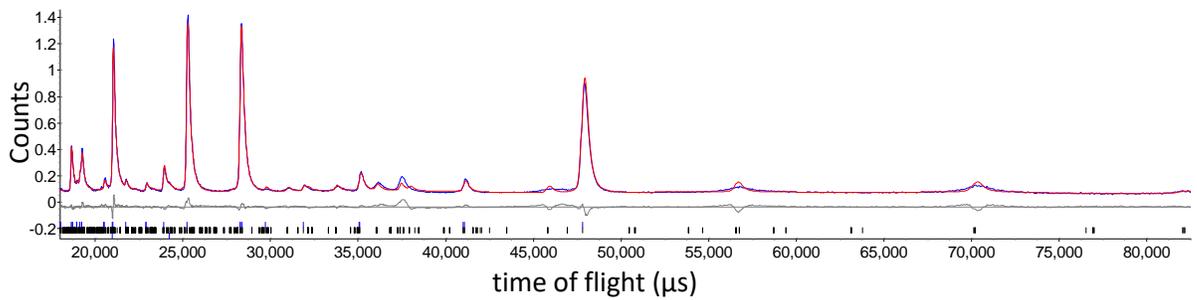
Appendix 4.09 Rietveld refinement profile using 2 K NPD data at 5 T applied magnetic field with Fe^{2+} and Pr^{3+} mode inclusion activated. The observed data is in blue, the calculated data is in red and the difference is in grey. Black ticks are magnetic reflections and blue ticks are nuclear reflections.

Appendix 4.10
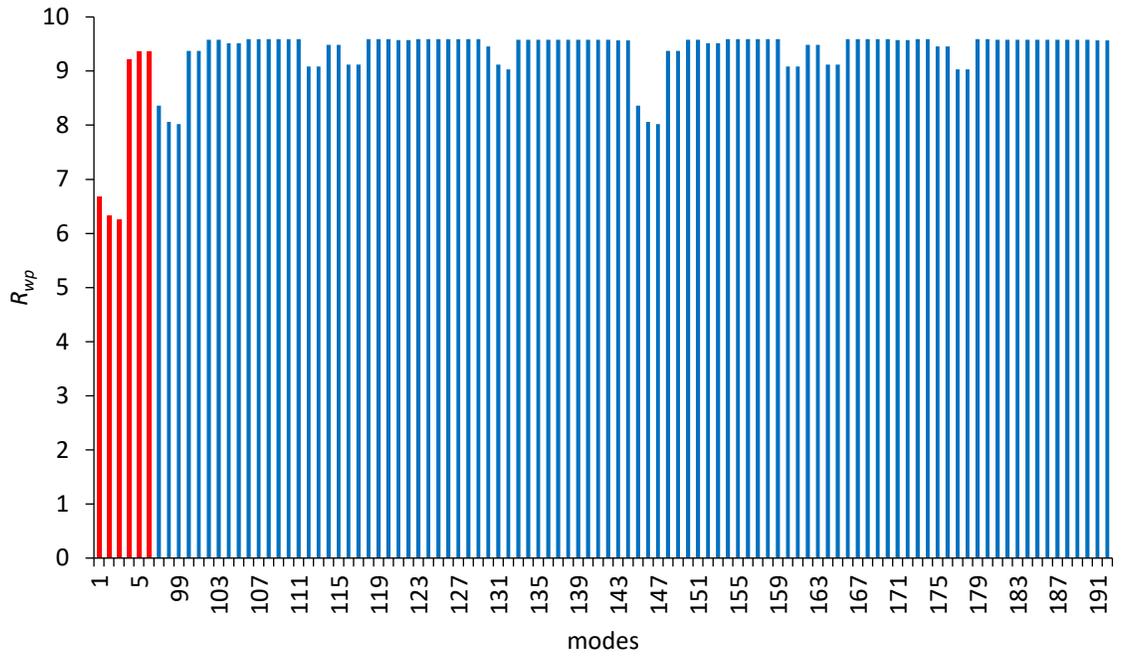
Appendix 4.10 NPD data at 2 K 5 T using bank 2 showing R_{wp} for the different modes for Pr^{3+}(red) and Fe^{2+} (blue)

Appendix 5.01
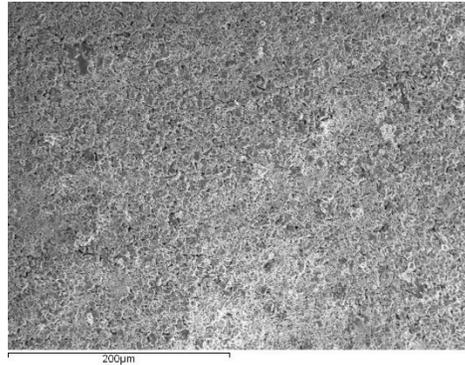
Appendix 5.01 Backscattered secondary electrons image of LaGaOS$_2$ taken at X34 magnification.

The sample was pressed into a pellet and divided into 12 sites. Each site was subjected to X300 magnification. Energy dispersive X-rays spectra were collected on each site at 10 different points
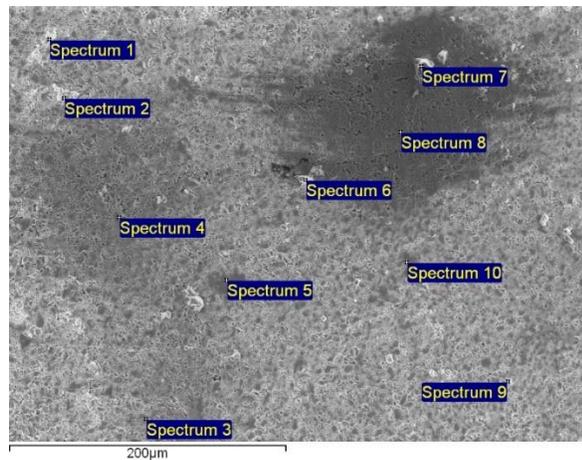
Appendix 5.01 Energy dispersive X-ray spectra collected at 10 different points on a site of LaGaOS$_2$ taken at X300 magnification.
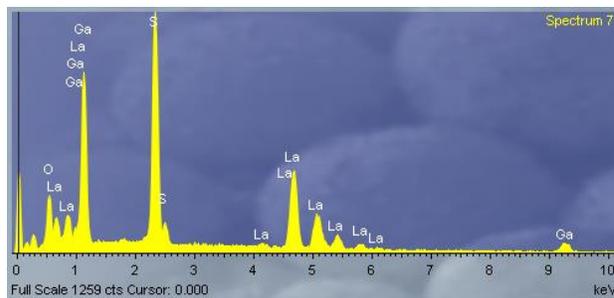
Appendix 5.01 Energy dispersive X-ray spectrum 7 showing the elements present at that point.

Appendix 5.02
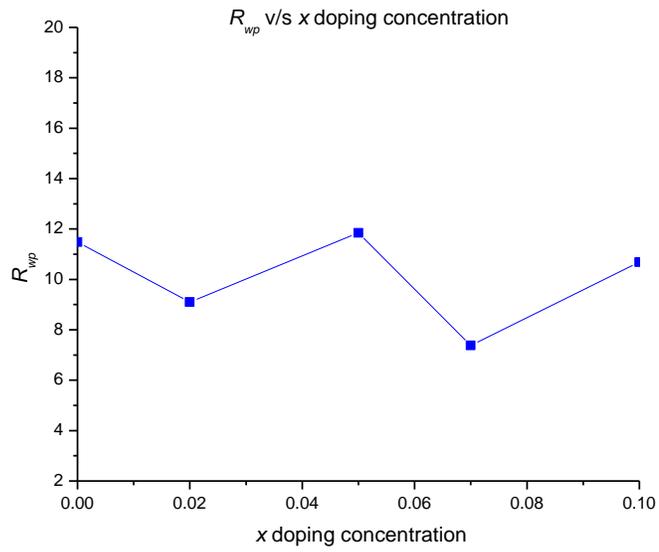
Appendix 5.02 R_{wp} against x doping concentration for $La_{1-x}Nd_xGaOS_2$. Data is shown in blue.
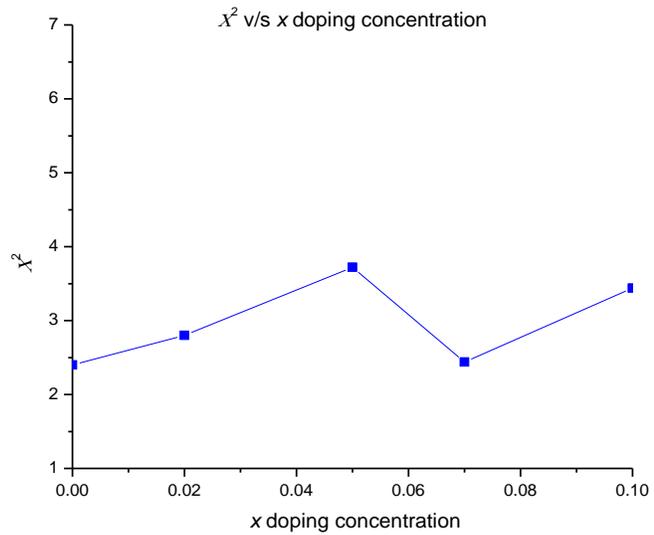
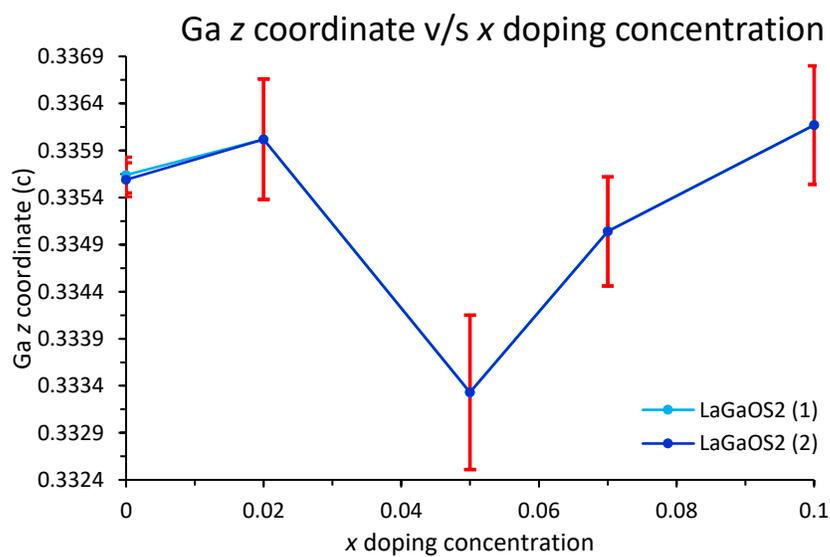Appendix 5.02 χ^2 against x doping concentration for $La_{1-x}Nd_xGaOS_2$. Data is shown in blue.
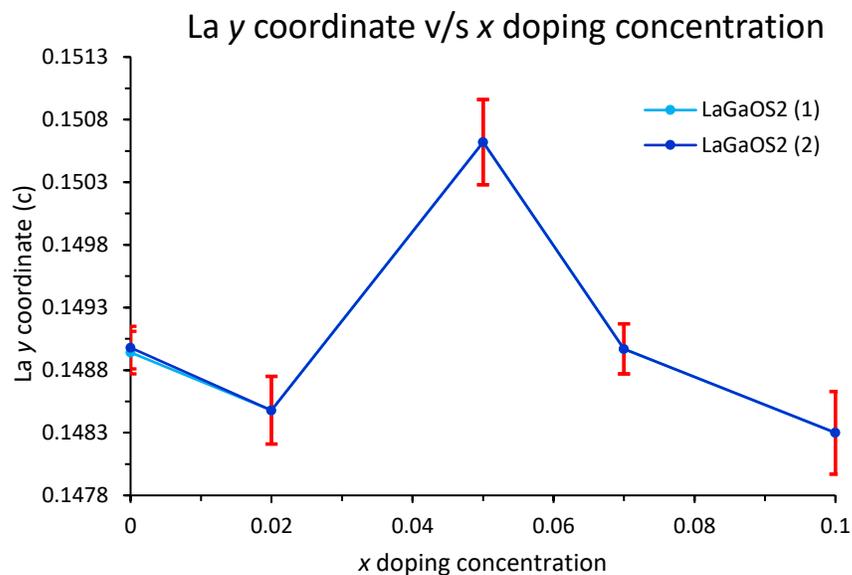
Appendix 5.02 La y coordinate against x doping concentration for La$_{1-x}$Nd$_x$GaOS$_2$. Data for LaGaOS$_2$ (1) and LaGaOS$_2$ (2) are shown in pale-blue and blue respectively and error bars in red.
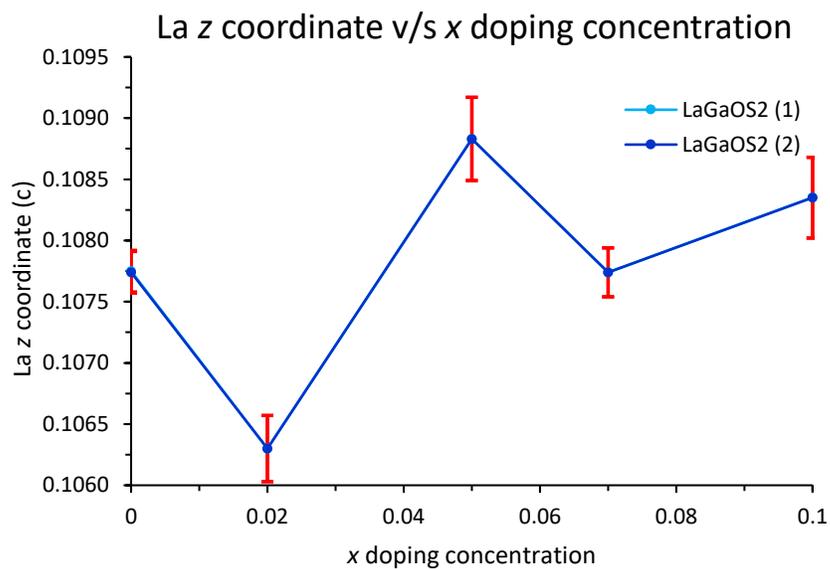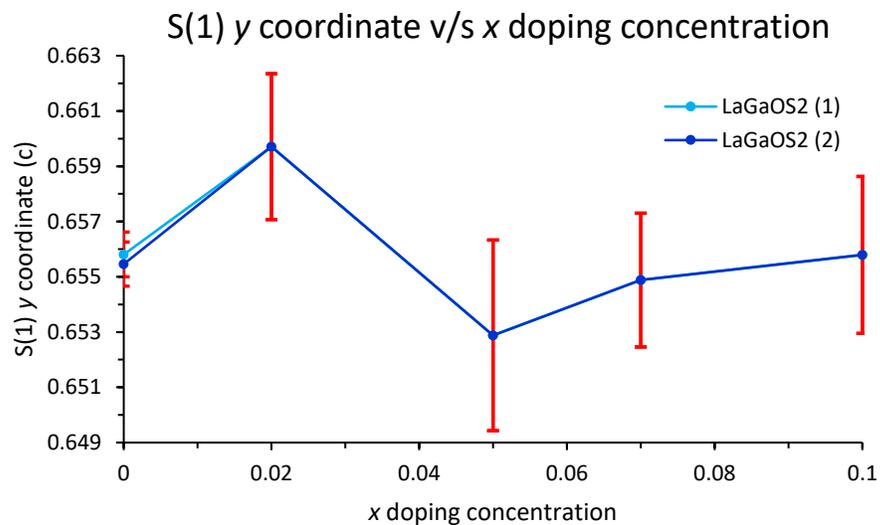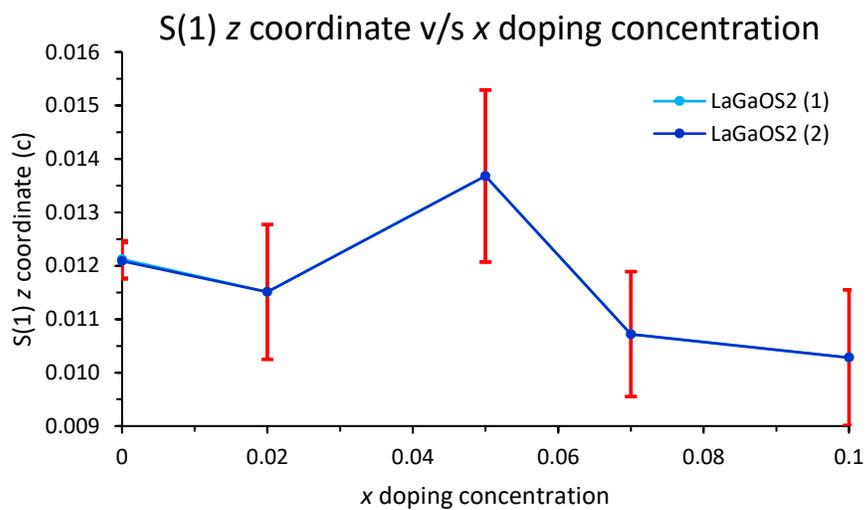

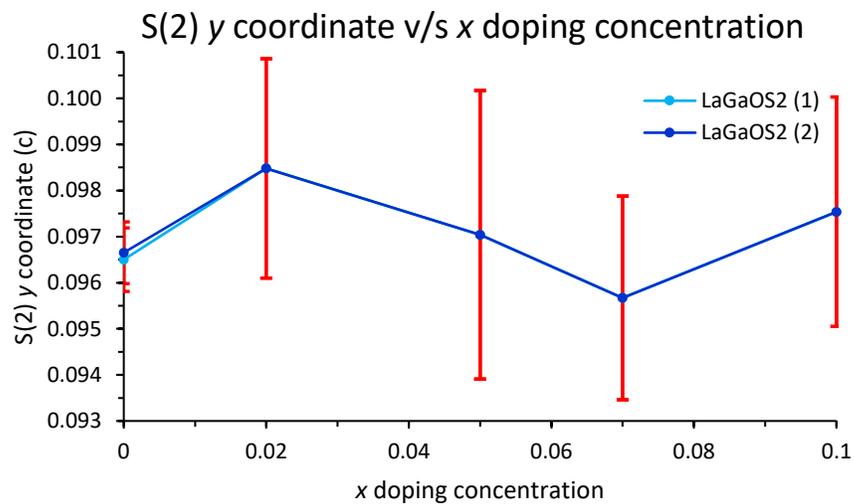Appendix 5.02 La z coordinate against x doping concentration for La$_{1-x}$Nd$_x$GaOS$_2$. Data for LaGaOS$_2$ (1) and LaGaOS$_2$ (2) are shown in pale-blue and blue respectively and error bars in red.
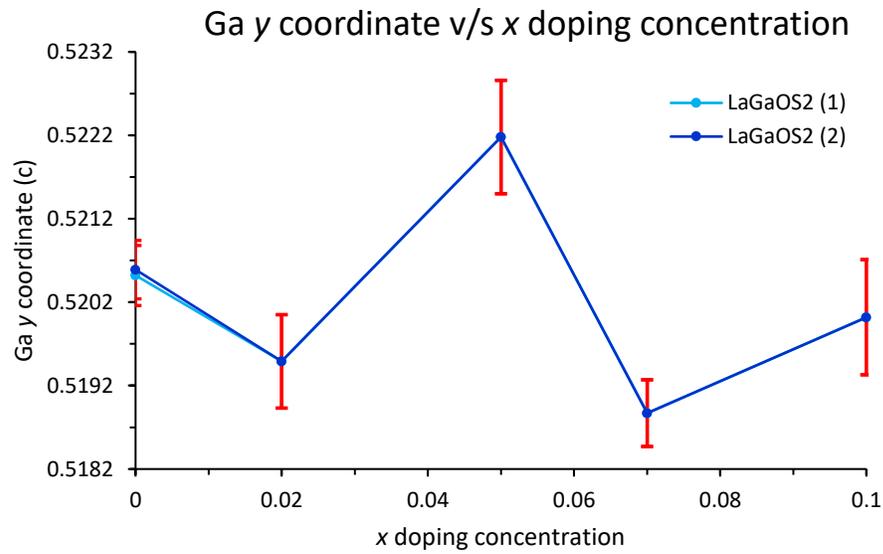
Appendix 5.02 Ga *y* coordinate against *x* doping concentration for $La_{1-x}Nd_xGaOS_2$. Data for $LaGaOS_2$ (1) and $LaGaOS_2$ (2) are shown in pale-blue and blue respectively and error bars in red.
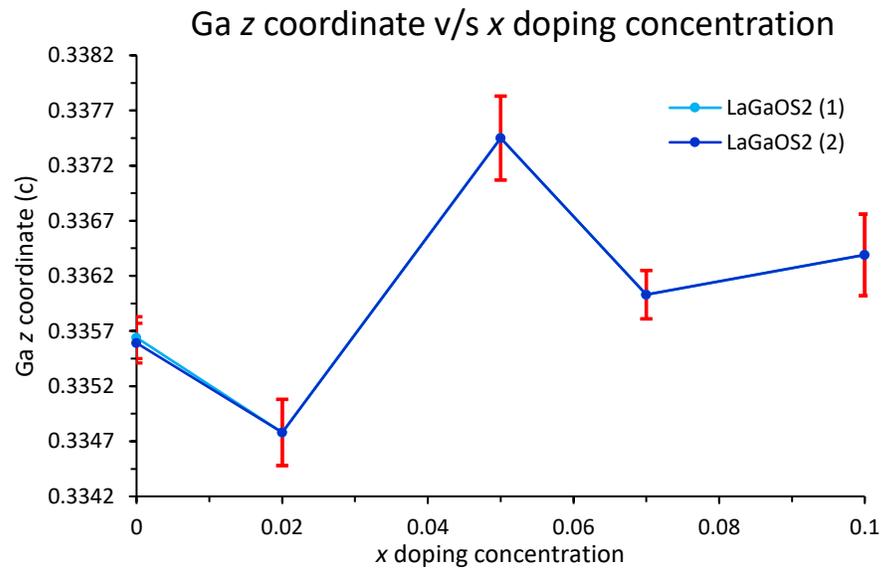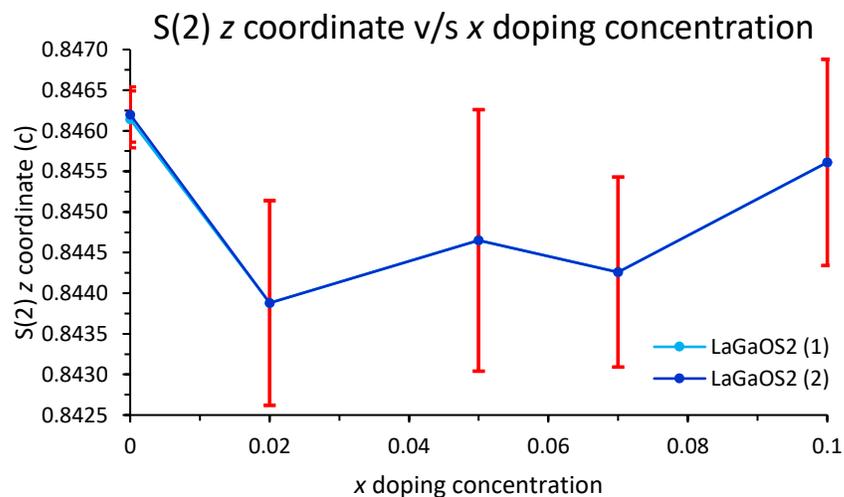

Appendix 5.02 Ga *z* coordinate against *x* doping concentration for $La_{1-x}Nd_xGaOS_2$. Data for $LaGaOS_2$ (1) and $LaGaOS_2$ (2) are shown in pale-blue and blue respectively and error bars in red.
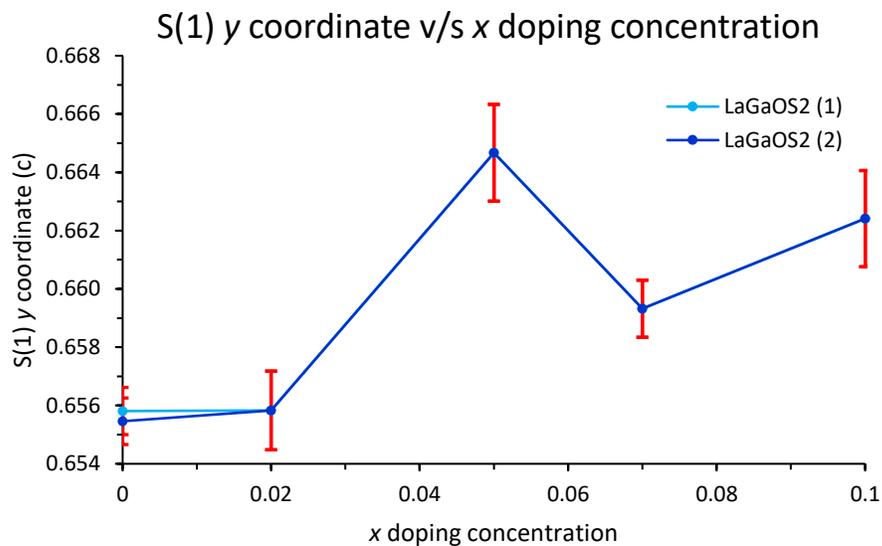
Appendix 5.02 S (1) y coordinate against x doping concentration for $La_{1-x}Nd_xGaOS_2$. Data for $LaGaOS_2$ (1) and $LaGaOS_2$ (2) are shown in pale-blue and blue respectively and error bars in red.
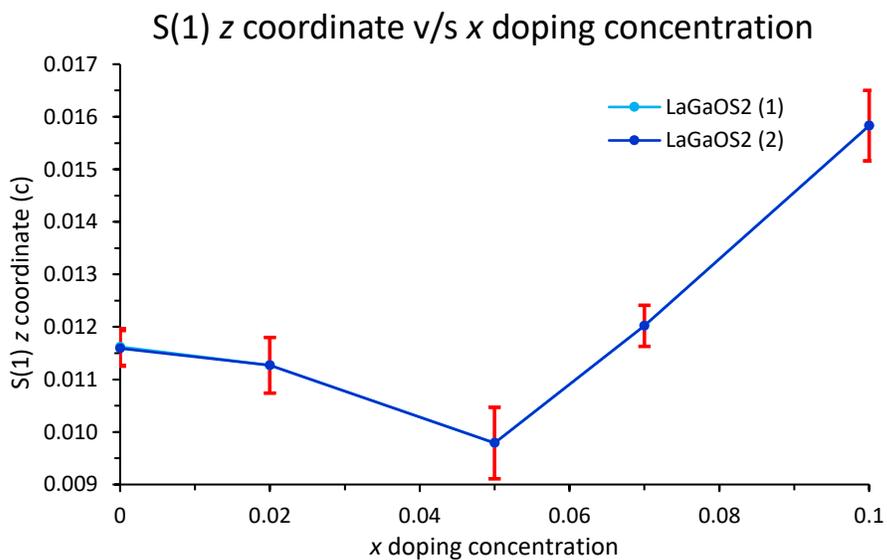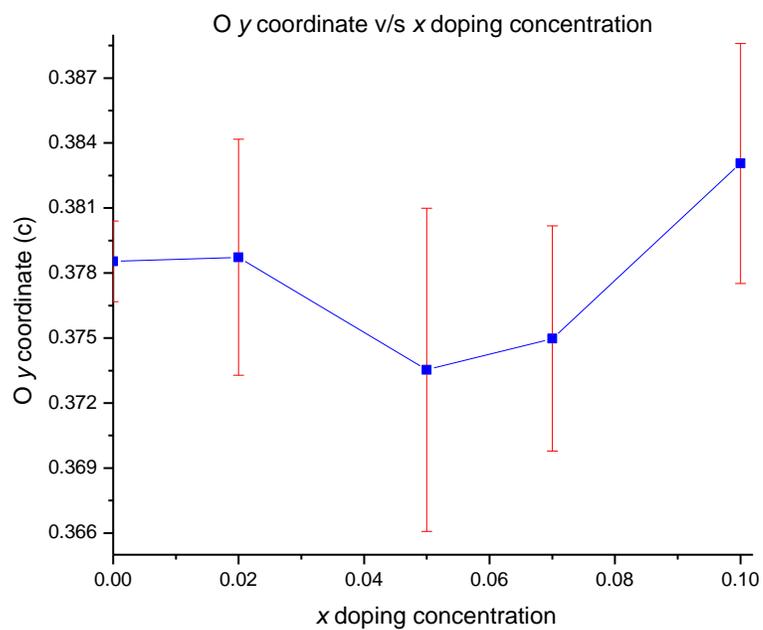

Appendix 5.02 S (1) z coordinate against x doping concentration for $La_{1-x}Nd_xGaOS_2$. Data for $LaGaOS_2$ (1) and $LaGaOS_2$ (2) are shown in pale-blue and blue respectively and error bars in red.
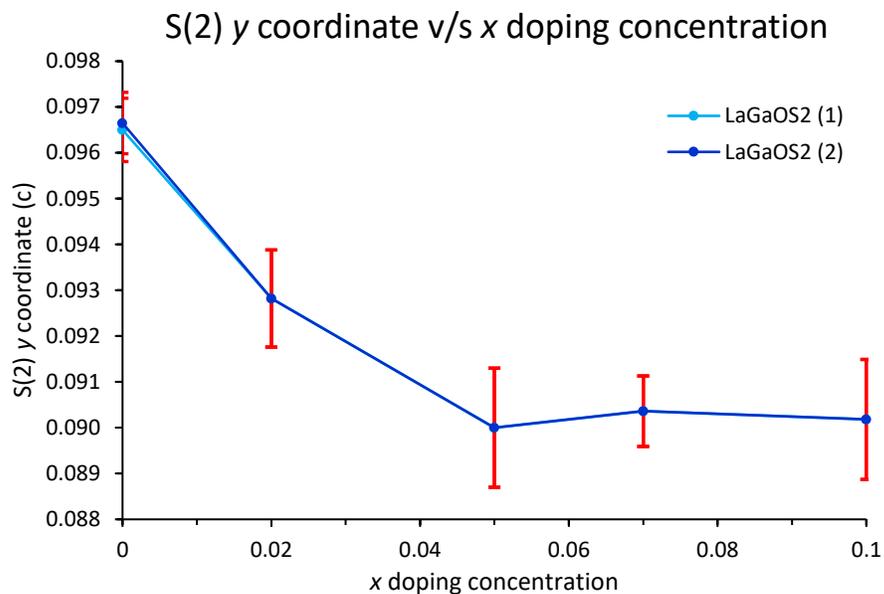
Appendix 5.02 S (2) *y* coordinate against *x* doping concentration for $La_{1-x}Nd_xGaOS_2$. Data for $LaGaOS_2$ (1) and $LaGaOS_2$ (2) are shown in pale-blue and blue respectively and error bars in red.
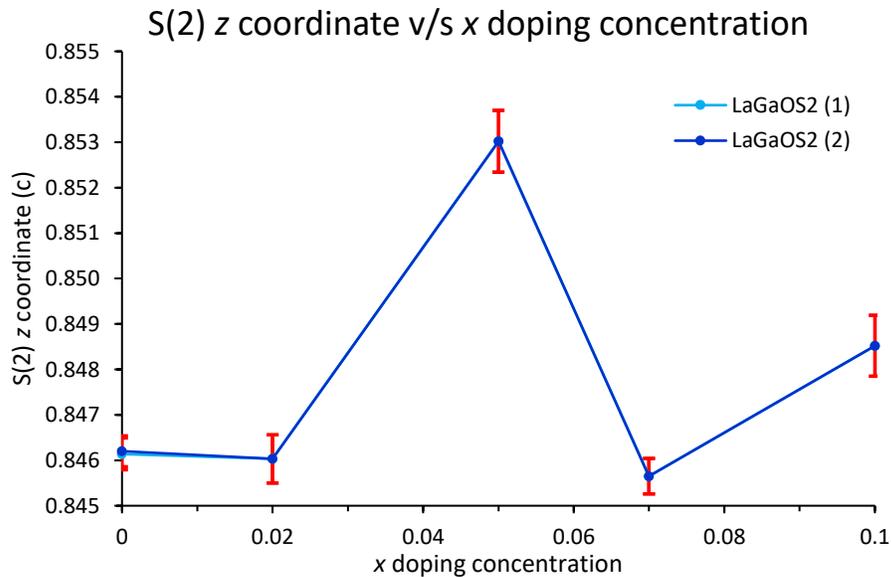

Appendix 5.02 S (2) *z* coordinate against *x* doping concentration for $La_{1-x}Nd_xGaOS_2$. Data for $LaGaOS_2$ (1) and $LaGaOS_2$ (2) are shown in pale-blue and blue respectively and error bars in red.
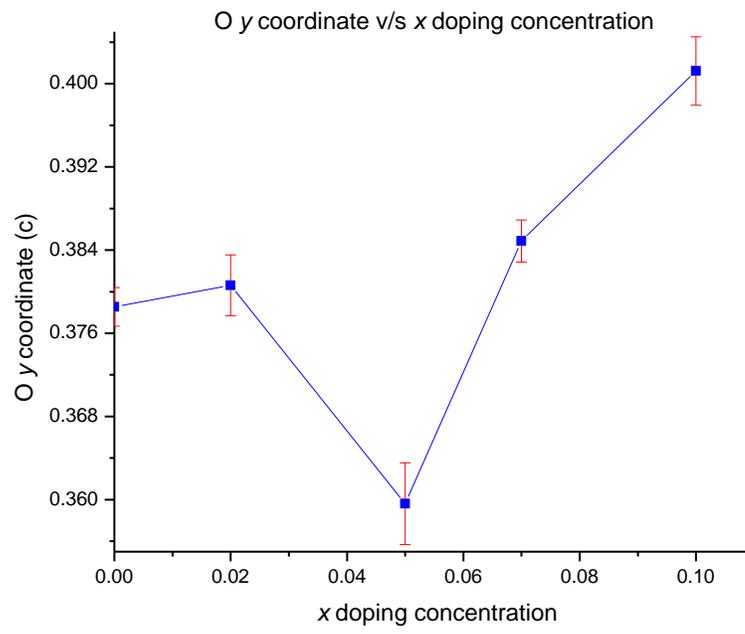
Appendix 5.02 O y coordinate against x doping concentration for $La_{1-x}Nd_xGaOS_2$. Data is shown in blue and error bars in red.
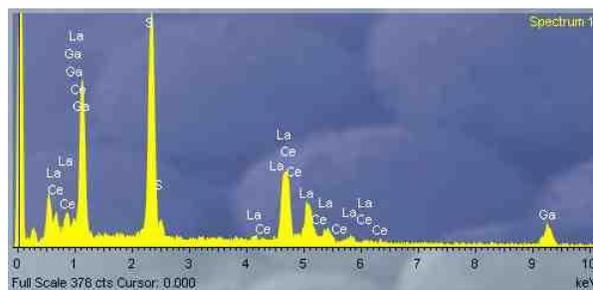
Appendix 5.03
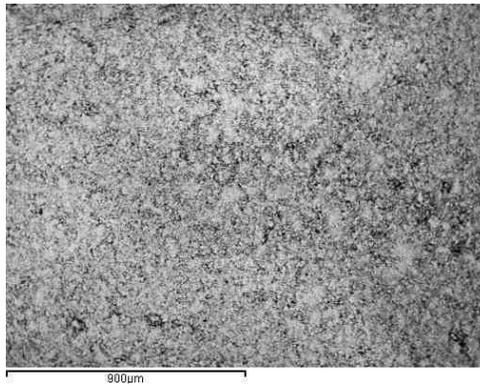
Appendix 5.03 Backscattered secondary electrons image of $La_{0.9}Nd_{0.1}GaOS_2$ taken at X70 magnification.

The sample was pressed into a pellet and divided into 10 sites. Each site was subjected to X878 magnification. Energy dispersive X-rays spectra were collected on each site at 10 different points
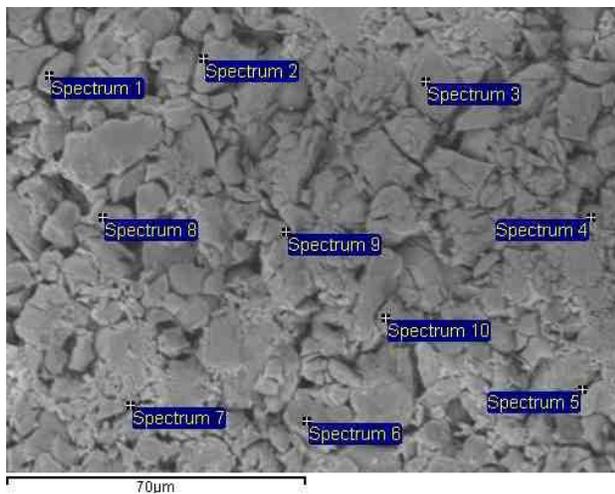
Appendix 5.03 Energy dispersive X-ray spectra collected at 10 different points on a site of $La_{0.9}Nd_{0.1}GaOS_2$ taken at X878 magnification.
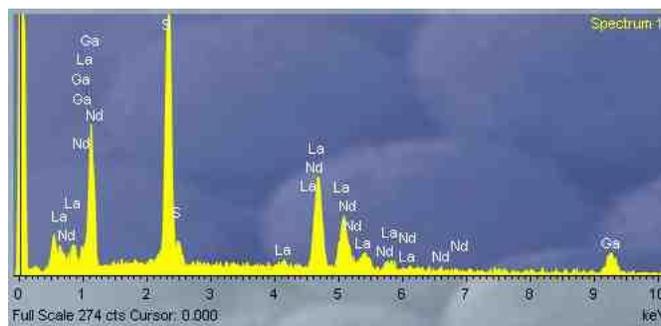

Appendix 5.03 Energy dispersive X-ray spectrum 1 showing the elements present at that point.
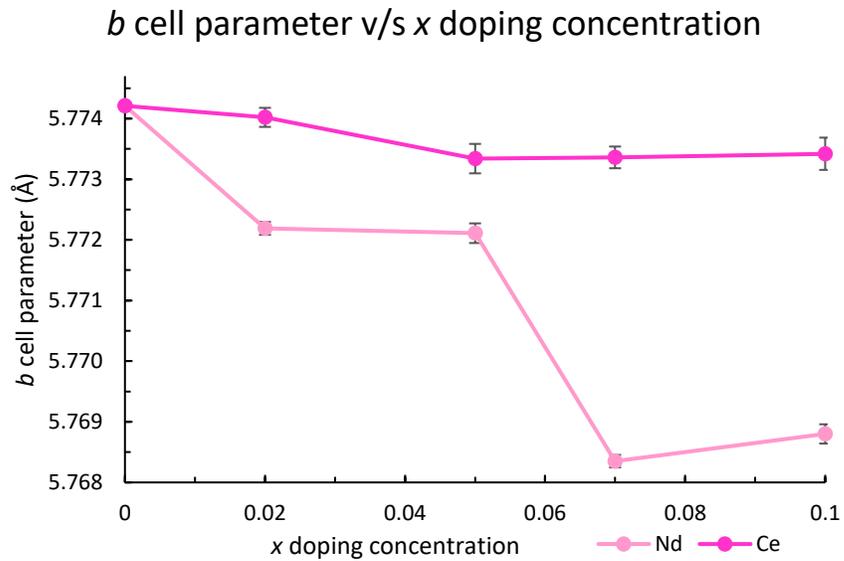
Appendix 5.04
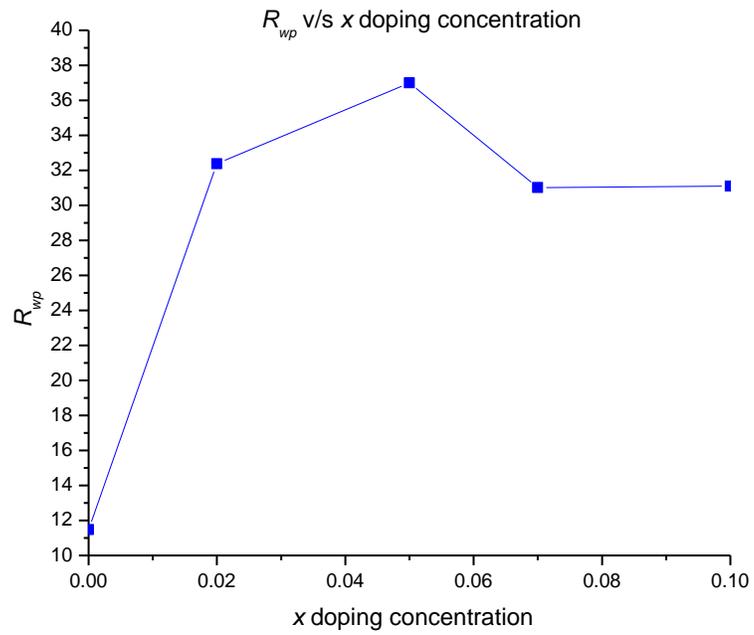
Appendix 5.04 R_{wp} against x doping concentration for La$_{1-x}$Ce$_x$GaOS$_2$. Data is shown in blue.
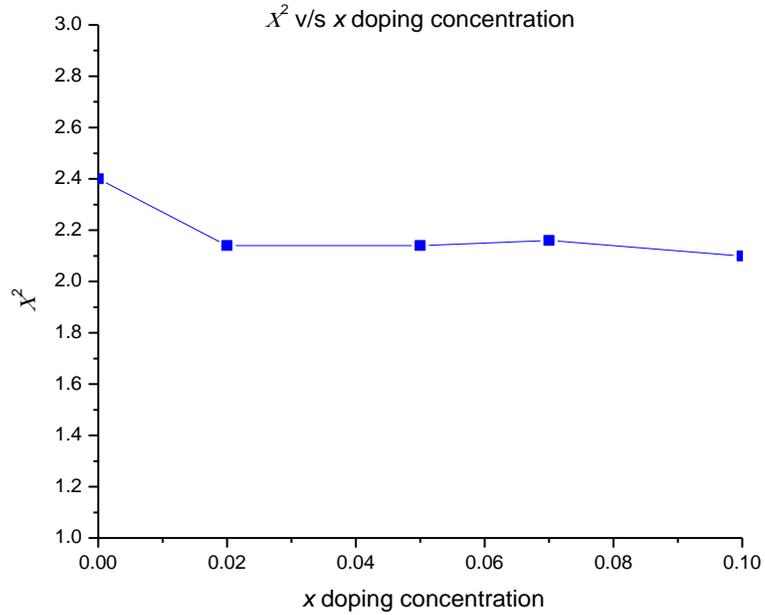
Appendix 5.04 χ^2 against x doping concentration for La$_{1-x}$Ce$_x$GaOS$_2$. Data is shown in blue.
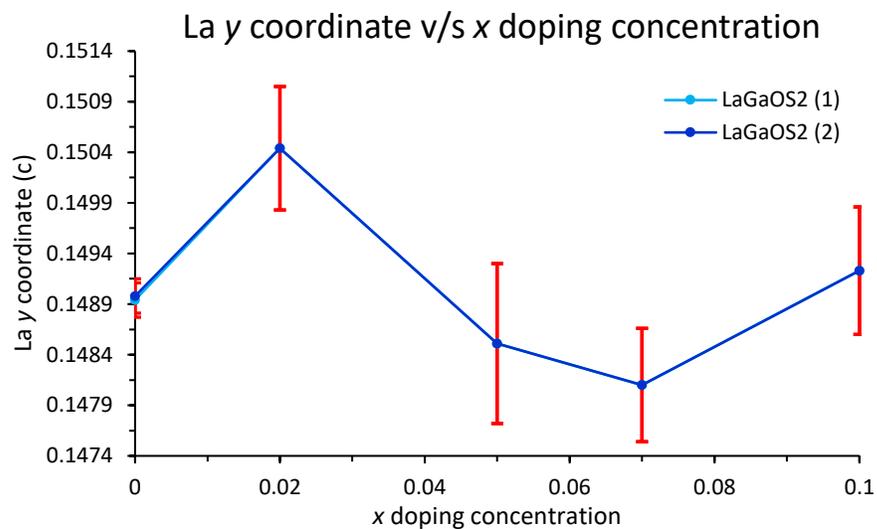
Appendix 5.04 La *y* coordinate against *x* doping concentration for La$_{1-x}$Ce$_x$GaOS$_2$. Data for LaGaOS$_2$ (1) and LaGaOS$_2$ (2) are shown in pale-blue and blue respectively and error bars in red.
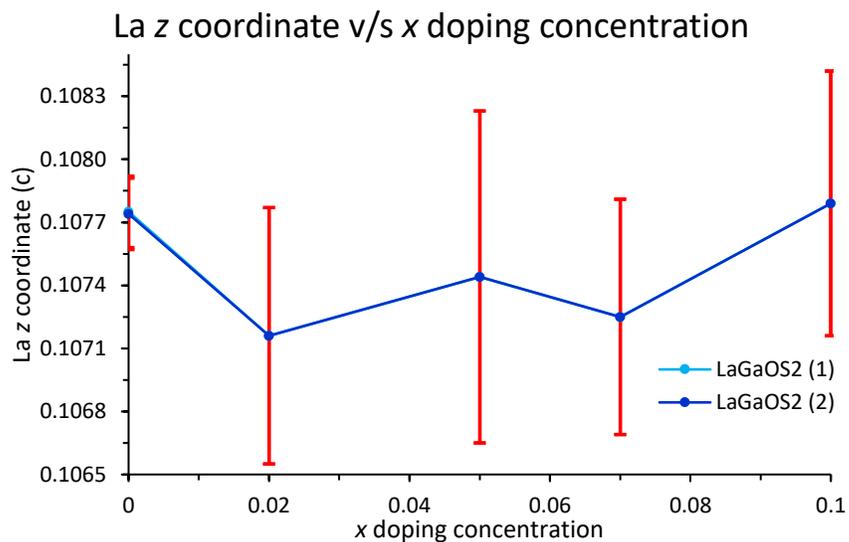
Appendix 5.04 La *z* coordinate against *x* doping concentration for La$_{1-x}$Ce$_x$GaOS$_2$. Data for LaGaOS$_2$ (1) and LaGaOS$_2$ (2) are shown in pale-blue and blue respectively and error bars in red.
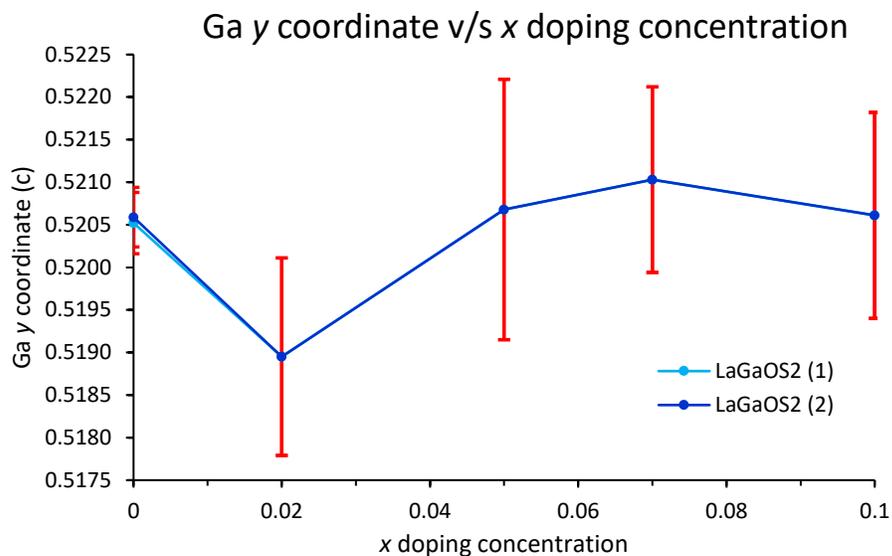
Appendix 5.04 Ga y coordinate against x doping concentration for $La_{1-x}Ce_xGaOS_2$. Data for $LaGaOS_2$ (1) and $LaGaOS_2$ (2) are shown in pale-blue and blue respectively and error bars in red.

Appendix 5.04 Ga z coordinate against x doping concentration for $La_{1-x}Ce_xGaOS_2$. Data for $LaGaOS_2$ (1) and $LaGaOS_2$ (2) are shown in pale-blue and blue respectively and error bars in red.

S(1) *y* coordinate v/s *x* doping concentration

Appendix 5.04 S (1) *y* coordinate against *x* doping concentration for $La_{1-x}Ce_xGaOS_2$. Data for $LaGaOS_2$ (1) and $LaGaOS_2$ (2) are shown in pale-blue and blue respectively and error bars in red.

S(1) *z* coordinate v/s *x* doping concentration

Appendix 5.04 S (1) *z* coordinate against *x* doping concentration for $La_{1-x}Ce_xGaOS_2$. Data for $LaGaOS_2$ (1) and $LaGaOS_2$ (2) are shown in pale-blue and blue respectively and error bars in red.

Appendix 5.04 S (2) y coordinate against x doping concentration for $La_{1-x}Ce_xGaOS_2$. Data for LaGaOS$_2$ (1) and LaGaOS$_2$ (2) are shown in pale-blue and blue respectively and error bars in red.

Appendix 5.04 S (2) z coordinate against x doping concentration for $La_{1-x}Ce_xGaOS_2$. Data for LaGaOS$_2$ (1) and LaGaOS$_2$ (2) are shown in pale-blue and blue respectively and error bars in red.

Appendix 5.04 O y coordinate against x doping concentration for $La_{1-x}Ce_xGaOS_2$. Data is shown in blue and error bars in red.
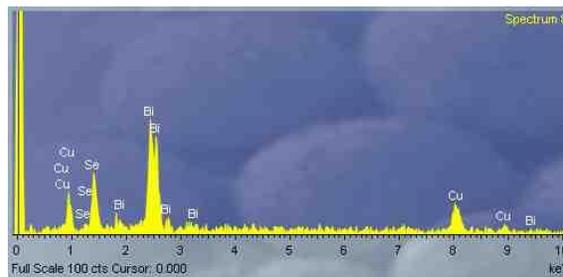
Appendix 5.05
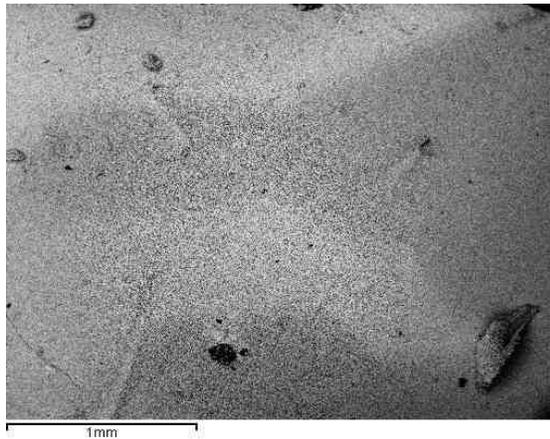
Appendix 5.05 Backscattered secondary electrons image of $La_{0.9}Ce_{0.1}GaOS_2$ taken at X44 magnification.

The sample was pressed into a pellet and divided into 10 sites. Each site was subjected to X894 magnification. Energy dispersive X-rays spectra were collected on each site at 10 different points
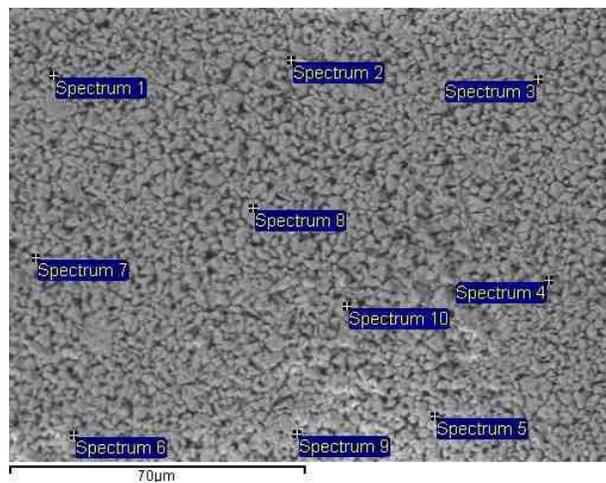

Appendix 5.05 Energy dispersive X-ray spectra collected at 10 different points on a site of $La_{0.9}Ce_{0.1}GaOS_2$ taken at X894 magnification.

Appendix 5.05 Energy dispersive X-ray spectrum 1 showing the elements present at that point.

272

Appendix 5.06

Name	Start BE (eV)	End BE (eV)	Height Counts/s	FWHM (eV)	Area (P) Counts/s.eV	Atomic %	Area (N) KE^0.6	PP Height CPS	PP Hgt (N)	PP At. %
S 2p Sulfide	164.88	157.18	2483.98	2.15	6083.55	95.91	48.76	2603.62	10.43	87.09
S 2p Oxidised	170.88	166.78	219.46	0.09	258.46	4.09	2.08	384.73	1.55	12.91

Appendix 5.06 XPS measurement showing S 2p data for La$_{0.9}$Ce$_{0.1}$GaOS$_2$.

Appendix 5.07

a cell parameter v/s *x* doping concentration
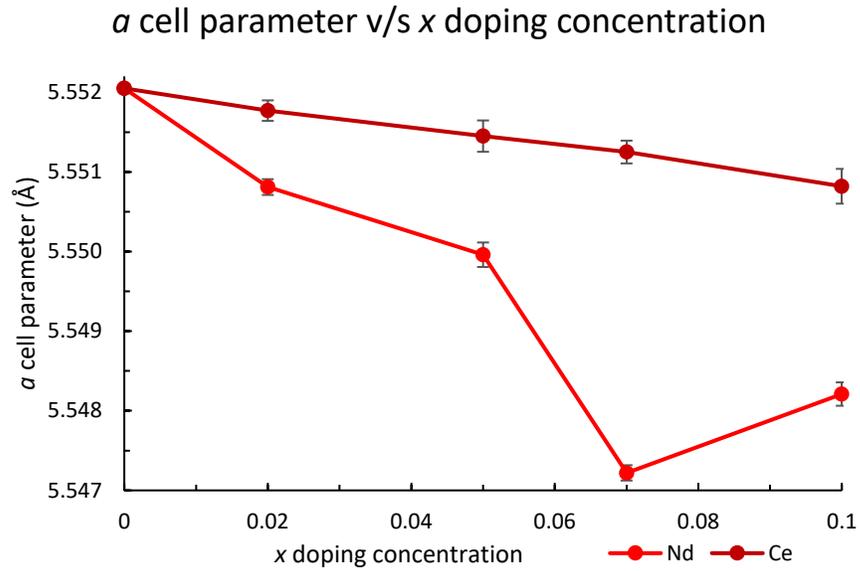
Appendix 5.07 *a* cell parameter against *x* doping concentration. Data for $La_{1-x}Nd_xGaOS_2$ is in red, $La_{1-x}Ce_xGaOS_2$ is in dark red and error bars are in black.

b cell parameter v/s *x* doping concentration

Appendix 5.07 *b* cell parameter against *x* doping concentration. Data for $La_{1-x}Nd_xGaOS_2$ is in light pink, $La_{1-x}Ce_xGaOS_2$ is in pink and error bars are in black.

c cell parameter v/s x doping concentration
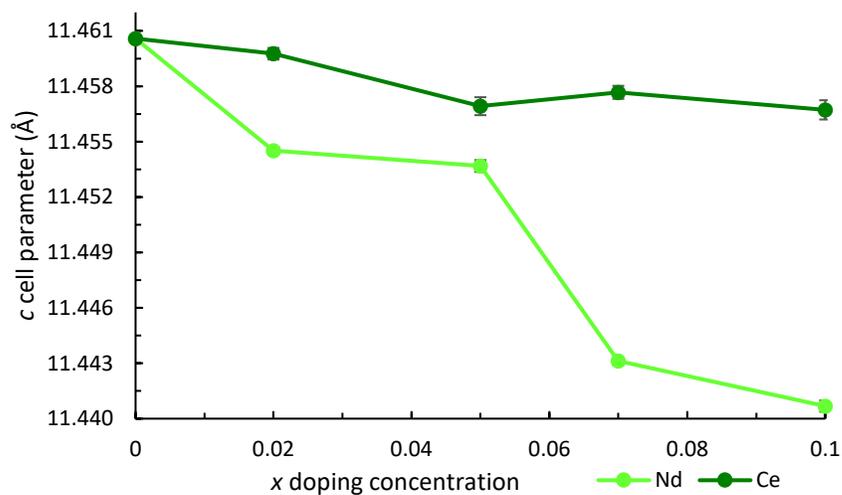
Appendix 5.07 *c* cell parameter against *x* doping concentration. Data for $La_{1-x}Nd_xGaOS_2$ is in green, $La_{1-x}Ce_xGaOS_2$ is in dark green and error bars are in black.

Volume v/s x doping concentration
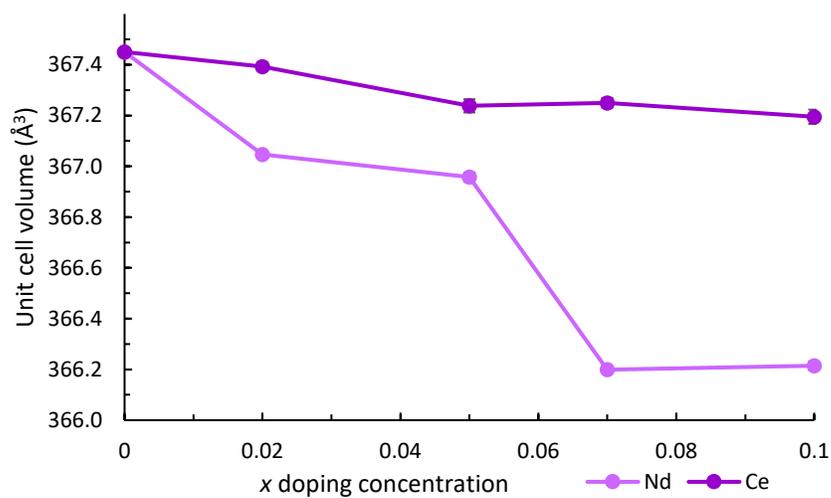
Appendix 5.07 Unit cell volume against *x* doping concentration. Data for $La_{1-x}Nd_xGaOS_2$ is in pale purple, $La_{1-x}Ce_xGaOS_2$ is in purple and error bars are in black.

Appendix 6.01
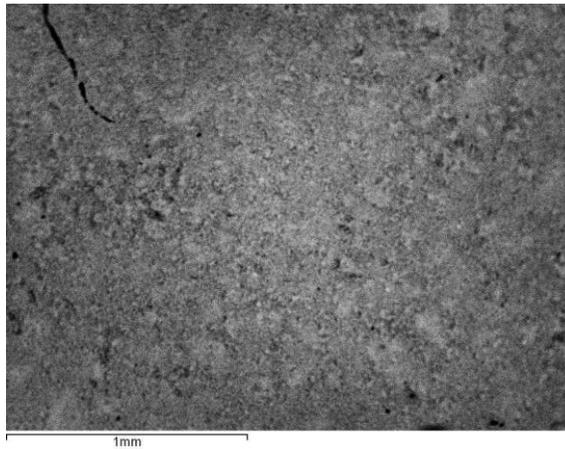

Appendix 6.01 Backscattered secondary electrons image of BiCuOSe taken at X54 magnification.

The sample was pressed into a pellet and divided into 12 sites. Each site was subjected to X900 magnification. Energy dispersive X-rays spectra were collected on each site at 10 different points
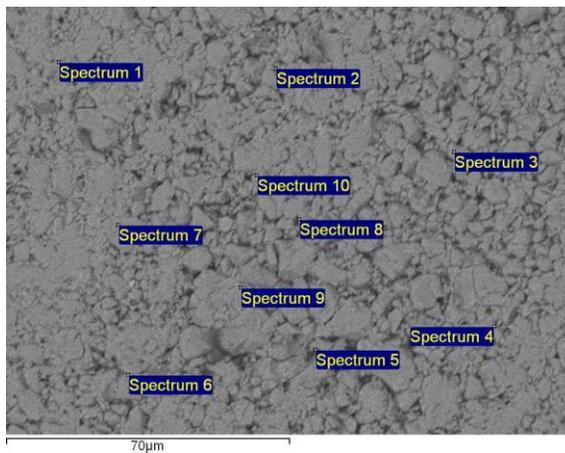

Appendix 6.01 Energy dispersive X-ray spectra collected at 10 different points on a site of BiCuOSe taken at X900 magnification.


Appendix 6.01 Energy dispersive X-ray spectrum 8 showing the elements present at that point.

Appendix 6.02
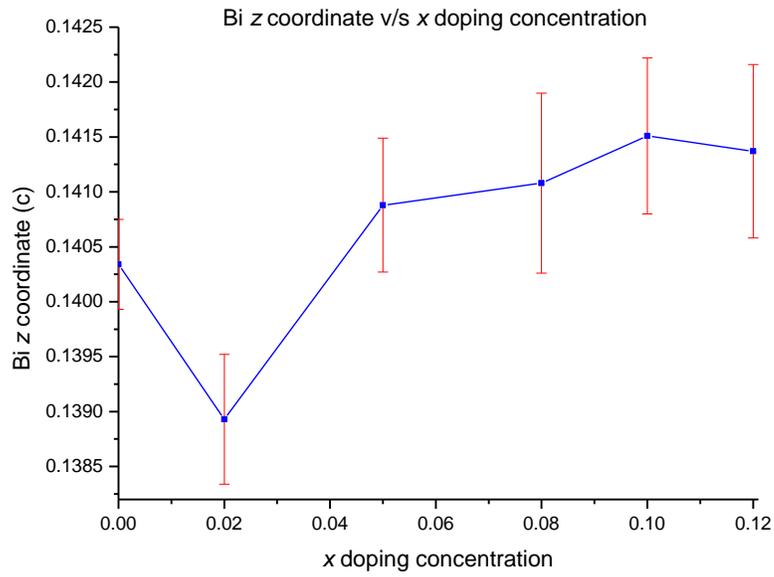
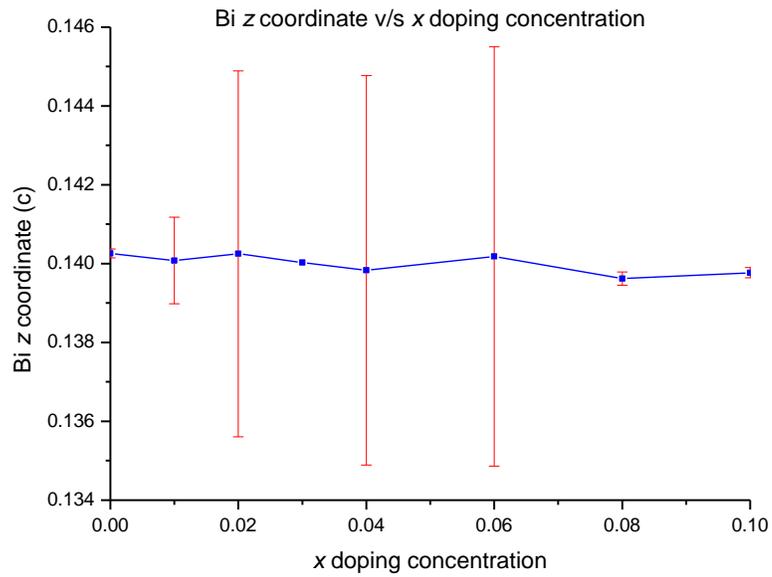Appendix 6.02 Bi z coordinate against x doping concentration for $BiCuO_{1-x}F_xSe$. Data is shown in blue and error bars in red
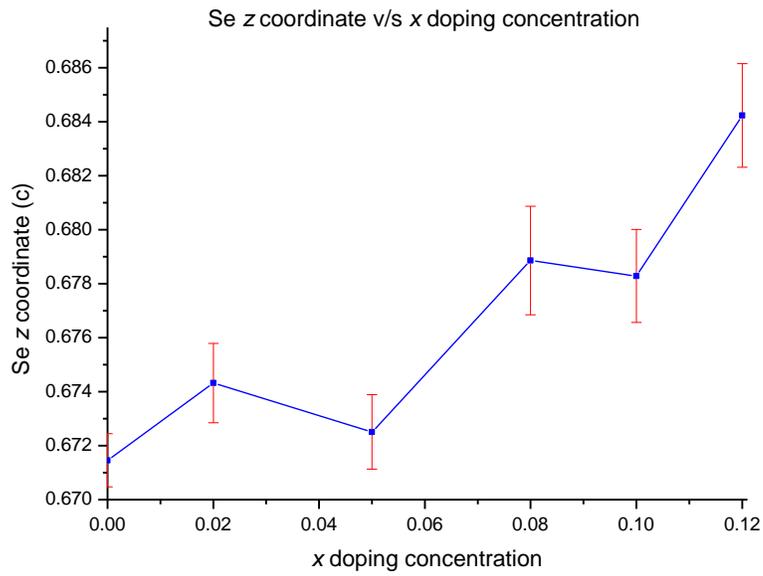
Appendix 6.02 Se z coordinate against x doping concentration for $BiCuO_{1-x}F_xSe$. Data is shown in blue and error bars in red
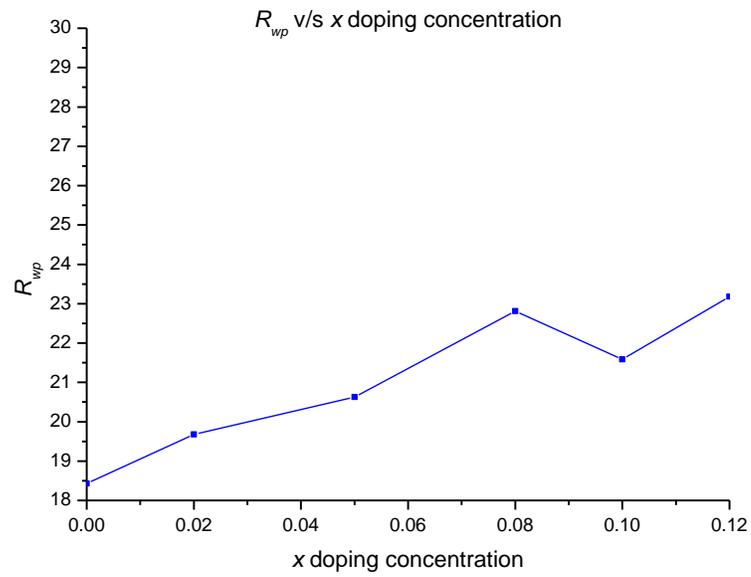
Appendix 6.02 R_{wp} against x doping concentration for $BiCuO_{1-x}F_xSe$. Data is shown in blue.
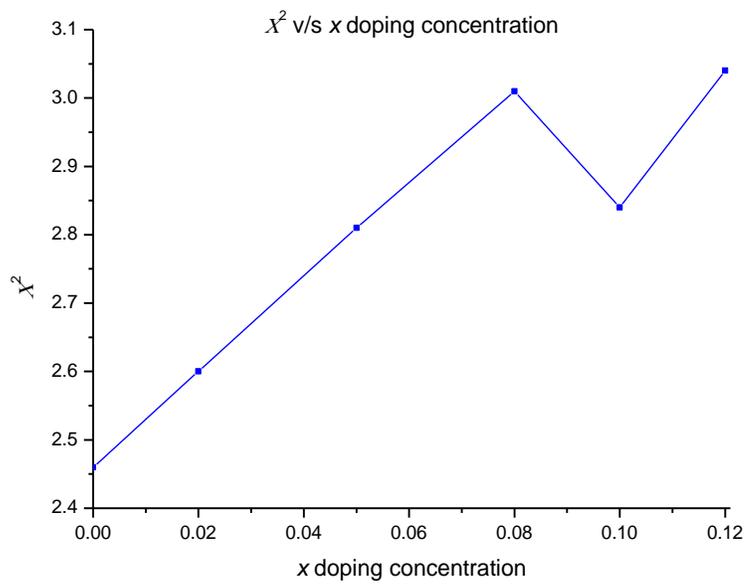
Appendix 6.02 χ^2 against x doping concentration for $BiCuO_{1-x}F_xSe$. Data is shown in blue.

Appendix 6.03
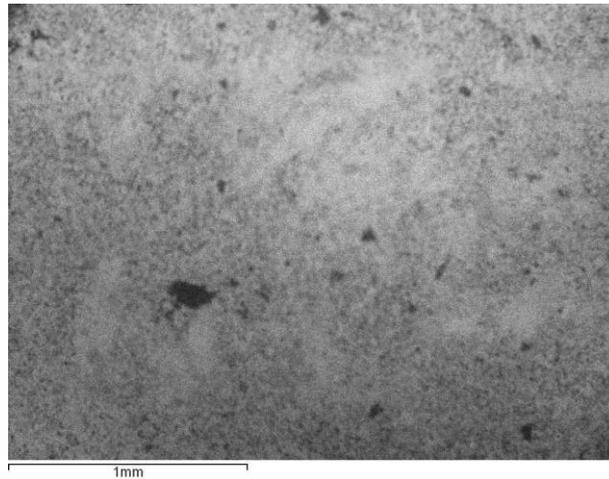
Appendix 6.03 Backscattered secondary electrons image of $BiCuO_{0.9}F_{0.1}Se$ taken at X50 magnification.

The sample was pressed into a pellet and divided into 10 sites. Each site was subjected to X201 magnification. Energy dispersive X-rays spectra were collected on each site at 10 different points
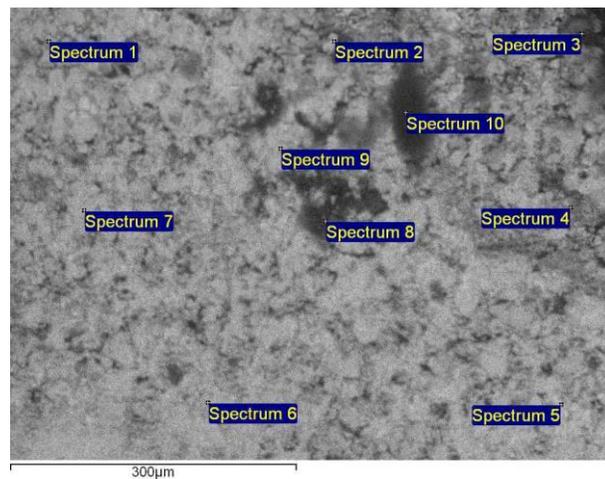
Appendix 6.03 Energy dispersive X-ray spectra collected at 10 different points on a site of $BiCuO_{0.9}F_{0.1}Se$ taken at X201 magnification.
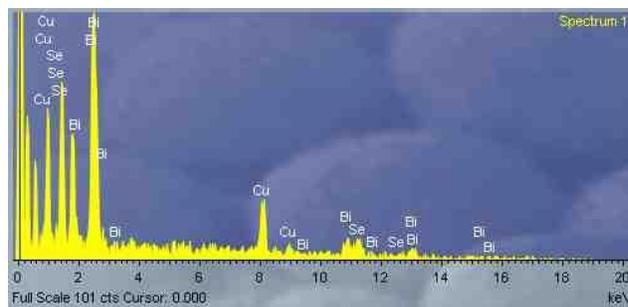
Appendix 6.03 Energy dispersive X-ray spectrum 1 showing the elements present at that point.

Appendix 6.04
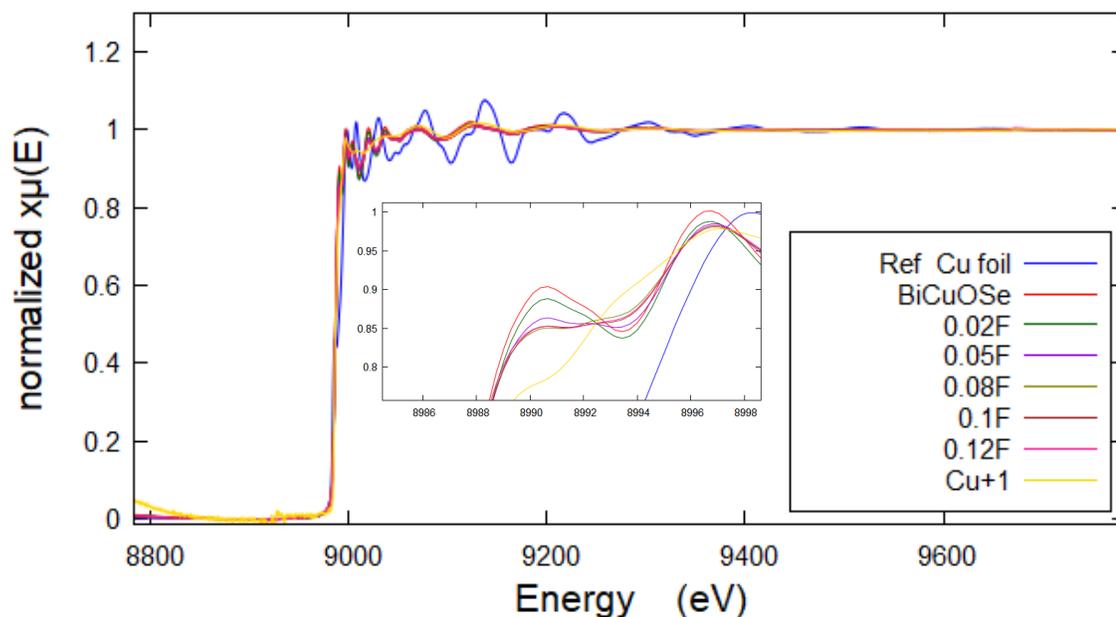
Appendix 6.04 Cu-*K* edge normalised energy spectra for BiCuO$_{1-x}$F$_x$Se for the Cu foil (blue), Cu^{+1} standard (yellow), pristine sample (red) and all the F-doped samples. The trend in intensity in the main edge is shown in the zoomed fit.
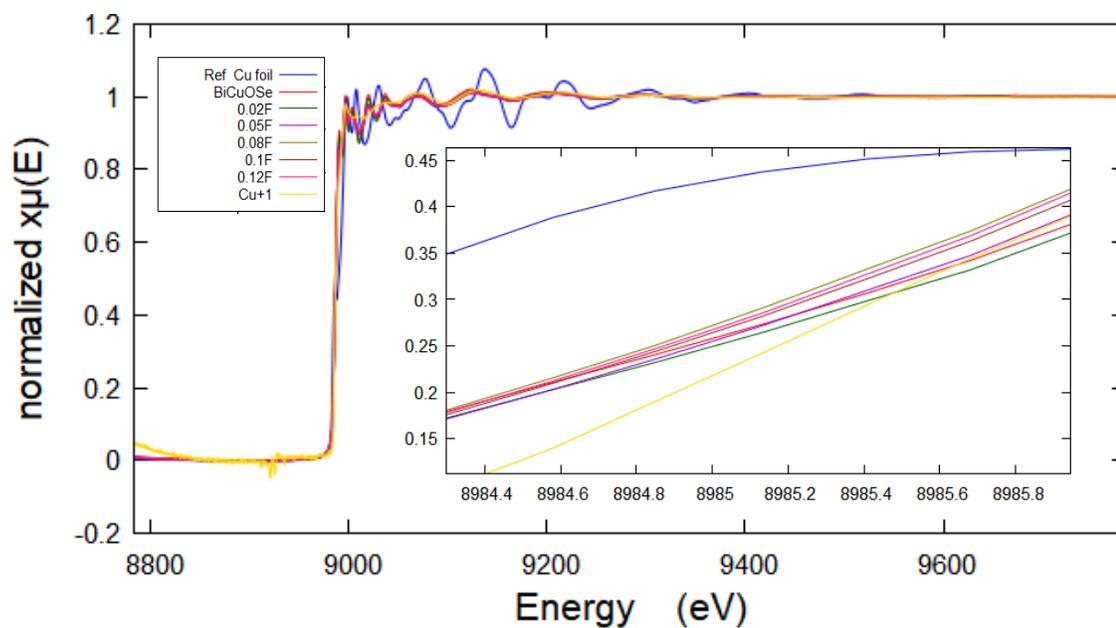

Appendix 6.04 Cu-*K* edge normalised energy spectra for BiCuO$_{1-x}$F$_x$Se for the Cu foil (blue), Cu^{+1} standard (yellow), pristine sample (red) and all the F-doped samples. The trend in intensity in the pre-edge is shown in the zoomed fit.

Appendix 6.05

Appendix 6.05 Bi z coordinate against x doping concentration for $Bi_{1-x}Ce_xCuOSe$. Data is shown in blue and error bars in red
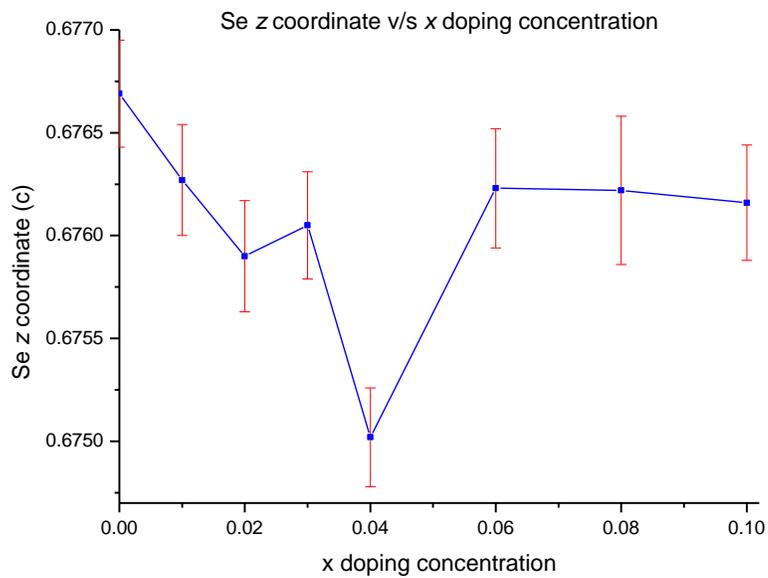
Appendix 6.05 Se z coordinate against x doping concentration for $Bi_{1-x}Ce_xCuOSe$. Data is shown in blue and error bars in red
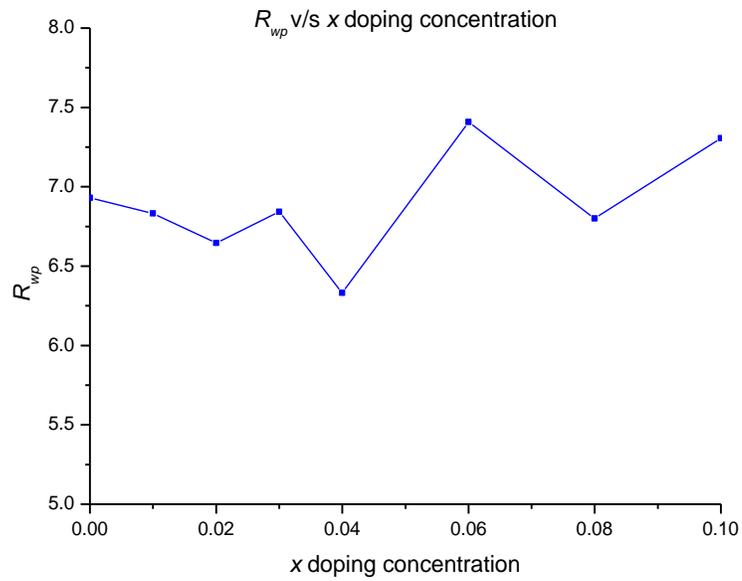
Appendix 6.05 R_{wp} against x doping concentration for $Bi_{1-x}Ce_xCuOSe$. Data is shown in blue.
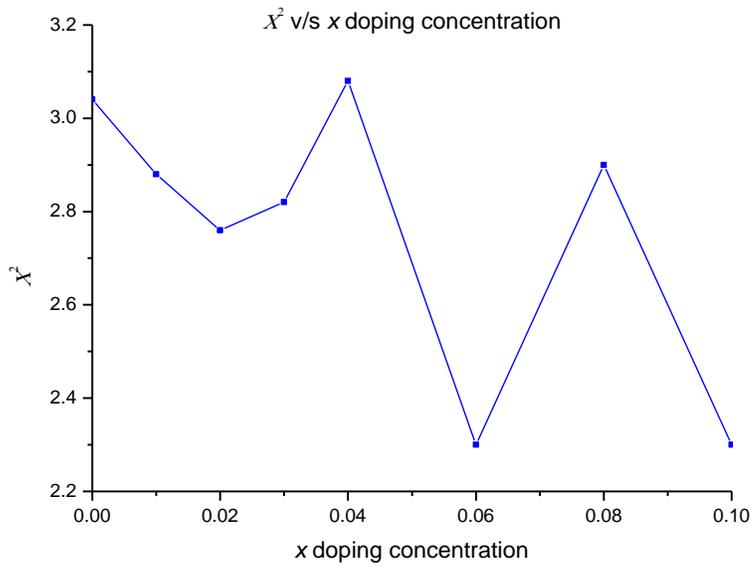
Appendix 6.05 χ^2 against x doping concentration for $Bi_{1-x}Ce_xCuOSe$. Data is shown in blue.

Appendix 6.06
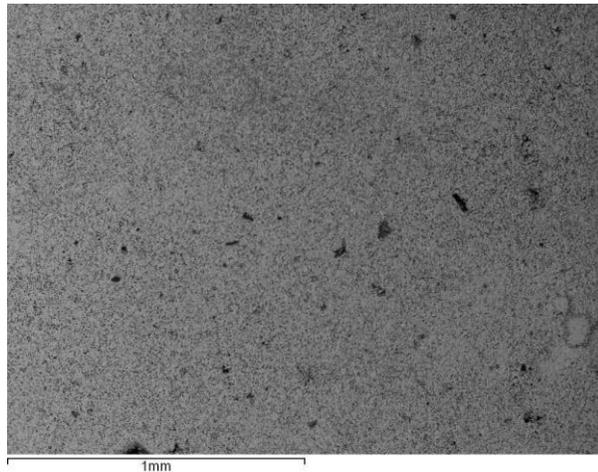
Appendix 6.06 Backscattered secondary electrons image of $Bi_{0.97}Ce_{0.03}CuOSe$ taken at X63 magnification.

The sample was pressed into a pellet and divided into 10 sites. Each site was subjected to X200 magnification. Energy dispersive X-rays spectra were collected on each site at 10 different points
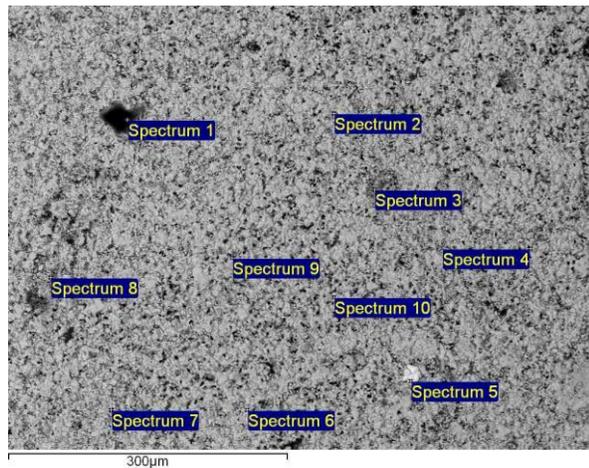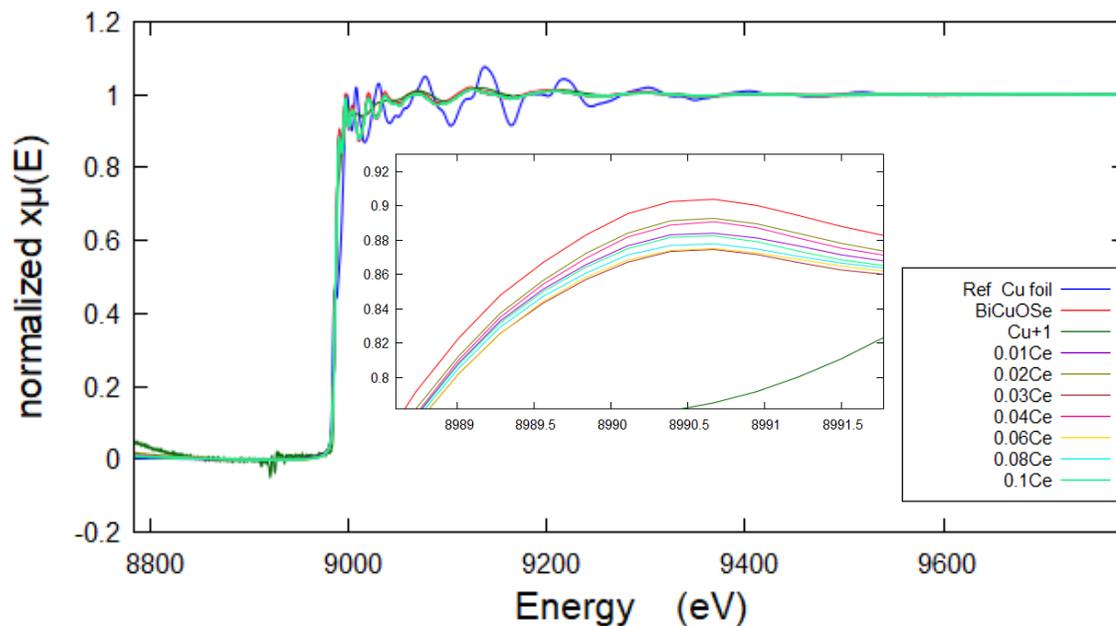

Appendix 6.06 Energy dispersive X-ray spectra collected at 10 different points on a site of $Bi_{0.97}Ce_{0.03}CuOSe$ taken at X200 magnification.
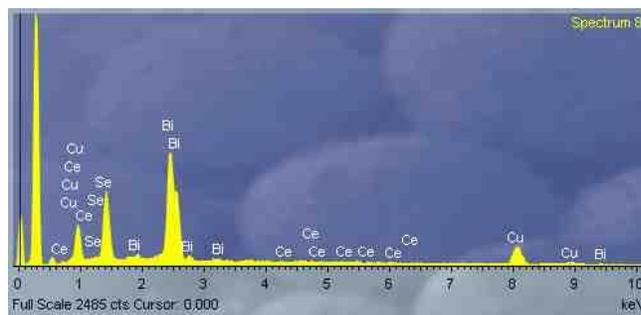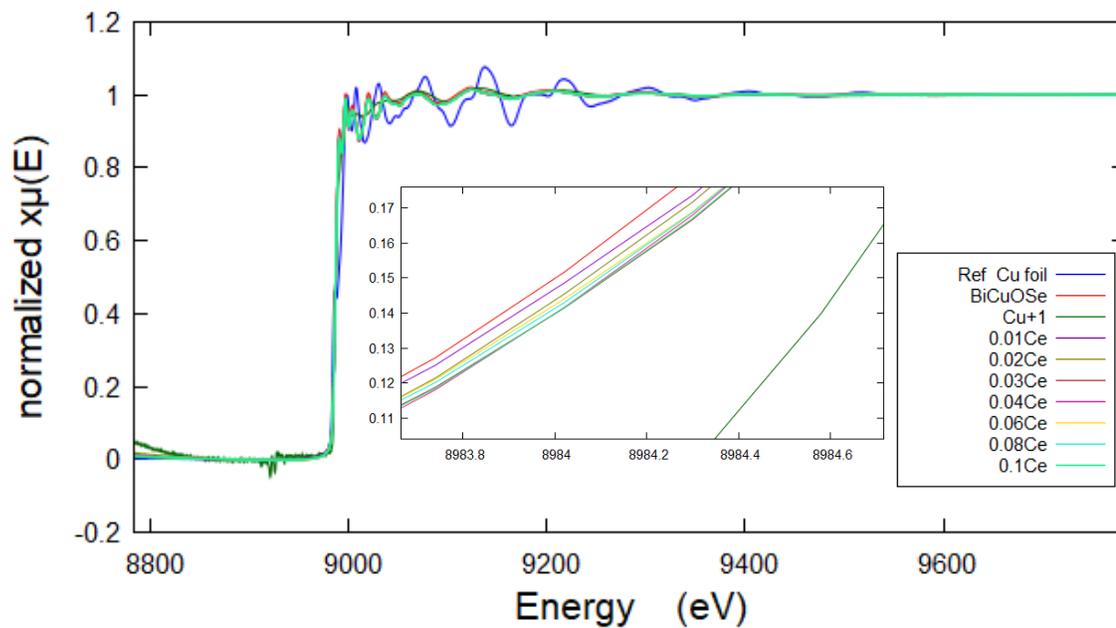

Appendix 6.06 Energy dispersive X-ray spectrum 8 showing the elements present at that point.
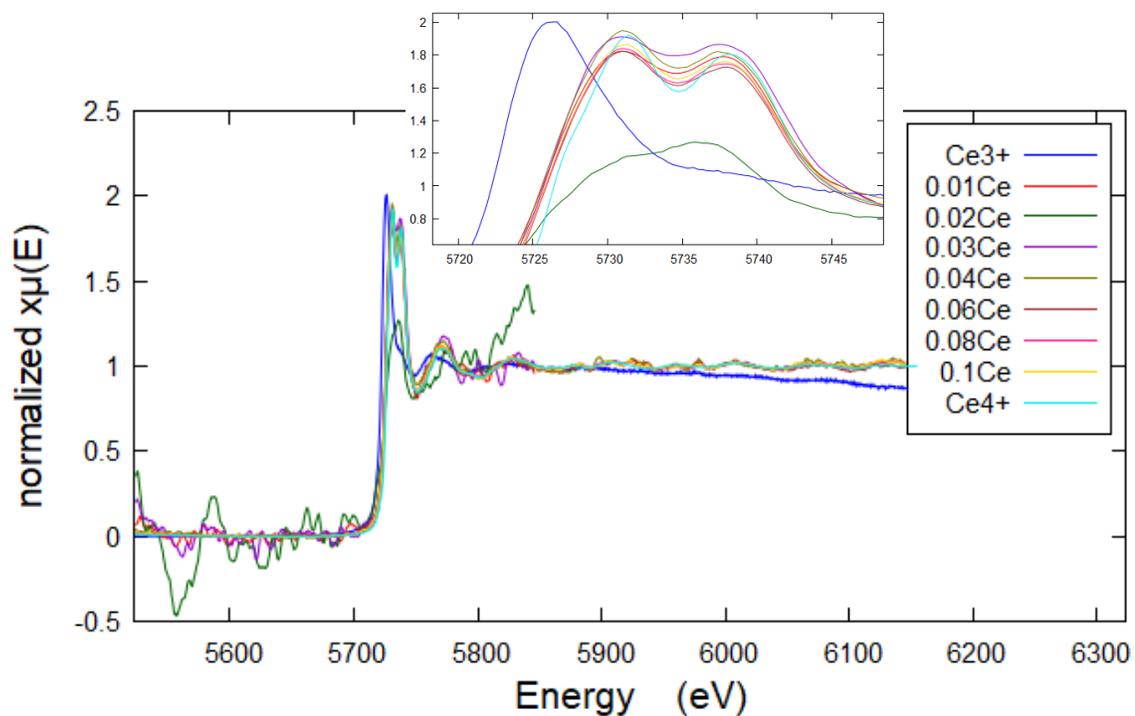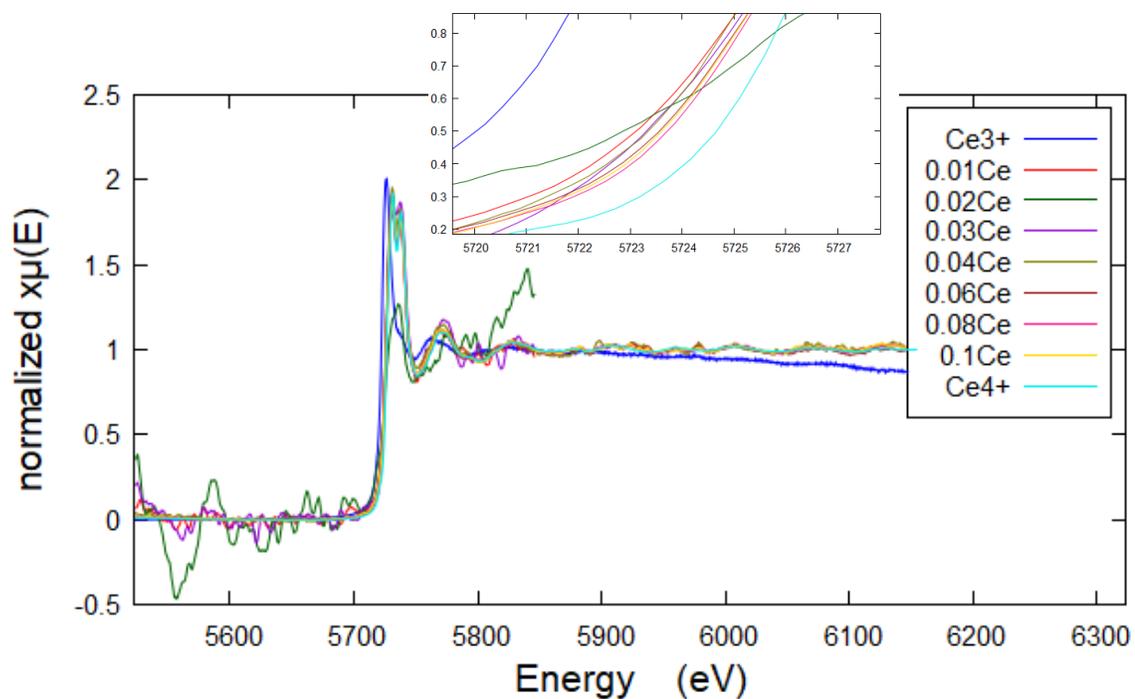
Appendix 6.07

Appendix 6.07 Cu-*K* edge normalised energy spectra for $Bi_{1-x}Ce_xCuOSe$ for the Cu foil (blue), Cu^{+1} standard (dark-green), pristine sample (red) and all the Ce-doped samples. The trend in intensity in the main edge is shown in the zoomed fit.


Appendix 6.07 Cu-*K* edge normalised energy spectra for $Bi_{1-x}Ce_xCuOSe$ for the Cu foil (blue), Cu^{+1} standard (dark-green), pristine sample (red) and all the Ce-doped samples. The trend in pre-edge is shown in the zoomed fit.

Appendix 6.07 Ce-L_3 edge normalised energy spectra for $Bi_{1-x}Ce_xCuOSe$ for the Ce^{+3} standard (blue), Ce^{+4} standard (aqua) and all the Ce-doped samples. The trend in intensity in the main edge is shown in the zoomed fit. The Ce samples have doublet peaks in the main edge suggesting presence of Ce^{4+}

Appendix 6.07 Ce-L_3 edge normalised energy spectra for $Bi_{1-x}Ce_xCuOSe$ for the Ce^{+3} standard (blue), Ce^{+4} standard (aqua) and all the Ce-doped samples. The trend in the pre-edge is shown in the zoomed fit.
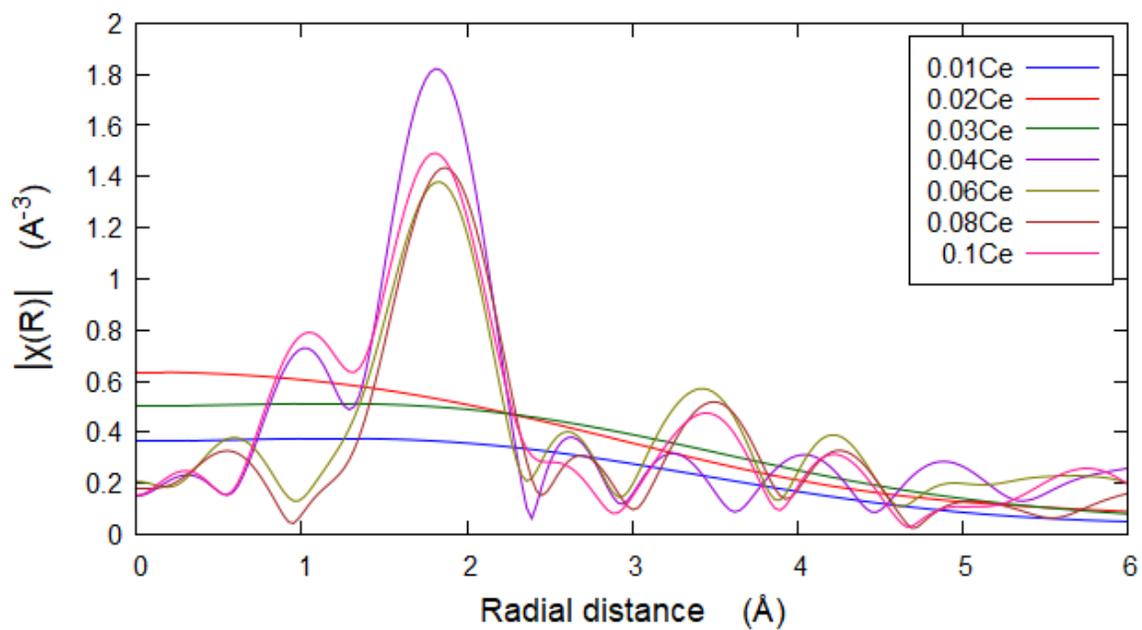
Appendix 6.07 k^3-weighted derivatives for $Bi_{1-x}Ce_xCuOSe$
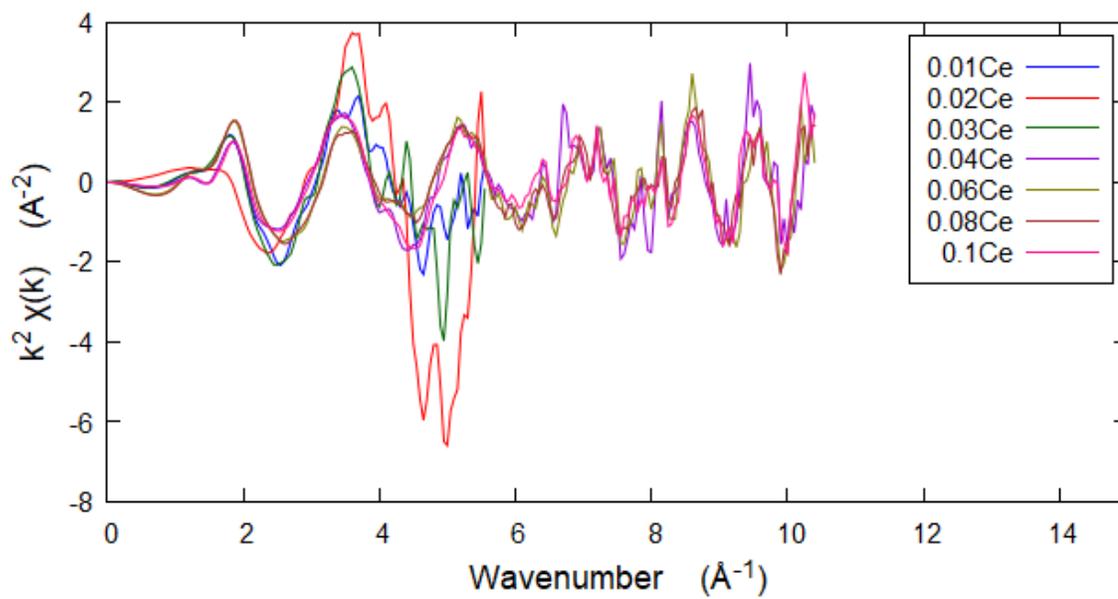
Appendix 6.07 Radial distributions for $Bi_{1-x}Ce_xCuOSe$